Nonreciprocal Transport Properties of Solid State Quantum Devices

Von der Fakultät für Elektrotechnik und Informationstechnik der Rheinisch-Westfälischen Technischen Hochschule Aachen zur Erlangung des akademischen Grades eines

Doktors der Naturwissenschaften

genehmigte Dissertation vorgelegt von

Philipp Bredol (M.Sc.)

aus Aachen

Berichter: Univ.-Professorin Dr. rer. nat. Regina Dittmann
Univ.-Professor Dr. rer. nat. Jochen Mannhart

Tag der mündlichen Prüfung 30.11.2021

Diese Dissertation ist auf den Internetseiten der Universitätsbibliothek online verfügbar.

Contents

1 Introduction **1**

2 Mesoscopic Transport Phenomena **5**
2.1 Aharonov-Bohm Oscillations 6
2.2 Universal Conductance Fluctuations 9
2.3 Conductance Quantization 11
2.4 Weak Localization 12
2.5 Summary 14

3 Scattering Theory and Application to Transport **15**
3.1 Eigenfunctions and Scattering States 15
3.2 The S-Matix and its Symmetries 19
3.3 Two-Lead Landauer-Büttiker Formula 23
3.4 Transport with Wave Packets 26
3.5 Wave-Packet Scattering Delay 29
3.6 Scattering Model of Example Systems 31
3.6.1 Symmetric and Asymmetric Potential Barriers 32
3.6.2 Aharonov-Bohm Interferometers 43
3.6.3 Disordered Conductors 52
3.7 Summary 59

4 Theoretical Description of Decoherence **61**
4.1 Decoherence in the Landauer-Büttiker Model 64
4.2 Quantum Trajectories 65
4.3 Lindblad Master Equation 68
4.4 Correspondence of Quantum Trajectories and the Lindblad Master Equation 70
4.5 Summary 72

5 Numerical Implementation of Stochastic Tight-Binding Schrödinger Equations **75**
5.1 Tight-Binding Models 76
5.2 Time Evolutions of Infinite Systems 81
5.2.1 Algorithm with Linear Scaling 82

5.2.2 The Probability Current in Tight-Binding Systems 86
5.2.3 Summary 88
5.3 Stochastic Dynamics 88
5.4 Benchmarking the Stochastic Model Against the Master Equation 93
5.5 Decoherence-Induced Nonreciprocal Transmission Probabilities 97
5.5.1 Potential Barriers 97
5.5.2 Quantum Dots 103
5.5.3 Asymmetric Aharonov-Bohm Interferometer 109
5.6 Summary 114

6 Comparison of the Novel Nonreciprocal Transport With the Transport Behavior Known Before 117

7 Magnetotransport Studies of Mesoscopic Gold Structures 119
7.1 Sample Preparation 120
7.2 Measurement Setup 121
7.3 Experimental Results 125
7.3.1 Residual Resistance Ratio 125
7.3.2 Universal Conductance Fluctuations 125
7.3.3 Aharonov-Bohm Oscillations 129
7.4 Discussion and Summary 134

8 Discussion and Outlook 135
8.1 Model Calculations 135
8.2 Experiments 137

9 Literature 139

Acronyms 151

Symbols 153

Acknowledgements 159

A Importable Expressions 161
A.1 Symmetric Potential Barrier 161
A.1.1 Reflection Coefficient $s_{11} = s_{22}$ 161
A.1.2 Transmission Coefficient $s_{12} = s_{21}$ 161
A.2 Asymmetric Potential Barrier 162
A.2.1 Left Side Reflection Coefficient s_{11} 162
A.2.2 Right Side Reflection Coefficient s_{22} 164
A.2.3 Transmission Coefficient $s_{12} = s_{21}$ 166
A.3 Aharonov-Bohm Interferometer 167
A.3.1 Reflection Coefficient $s_{11} = s_{22}$ 167
A.3.2 Left to Right Transmission Coefficient s_{21} 167

A.3.3 Right to Left Transmission Coefficient s_{12} 168

B Numerical Examples of Quantum Trajectories and Current Integrals 169

C Fabrication Recipes 177

1 Introduction

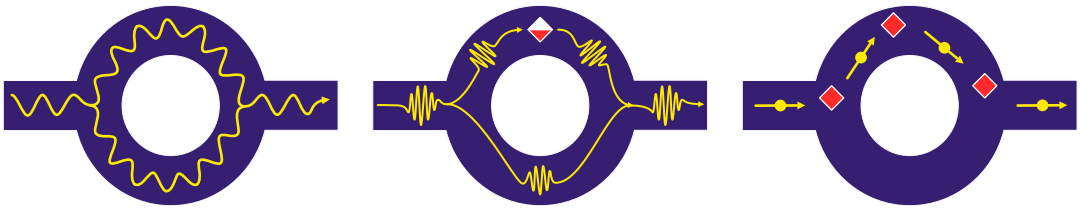
Electronic devices are used for a broad range of applications in our everyday lives. Most of these devices can be entirely understood by applying semiclassical physics, namely by considering that individual carriers are subject to both diffusion according to concentration gradients and drift according to external fields. Some devices, for example flash memory cells or superconducting single-photon detectors, can only be completely described if quantum mechanical effects, such as quantum tunneling or superconductivity, are taken into account. Furthermore, the logic gates and qubits used in quantum information technology directly take advantage of the coherent superposition of quantum states, which allows the devices to function in ways that contradict classical intuition.

From the recent activities of the research community, it seems that the pool of ideas and concepts for electronic devices based on classical physics is mostly exhausted and that the realm of quantum electronics is being vividly explored, yielding countless publications and an ever growing number of promising phenomena for novel device applications [1–5].

Interestingly, classical and quantum physics do not harmonize well when it comes to electronic devices. For classical electronic devices, quantum effects are usually undesired, as they may lead to detrimental behavior for small device sizes. For example, the tunnel effect causes unwanted leakage currents through the thin gate dielectrics of field effect transistors. For quantum electronics, the classical behavior is unwanted, because it leads, for example, to a reduction of the quantum coherence times of qubits. Thus, in the development of quantum and classical electronics, it is natural to avoid the respective other realm as far as possible. Indeed, the transition regime between quantum and classical physics has not received much attention for device development.

To illustrate our understanding of the motion of particles, Fig. 1.1a sketches the picture put forward by quantum physics, Fig. 1.1c shows the corresponding picture for classical physics, and Fig. 1.1b represents the transition regime. In this thesis, it is shown that this transition regime is more than a linear combination of the two limiting cases: The interplay of quantum coherence and irreversibility gives rise to novel phenomena with possible applications for electronic devices.

It is well known that the size of a system decides whether classical or quantum-mechanical laws apply. The electrons' motion around the atomic nuclei is governed by quantum mechanics, whereas the motion of electrons in the cathode ray tube inside an older television is properly described by considering classical trajectories of point-like particles. In the early days of quantum physics, it was discussed whether a natural boundary between the classical and the quantum world exists. Today we know that this is most likely not the case. Experiments have shown that quantum interference of large molecules is possible [6], therefore there is no sharp boundary between the quantum and



(a) (b) (c)

Figure 1.1: The key to electronic device design is to understand the motion of carriers. (a) In the purely quantum mechanical limit, this motion is governed by the Schrödinger equation, which describes particle states with extended wave functions and allows interference according to the phases of these wave functions. (c) In contrast, in the classical case, particles are localized objects that bounce off obstacles and move along classical trajectories. (b) In the transition regime, quantum mechanical interference is weakened by phase randomizing collisions with obstacles. Reprinted from [D].

the classical world. When modeling an electronic device, we have to choose the correct framework manually. In the case where the size of the system under consideration can be clearly labeled "microscopic" or "macroscopic", this choice is simple. If, however, the system size is somewhere in between the two regimes, that is, "mesoscopic", it is not immediately clear which equations of motion should be applied. For example, the electronic properties of large biomolecules and organic semiconductors depend on both classical and quantum aspects of the electrons.

The root of this problem is that neither quantum mechanics nor classical mechanics are capable of completely describing our reality. The related philosophical questions regarding the interpretation of quantum mechanics and are open for almost 100 years [7–13]. Although these questions are challenging from a theoretical point of view, the experimental exploration of the transition regime is straightforward. It is possible to manufacture structures, electronic circuits and even mechanical machines with nanoscopic length scales. Of course, it is also possible to manufacture these in any larger size—up to hundreds of meters. A complete theoretical description holding through all these length scales is very challenging; however, the experimental realization is straightforward. Therefore, in this thesis we do not intend to find complete answers to the involved theoretical or even philosophical questions. Instead, arguments and numerical evidence are presented for physics that is forbidden in both the classical regime and in quantum mechanics, but is allowed in the transition regime.

Chapter 2 starts with an overview of the history of quantum transport experiments. In theses experiments, quantum effects are directly observable by studying the properties of electronic devices. Chapter 3 then introduces the Landauer-Büttiker transport picture, which is capable of explaining the previously shown quantum transport effects. In addition, it is shown that fundamental reasons imply certain symmetries in this trans-

port picture. However, the basic Landauer-Büttiker picture does not incorporate the decoherence of quantum states, which is important under realistic conditions. Chapter 4 therefore introduces a series of theoretical methods to include decoherence into the Landauer-Büttiker transport picture. It is also shown that the fundamental reasons for the previously found symmetries do not necessarily apply if decoherence is considered. This raises the question of whether these symmetries can be violated in the presence of decoherence. Chapter 5 presents numerical results obtained by combining the Landauer-Büttiker picture and decoherence. These results in fact indicate that the considered symmetries may be violated under appropriate conditions. In Chapter 6, experimental predictions for quantum transport are discussed and Chapter 7 presents preliminary experimental results. The results shown pave the way towards novel electronic devices and a better understanding of the transition regime between classical and quantum physics.

The results and arguments reported in this thesis have also been presented in several publications, which are referenced in the text by the letters [A–E].

Mesoscopic Transport Phenomena

2

Mesoscopy denotes the intermediate length scale between the macroscopic and the nanoscopic realm. One could approximately assign the range from length scales around 10 nm to around 10 µm, but of course there is no rigorous boundary. The characteristic of mesoscopy is that the coherence length and the system size are comparable. The coherence length is usually defined phenomenologically and specifies the length scale, on which carriers maintain their quantum mechanical phase [14]. If the coherence length is much larger than the system size, quantum mechanical intereference effects have to be considered. For transport, this regime is also called the "ballistic" transport regime. If the coherence length is much smaller than the system size, the (semi)classical equations of motion have to be applied. Mesoscopic physics is about the transition regime, where classical effects such as Joule heating and irreversibility occur, but also purely quantum mechanical effects as interference and quantization are observed.

Mesoscopic effects are essential to understand the motion of carriers in small conductors at low temperatures. These effects can be studied with transport experiments, which measure the response of electronic devices to an applied voltage (or current) bias and often to an applied magnetic field (Fig. 2.1). Early experiments in this direction were done by studying small metal structures at sub-Kelvin temperatures. During the 1970's the first commercial dilution refrigerators became available, allowing to reach stable temperatures down to a few milli-Kelvin. The other technological challenge was given by the necessary structure size being less than 100 nm, which was beyond the range of optical lithography and therefore required the use of electron-beam lithography (EBL). The first demonstrations of electron beam lithography were done in the early 1960's [15, 16], before the discovery of electron sensitive resists. The pattern transfer was done abusing the inevitable contamination caused by the electron beam. High energy electrons that collide with hydrocarbon contaminants in the chamber vacuum lead to a gradual deposition of a carbon rich layer wherever the electron beam is pointed at. This contamination was used to draw patterns which later acted as an etch mask for ion milling. This technique is known as "contamination lithography".

Broers, who invented the contamination lithography in Cambridge in 1963 [15] later joined the IBM research center in Yorktown Heights, where he worked with R. B. Laibowitz, C. P. Umbach, S. Washburn and R. A. Webb on the transport measurements in small samples [17]. The following Sections 2.1 and 2.2 summarize the results of these early experiments on small metallic wires and loops, namely the discovery of Aharonov-Bohm (AB) conductance oscillations for transport in a solid and the observation of universal conductance fluctuations (UCF). At a similar time advances in molecular beam epitaxy (MBE) enabled high coherence lengths in the two-dimensional electron gas (2DEG) hosted by GaAs heterostructures [18]. The advantages of this 2DEG over

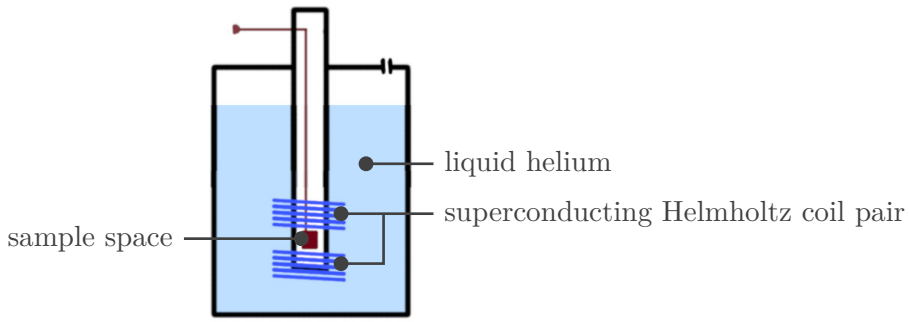


Figure 2.1: Coarse sketch of a typical low-temperature measurement setup. A large liquid helium bath serves as a heat sink with a temperature of 4.2 K. Additional low temperature technology (e.g. expansion valves or a dilution refrigerator, not shown) may be used to cool the sample volume to even lower temperatures. The sample space is enclosed by a pair of superconducting coils, which provide a homogeneous tunable magnetic field with up to several 10 T flux density.

the metallic electron systems are the intrinsically lower dimensionality, the gate tunability and lower scattering rate. With the GaAs heterostructures it was shown that the electrical conductance of small channels, measured as a function of the channel width, features plateaus at integer multiples of the conductance quantum.

2.1 Aharonov-Bohm Oscillations

The phenomenon known as the Aharonov-Bohm effect is a simple but peculiar consequence of the quantum dynamics of a charged particle in the presence of an electromagnetic vector potential $\boldsymbol{A}$: According to the Schrödinger equation a particle that travels along a path $\boldsymbol{l}$ gathers a phase shift proportional to $\boldsymbol{A}$ integrated along $\boldsymbol{l}$. This is surprising, because in the classical picture, the magnetic field $\boldsymbol{H}$ is the force field that affects moving particles, $\boldsymbol{A}$ is merely a mathematical construct to simplify calculations. In particular, $\boldsymbol{H}$ may vanish in a certain volume where $\boldsymbol{A}$ is finite. The Schrödinger equation therefore implies that the magnetic field may manipulate particles traveling through a region despite being zero valued in that region.

Such an effect was first mentioned in 1939 by Werner Franz, and was rediscovered multiple times in the following decades [19]. The topic did not receive much attention until the work of Aharonov and Bohm in 1959 [20], which eventually sparked the interest of experimentalists. With the high precision electron optics available in electron microscopes and after the realization of an electron biprism by G. Möllenstedt and H. Düker [21], testing the claims in the laboratory became feasible. Indeed, the experiments found phase shifts according to the electromagnetic vector potential even if the magnetic field was negligibly small along the electron paths [22] or even shielded with a superconductor

[23].

In contrast, AB effect related experiments in small conducting samples are usually not trying to demonstrate the effect of $\boldsymbol{A}$ on the carriers with $\boldsymbol{H}$ shielded from the electron paths, but are aimed to study the coherent electron dynamics in the solid. The setups usually employ a sample of a few $10\,\mathrm{mm}^2$ size with planar nanostructures on its surface which is placed inside a solenoid which alltogether is placed in a cryostat. The solenoid applies a tunable transverse magnetic field and the cryostat stabilizes a selected temperature in the range of typically 10 mK to 10 K at the sample site. Information about the coherent motion of electrons is inferred from the measurement and analysis of the sample conductance as a function of $\boldsymbol{H}$. The challenges to observe coherent carrier motion in a solid state device are the high levels of disorder in these systems and the thermal noise affecting virtually any observable.

As mentioned in the introduction of this chapter, the first successful measurement of AB conductance oscillations was performed by Webb et al. in 1985 [24–26]. The central observation of the paper is that the conductance of small normal metal rings shows periodic modulations as a function of the applied magnetic field $\boldsymbol{H}$. Moreover, the field period of these modulations is precisely given by the field that corresponds to one magnetic flux quantum $\boldsymbol{\Phi}_0 = h/q$ within the ring (Fig. 2.2). Here, h is the Planck constant and q is the elementary charge. Briefly speaking, the electrons traveling from the top contact to the bottom contact of the ring shown in Fig. 2.2 pass through the left and the right half of the ring simultaneously. The phase shift between these two paths is proportional to the magnetic flux that penetrates the ring. Sweeping $\boldsymbol{H}$ and thus the magnetic flux density causes alternating constructive and destructive interference with a period given by the magnetic flux quantum.

For this thesis the symmetry properties of particle transport through structures of given symmetries are of particular interest. Rather simple arguments (Section 3.2) show that the conductance G of any nonmagnetic device with only two leads is symmetric with respect to the reversal of an applied magnetic field $G(\boldsymbol{H}) = G(-\boldsymbol{H})$. In the reported data from [24] the conductance is, however, asymmetric with respect to the magnetic field, likely due to the presence of magnetic impurities in the sample[1].

Later experiments adopted this concept of electron interferometry to measure the quantum mechanical phase shifts of electrons being transmitted through nanostructures. The idea is to embed, e.g. a quantum dot into one of the two electron paths, and to deduce the phase shift caused by traveling through the dot from the resulting conductance modulation pattern. In particular the transmission phase of a Kondo impurity, which theory predicts to be exactly $\pi/2$, attracted experimentalists [27, 28]. Many of these experiments ran into problems with the so-called phase rigidity. As mentioned before, the conductance of any device with two leads is symmetric in $\boldsymbol{H}$, which implies that the conductance oscillations can only feature a minimum or a maximum at zero applied

[1] The authors of [24] claim that the asymmetry is in accordance with the multi channel Landauer formula (Section 3.3). However, the required uneven occupation of channels is not justified close to thermal equilibrium and many later experiments achieved highly symmetric $G(\boldsymbol{H})$ curves under comparable conditions.

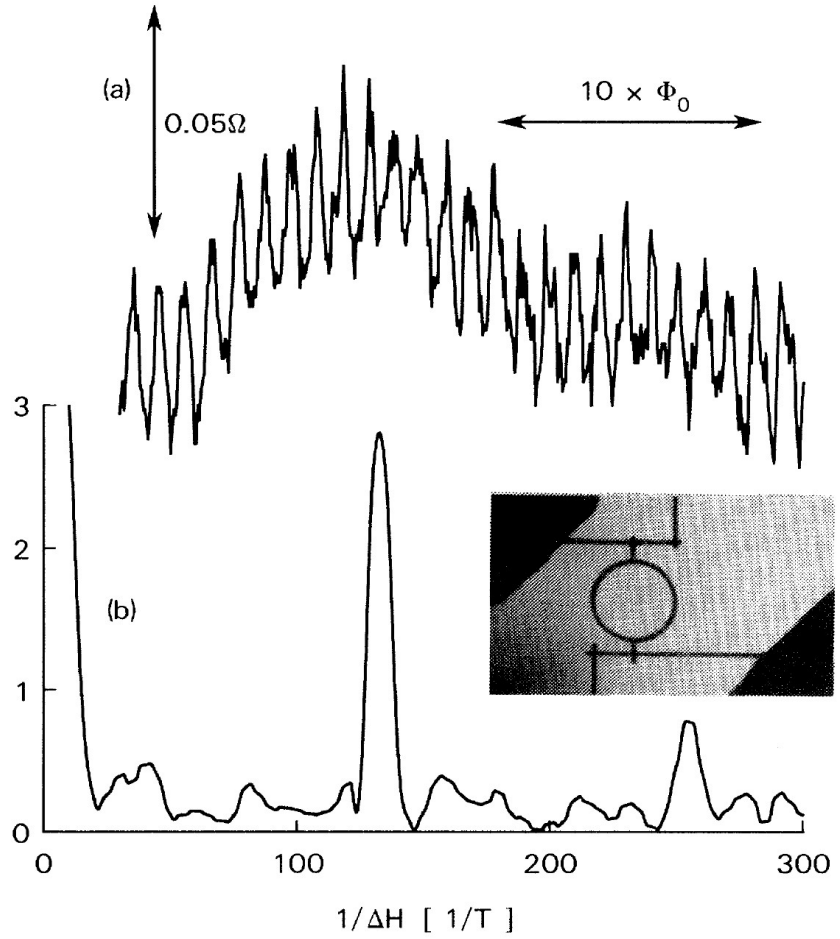


Figure 2.2: (a) The magnetoconductance of a gold ring with a diameter of 784 nm (inset) measured at 10 mK oscillates as function of the applied magnetic field. The vertical and horizontal arrows indicate the scales of the resistance and magnetic flux, $\mathbf{\Phi}_0$ being the magnetic flux quantum. The resistance oscillation amplitude is about 0.1 % of the mean device resistance of $\approx 30\,\Omega$ [24]. (b) The Fourier transform of a large magnetic field range reveals two clear peaks at the frequencies corresponding to periods of one magnetic flux quantum within the ring area $\approx 130\,\mathrm{T}^{-1}$) and the second harmonic of that frequency $\approx 260\,\mathrm{T}^{-1}$). Reprinted figure with permission from R. A. Webb et al., Phys. Rev. Lett. **54**, 2696–2699 (1985) [24]. Copyright 2022 by the American Physical Society.

magnetic field. Any other value does not satisfy the required field symmetry. The resulting inability to continuously tune the interference pattern makes the measurement of a phase shift via interferometry very challenging with a two-lead interferometer.

A comparison with the optical analog, the Mach-Zehnder interferometer, reveals that one needs a four-lead device for the measurement of transmission phases. The symmetry arguments that cause the phase rigidity only hold for devices with two leads, for devices with four leads the phase rigidity is not required. Suitably designing a four-lead interferometer enables the continuous shifting of the oscillation pattern [29]. Note that "two-lead" and "four-lead" measurement does *not* refer to the number of wires that are used in the cryostat to contact the sample. All precision measurements on mesoscopic devices are performed with two separate wire pairs for current sourcing and voltage probing ("four-wire" configuration). In contrast, the characteristic of a two-lead measurement is that only two leads with a length above the phase coherence length l_Φ are attached to the nanostructure. In a distance of a few l_Φ from the nanostructure, the leads may split into many contacts which serve as separate source and measurement wires. A clear demonstration how switching between two-lead and four-lead measurements turns the phase rigidity on and off is presented in [30]. The following chapters of this thesis concern two-lead AB interferometers that are subject to phase rigidity.

2.2 Universal Conductance Fluctuations

The conductance of small conductors fluctuates as a function of the applied magnetic field. The fluctuation pattern is random from sample to sample but is reproduced with every field sweep for a given sample. The origin of these fluctuations is the interference of microscopic electron paths through the disordered conductor. The magnetic field causes phase shifts of these paths and thus affects their individual interference conditions. Naturally, the total conductance is given by the transmission probability resulting from the sum of all microscopic transmission amplitudes. For devices much larger than the electron coherence length the effects of the microscopic interference average out. In small devices, however, the universal conductance fluctuations are relevant.

These fluctuations are a generic concept that commonly arises from the combination of phase coherence and disorder. The optical analogue of these fluctuations is given by the speckle pattern that is generated by coherent light illuminating a disordered (rough) reflective surface. The reflected light spot has a "noisy" character with a random, static and reproducible intensity pattern. Only if the disordered surface or the beam is moved, the pattern changes to another random speckle pattern. Again, this is only observed for coherent light sources. If the coherence length is smaller than the disorder scale of the surface, the distribution of the reflection intensity is smooth without any random fluctuations.

Figure 2.3 shows an early measurement of UCF in a small gold wire [31]. On the first glance one might guess that the noisy curve results from the measurement equipment as the amplitude is small. However, repeated measurements reproduce the same fluctuation pattern. After warming to room temperature or changing the sample wiring a new

fluctuation pattern is likely measured. Obviously, different samples show different UCF patterns. These observations are readily understood by recalling that the fluctuation pattern is a fingerprint of the sample's detailed disorder configuration, which is defined by grain boundaries, impurity locations, lattice defect locations, etc. At low temperatures none of these change with time, but at room temperature impurities and lattice defects may become mobile. Likewise, the small electrostatic discharges caused by carelessly replugging wires connected to the sample correspond to huge field gradients and energy densities for the nanostructure in the cryostat. Hence, changes in the lattice of defect locations are anticipated by treating the sample in such a manner.

The amplitude of the fluctuations increases with lower temperature and typically saturates at a value around G_0R^2, where the R is the device resistance and the G_0 is the conductance quantum. The conductance quantum corresponds to the conductance of a single ballistic "channel" (Section 3.3). If one of these channels is added in parallel to a resistance R, the resistance changes by

$$\Delta R = R - R_{\mathrm{tot}} = R - \frac{R}{1 + G_0 R} = \frac{G_0 R^2}{1 + G_0 R} \approx G_0 R^2, \tag{2.1}$$

using the assumption that $R \ll 1/G_0$ and thus $G_0R \ll 1$. This is compatible with the microscopic picture of a disordered network of ballistic channels with the interference conditions at the intersections being tuned by the magnetic field. In such a network the total transmission fluctuates by an amount corresponding to one channel if the magnetic field is swept [31].

Being a coherent transport effect, the UCF signal is well suited to extract the coherence length of carriers in the material [32, 33]. The smallest magnetic field change that still causes a change of the conductance on the order of G_0, corresponds to one magnetic flux quantum in an area with a circumference of the phase coherence length l_Φ. If $l_\Phi = 0.5\,\mu\mathrm{m}$ for example, then two random paths that may still interfere with each other enclose an average area[2] of order $0.05\,\mu\mathrm{m}^2$. A transverse magnetic flux density of $\boldsymbol{B} \approx 0.1\,\mathrm{T}$ adds one magnetic flux quantum to this area which would be the smallest field scale visible in the UCF in that case. In [33], more sophisticated data analysis techniques are presented that follow this idea and enable an accurate determination of the phase coherence length from UCF measurements. A practical example for such an analysis is shown in [B].

As mentioned for the AB rings above, the UCF signal of two-lead devices is required to be symmetric with respect to zero magnetic field. In earlier publications magnetic field asymmetries were often explained to be in accordance with the many-channel Landauer formula [24, 34] but in retrospect it is more likely that these samples were not free of magnetic impurities. In fact, demonstrating the symmetry of the magnetoconductance curve with respect to magnetic field reversal is used as a validation of a clean two-lead measurement configuration with negligible leakage currents and low densities of magnetic impurities.

[2]Estimated by half the area enclosed by a circle with a circumference of $2l_\Phi$.

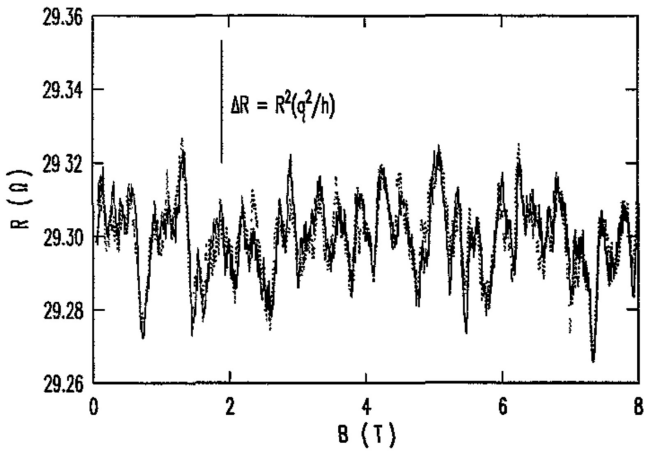


Figure 2.3: Plot showing the UCF observed in a small gold wire at 10 mK. The wire length is 400 nm, the cross section is 40 nm × 40 nm. The dashed line shows a second field sweep, demonstrating the reproducibility of the fluctuation pattern. The scalebar shows that the oscillation amplitude is comparable to one conductance quantum being added or removed in parallel to the device. Reproduced with permission from S. Washburn and R. A. Webb, Rep. Prog. Phys. **55**, 1311–1383 (1992) [31]. Copyright 2022 by IOP Publishing. All rights reserved.

2.3 Conductance Quantization

As discussed in the previous section, the understanding of UCF is based on a description of conductors as a disordered network of ballistic channels, each with a conductance of G_0. This model leads to the question whether it is possible to isolate single ballistic channels and to directly measure their conductance. To achieve this goal with metals one would need to create a chain of single atoms because of the metal's immense carrier concentration. Today, this is impossible with lithographic techniques. Alternatively it is possible to thin down a metallic wire by stretching it until it eventually breaks [35] or to reduce the diameter by electrochemical etching [36] while measuring the conductance. These experiments indeed reveal the expected quantized conductance, just before the samples break. The drawback of this technique is the irreversible, destructive nature of the experiment and hence the lack of control — it is impossible to reproducibly tune to one channel, then to five channels and back to three channels, for example.

Instead of physically thinning and finally breaking a wire, one can also use electric fields. The 2DEG in GaAs based heterostructures offers the possibility to continuously tune the carrier concentration and device geometry by means of electrostatic gating. Moreover, by doping and heterostructure design the total carrier concentration can be varied by orders of magnitude. Thanks to the high standards of molecular beam epitaxy (MBE) growth of GaAs heterostructures, low temperature mean free paths of up to

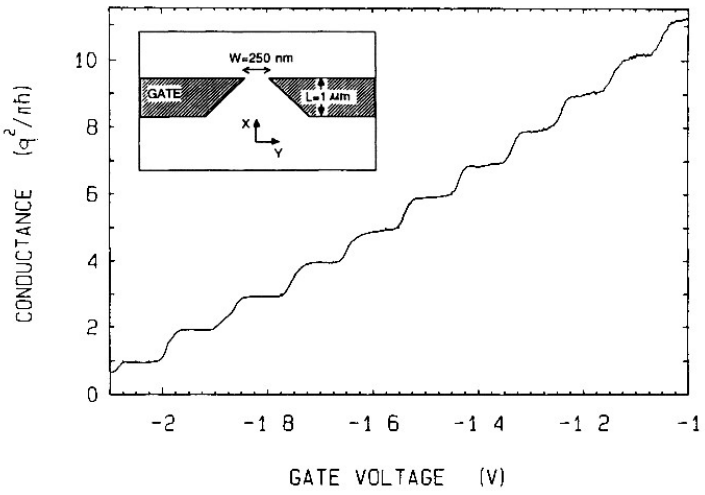


Figure 2.4: The conductance of a gated constriction (inset) changes in discrete steps as a function of the applied gate voltage. The stepsize is given by the conductance quantum $G_0 = q^2/\pi\hbar$. The point contact was fabricated on a MBE grown high-mobility GaAs-AlGaAs heterostructure and was measured at 0.6 K. Reprinted figure with permission from B. J. van Wees et al., Phys. Rev. Lett. **60**, 848–850 (1988) [37]. Copyright 2022 by the American Physical Society.

the order of 100 µm are possible [38, 39] and many micrometers are commonly achieved. Thus, the required minimal feature size to observe conductance quantization is ≈ 100 nm and in the range of lithographic techniques. Data from the first publication [37] demonstrating clear conductance steps at a gate defined constriction in a GaAs 2DEG are presented in Fig. 2.4. A review of the early experiments utilizing similar gate-defined 2DEG structures is given in [40].

2.4 Weak Localization

In the literature, the term "weak localization" is used for a range of quantum corrections to the conductance, including AB oscillations [42]. In the majority of articles, however, weak (anti) localization refers to a specific quantum correction, namely a peaking behavior of the magnetoresistance (conductance) at zero field [43–48], which is the definition adopted here. A simplified picture to understand this peak starts with the disordered network of ballistic channels used to describe the UCF. We now consider a specific path through the network that starts from one of the device's leads, proceeds in the device and returns to its point of origin. Because the starting point and the endpoint are identical, the electrons can travel through each of these paths in two directions. If the coherence length is larger than the considered path length then the electrons travel in both directions simultaneously and self interfere afterwards. Without an applied magnetic field and

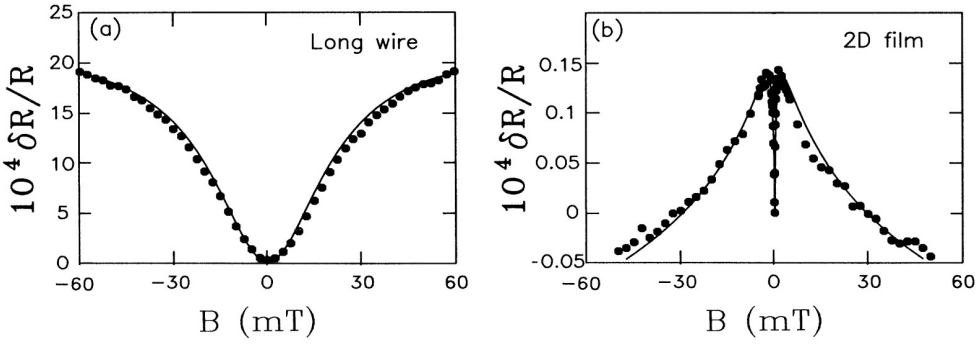


Figure 2.5: Plots showing weak-localization peaks for a thin Ag wire (a) and a thin Ag film (b). Both measurements were done at 2 K. Clear extrema at $\boldsymbol{B} = 0$ are observed which are attributed to weak localization. Reprinted figure with permission from V. Chandrasekhar et al., Phys. Rev. B **44**, 11203–11220 (1991) [41]. Copyright 2022 by the American Physical Society.

without magnetic impurities the total phase traveled in each of the directions is equal and the self interference is therefore constructive. A magnetic field, however, introduces a phase difference between the two directions and thereby reduces the probability that the electron returns to its origin. Clearly, all possible closed paths contribute to the total reflection probability, because they end in the same lead that they started from. The more of these paths exist and the higher their probabilities, the larger is the device resistance increase they cause. Therefore, the largest resistance is found at zero field and the resistance drops gradually as magnetic field increases.

This simplified picture is already applicable to the many materials with negligible spin-orbit interaction. With spin-orbit coupling, however, an additional direction-dependent phase shift enters even if no magnetic field is applied. In this case, the absence of an applied magnetic field may correspond to destructive interference which reduces the total reflection probability. This reduction of the reflection probability — or decrease of the resistance — gets gradually suppressed by an applied magnetic field. The resistance may then feature a minimum at zero field.

Hikami et al. derived a low-field conductance formula for disordered networks. Their model only depends on the phase coherence length, the elastic mean free path and the spin-orbit coupling strength [49]. Today, this formula carries their name and is frequently used to fit magnetotransport data for small fields. Figure 2.5 shows an early example for studies of the weak localization from the literature. Transport data can be fit with the Hikami-Larkin-Nagaoka-formula to extract the carrier phase coherence length. Together with the analysis of UCF data, the fits to the weak localization peak are today the standard methods to determine the carrier phase coherence length.

2.5 Summary

On the one hand, mesoscopic devices feature quantum mechanical interference effects known from the microscopic world of atoms and molecules. On the other hand classical aspects such as diffusion, dissipation and thermodynamic noise known from our everyday macroscopic world are also important for mesoscopic devices. Temperature, sample size and disorder strength serve as tuning parameters to adjust the ratio of quantum and classical aspects. Magnetotransport measurements of small structures are a convenient and powerful method to probe the coherent dynamics of the carriers in the solid.

Important quantum transport characteristics are the AB conductance oscillations in small rings, the UCF in small disordered systems, the conductance quantization in narrow constrictions and the weak localization peak at zero field. These phenomena are well explained within the framework of the transport theory developed by Rolf Landauer, Markus Büttiker and Yoseph Imry, which is presented in the next chapter. In the following, the symmetries of mesoscopic transport are the main concern. AB interferometers and UCF are well suited to study these symmetries.

Scattering Theory and Application to Transport

3

This chapter first gives a quick introduction to quantum mechanics and scattering theory of single nonrelativistic particles, starting from the Schrödinger equation and arriving at the scattering matrix and its basic properties. Next, the theory of mesoscopic transport as mainly developed by Rolf Landauer, Markus Büttiker and Yoseph Imry is reviewed. Their view on the subject will be referred to as the Landauer-Büttiker picture or the Landauer-Büttiker formalism. The central idea is to relate the transport problem to a scattering problem of individual electrons. The Landauer-Büttiker formalism successfully explains many low temperature transport phenomena in metallic and semiconducting samples if the electronic correlations are weak [14].

Afterwards implications of the Landauer-Büttiker picture are discussed that go beyond the usual scope. Wave packets and the wave-packet scattering delay are introduced and their significance for transport is shown. Finally the theory is applied to a series of example systems that feature typical properties of quantum transport, namely the conductance quantization, multiple-path interference leading to the Aharonov-Bohm (AB) effect, tunnel currents and universal conductance fluctuations (UCF).

This chapter especially considers the symmetries of the two-lead scattering problem. For further information about the notation, see Chapter 9. To keep the analytical expressions short and readable, we employ the following natural units: The reduced Planck constant $\hbar$, the elementary charge q and the particle mass m are set to unit-less constant numerical values $\hbar = q = 2m = 1$. This also implies that energies, times, lengths, etc. are given by unit-less numbers, which simplifies the discussion of the symmetry properties of the expressions. A conversion to SI-units by replacing the natural constants with their SI-values is straightforward. A thorough introduction to quantum mechanics and the scattering theory of one-dimensional potentials is given in [42, 50].

3.1 Eigenfunctions and Scattering States

The basis of the Landauer-Büttiker picture is the scattering theory of nonrelativistic particles. A system with N leads is described by the Hamiltonian $\hat{\boldsymbol{H}}$. Given that an electron is injected at lead α, the central question then is: What are the respective probabilities for the electron to leave through each of the other leads? Applied to electronic transport, the question is: How is the electrical current incident on lead α of an electronic device distributed among the leads $1 \dots N$?

The motion of particles in mesoscopic devices is governed by the quantum mechanical equation of motion, the Schrödinger equation. The full description of a particle's state is encoded in its wave function $\boldsymbol{\psi}$ and the statistics of physical observables is calculated by applying the corresponding Hermitian operators to the wave function. The Schrödinger

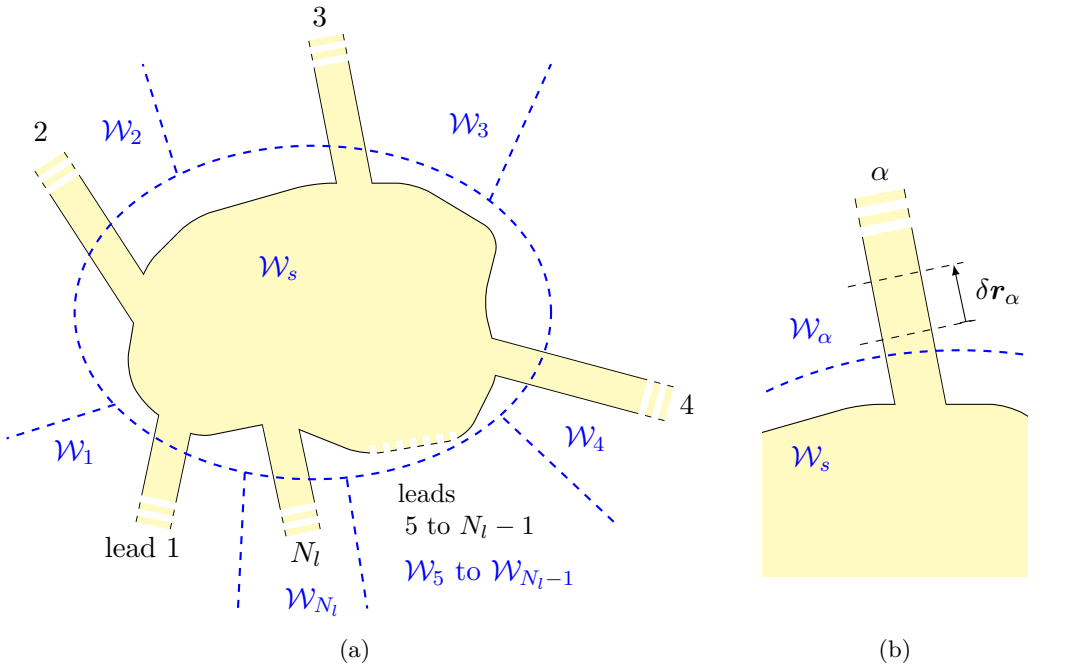


Figure 3.1: (a) Sketch of the general form of a scattering problem with N_l leads, corresponding to a mesoscopic device with N_l attached leads. The blue dashed line sketches the boundaries of the scattering region $\mathcal{W}_s$ and the lead regions $\mathcal{W}_\alpha$. (b) Magnification of the section where the lead α is attached to the system. The Hamiltonian in the scattering region $\mathcal{W}_s$ may be arbitrary, in the leads it is strictly periodic. The vector $\delta \boldsymbol{r}_\alpha$ describes the translational symmetry of the Hamiltonian in $\mathcal{W}_\alpha$.

equation,

$$\partial_t \boldsymbol{\psi}(t) = -i\hat{\boldsymbol{H}}\boldsymbol{\psi}(t), \tag{3.1}$$

describes the time evolution of wave functions. It rests on the energy operator, that is, the Hamiltonian $\hat{\boldsymbol{H}}$. The fundamental solution to this linear differential equation is

$$\boldsymbol{\psi}(t) = \exp\left(-i\hat{\boldsymbol{H}}(t-t_0)\right)\boldsymbol{\psi}(t_0) \tag{3.2}$$

$$= \hat{\boldsymbol{U}}(t_0, t)\boldsymbol{\psi}(t_0), \tag{3.3}$$

with t_0 referring to a time at which the wave function is known. The exponential expression is called the time-evolution operator $\hat{\boldsymbol{U}}$, which is a function of start time and the end time of the evolution. If applied to a wave function, it evolves the wave function by the given time span. The evaluation of the operator exponential is trivial, if the Hamiltonian $\hat{\boldsymbol{H}}$ is brought into diagonal form. Being an observable, $\hat{\boldsymbol{H}}$ is guaranteed to be Hermitian and thus always has orthogonal eigenfunctions $\boldsymbol{\phi}_\xi$ and real eigenvalues E_ξ such that

$$\hat{\boldsymbol{H}} = \int \boldsymbol{\phi}_\xi E_\xi \boldsymbol{\phi}_\xi^\dagger \mathrm{d}\xi. \tag{3.4}$$

If the system was finite, these $\boldsymbol{\phi}_\xi$ and E_ξ would be the eigenfunctions and eigenvalues of the Hamiltonian $\hat{\boldsymbol{H}}$ and the $\boldsymbol{\phi}_\xi$ would span a basis of the space of all possible wave functions, the Hilbert space. This basis spanned by the eigenfunctions is called the eigenbasis. However, because the leads are infinitely long, the $\boldsymbol{\phi}_\xi$ are note necessarily normalizable. Therefore, they are not part of the Hilbert space themselves and thus no wave functions in a strict sense and are called "scattering states" of the system instead. Despite not being normalizable, every possible wave function $\boldsymbol{\psi}$ has a unique scattering state decomposition

$$\boldsymbol{\psi} = \int a_\xi \boldsymbol{\phi}_\xi \mathrm{d}\xi, \tag{3.5}$$

with the scalar coefficients $a_\xi = \boldsymbol{\phi}_\xi^\dagger \boldsymbol{\psi}$. For the finite system, this would be the eigenbasis representation. For the system with infinite leads, however, the a_ξ may be chosen such that Eq. 3.5 results in a nonnormalizable wave function. Therefore, in a strict sense, the scattering states $\boldsymbol{\phi}_\xi$ do not span a basis of the Hilbert space. However, a correct distinction of these subtle differences is not helpful for the topics discussed in this thesis. The terms eigenfunctions and eigenbasis will thus be used for both finite and infinite systems in the following. Equation 3.5 is important, because the time evolution is straightforward is this representation.

$$\boldsymbol{\psi}(t) = \hat{\boldsymbol{U}}(t_0, t)\boldsymbol{\psi}(t_0) \tag{3.6}$$

$$= \int a_\xi(t_0) \exp\left(-iE_\xi(t-t_0)\right) \boldsymbol{\phi}_\xi \mathrm{d}\xi. \tag{3.7}$$

In the eigenbasis representation of a wave function $\boldsymbol{\psi}$, the time evolution is simply a rotation of the complex phase of each $\boldsymbol{\phi}_\xi$ with an angular frequency given by E_ξ. Being eigenvectors and eigenvalues of the energy operator, the $\boldsymbol{\phi}_\xi$ are states with a sharp energy of E_ξ. Once $\hat{\boldsymbol{H}}$ has been diagonalized, it is straightforward to calculate the time evolution of any wave function.

Despite the general character of the system sketched in Fig. 3.1a, its Hamiltonian has a specific property in the infinite leads: it is periodic. Each lead is characterized by a lattice vector of a periodic lead $\delta\boldsymbol{r}_\alpha$, such that $\hat{\boldsymbol{H}}(\boldsymbol{r}) = \hat{\boldsymbol{H}}(\boldsymbol{r} + \delta\boldsymbol{r}_\alpha)$, if both $\boldsymbol{r}$ and $\boldsymbol{r} + \delta\boldsymbol{r}_\alpha$ lie within $\mathcal{W}_\alpha$, the region of lead α. Here, $\boldsymbol{r}$ denotes the position. This condition includes leads with periodically repeating potentials or shapes, but also leads without any position dependent structure. The latter case is described by $\delta\boldsymbol{r} \to 0$. This periodicity of $\hat{\boldsymbol{H}}$ enables the separation of the eigenfunctions $\boldsymbol{\phi}_\xi$ into products of functions with the same periodicity as $\hat{\boldsymbol{H}}$ and into plane waves. The general form of $\boldsymbol{\phi}_\xi$ in the region of lead α (that is, outside of $\mathcal{W}_s$) is given by incoming and outgoing plane waves

$$\boldsymbol{\phi}_\xi(\boldsymbol{r}) = \Bigg(\sum_{\alpha i} \mathcal{A}^-_{\alpha i} \boldsymbol{\phi}^-_{\alpha i}(\boldsymbol{r}) \underbrace{\exp\left(i\boldsymbol{k}_{\alpha i}(E_\xi)\boldsymbol{r}\right)}_{\textbf{(I)}} + \mathcal{A}^+_{\alpha i} \boldsymbol{\phi}^+_{\alpha i}(\boldsymbol{r}) \underbrace{\exp\left(-i\boldsymbol{k}_{\alpha i}(E_\xi)\boldsymbol{r}\right)}_{\textbf{(II)}} \Bigg), \tag{3.8}$$

$$\boldsymbol{\phi}^-_{\alpha i}(\boldsymbol{r}) = \boldsymbol{\phi}^-_{\alpha i}(\boldsymbol{r} + \delta\boldsymbol{r}_\alpha) \tag{3.9}$$

$$\boldsymbol{\phi}^+_{\alpha i}(\boldsymbol{r}) = \boldsymbol{\phi}^+_{\alpha i}(\boldsymbol{r} + \delta\boldsymbol{r}_\alpha) \tag{3.10}$$

with the lead index α, the channel index i (discussed in the next section), the amplitudes $\mathcal{A}^+_{\alpha i}$ and $\mathcal{A}^-_{\alpha i}$ of the incoming and outgiong plane waves and the respective wave front shapes $\boldsymbol{\phi}^+_{\alpha i}$ and $\boldsymbol{\phi}^-_{\alpha i}$. Several points are notable about this form of the $\boldsymbol{\phi}_\xi$:

1. The wave front shapes $\boldsymbol{\phi}^+_{\alpha i}$ and $\boldsymbol{\phi}^-_{\alpha i}$ are periodic with the same periodicity as the lead Hamiltonian.

2. The term (I) in Eq. 3.8 describes a plane wave propagating in the direction of $\boldsymbol{k}_{\alpha i}(E_\xi)$ and the term (II) in Eq. 3.8 describes a plane wave propagating in $-\boldsymbol{k}_{\alpha i}(E_\xi)$ direction. By convention, $\boldsymbol{k}_{\alpha i}$ points towards $\mathcal{W}_s$, then $\boldsymbol{\phi}^+_{\alpha i}$ and $\boldsymbol{\phi}^-_{\alpha i}$ are specifying the wave front shape of the incoming and outgoing plane waves.

3. The continuous index ξ only occurs in the wave vector $\boldsymbol{k}_{\alpha i}(E_\xi)$, all other quantities depend on discrete indices only.

4. The wave front shapes $\boldsymbol{\phi}^+_{\alpha i}$ and $\boldsymbol{\phi}^-_{\alpha i}$ are not normalizable as a whole, but are normalized within one period length $\delta\boldsymbol{r}_\alpha$. They span a basis of the lead wave functions.

5. The wave front shapes $\boldsymbol{\phi}^+_{\alpha i}$ and $\boldsymbol{\phi}^-_{\alpha i}$ do not directly depend on the continuous eigenfunction index ξ, but on the discrete channel index i, which will be discussed below.

6. The amplitudes $\mathcal{A}^+_{\alpha i}$ and $\mathcal{A}^-_{\alpha i}$ are complex scalars.

For the plane waves, the time evolution by a time span t is equivalent to a spatial translation of the wave function by $Et\boldsymbol{k}/|\boldsymbol{k}|^2$, infinite time evolution corresponds to infinite spatial translation. Any interaction of a time dependent wave function with the finite scattering region therefore vanishes in the limit $t \to \infty$.

The wave front shapes $\boldsymbol{\phi}^+_{\alpha i}$ and $\boldsymbol{\phi}^-_{\alpha i}$ depend on two discrete indices. This permits the definition of scattering channels (Fig. 3.2). Due to the infinite leads the number of eigenfunctions and eigenvalues of $\hat{\boldsymbol{H}}$ is infinite, the index ξ is continuous. However, in the general case the leads have a finite width, which causes degeneracies. For each of these degenerate eigenfunctions the plane wave terms are identical, but the $\boldsymbol{\phi}^+_{\alpha i}$ ($\boldsymbol{\phi}^-_{\alpha i}$) differ, as governed by the channel index i.

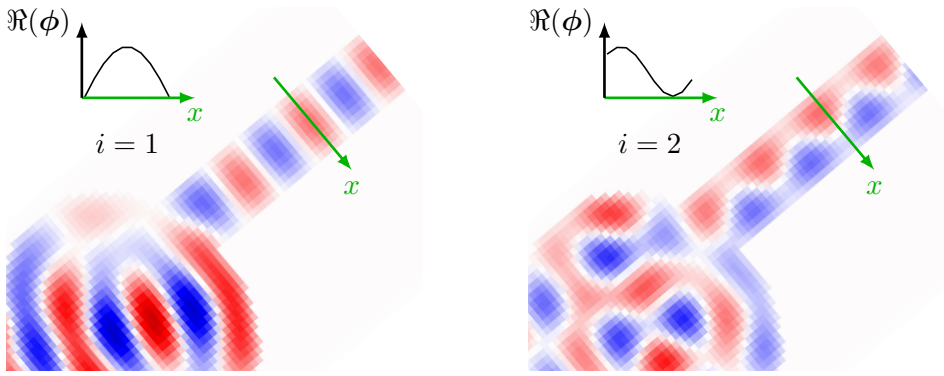
In the simplest case, the leads have no inner structure $\delta\boldsymbol{r}_\alpha \to 0 \ \forall \ \alpha$ and are strictly one-dimensional. Then $\boldsymbol{\phi}^+_{\alpha i} = \boldsymbol{\phi}^-_{\alpha i} = 1$ and all leads host exactly one channel, the channel index i is obsolete. If the lateral extension of the leads is not negligible, $\boldsymbol{\phi}^+_{\alpha i}$ and $\boldsymbol{\phi}^-_{\alpha i}$ are functions of $\boldsymbol{r}$ along the directions orthogonal to the $\delta\boldsymbol{r}_\alpha$. They characterize the wave fronts that are supported by the lead. The discrete channel index i then runs from 1 to the number of scattering channels M.

3.2 The S-Matix and its Symmetries

From the general form of the eigenfunctions given in Eq. 3.8 we saw that they always form plane waves in the leads. The wave function in the scattering region $\mathcal{W}_s$ defines boundary conditions for these plane waves. The idea of the scattering matrix is to extract only this relationship between the plane waves in the leads dropping the often unnecessary details of the wave function in the scattering region. Thus, the scattering matrix is defined as the linear map of the vectors of the amplitudes $\mathcal{A}^+$ of incoming plane waves onto the respective vectors of the amplitudes $\mathcal{A}^-$ of outgoing plane waves. For a problem with N_l leads and M channels in each lead, the total number of channels equals $N_l M$. The scattering matrix $\boldsymbol{S}$ therefore has $N_l M \times N_l M$ entries. The entries s_{mn} of $\boldsymbol{S}$ characterize the complex amplitude of the outgoing plane wave in scattering channel m, if a plane wave with amplitude one is incident on channel n,

$$\begin{pmatrix} \mathcal{A}^-_{1,1} \\ \mathcal{A}^-_{1,2} \\ \cdots \\ \mathcal{A}^-_{N_l,M} \end{pmatrix} = \boldsymbol{S} \cdot \begin{pmatrix} \mathcal{A}^+_{1,1} \\ \mathcal{A}^+_{1,2} \\ \cdots \\ \mathcal{A}^+_{N_l,M} \end{pmatrix}. \tag{3.11}$$

We can now come back to our central question, which is now slightly modified: Where does a particle with energy E incident via lead α and channel i leave the system? The



(a) (b)

Figure 3.2: Illustration of a lead with multiple scattering channels, which are enumerated by the channel index i. The color profile sketches the real part of the eigenfunctions. (a) Channel 1 corresponds to the lowest energy eigenfunction for a given wave length. The inset sketches the wave front, given by the cross section of the wave function in the lead (green arrow). (b) Due to the finite lead width a second state with the same wavelength but a higher energy exists. The states are distinguishable by their wave front shapes, again shown in the inset plot.

wave function representing this particle contains incoming plane waves of that channel only. Incoming plane waves are completely absent in all other channels of this lead and in all other leads. In other words, all amplitudes $\mathcal{A}^+_{\alpha i}$ of incoming plane waves are zero except for one. Once the scattering matrix is known, Eq. 3.11 yields the vector of all amplitudes $\mathcal{A}^-_{\alpha i}$ of the outgoing plane waves, which answers our central question. Figure 3.3 illustrates the situation for a simple system with two one-dimensional leads.

Is it possible to design a device with an arbitrary scattering matrix? No, $\boldsymbol{S}$ must be unitary under all circumstances to fulfill probability conservation: Each entry in the vector of all amplitudes $\mathcal{A}^+$ of incoming plane waves (Eq. 3.11) represents a certain probability current flowing from the respective lead into the scattering region. To satisfy probability current conservation, the resulting total incoming current must be exactly compensated by the total outgoing current. The outgoing currents are characterized by the respective amplitudes $\mathcal{A}^-$ of the outgoing plane waves. In order probability current conservation for all possible constellations of incoming waves, the map implied by $\boldsymbol{S}$ must be norm-preserving, hence unitary.

Despite the general character of the scattering problem (Fig. 3.1), the mere requirement of probability conservation constrains the possible scattering matrices $\boldsymbol{S}$ strongly, because the unitary matrices are only a small subset of the set of all matrices. In this thesis the case of two single-channel leads is of special importance, because it describes a large class of electronic devices. The constraints for such two-lead devices required by

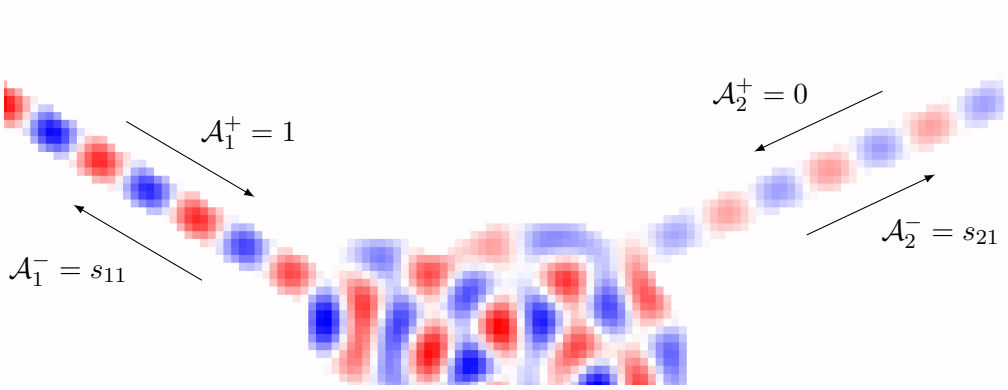


Figure 3.3: Illustration of the interpretation of the scattering coefficients between two single-channel leads with index 1 and 2. The color profile sketches the real part of the eigenfunction. If the amplitude $\mathcal{A}^+$ of the incoming plane wave is unity in lead 1 and zero in all other leads the resulting amplitudes $\mathcal{A}^-$ of the outgoing plane waves are given by columns 1 of the scattering matrix $\boldsymbol{S}$. Diagonal elements of $\boldsymbol{S}$ describe the reflection, off-diagonal elements describe the transmission of plane waves.

unitarity imply reciprocity relations, which describe the behavior under exchange of the electrical contacts. The resulting implications for electronic devices will be discussed in the following sections, here we will first introduce the fundamental properties of the two-lead scattering matrix and how it transforms under symmetry operations.

For devices with two strictly one-dimensional leads the scattering matrix $\boldsymbol{S}$ has 2×2 entries. The entries of the scattering matrix are s_{mn}, then the unitarity condition results in four independent equations:

$$\boldsymbol{S}^\dagger \boldsymbol{S} = \mathbb{1} \tag{3.12}$$

$$\iff \quad |s_{11}| = |s_{22}| \tag{3.13}$$

$$\wedge \quad |s_{12}| = |s_{21}| \tag{3.14}$$

$$\wedge \quad |s_{11}|^2 + |s_{21}|^2 = 1 \tag{3.15}$$

$$\wedge \quad \arg(s_{11}) + \arg(s_{22}) = \arg(s_{21}) + \arg(s_{12}) + \pi. \tag{3.16}$$

Equation 3.13 states that a plane wave incident from lead one is reflected with same magnitude as a plane wave incident from lead two. Equation 3.14 requires the corresponding behavior for the transmission. The magnitude of the transmitted wave is the same regardless of whether it travels in the $1 \to 2$ or in the $2 \to 1$ direction. The only possible difference for the two transmission directions is the shift of the plane wave's phase. Equation 3.15 represents the current conservation: The sum of transmitted and

reflected current, each being proportional to the squared absolute values of the complex wave amplitudes, must equal the respective current of the incoming wave, which is unity as defined in Eq. 3.11. Finally, Eq. 3.16 presents a constraint on the phase factors of the reflection and transmission coefficients.

These constraints may also be formulated as symmetries with respect to the lead-exchange operator $\hat{\boldsymbol{\mathcal{P}}}$ and the time-reversal operator $\hat{\boldsymbol{\mathcal{T}}}$. To find how $\boldsymbol{S}$ transforms under these symmetry operations, it is instructive to apply the two operators to Eq. 3.11, which for two single-channel leads is given by

$$\begin{pmatrix} \mathcal{A}_1^- \\ \mathcal{A}_2^- \end{pmatrix} = \boldsymbol{S} \begin{pmatrix} \mathcal{A}_1^+ \\ \mathcal{A}_2^+ \end{pmatrix}. \tag{3.17}$$

The definition of the amplitudes $\mathcal{A}^+$ and $\mathcal{A}^-$ of the incoming and outgoing plane waves by Eq. 3.8 gives insight into the effect of $\hat{\boldsymbol{\mathcal{T}}}$ on the complex amplitudes. Since the time-reversal of the wave function $\boldsymbol{\phi}$ is obtained by complex conjugation $\boldsymbol{\phi}^*$, under time-reversal $\mathcal{A}^+$ becomes $(\mathcal{A}^-)^*$ and $\mathcal{A}^-$ becomes $(\mathcal{A}^+)^*$. Hence, the time-reversal of Eq. 3.17 yields

$$\begin{pmatrix} (\mathcal{A}_1^+)^* \\ (\mathcal{A}_2^+)^* \end{pmatrix} = \hat{\boldsymbol{\mathcal{T}}}\, \boldsymbol{S}\, \hat{\boldsymbol{\mathcal{T}}}^{-1} \begin{pmatrix} (\mathcal{A}_1^-)^* \\ (\mathcal{A}_2^-)^* \end{pmatrix}. \tag{3.18}$$

This equation is formally identical to the inverted and conjugated Eq. 3.17:

$$\begin{pmatrix} (\mathcal{A}_1^+)^* \\ (\mathcal{A}_2^+)^* \end{pmatrix} = \left(\boldsymbol{S}^{-1}\right)^* \begin{pmatrix} (\mathcal{A}_1^-)^* \\ (\mathcal{A}_2^-)^* \end{pmatrix}. \tag{3.19}$$

Since $\boldsymbol{S}$ is unitary, $\boldsymbol{S}^{-1} = \boldsymbol{S}^\dagger$, the time-reversed scattering matrix is simply the transposed matrix

$$\hat{\boldsymbol{\mathcal{T}}}\, \boldsymbol{S}\, \hat{\boldsymbol{\mathcal{T}}}^{-1} = \left(\boldsymbol{S}^{-1}\right)^* = \boldsymbol{S}^{\mathrm{T}}. \tag{3.20}$$

Applying the lead-exchange operator $\hat{\boldsymbol{\mathcal{P}}}$ swaps the channel indices of the amplitudes $\mathcal{A}^+$ and $\mathcal{A}^-$ of the incoming and outgoing plane waves. Therefore, transforming Eq. 3.17 with $\hat{\boldsymbol{\mathcal{P}}}$ we obtain

$$\begin{pmatrix} \mathcal{A}_2^- \\ \mathcal{A}_1^- \end{pmatrix} = \hat{\boldsymbol{\mathcal{P}}}\, \boldsymbol{S}\, \hat{\boldsymbol{\mathcal{P}}}^{-1} \begin{pmatrix} \mathcal{A}_2^+ \\ \mathcal{A}_1^+ \end{pmatrix}. \tag{3.21}$$

A comparison with Eq. 3.17 leads us to the transformed scattering matrix:

$$\hat{\boldsymbol{\mathcal{P}}}\, \boldsymbol{S}\, \hat{\boldsymbol{\mathcal{P}}}^{-1} = \hat{\boldsymbol{\mathcal{P}}} \begin{pmatrix} s_{11} & s_{12} \\ s_{21} & s_{22} \end{pmatrix} \hat{\boldsymbol{\mathcal{P}}}^{-1} = \begin{pmatrix} s_{22} & s_{21} \\ s_{12} & s_{11} \end{pmatrix}. \tag{3.22}$$

The symmetry transformations of the scattering matrix shown in this section are published in [C]. To sum up, $\hat{\boldsymbol{\mathcal{P}}}$ exchanges s_{11} and s_{22}, as well as s_{12} and s_{21}. $\hat{\boldsymbol{\mathcal{T}}}$ exchanges s_{12} and s_{21} only. Considering the implications of the unitarity of $\boldsymbol{S}$ given in Eq. 3.13–3.16 we see that the absolute values of the scattering coefficients s are always symmetrical with respect to $\hat{\boldsymbol{\mathcal{P}}}$ and $\hat{\boldsymbol{\mathcal{T}}}$, even if $\hat{\boldsymbol{H}}$ breaks the respective symmetry.

3.3 Two-Lead Landauer-Büttiker Formula

In 1957, R. Landauer started pursuing ideas that lead to the description of electrical conduction in mesoscopic devices with scattering theory [51, 52]. The dominant view then was that the electrical field is the external stimulus which accelerates carriers and causes current flow. This acceleration happens along the mean free path between inelastic scattering at the atomic nuclei or defects, which limits the velocities and results in a current proportional to the applied electrical field. The corresponding theoretical toolsets typically treated the external fields as small perturbations of the system Hamiltonian and applied perturbation theory in $\hat{\boldsymbol{H}}$ to calculate the various responses of the system to the perturbing potential. The linear response theory for mesoscopic conduction was mainly developed by R. Kubo [53].

Landauer suggested to approach the problem from a different angle, namely treating the electric current as the external stimulus and the electrical field as the consequence caused by the "pile-up" of charges. The fact that the often exactly calculable eigenstates of scattering problems are associated with a constant current makes this approach attractive. Section 3.2 introduced the general form of the eigenstates of a system with discrete leads, with the plane waves corresponding to incoming and outgoing lead currents. If the scattering problem is diagonalizable, the conductivity can then be evaluated exactly, that is, without invoking perturbation theory. Figure 3.4 sketches the simplified case with two one-dimensional leads. The generally momentum dependent scattering coefficients s_{mn} specify the ratios of the complex wave amplitudes, their squared absolute values $|s_{mn}|^2$ represent the transmission and reflection probabilities of particles.

The result of earlier publications considered the voltage across the device as measured directly in the leads. The conductance was then deduced from the ratio of the current through the device to this voltage. This calculation implies that a two-lead system with strictly one-dimensional leads and a transmission probability of $|s_{12}|^2$ has an electrical conductance $\tilde{G}_{12}$ of

$$\tilde{G}_{12} = \underbrace{\frac{2q^2}{h}}_{G_0} \frac{|s_{12}|^2}{|s_{11}|^2} \tag{3.23}$$

with the elementary charge q, the Planck constant h and the conductance quantum G_0. This conductance $\tilde{G}_{12}$ was supposed to be measured by a fictitious four-wire measurement with nanoscopic voltage probes attached directly adjacent to the mesoscopic system. These nanoscopic voltage probes were considered not to have the character of baths. However, since the experiments use macroscopic voltmeters attached to wires of macroscopic length which act as thermal baths, this conductance was never measured. To solve this problem, the conductance needs to be calculated using the voltages measured deep inside the reservoirs attached to the device's leads as given by the reservoirs' Fermi level difference [54, 55]. In this case the conductance of the two-lead device is given by

$$G_{12} = G_0 |s_{12}|^2 \tag{3.24}$$

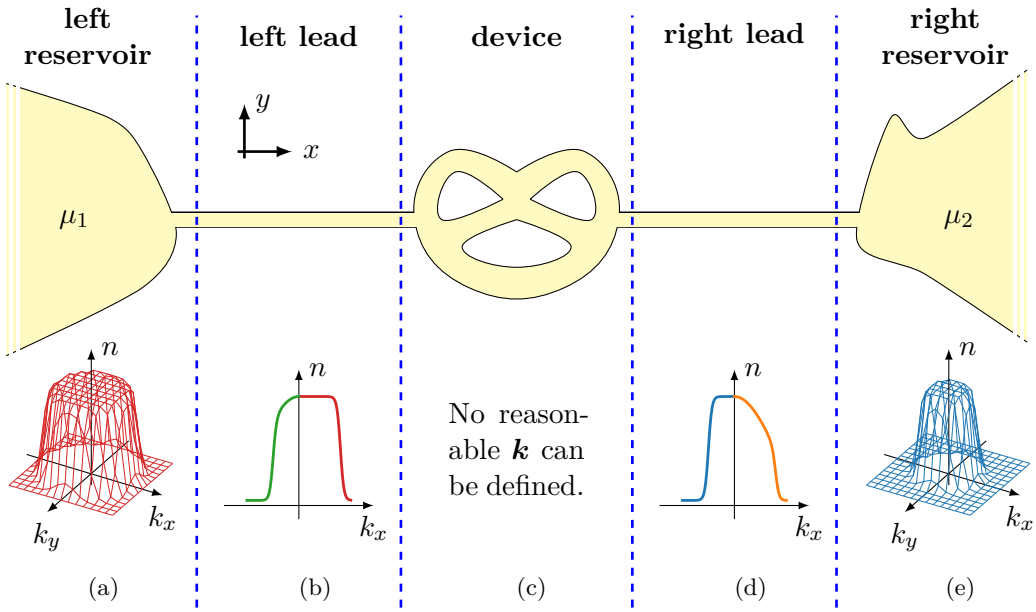


Figure 3.4: Mesoscopic two-lead device connected to two large reservoirs by two one-dimensional leads. (a,e) The carrier statistics in each reservoir is given by the Fermi distribution. A continuum of momenta in all directions exists, states with momenta in all directions k_x and k_y are equally populated up to a total momentum according to the reservoirs' Fermi levels μ_1 and μ_2, respectively. In this example, the Fermi level μ_1 of the left reservoir is higher than the Fermi level μ_2 the right reservoir, as sketched by the plots of the reservoir populations n. (b,d) In the one-dimensional leads, the momentum is defined only in the direction of the lead k_x. In the left lead, the statistics of carriers traveling to the right (red) is given by the Fermi distribution from the reservoir. The distribution of carriers traveling to the left (green) is composed of the reflected carriers from the left and the transmitted carriers from the right. The distribution in the right lead (blue and orange) is analogous. (c) In the device it is usually not reasonable to define a wave vector $\boldsymbol{k}$, because the device geometry is not periodic in general.

The difference between these two equations for the electrical conductance becomes obvious for the case of perfect transmission, $|s_{12}|^2 = 1$. For this case Eq. 3.23 yields $\tilde{G} \to \infty$, whereas Eq. 3.24 predicts a finite conductance $G = G_0$. Initially, an infinite conductance was expected for the case of perfect transmission and Eq. 3.23 was assumed to be correct in the earlier publications. However, following experiments exploring the transport through narrow, gate tunable constrictions beautifully demonstrated the quantization of the conductance in units of G_0 [40] (Section 2.3), which shows that Eq. 3.24 is to be used for most practical purposes.

The interpretation of the Landauer-Büttiker formula (Eq. 3.24) is obtained by considering that the reservoirs 1 and 2 constantly emit electrons at energies up to their Fermi energy μ_1 or μ_2. The emitted electrons are thermal, they neither feature correlations nor quantum coherence. Their reflection and transmission probabilities are given by the squared absolute values of the scattering coefficients $|s|^2$. Because of $|s_{21}| = |s_{12}|$, the two resulting currents cancel each other except if the two Fermi levels differ: $\mu_1 \neq \mu_2$.

The generalization of the formalism to many channels and leads is straightforward and improves the compatibility with experimental results [34]. The focus of this thesis, however, are the symmetries governing the two-lead transport, in particular those implied by the unitarity of scattering matrix $\boldsymbol{S}$. Therefore we only consider the case of two strictly one-dimensional leads.

The scattering matrix of the corresponding scattering problem has 2×2 entries. As we have seen in Eq. 3.13 and 3.14 the absolute values of the scattering coefficient are strictly constrained by unitarity. Owing to $|s_{21}| = |s_{12}|$ all two-lead devices must have the same conductance in forward and reverse direction $G_{21} = G_{12}$. This so-called two-lead reciprocity also holds for arbitrarily asymmetric structures, a ballistic diode cannot exist in the linear response regime.

Another symmetry with experimental relevance is the symmetry with respect to magnetic field reversal. Given that the system without applied magnetic field is time-reversal symmetric, a reversal of the external magnetic field is fully equivalent to the reversal of time for the transmission probabilities. As we have seen above the time-reversal always leaves the conductance unchanged, therefore the conductance has to be symmetric with respect to magnetic field reversal $G(B) = G(-B)$. Demonstrating the magnetic field symmetry of the magnetoconductance has become a standard method to test the clean two-lead measurement configuration and the cleanliness of the sample with respect to magnetic impurities.

The symmetries $G_{21} = G_{12}$ and $G(B) = G(-B)$ are ultimately caused by the unitarity of $\boldsymbol{S}$. It is impossible to break the two-lead reciprocity for the transmission and reflection probabilities by any means, the magnetic field symmetry cannot be broken without built-in magnetic moments. The consequences for asymmetric AB-rings or ratchets are remarkable and are discussed in Section 3.6.

3.4 Transport with Wave Packets

We have seen that the analysis of the eigenfunctions of a scattering problem yields the scattering coefficients and thereby also the electrical conductance of the device. As stated in the introduction of the chapter, the Schrödinger equation and the validity of the wave function description is limited to the realm of small length and time scales. The nonnormalizable, time-independent eigenfunctions of scattering theory do thus not describe real particles which correspond to time-dependent wave packets of finite width. The most prominent example for such wave packets is the Gaussian wave packet defined as

$$\boldsymbol{\psi}_{\mathrm{pck}}(k,t) = \frac{1}{\sqrt{2\sigma_k}\pi^{3/4}} \exp\left(\frac{-(k-k_0)^2}{2\sigma_k^2} - ix_0k - iE(k)t\right), \tag{3.25}$$

in momentum representation with the central momentum k_0, the central position x_0, the momentum spread σ_k and the momentum-dependent energy $E(k)$. Figure 3.5 shows the comparison of a one-dimensional Gaussian wave packet with an eigenfunction. The eigenstate is periodic in position space and infinitely continues in both x directions. In momentum space the eigenfunction is given by the infinitely narrow delta distribution. Neither infinite nor vanishing size occur in physical reality. The wave packet has a finite extension in both position and momentum space. If the wave-packet spread in momentum space is decreased, its position space spread increases and vice versa. The smallest possible product of both widths is $\hbar/2$, as required by the uncertainty relation.

Any wave function, therefore any wave packet, can be written in the eigenbasis, that is, as a linear combination of system eigenfunctions. Owing to the linearity of the Schrödinger equation, the time evolution of the wave packet is determined by the dynamic phase factors of the eigenfunctions forming it, which are given by plane waves in the leads of the scattering problem. Thus, the scattering matrix remains a valid description of the scattering process also for a wave packet.

We once again consider the scattering problem with two one-dimensional leads. Lead 1 extends in negative and lead 2 in positive x direction. If the wave packet given in Eq. 3.25 is placed on the left of the scattering region, the transmitted packet $\boldsymbol{\psi}_{\mathrm{tr}}$ on the right is obtained by multiplying with the generally momentum-dependent, complex scattering coefficient $s_{21}(k)$:

$$\boldsymbol{\psi}_{\mathrm{tr}}(k,t) = \frac{s_{21}(k)}{\sqrt{2\sigma_k}\pi^{3/4}} \exp\left(\frac{-(k-k_0)^2}{2\sigma_k^2} - ix_0k - iE(k)t\right). \tag{3.26}$$

The transmission probability P_{tr} of the wave packet is given by the integrated probability of the transmitted packet. Obviously, this probability equals the integrated probability of the original packet multiplied by $|s_{21}(k)|^2$:

$$P_{\mathrm{tr}} = \int |\boldsymbol{\psi}_{\mathrm{tr}}(k,t)|^2 \mathrm{d}k = \int |s_{21}(k)|^2 \cdot |\boldsymbol{\psi}(k,t)|^2 \mathrm{d}k. \tag{3.27}$$

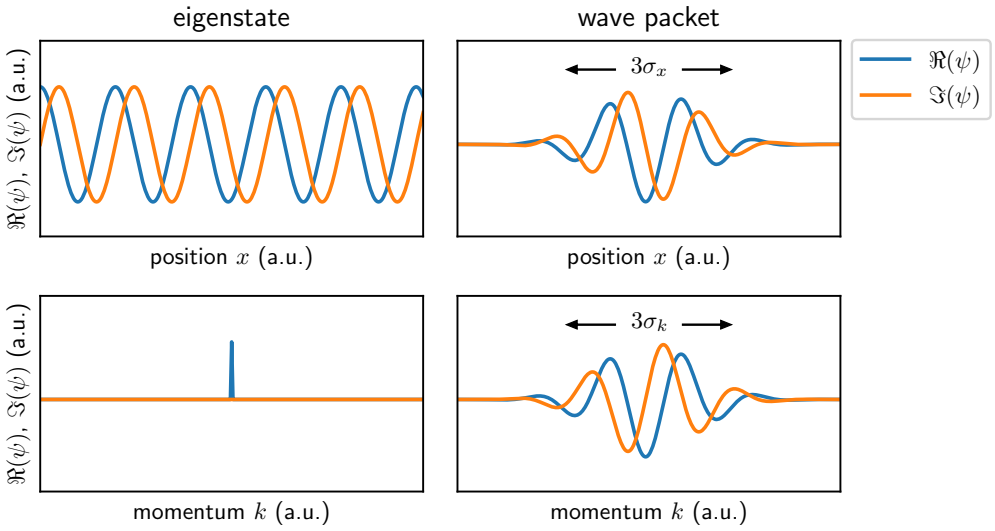


Figure 3.5: Comparison of a system eigenstate (left) and a Gaussian wave packet (right) in a one-dimensional waveguide. For both wave functions the real part $\Re(\psi)$ and imaginary part $\Im(\psi)$ are plotted in the position basis (top) and the momentum basis (bottom) representation. For the wave packet the momentum spread σ_k and the position spread σ_x are indicated by the arrows.

In other words, the transmission probability of a wave packet is given by the weighted plane wave transmission probabilities. Owing to $|s_{21}(k)| = |s_{12}(k)|$ for any k, the same two-lead reciprocity that applies for plane waves also applies to any superposition of plane waves. The transmission probability from lead 1 to lead 2 is always equal to the transmission probability in the opposite direction, if the original wave packets have the same momentum distribution. For the Gaussian packets treated here this requires that for both wave packets the central momentum $|k_0|$ as well as the momentum spread σ_k have to be equal. The same arguments with respect to the transmission probability of wave packets are applicable to the reflection probabilities.

The usual interpretation of the Landauer-Büttiker formula regards plane waves being emitted by reservoirs. However, these infinite wave functions with a sharp energy are no realistic description of electron states. Because the transmission probability is also defined for wave packets, not only for plane waves, the Landauer-Büttiker formula can be applied for wave packets as well. Instead of plane waves being emitted up to the Fermi energy of the reservoir, wave packets formed by states around the Fermi energy are emitted. This picture forms the basis of semiclassical theory and holds for finite temperatures and Fermi levels, such that enough states around the Fermi edge are available for the formation of wave packets.

Again due to the linearity of the Schrödinger equation, the choice of the wave function being emitted by the reservoirs does not matter for the resulting transmission prob-

abilities. The total transmission probability of any wave function solely depends on the momentum (or energy) distribution and thus the eigenbasis coefficients. Therefore, the two-lead conductance reciprocity $G_{21} = G_{12}$ and the magnetic field symmetry $G(B) = G(-B)$ mentioned in Section 3.3 also hold for wave packets. However, these only hold if one compares the system at sufficiently early with the system at sufficiently late times, such that the overlaps of the initial and final wave function with the scattering region vanish.

The dynamics between initial and final states, however, depends on the wave-packet shape and the scattering coefficients' phases. The unitarity conditions fully constrain the absolute values of the scattering coefficients (Eq. 3.13, 3.14 and 3.15) but leave three degrees of freedom for the respective phases (Eq. 3.16). The asymmetries $\arg(s_{21}) \neq \arg(s_{12})$ and $\arg(s_{11}) \neq \arg(s_{22})$ are allowed in principle insofar that they are compatible with the unitarity of the scattering matrix $\boldsymbol{S}$. The *dynamics* of the transmission and reflection process may therefore very well be nonreciprocal. This is an essential insight of this thesis.

The idea of nonreciprocal dynamics even in the two-lead systems was first published in [56]. A more rigorous calculation proving the reciprocity at late times and the nonreciprocity of the dynamics is published in the appendix of [D].

Section 3.2 introduced the lead-exchange operator $\hat{\boldsymbol{\mathcal{P}}}$ and the time-reversal operator $\hat{\boldsymbol{\mathcal{T}}}$ and their effect on the two-lead scattering matrix. There it was shown that the absolute values of the scattering coefficients are always symmetrical with respect to $\hat{\boldsymbol{\mathcal{P}}}$ and $\hat{\boldsymbol{\mathcal{T}}}$, due to the unitarity of $\boldsymbol{S}$. This is obviously not the case for the phases. We recall the symmetry relations with respect to the exchange of the the leads and to the reversal of time:

$$\hat{\boldsymbol{\mathcal{P}}}\,\boldsymbol{S}\,\hat{\boldsymbol{\mathcal{P}}}^{-1} = \boldsymbol{S} \qquad \Leftrightarrow s_{11} = s_{22} \ \wedge \ s_{21} = s_{12}, \tag{3.28}$$

$$\hat{\boldsymbol{\mathcal{T}}}\,\boldsymbol{S}\,\hat{\boldsymbol{\mathcal{T}}}^{-1} = \boldsymbol{S} \qquad \Leftrightarrow s_{21} = s_{12}, \tag{3.29}$$

$$\hat{\boldsymbol{\mathcal{P}}}\,\hat{\boldsymbol{\mathcal{T}}}\,\boldsymbol{S}\,\hat{\boldsymbol{\mathcal{T}}}^{-1}\,\hat{\boldsymbol{\mathcal{P}}}^{-1} = \boldsymbol{S} \ \Leftrightarrow \ s_{11} = s_{22}. \tag{3.30}$$

Equation 3.28 is a trivial statement: If the scattering matrix is symmetric with respect to lead exchange, reflection coefficients from both sides and transmission coefficients for both directions must be the same by their absolute values and phases. As Eq. 3.29 clarifies, time-reversal invariance governs the reciprocity of the transmission coefficients. Because the absolute values of s_{21} and s_{12} are always required to be identical, time-reversal asymmetry of the scattering matrix results in different phases of s_{21} and s_{12}. Broken time-reversal symmetry of the scattering matrix automatically implies a broken lead-exchange symmetry as well, as Eq. 3.28 and 3.29 show. However, as Eq. 3.30 reveals, the symmetry of the scattering matrix with respect to a combination of lead exchange and time-reversal $\hat{\boldsymbol{\mathcal{P}}}\hat{\boldsymbol{\mathcal{T}}}$ decides if the reflection coefficients from both sides are exactly equal or if they differ by a phase factor.

Illustrative example systems are presented in Section 3.6. There, systems that fulfill Eq. 3.29 but break Eq. 3.30 and systems that fulfill Eq. 3.30 but break Eq. 3.29 are

studied. Furthermore, the effects of asymmetric scattering coefficients' phases on time evolutions of wave packets are presented. A subset of these calculations is published in [C].

3.5 Wave-Packet Scattering Delay

As we saw in the previous section, three degrees of freedom are left unconstrained for the phases Φ_{mn} of the scattering coefficient s_{mn} by the unitarity condition, whereas the four absolute values are characterized by one single free parameter. Device properties that depend on the scattering phase Φ_{mn} can therefore be engineered with more freedom than those derived from the scattering coefficient's absolute values. We saw in Section 3.3 that the transmission probability and hence conductance belong to the latter category. Which measurable device properties are based on the phases?

Generally speaking, the phases determine the temporal aspects of the scattering process; they determine the dynamics of the wave-packet transport. This was first systematically analyzed for quantum mechanical scattering problems by E. P. Wigner and L. Eisenbud in 1947 [57]. In a later publication [58] they defined a characteristic time delay as the derivative of the scattering phase with respect to the particle energy:

$$\tau_{mn} = \hbar \frac{\partial \Phi_{mn}}{\partial E}, \tag{3.31}$$

with the scattering phase Φ_{mn}. The concept was later generalized to scattering matrices of arbitrary sizes [59]. Subsequent work demonstrated the connection of these delay times with nonlinear transport [60, 61], AC transport [62, 63] and the partial density of states [64].

Because we mainly discuss two-lead systems in this thesis, the definition Eq. 3.31 will be used in the following. In experimental setups the wave-packet scattering delay is typically a few nanoseconds for photons or smaller than picoseconds for electrons. It took over 50 years until the development of ultra-fast pulsed laser sources allowed the first direct measurement of the wave-packet scattering delay. In 2000, the polarization and incidence-angle dependent delay of a photon being reflected by an optical refraction grating was measured via correlation techniques [65]. With further improvements in detector sensitivity and time-resolution, the delay caused by near-resonant photon scattering off gas atoms was eventually measured by time-resolved photon counting in 2013 [66].

Recent experiments in 2019 succeeded in measuring the electron wave-packet dynamics in semicondutor quantum dots, paving the way to time resolved single electron counting in mesoscopic devices [67]. With these technological advances it is now possible to search for predicted phenomena related to the wave-packet scattering delay. One example is the work of Z. Ringel, Y. Imry, and O. Entin-Wohlman, who suggested a quantum correction to the classical capacitance caused by the wave-packet scattering delay [68]. A second example is the routing and processing of quantum information carried by moving carriers, so-called "flying qubits". For the design of such quantum gates the wave-packet scattering delay is essential [69].

The definition (Eq. 3.31) can be readily understood by analyzing the scattered Gaussian wave packet (Eq. 3.26),

$$\boldsymbol{\psi}_{\mathrm{tr}}(k,t) = \frac{s_{mn}(k)}{\sqrt{2\sigma_k}\pi^{3/4}} \exp\left(\frac{-(k-k_0)^2}{2\sigma_k^2} - ix_0k - ik^2t\right), \tag{3.32}$$

with a parabolic dispersion $E(k) = k^2$. The parabolic dispersion describes the behavior only for momenta $k \ll 1/\delta\boldsymbol{r}$ that are much smaller than the scale given by the inverse lead period. In this chapter, we will consider leads without inner structure (except for Section 3.6.3), hence $\delta\boldsymbol{r} \to 0$ and the parabolic dispersion is accurate for all k.

Next, we write the scattering coefficient s_{mn} in polar representation and move the phase into the argument of the exponential function. Furthermore, we rearrange the imaginary part of the argument to reveal the motion of the wave-packet center:

$$\boldsymbol{\psi}_{\mathrm{tr}}(k,t) = \frac{|s_{mn}(k)|}{\sqrt{2\sigma_k}\pi^{3/4}} \exp\left(\frac{-(k-k_0)^2}{2\sigma_k^2} - ix_0k - ik^2t + i\Phi_{mn}(k)\right) \tag{3.33}$$

$$= \frac{|s_{mn}(k)|}{\sqrt{2\sigma_k}\pi^{3/4}} \exp\left(\frac{-(k-k_0)^2}{2\sigma_k^2} - ik\left(x_0 + k\left(t - \frac{\Phi_{mn}(k)}{k^2}\right)\right)\right). \tag{3.34}$$

In the trivial case of $s_{mn}(k) = 1$ and $\Phi_{mn}(k) = 0$ the wave packet is centered around $x_0 + kt$. It moves with a momentum-dependent velocity, which causes it to disperse as it propagates. The component of $\Phi_{mn}(k)$ that is proportional to k^2 determines the time delay caused by the scattering process that $s_{mn}(k)$ describes. Owing to the dispersion relation $E \propto k^2$ this term is given by the leading order of the derivative of $\Phi_{mn}(k)$ with respect to E.

For wave packets with a narrow momentum distribution, $\Phi_{mn}(k)$ is approximately proportional to k^2 in the relevant k range. In this case, τ_{mn} does not depend on k and the wave-packet envelope is not changed by the transmission of reflection process. The usual spatial broadening of wave packets, induced by the nonlinear dispersion relation, still applies of course.

Negative wave-packet scattering delays are possible, for example if an attractive potential accelerates the wave packet. Nevertheless there is a lower limit which depends on the size of the scattering region. This limit can be understood as the natural consequence of causality but it is also possible to derive the limit only from the fundamental properties of the scattering matrix [58]. An upper limit for the wave-packet scattering delay does not exist, indeed a diverging positive τ is the fingerprint of the vicinity to a resonance [66, 70], an eigenstate that vanishes in all leads, a so-called bound state (trivial case of Eq. 3.8, all $\mathcal{A}^+_{i\alpha} = \mathcal{A}^-_{i\alpha} = 0$). For the bound state itself the wave-packet scattering delay is therefore not defined. It does not interact with the leads and cannot be populated by injecting wave packets from any lead. Wave functions formed from bound states are not able to leave the scattering region under time evolution.

In this thesis the wave-packet scattering delay plays the role of an established temporal characteristic of an elastic scattering process that is explicitly dependent on the scattering phase. In contrast to the scattering coefficients' absolute values, which control the

ballistic conductance, the scattering phases and thus the wave-packet scattering delays are not necessarily reciprocal in two-lead devices. Directly measurable consequences of the wave-packet scattering delay for quantum transport are presented in [67–69]. Due to the weaker symmetry constraints of τ_{mn}, the related phenomena may be tailored with more freedom than the conductance. In particular the two-lead conductance reciprocity $G_{12} = G_{21}$ and the magnetic field symmetry $G(B) = G(-B)$ are not required to be valid for the wave-packet scattering delay, generally $\tau_{12} \neq \tau_{21}$ and $\tau(B) \neq \tau(-B)$ are allowed.

3.6 Scattering Model of Example Systems

The previous sections introduced the scattering theory of quantum mechanics and the Landauer-Büttiker picture. To calculate the ballistic conductance of a device from its Hamiltonian, first the eigenfunctions $\boldsymbol{\phi}$ are obtained. Second, the scattering matrix $\boldsymbol{S}$ is extracted from the eigenfunctions. The ballistic conductance is proportional to the squared absolute value of the transmission coefficient. We saw that in the case of two one-dimensional leads the unitarity of $\boldsymbol{S}$ fully constrains the absolute values of the scattering coefficients, however three unconstrained degrees of freedom remain for the complex phases. The wave-packet scattering delay was introduced as an observable quantity that directly depends on these phases.

In this section, a series of scattering problems is presented to demonstrate the application of the previously introduced methods and to study the discussed symmetries. The systems are chosen to display typical quantum transport effects such as multi-path interference, quantum tunneling and universal conductance fluctuations. All systems except for the last one are treated analytically, in the last example a numerically solvable tight-binding model is applied. For each system the scattering coefficients are found and time evolutions of Gaussian wave packets are presented to study the temporal aspects of wave-packet transport.

All following examples consider a three-dimensional scattering region and two one-dimensional leads. Lead 1 extends in negative x direction and starts at $x = -\frac{1}{2}L_x$, lead 2 extends in positive x direction and starts at $x = \frac{1}{2}L_x$. Accordingly, the scattering region has a length of L_x in x-direction. As in the previous sections, all terms and values are given in the natural units $\hbar = q = 2m = 1$.

3.6.1 Symmetric and Asymmetric Potential Barriers

A potential barrier of variable width and height placed between the leads represents a prototypical system to study elastic scattering. In addition, asymmetric barriers with different heights on their left and right sides, are considered, to study the effects of the barrier asymmetry on quantum transport.

The Hamiltonian describing such barriers is

$$\hat{\boldsymbol{H}}_{\mathrm{bar}} = -\partial_x^2 + \mathcal{V}_{\mathrm{bar}}(x), \tag{3.35}$$

$$\mathcal{V}_{\mathrm{bar}}(x) = \begin{cases} \frac{x}{L_x}\left(\mathcal{V}_{\mathrm{R}} - \mathcal{V}_{\mathrm{L}}\right) + \frac{1}{2}\left(\mathcal{V}_{\mathrm{R}} + \mathcal{V}_{\mathrm{L}}\right) & \text{for } -\frac{1}{2}L_x \leq x \leq \frac{1}{2}L_x \\ 0 & \text{else} \end{cases}, \tag{3.36}$$

with the left side potential $\mathcal{V}_{\mathrm{L}}$ the right side potential $\mathcal{V}_{\mathrm{R}}$ and the barrier width L_x. We begin with the case of a symmetric potential barrier $\mathcal{V} \coloneqq \mathcal{V}_{\mathrm{L}} = \mathcal{V}_{\mathrm{R}}$. The eigenfunctions and eigenvalues are found by solving the Schrödinger equation $\hat{\boldsymbol{H}}\boldsymbol{\phi} = E\boldsymbol{\phi}$. The Ansatz for the symmetric barrier is given by

$$\boldsymbol{\phi}_{\mathrm{sbar}}(x) = \begin{cases} \mathcal{A}_{\mathrm{L}}^{-}e^{-ikx} + \mathcal{A}_{\mathrm{L}}^{+}e^{ikx} & \text{for } x < -\frac{1}{2}L_x \\ \mathcal{A}_{\mathrm{CL}}e^{-i\kappa x} + \mathcal{A}_{\mathrm{CR}}e^{i\kappa x} & \text{for } -\frac{1}{2}L_x \leq x \leq \frac{1}{2}L_x \\ \mathcal{A}_{\mathrm{R}}^{-}e^{ikx} + \mathcal{A}_{\mathrm{R}}^{+}e^{-ikx} & \text{for } x > \frac{1}{2}L_x \end{cases}, \tag{3.37}$$

$$k = \sqrt{E}, \tag{3.38}$$

$$\kappa = \sqrt{E - \mathcal{V}}, \tag{3.39}$$

with the left side incoming and outgoing plane wave amplitudes $\mathcal{A}_{\mathrm{L}}^{+}$ and $\mathcal{A}_{\mathrm{L}}^{-}$, the central region left and right moving plane wave amplitudes $\mathcal{A}_{\mathrm{CL}}$ and $\mathcal{A}_{\mathrm{CR}}$ and the right side incoming and outgoing plane wave amplitudes $\mathcal{A}_{\mathrm{R}}^{+}$ and $\mathcal{A}_{\mathrm{R}}^{-}$. The momentum k in the leads is given by the simple quadratic dispersion given in Eq. 3.38. The designation "momentum" for the corresponding variable κ on top of the barrier is only valid for $E \geq \mathcal{V}$ because it is purely imaginary otherwise. Therefore, we use the more general term "propagation constant" for κ here.

To find the values for the six free parameters in Eq. 3.37, we need to specify boundary conditions at the potential discontinuities $x = \pm\frac{1}{2}L_x$. We find four of these equations by requiring smoothness of the wave function $\boldsymbol{\phi}_{\mathrm{sbar}}(x)$ and the first derivative $\partial_x\boldsymbol{\phi}_{\mathrm{sbar}}(x)$

$$\mathcal{A}_{\mathrm{L}}^{-}e^{-ikx} + \mathcal{A}_{\mathrm{L}}^{+}e^{ikx} = \mathcal{A}_{\mathrm{CL}}e^{-i\kappa x} + \mathcal{A}_{\mathrm{CR}}e^{i\kappa x} \qquad \big|_{x=-\frac{1}{2}L_x}, \tag{3.40}$$

$$ik\left(-\mathcal{A}_{\mathrm{L}}^{-}e^{-ikx} + \mathcal{A}_{\mathrm{L}}^{+}e^{ikx}\right) = i\kappa\left(-\mathcal{A}_{\mathrm{CL}}e^{-i\kappa x} + \mathcal{A}_{\mathrm{CR}}e^{i\kappa x}\right)\big|_{x=-\frac{1}{2}L_x}, \tag{3.41}$$

$$\mathcal{A}_{\mathrm{CL}}e^{-i\kappa x} + \mathcal{A}_{\mathrm{CR}}e^{i\kappa x} = \mathcal{A}_{\mathrm{R}}^{-}e^{ikx} + \mathcal{A}_{\mathrm{R}}^{+}e^{-ikx} \qquad \big|_{x=\frac{1}{2}L_x}, \tag{3.42}$$

$$i\kappa\left(-\mathcal{A}_{\mathrm{CL}}e^{-i\kappa x} + \mathcal{A}_{\mathrm{CR}}e^{i\kappa x}\right) = ik\left(\mathcal{A}_{\mathrm{R}}^{-}e^{ikx} - \mathcal{A}_{\mathrm{R}}^{+}e^{-ikx}\right) \qquad \big|_{x=\frac{1}{2}L_x}. \tag{3.43}$$

We merge these four equations into two to eliminate the amplitudes of the internal plane waves $\mathcal{A}_{\mathrm{CL}}$ and $\mathcal{A}_{\mathrm{CR}}$ and obtain

$$\begin{aligned}
&\kappa\left(\mathcal{A}_{\mathrm{L}}^{+}+\mathcal{A}_{\mathrm{L}}^{-}e^{iL_x k}\right)-k\left(\mathcal{A}_{\mathrm{L}}^{+}-\mathcal{A}_{\mathrm{L}}^{-}e^{iL_x k}\right)e^{-\frac{iL_x(\kappa+k)}{2}}\\
&\quad=\left(\mathcal{A}_{\mathrm{R}}^{+}\kappa+\mathcal{A}_{\mathrm{R}}^{+}k+\mathcal{A}_{\mathrm{R}}^{-}\kappa e^{iL_x k}-\mathcal{A}_{\mathrm{R}}^{-}k e^{iL_x k}\right)e^{\frac{iL_x(\kappa-k)}{2}}, \qquad (3.44)\\
&\kappa\left(\mathcal{A}_{\mathrm{R}}^{+}+\mathcal{A}_{\mathrm{R}}^{-}e^{iL_x k}\right)-k\left(\mathcal{A}_{\mathrm{R}}^{+}-\mathcal{A}_{\mathrm{R}}^{-}e^{iL_x k}\right)e^{-\frac{iL_x(\kappa+k)}{2}}\\
&\quad=\left(\mathcal{A}_{\mathrm{L}}^{+}\kappa+\mathcal{A}_{\mathrm{L}}^{+}k+\mathcal{A}_{\mathrm{L}}^{-}\kappa e^{iL_x k}-\mathcal{A}_{\mathrm{L}}^{-}k e^{iL_x k}\right)e^{\frac{iL_x(\kappa-k)}{2}}. \qquad (3.45)
\end{aligned}$$

The scattering coefficient s_{11} describes the plane wave leaving to the left if a plane wave with unity amplitude is incoming from the left. To extract s_{11} from Eq. 3.44 and 3.45, we set the amplitudes of the left and right side incoming plane waves $\mathcal{A}_{\mathrm{L}}^{+}=1$ and $\mathcal{A}_{\mathrm{R}}^{+}=0$, eliminate the amplitude of the plane wave arriving from the right $\mathcal{A}_{\mathrm{R}}^{+}$ and solve for the amplitude of the plane wave arriving from the left $\mathcal{A}_{\mathrm{L}}^{+}$. The remaining scattering coefficient s_{mn} are calculated analogously. Because of the symmetry of the system with respect to the lead-exchange operator $\hat{\boldsymbol{\mathcal{P}}}$ full reciprocity of the scattering coefficients holds: $s_{11}=s_{22}$ and $s_{21}=s_{12}$. Their expressions read[1]:

$$s_{11,\mathrm{sbar}}=s_{22,\mathrm{sbar}}=\frac{\left(\kappa^2e^{2iL_x\kappa}-\kappa^2-k^2e^{2iL_x\kappa}+k^2\right)e^{-iL_xk}}{-\kappa^2e^{2iL_x\kappa}+\kappa^2+2\kappa ke^{2iL_x\kappa}+2\kappa k-k^2e^{2iL_x\kappa}+k^2}, \qquad (3.46)$$

$$s_{21,\mathrm{sbar}}=s_{12,\mathrm{sbar}}=\frac{4\kappa ke^{iL_x(\kappa-k)}}{-\kappa^2e^{2iL_x\kappa}+\kappa^2+2\kappa ke^{2iL_x\kappa}+2\kappa k-k^2e^{2iL_x\kappa}+k^2}. \qquad (3.47)$$

A subtle role is played by the exponential terms in these expressions. The parameters k and L_x are guaranteed to be real and positive, their occurrence in the argument of the exponential function only rotates the phase of the term. However, $\kappa=\sqrt{E-\mathcal{V}}$ is only positive and real if $E\geq\mathcal{V}$. For $E<\mathcal{V}$ the propagation constant κ is purely imaginary and leads to exponentially decaying absolute values of the exponential terms. To simplify the expression for the transmission coefficients, we define the real part κ_{r} and the imaginary part κ_{i} of the propagation constant, $\kappa=\kappa_{\mathrm{r}}+i\kappa_{\mathrm{i}}$ with $\kappa_{\mathrm{r}},\kappa_{\mathrm{i}}\in\mathbb{R}$. For the first case $E\geq\mathcal{V}$ we obtain $\kappa_{\mathrm{r}}=\sqrt{E-\mathcal{V}}$ and $\kappa_{\mathrm{i}}=0$, for the second case $E<\mathcal{V}$ we

[1] Importable expressions for Python's sympy package, for Matlab, Octave, Mathematica and Maple can be found in appendix chapter A.1

obtain $\kappa_\mathrm{r} = 0$ and $\kappa_\mathrm{i} = \sqrt{\mathcal{V} - E}$. With these replacements we and obtain

$$|s_{21,\mathrm{sbar}}|^2 = \begin{cases} \left(\dfrac{16\kappa_\mathrm{r}^2 k^2}{2\kappa_\mathrm{r}^4 + 12\kappa_\mathrm{r}^2 k^2 + 2k^4 + 2\left(-\kappa_\mathrm{r}^4 + 2\kappa_\mathrm{r}^2 k^2 - k^4\right)\cos\left(2L_x\kappa_\mathrm{r}\right)} \right)^2 & \text{for } E \geq \mathcal{V}, \\ \left(\dfrac{16\kappa_\mathrm{i}^2 k^2}{\left(-2\kappa_\mathrm{i}^4 + 12\kappa_\mathrm{i}^2 k^2 - 2k^4 + 2\left(\kappa_\mathrm{i}^4 + 2\kappa_\mathrm{i}^2 k^2 + k^4\right)\cosh\left(2L_x\kappa_\mathrm{i}\right)} \right)^2 & \text{else.} \end{cases} \tag{3.48}$$

The transmission probability $|s_{21,\mathrm{sbar}}|^2$ approaches unity for $E \gg \mathcal{V}$ (first case, $k \to \infty$ and $\kappa_\mathrm{r} \to \infty$) and zero for $E \ll \mathcal{V}$ (second case, k is constant and $\kappa_\mathrm{i} \to \infty$). Nevertheless, at $E < \mathcal{V}$ the transmission always remains finite but becomes exponentially small with increasing L_x. An electrical current may even flow through an insulator if only it is thin enough, a phenomenon known as quantum tunneling (Fig. 3.7).

Also remarkable is the behavior of deep wells (first case, k constant and κ_r finite, large). One might expect that they behave similar to low barriers and offer high transmission. In fact, transparency is only reached if the cosine in the denominator equals one, so $L_x\kappa = n\pi$ with integer n. If this resonance condition is not met, the transmission probability drops, in some cases even to zero.

These statements about the transmission probability are well known and of course also hold for the ballistic conductance of a potential barrier. Considering wave packets, the probabilities do not contain any temporal information on the scattering process, which is encoded in the phases of the scattering coefficients. Figures 3.6 and 3.7 show the wave-packet scattering delays (Section 3.5) for the three systems. As mentioned above reflection and transmission coefficients are reciprocal by absolute value and phase ($s_{11} = s_{22},\ s_{21} = s_{21}$) due to the symmetry of the system with respect to the lead-exchange operator $\hat{\boldsymbol{\mathcal{P}}}$. In this case the constraint on the phases implied by unitarity (Eq. 3.16) reads

$$2\arg(s_{11}) = 2\arg(s_{21}) + \pi \tag{3.49}$$

$$\Rightarrow \partial_E \arg(s_{11}) = \partial_E \arg(s_{21}), \tag{3.50}$$

which reveals that $\tau_{11} = \tau_{22}$ for any choice of parameters. Figures 3.6 and 3.7 confirm that transmission and reflection delays are identical. The full analytical expressions for the delays are inconveniently large, but can be easily calculated from the expressions for the scattering coefficients with any symbolic mathematics software (Appendix A.1).

If the width and the height of the barrier are comparable to the energy and wavelength of the incident plane waves (Fig. 3.6), the wave-packet scattering delay monotonically falls with k. The divergence in the limit of small energies is due to the finite barrier penetration even at these low energies. Wave packets are not reflected exactly at the potential step but slightly behind it. Due to the small velocities of these low energy wave packets the small lateral offset corresponds to large delays. In the limit of large k the transmission probability approaches one and the delay approaches zero, high energy particles are not affected by the barrier.

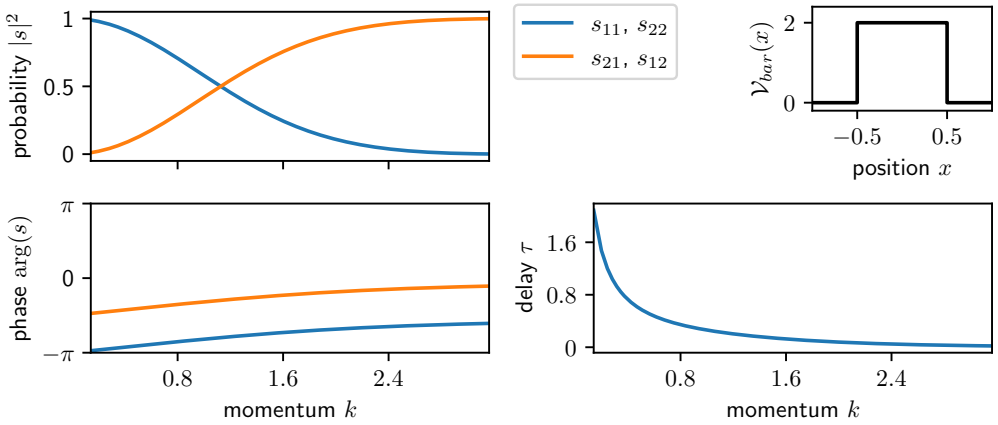


Figure 3.6: Plots showing the scattering coefficients in polar representation (left), scattering potential (top right), and wave-packet scattering delays (bottom right) of the symmetric potential barrier with $\mathcal{V} = 2$ and $L_x = 1$. Reflection and transmission delays are identical due to $\hat{\boldsymbol{\mathcal{P}}}$ symmetry. A wave-packet scattering delay of zero is defined as the transmission delay of a perfect waveguide or the reflection delay of a perfect mirror at $x = 0$. Particles with energies below the barrier height are reflected and particles with a higher energy are transmitted. For energies above the barrier height $k > \sqrt{2}$, the wave-packet scattering delay τ approaches zero, for small energies τ diverges. In the wave-packet scattering delay plot the orange curve is not visible, because it completely overlaps with the blue curve (Eq. 3.50).

In the case of the tunneling barrier, for which the barrier height is much higher than the particle energy but the width is small (Fig. 3.7), the wave-packet scattering delay peaks at small widths and monotonically falls with larger barrier widths. The delay is positive as long as significant transmission (tunneling) takes place and drops below zero when the reflection probability is close to unity. The positive delays in the tunneling regime show that the tunneling process is slower than free the propagation. The negative delays occur because the reflection delay is relative to the perfect reflection at $x = 0$. With increasing L_x the reflection takes place further and further away from $x = 0$, which implies that the reflected wave packet returns quicker than a hypothetical wave packet reflected at the origin.

To elucidate the consequences of the wave-packet scattering delay we examine the wave-packet time evolutions. As derived in Section 3.4 the transmission and reflection probabilities for the wave packets are given by the averaged plane wave transmission and reflection probabilities $|s_{mn}|^2$. The time dependence of the wave-packet transmission and reflection process is encoded in the scattering phases $\arg(s_{mn})$.

The expression for the time-dependent Gaussian wave packet in the momentum basis is given in Eq. 3.25 and is valid for a sufficiently long waveguide. Hence, it is applicable to our barrier if the wave packet is sufficiently far away from the scattering region. Therefore, we place the packet's center at least $3\sigma_x$ away from the scattering region, which implies an initial wave-packet overlap with the scattering region of $< 3 \times 10^{-5}$. Here $\sigma_x = 1/\sigma_k$ is the position spread. To place an initial right moving wave packet on the left of the barrier, we construct the packet from system eigenfunctions $\boldsymbol{\phi}_{\text{bar}}$ (Eq. 3.37) characterized by a right moving plane wave with amplitude unity on the left of the barrier and by the absence of left moving plane waves on the right of the barrier[2]: $\mathcal{A}^+_{\text{L}} = 1$ and $\mathcal{A}^+_{\text{R}} = 0$. To place a left moving wave packet on the right side of the barrier we accordingly use eigenfunctions with $\mathcal{A}^+_{\text{L}} = 0$ and $\mathcal{A}^+_{\text{R}} = 1$.

These two eigenfunction types only contribute plane waves moving in the direction in which the packet's central momentum k_0 is pointing. However, as one can see immediately from Eq. 3.25, every wave packet has a (usually exponentially small) content of plane waves moving in the opposite direction. Thus, for the complete description of the wave packet on the left side of the barrier we also need eigenfunctions with $\mathcal{A}^-_{\text{L}} = 1$ and $\mathcal{A}^-_{\text{R}} = 0$. For the wave packets on the right we achieve completeness by incorporating the eigenfunctions with $\mathcal{A}^-_{\text{L}} = 0$ and $\mathcal{A}^-_{\text{R}} = 1$. With these considerations we can write

[2]Recall that due to the four boundary conditions given in Eq. 3.40–3.43, only two of the six complex amplitudes in the Ansatz function can be freely chosen. Therefore, the eigenfunction is completely specified by specifying two amplitudes.

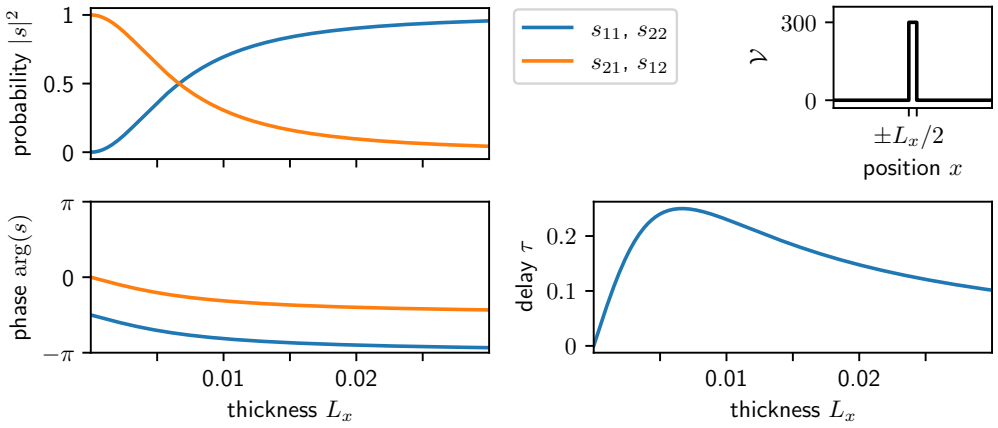


Figure 3.7: Plots showing the scattering coefficients in polar representation (left), scattering potential (top right), and wave-packet scattering delays (bottom right) of the symmetric tunnel barrier with $\mathcal{V} = 300$. The scattering coefficients and the wave-packet scattering delay are given as a function of the barrier thickness L_x. The barrier is much higher than the particle energy $E = 1$, still the barrier becomes transparent if it is sufficiently thin. In the limit of small thicknesses the delay approaches zero. For infinite thicknesses the reflection delay approaches negative infinity, because the potential edge which is the reflection plane, moves into infinity. In the wave-packet scattering delay plot the orange curve is not visible, because it completely overlaps with the blue curve (Eq. 3.50).

down an expression for wave packet placed on the left or the right in the system:

$$\boldsymbol{\psi}_{\mathrm{bar}}(x,t) = \int \boldsymbol{\psi}_{\mathrm{pck}}(k,t)\tilde{\boldsymbol{\phi}}_{\mathrm{bar}}(k,x)\mathrm{d}k, \tag{3.51}$$

$$\tilde{\boldsymbol{\phi}}_{\mathrm{bar}}(k,x) = \begin{cases} \boldsymbol{\phi}_{\mathrm{bar}}(k,x)|_{\mathcal{A}_{\mathrm{L}}^{+}=1,\mathcal{A}_{\mathrm{R}}^{+}=0} & \text{if } x_0 < 3\sigma_x \text{ and } k > 0, \\ \boldsymbol{\phi}_{\mathrm{bar}}(k,x)|_{\mathcal{A}_{\mathrm{L}}^{-}=1,\mathcal{A}_{\mathrm{R}}^{-}=0} & \text{if } x_0 < 3\sigma_x \text{ and } k < 0, \\ \boldsymbol{\phi}_{\mathrm{bar}}(k,x)|_{\mathcal{A}_{\mathrm{R}}^{-}=1,\mathcal{A}_{\mathrm{L}}^{-}=0} & \text{if } x_0 > 3\sigma_x \text{ and } k > 0, \\ \boldsymbol{\phi}_{\mathrm{bar}}(k,x)|_{\mathcal{A}_{\mathrm{R}}^{+}=1,\mathcal{A}_{\mathrm{L}}^{+}=0} & \text{if } x_0 > 3\sigma_x \text{ and } k < 0. \end{cases} \tag{3.52}$$

The integral Eq. 3.51 has to be solved numerically, closed solutions exist only for special parameter choices. Figure 3.8 shows the time evolutions of the probability density for different wave packets being scattered by the barriers introduced in Figs. 3.6 and 3.7. The total transmitted (reflected) fraction of the wave packets matches the respective scattering probabilities. In addition, the wave-packet evolutions present detailed dynamics of the scattering process in the scattering region.

The focus of this thesis lies on the symmetries of quantum transport, therefore the case of $\mathcal{V}_{\mathrm{L}} \neq \mathcal{V}_{\mathrm{R}}$, hence broken lead exchange symmetry is discussed next. For this asymmetric potential barrier the Ansatz function is given by

$$\boldsymbol{\phi}_{\mathrm{abar}}(x) = \begin{cases} \mathcal{A}_{\mathrm{L}}^{-}e^{-ikx} + \mathcal{A}_{\mathrm{L}}^{+}e^{ikx} & \text{for } x < -\frac{1}{2}L_x, \\ \mathcal{A}_{\mathrm{CA}}\,\mathrm{Ai}(\gamma) + \mathcal{A}_{\mathrm{CB}}\,\mathrm{Bi}(\gamma) & \text{for } -\frac{1}{2}L_x \leq x \leq \frac{1}{2}L_x, \\ \mathcal{A}_{\mathrm{R}}^{-}e^{ikx} + \mathcal{A}_{\mathrm{R}}^{+}e^{-ikx} & \text{for } x > \frac{1}{2}L_x, \end{cases} \tag{3.53}$$

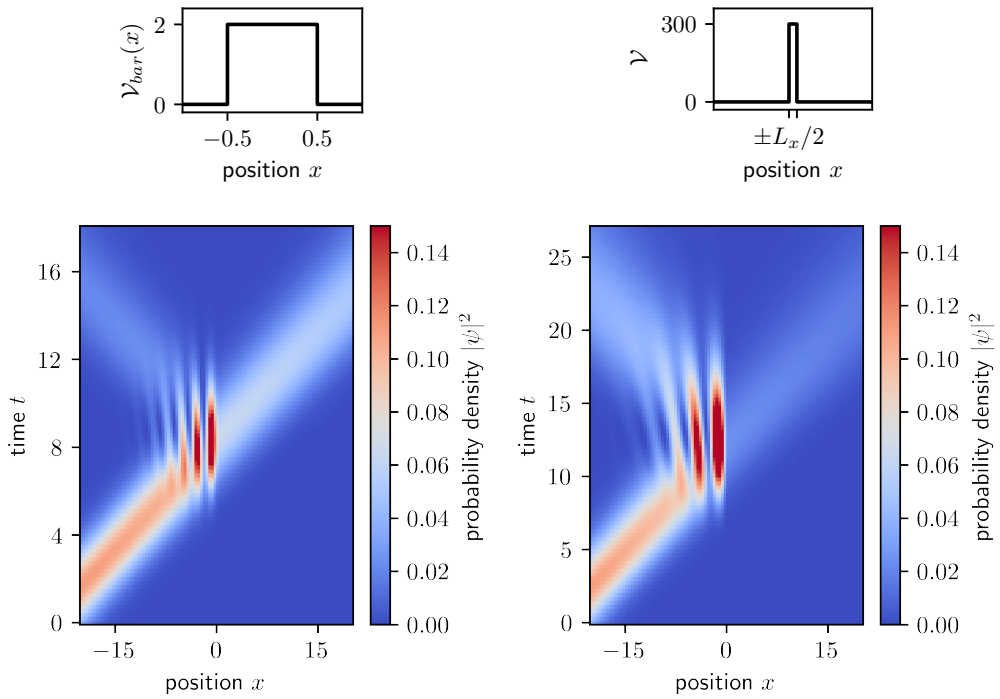
$$k = \sqrt{E}, \tag{3.54}$$

$$\gamma = \frac{L_x\left(\mathcal{V}_{\mathrm{L}} + \mathcal{V}_{\mathrm{R}} - 2E\right) - 2x\left(\mathcal{V}_{\mathrm{L}} - \mathcal{V}_{\mathrm{R}}\right)}{2\left(L_x\left(\mathcal{V}_{\mathrm{R}} - \mathcal{V}_{\mathrm{L}}\right)\right)^{\frac{2}{3}}}, \tag{3.55}$$

with the Airy functions Ai and Bi, the central region Airy function amplitudes $\mathcal{A}_{\mathrm{CA}}$ and $\mathcal{A}_{\mathrm{CB}}$ and the Airy function argument γ. Repeating the steps used for the symmetric barrier yields the scattering matrix of the system. The expressions are inconveniently long and are therefore not presented here, but given as importable expressions for common mathematical software packages in Appendix A.2.

The results of numerical evaluation of the transmission probabilities, the phases and the wave-packet scattering delays are given in Figs. 3.9 and 3.10. The transmission and reflection probabilities are fully reciprocal as required by unitarity. Due to the broken $\hat{\boldsymbol{\mathcal{P}}}$ symmetry, however, the phases and delays do not follow Eq. 3.49 and 3.50, respectively. Two systems similar to the systems discussed in Figs. 3.6 and 3.7 are demonstrated.

The first example (Fig. 3.9) shows an asymmetric potential barrier with comparable height and width. The transmission probabilities match qualitatively those of the symmetric counterpart (Fig. 3.6). The transmission of particles with energies below the



(a) (b)

Figure 3.8: Colormaps showing the time evolutions of wave packets being scattered by the potentials introduced in Fig. 3.6 and Fig. 3.7. (a) The potential barrier with $\mathcal{V} = 2$, $L_x = 1$ scattering a wave packet with $k_0 = 1.5$ and $\sigma_k = 0.2$. At $t = 0$ the packet is centered around $x_0 = -25$. Part of the packet is transmitted (upper right part of the plot), the rest is reflected (upper left part of the plot). (b) Despite the tunnel barrier being much higher ($\mathcal{V} = 300$) than the particle's energy $E = k^2 = 1$ the wave packet penetrates the barrier and is partly transmitted. The barrier thickness is $L_x = 0.01$. The width and the initial position of the packet are $\sigma_k = 0.2$ and $x_0 = -25$.

barrier height are blocked, those above are transmitted. In contrast, the scattering coefficients' phases are only reciprocal for $k \ll 1$. For higher momenta (energies) reflection on the left and on the right side of the barrier cause different phase shifts. Calculating the corresponding wave-packet scattering delays shows that at $k > 1$ reflection at lead 1 takes longer than reflection at lead 2. However, the reflection phase and delay is only significant for $k < 3$, because the reflection probability is close to zero otherwise.

The second system is given by the asymmetric tunnel barrier (Fig. 3.10), which for low values of L_x is also similar to its symmetric sibling. As one expects, for a thin barrier the exact barrier shape does not matter, only its height is important. Consequently, the effect of that the barrier asymmetry on the phases and delays is negligible for small L_x. With increasing barrier thickness the impact of the asymmetry grows, in this example for $L_x > 0.06$ the wave-packet scattering delays for reflection at lead 1 and reflection at lead 2 differ significantly.

Just as we have done for the symmetric potential barrier, calculating the time evolutions of wave packets illustrates the scattering dynamics (Fig. 3.11). This time we focus on the comparison of the wave packet incoming from the left with the mirrored wave packet incoming from the right. For the $\mathcal{V}_\mathrm{L} = 1$, $\mathcal{V}_\mathrm{R} = 3$, $L_x = 4$ barrier (Fig. 3.9) nonreciprocal wave-packet scattering delays τ_{11} and τ_{22} combined with a significant reflection probability occur in the $1 < k < 2$ range. Accordingly, the wave packets in Fig. 3.11 with a central momentum of $k_0 = \pm 1.5$ are reflected nonreciprocally. One nonreciprocal property is the delay: the reflection from the right is completed faster than the reflection from the left. Another aspect is the wave function shape within and around the scattering region. The reflection on the right side resembles the behavior shown in Fig. 3.8a with a standing wave forming in front of the barrier. The wave packet approaching from the left is more localized within the scattering region during the reflection process, the standing wave is less pronounced.

The nonreciprocity of the asymmetric tunneling barrier is negligible as long as tunneling happens with a considerable probability. As shown in Fig. 3.10 the reflection delays are only nonreciprocal if the barrier is thick and the transmission probability low. The wave-packet evolutions for the thin barrier qualitatively match those already shown in Fig. 3.8b, therefore they are not further discussed here.

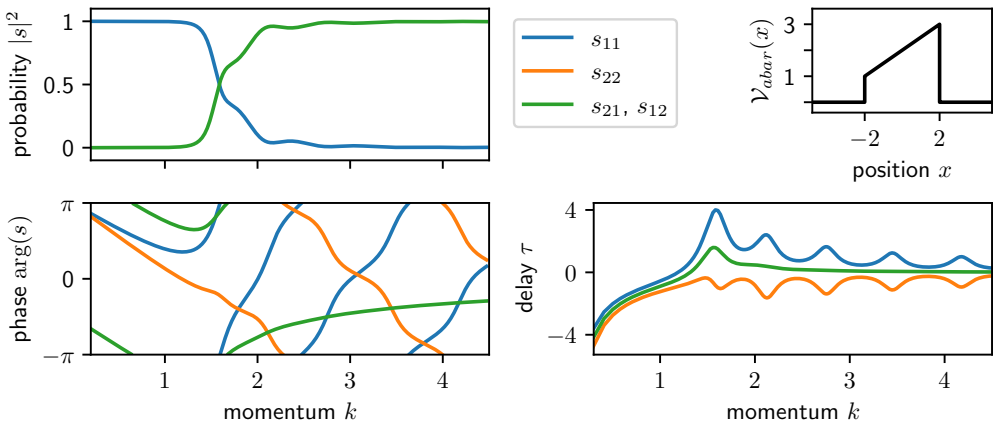


Figure 3.9: Plots showing the scattering coefficients in polar representation (left), scattering potential (top right), and wave-packet scattering delays (bottom right) of the asymmetric potential barrier with $L_x = 4$, $\mathcal{V}_\mathrm{L} = 1$ and $\mathcal{V}_\mathrm{R} = 3$. Only two colors are visible in the probability plot, because the two reflection probabilities are identical. The phases and hence the wave-packet scattering delays are nonreciprocal, especially near momenta corresponding to the barrier height.

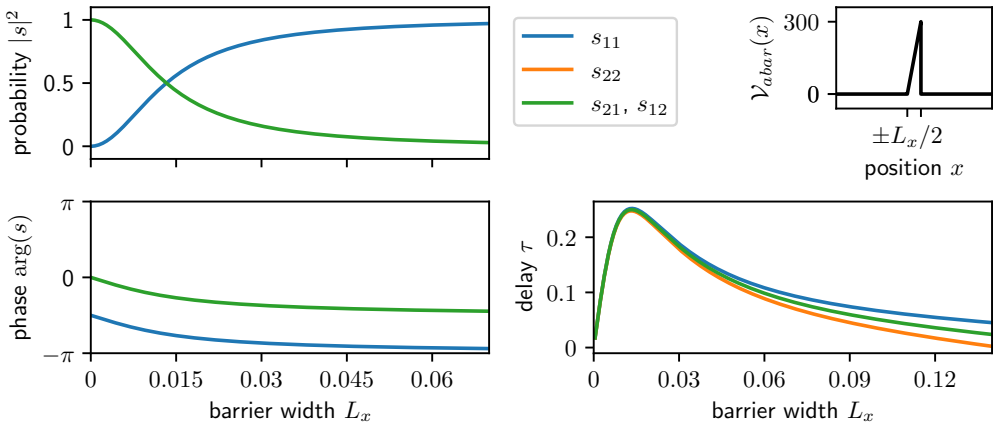


Figure 3.10: Plots showing the scattering coefficients in polar representation (left), scattering potential (top right), and wave-packet scattering delays (bottom right) of the asymmetric tunneling barrier with $\mathcal{V}_\mathrm{L} = 0$, $\mathcal{V}_\mathrm{R} = 300$ at the particle energy $E = 1$. Only two colors are visible in the probability plot, because the two reflection probabilities are identical. Despite the phases not being exactly reciprocal, no difference between the reflection phases is visible in the plotted range. However, the nonreciprocity is visible in the phases' derivatives, which are the wave-packet scattering delays.

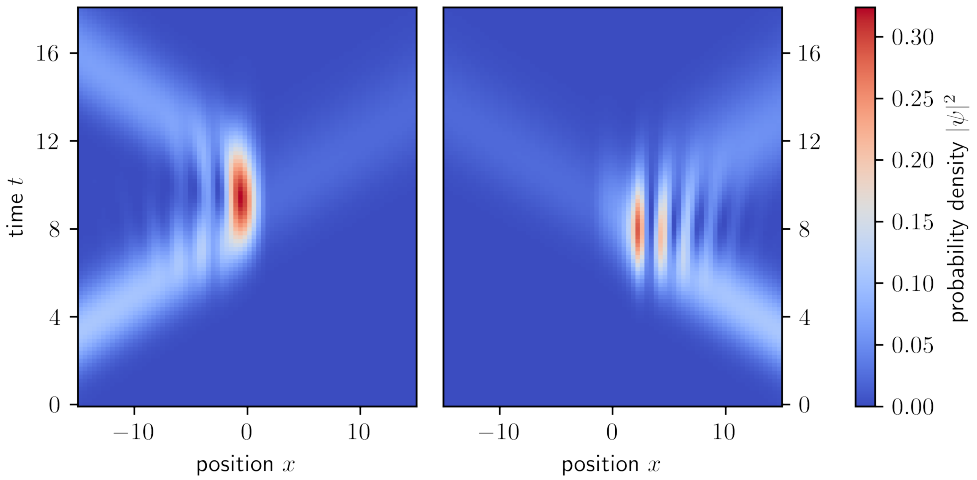


Figure 3.11: Colormaps showing the time evolutions of wave packets incident on the asymmetric potential barrier with barrier parameters $\mathcal{V}_\mathrm{L} = 1$, $\mathcal{V}_\mathrm{R} = 3$ and $L_x = 4$ introduced in Fig. 3.9. With the wave-packet parameters $k_0 = \pm 1.5$, $\sigma_k = 0.2$ and $x_0 = \mp 25$ the reflection from the left takes longer than the reflection from the right, as anticipated from the wave-packet scattering delays.

3.6.2 Aharonov-Bohm Interferometers

The asymmetric potential barriers presented in Fig. 3.9 show the behavior of time-reversal symmetric systems with broken $\hat{\boldsymbol{\mathcal{P}}}$ symmetry for which the complex *reflection* coefficients differ by a phase factor (Eq. 3.28). This section is about systems with a broken time-reversal symmetry that feature *transmission* coefficients that differ by a phase factor (Eq. 3.29). An easily implementable and experimentally well controllable method to break the symmetry with respect to the time-reversal operator $\hat{\boldsymbol{\mathcal{T}}}$ are magnetic fields.

With an applied magnetic field $\boldsymbol{H}$ the electrons moving along a path $\boldsymbol{l}$ in the mesoscopic device experience an additional phase shift given by the path integral of the electromagnetic vector potential $\boldsymbol{A}$ along $\boldsymbol{l}$. Asymmetric AB interferometers were previously suggested to achieve asymmetric transport under specific conditions [71, 72]. The unusual properties of the electron dynamics in AB rings with broken $\hat{\boldsymbol{\mathcal{P}}}$ symmetry, however, were first published in [56]. Here, we discuss the theoretical description of the AB effect in mesoscopic metallic or semiconducting rings according to the Landauer-Büttiker picture and extend this to wave-packet transport.

We use a simplified single-channel model again, modeling the narrow wires and ring arms as one-dimensional waveguides. The Hamiltonian $\hat{\boldsymbol{H}}$ in the waveguides is given by

$$\hat{\boldsymbol{H}}_{\mathrm{AB}} = (i\nabla - \boldsymbol{A})^2 \,, \tag{3.56}$$

with the Nabla operator ∇. The areas where the leads are attached to the ring are treated (see Fig. 3.12) as three lead sub-devices and are modeled by a 3×3 scattering matrix. To further simplify the model, we assume that these areas act as ideal beam splitters described by the energy-independent scattering matrix

$$\boldsymbol{S}_{\mathrm{BS}} = \begin{pmatrix} 0 & \frac{1}{\sqrt{2}} & \frac{1}{\sqrt{2}} \\ \frac{1}{\sqrt{2}} & -\frac{1}{2} & \frac{1}{2} \\ \frac{1}{\sqrt{2}} & \frac{1}{2} & -\frac{1}{2} \end{pmatrix} . \tag{3.57}$$

In the following, the primary goal is to analyze the effect of the system symmetries, not to explain experimental results quantitatively. Figure 3.12 shows a sketch of the corresponding model of the AB ring: The model is parametrized by the path length d, the path length difference δd and the enclosed magnetic flux $\boldsymbol{\Phi}$. The effect of time-reversal $\hat{\boldsymbol{\mathcal{T}}}$ is obvious, the sign of $\boldsymbol{\Phi}$ is flipped and the remaining system is left unchanged. Applying the lead-exchange operator $\hat{\boldsymbol{\mathcal{P}}}$ to the system left-right mirrors the device, which is equivalent to flipping the sign of $\boldsymbol{\Phi}$ but leaving the system geometry unchanged. Therefore, the system is symmetric with respect to the combined operation $\hat{\boldsymbol{\mathcal{P}}}\hat{\boldsymbol{\mathcal{T}}}$. Equations 3.28 and 3.29 are broken but Eq. 3.30 is fulfilled. The reflection coefficients from both sides are identical. The transmission coefficients differ by a phase factor (Figs. 3.13 and 3.14).

To formulate the Schrödinger equation of the system, the electromagnetic vector potential $\boldsymbol{A}$ that generates the desired magnetic field is required. A homogeneous magnetic field perpendicular to the interferometer plane which creates the magnetic flux $\boldsymbol{\Phi}$ in the loop is obtained by choosing $A_x = \boldsymbol{\Phi} y/(d + \delta d)$ and $A_y = A_z = 0$. The Ansatz function

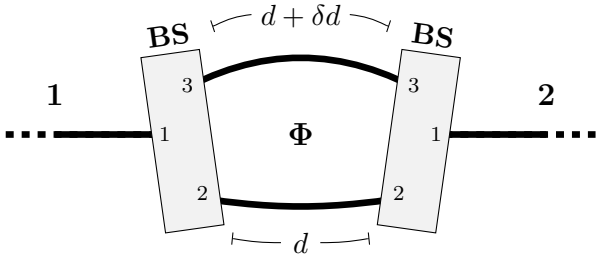


Figure 3.12: Sketch of the model of an asymmetric AB interferometer composed of two beam splitters described by the ideal beam-splitter scattering matrix $\boldsymbol{S}_{\mathrm{BS}}$ and four waveguides. The upper and lower interferometer arm have two different lengths d and $d + \delta d$ and enclose the magnetic flux $\mathbf{\Phi}$. Reprinted from [C].

reads

$$\phi_{\mathrm{AB}}(x,y) = \begin{cases} \mathcal{A}_{\mathrm{L}}^{-} e^{-ik_{\mathrm{L}}x} + \mathcal{A}_{\mathrm{L}}^{+} e^{ik_{\mathrm{R}}x} & \text{for } x < -\frac{1}{2}d \text{ and } y = 0, \\ \mathcal{A}_{\mathrm{CL}} e^{-ik_{\mathrm{L}}x} + \mathcal{A}_{\mathrm{CR}} e^{ik_{\mathrm{R}}x} & \text{for } -\frac{1}{2}d \leq x \leq \frac{1}{2}d \text{ and } y = 0, \\ \mathcal{A}_{\mathrm{DL}} e^{-ik_{\mathrm{L}}x} + \mathcal{A}_{\mathrm{DR}} e^{ik_{\mathrm{R}}x} & \text{for } -\frac{1}{2}(d+\delta d) \leq x \leq \frac{1}{2}(d+\delta d) \text{ and } y = 1, \\ \mathcal{A}_{\mathrm{R}}^{+} e^{-ik_{\mathrm{L}}x} + \mathcal{A}_{\mathrm{R}}^{-} e^{ik_{\mathrm{R}}x} & \text{for } x > \frac{1}{2}d \text{ and } y = 0, \end{cases} \tag{3.58}$$

$$k = \sqrt{E}, \tag{3.59}$$

$$k_{\mathrm{L}} = k - A_x, \tag{3.60}$$

$$k_{\mathrm{R}} = k + A_x, \tag{3.61}$$

with A_x denoting the x-component of $\boldsymbol{A}$, the left side incoming and outgoing plane wave amplitudes $\mathcal{A}_{\mathrm{L}}^{+}$ and $\mathcal{A}_{\mathrm{L}}^{-}$, the central region left and right moving plane wave amplitudes of the lower and upper arm $\mathcal{A}_{\mathrm{CL}}$, $\mathcal{A}_{\mathrm{CR}}$, $\mathcal{A}_{\mathrm{DL}}$ and $\mathcal{A}_{\mathrm{DR}}$ and the right side incoming and outgoing plane wave amplitudes $\mathcal{A}_{\mathrm{R}}^{+}$ and $\mathcal{A}_{\mathrm{R}}^{-}$. In the leads and the lower interferometer arm $y = 0$ and $\boldsymbol{A} = 0$, leading to the usual quadratic dispersion $k_{\mathrm{L}} = k_{\mathrm{R}} = k = \sqrt{E}$. In the upper interferometer arm with $y = 1$ and $A_x = \mathbf{\Phi}/(d + \delta d)$ this is not the case anymore and two different dispersions k_{L} and k_{R} apply for the two propagation directions. The piecewise definition of $\phi_{\mathrm{AB}}(x,y)$ fulfills Eq. 3.56 in the respective regions. The boundary conditions are given by the incoming and outgoing wave functions at the

positions of the beam splitter leads and the ideal beam-splitter scattering matrix $\boldsymbol{S}_{\mathrm{BS}}$:

$$\begin{pmatrix} \mathcal{A}_{\mathrm{L}}^{-} e^{-ik_{\mathrm{L}}x}|_{x=-\frac{1}{2}d} \\ \mathcal{A}_{\mathrm{CR}} e^{ik_{\mathrm{R}}x}|_{x=-\frac{1}{2}d} \\ \mathcal{A}_{\mathrm{DR}} e^{ik_{\mathrm{R}}x}|_{x=-\frac{1}{2}(d+\delta d)} \end{pmatrix} = \boldsymbol{S}_{\mathrm{BS}} \begin{pmatrix} \mathcal{A}_{\mathrm{L}}^{+} e^{ik_{\mathrm{R}}x}|_{x=-\frac{1}{2}d} \\ \mathcal{A}_{\mathrm{CL}} e^{-ik_{\mathrm{L}}x}|_{x=-\frac{1}{2}d} \\ \mathcal{A}_{\mathrm{DL}} e^{-ik_{\mathrm{L}}x}|_{x=-\frac{1}{2}(d+\delta d)} \end{pmatrix}, \tag{3.62}$$

$$\begin{pmatrix} \mathcal{A}_{\mathrm{R}}^{-} e^{ik_{\mathrm{R}}x}|_{x=\frac{1}{2}d} \\ \mathcal{A}_{\mathrm{CL}} e^{-ik_{\mathrm{L}}x}|_{x=\frac{1}{2}d} \\ \mathcal{A}_{\mathrm{DL}} e^{-ik_{\mathrm{L}}x}|_{x=\frac{1}{2}(d+\delta d)} \end{pmatrix} = \boldsymbol{S}_{\mathrm{BS}} \begin{pmatrix} \mathcal{A}_{\mathrm{R}}^{+} e^{-ik_{\mathrm{L}}x}|_{x=\frac{1}{2}d} \\ \mathcal{A}_{\mathrm{CR}} e^{ik_{\mathrm{R}}x}|_{x=\frac{1}{2}d} \\ \mathcal{A}_{\mathrm{DR}} e^{ik_{\mathrm{R}}x}|_{x=\frac{1}{2}(d+\delta d)} \end{pmatrix}. \tag{3.63}$$

With these six equations we can eliminate the four complex amplitudes $\mathcal{A}_{\mathrm{CL}}$, $\mathcal{A}_{\mathrm{CR}}$, $\mathcal{A}_{\mathrm{DL}}$ and $\mathcal{A}_{\mathrm{DR}}$ of the plane waves in the two interferometer arms. Two equations that only contain the incoming and outgoing plane wave amplitudes of the leads remain which provide the scattering coefficients of the system.[3]

$$s_{11,\mathrm{AB}} = s_{22,\mathrm{AB}} = \frac{\left(e^{i\boldsymbol{\Phi}} - e^{i(k\delta d+2\boldsymbol{\Phi})} + e^{i(2k\delta d+\boldsymbol{\Phi})} - e^{ik\delta d}\right) e^{ikd}}{-4e^{i\boldsymbol{\Phi}} + e^{i(2kd+\boldsymbol{\Phi})} + e^{i(k\delta d+2kd+2\boldsymbol{\Phi})} + e^{i(2k\delta d+2kd+\boldsymbol{\Phi})} + e^{ik(\delta d+2d)}} \tag{3.64}$$

$$s_{21,\mathrm{AB}} = \frac{2\left(-e^{i(k\delta d+\boldsymbol{\Phi})} + e^{i(k\delta d+2kd+\boldsymbol{\Phi})} + e^{2ik(\delta d+d)} - 1\right) e^{i\boldsymbol{\Phi}}}{-4e^{i\boldsymbol{\Phi}} + e^{i(2kd+\boldsymbol{\Phi})} + e^{i(k\delta d+2kd+2\boldsymbol{\Phi})} + e^{i(2k\delta d+2kd+\boldsymbol{\Phi})} + e^{ik(\delta d+2d)}} \tag{3.65}$$

$$s_{12,\mathrm{AB}} = \frac{2\left(-e^{i\boldsymbol{\Phi}} + e^{i(2k\delta d+2kd+\boldsymbol{\Phi})} - e^{ik\delta d} + e^{ik(\delta d+2d)}\right)}{-4e^{i\boldsymbol{\Phi}} + e^{i(2kd+\boldsymbol{\Phi})} + e^{i(k\delta d+2kd+2\boldsymbol{\Phi})} + e^{i(2k\delta d+2kd+\boldsymbol{\Phi})} + e^{ik(\delta d+2d)}} \tag{3.66}$$

In these expressions the dispersion relation is given by $k = \sqrt{E}$ as defined above. We note here that k does not correspond to the canonical momentum anymore due to the presence of $\boldsymbol{A}$. All scattering coefficients have a convoluted periodic dependence on the parameters k, d, δd and $\boldsymbol{\Phi}$. The periodicity in $\boldsymbol{\Phi}$ is leading to the famous AB oscillations of the magneto conductance of mesoscopic rings. Figures 3.13, 3.14 and 3.15 show the $\boldsymbol{\Phi}$ periodicity and the quasi periodicity with respect to k of the probabilities, phases and delays.

The core phenomenon of mesoscopic AB rings are of course the magneto conductance oscillations. We discussed the fundamental conductance symmetries $G_{21} = G_{12}$ and $G(\boldsymbol{B}) = G(-\boldsymbol{B})$ above that are a direct consequence of the unitarity of the two-lead scattering matrix. Applied to AB rings, these cause the so-called phase rigidity (see Section 2.1, [30]). The conductance oscillation always feature either a maximum or a

[3] Importable expressions for Python's sympy package, for Matlab, Octave, Mathematica and Maple can be found in appendix chapter A.3

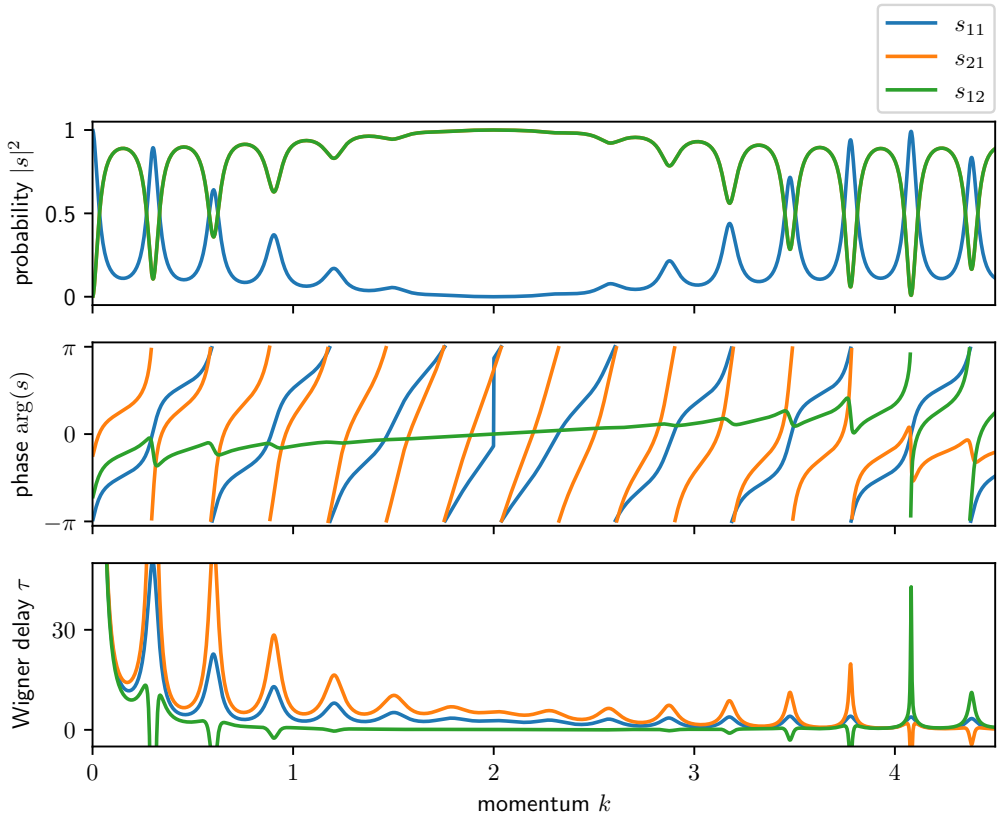


Figure 3.13: Plots of the scattering coefficients in polar representation and wave-packet scattering delays of the asymmetric AB interferometer shown in Fig. 3.12. As required by unitarity the transmission and reflection probabilities are always reciprocal, hence only two curves are visible in the probabilities plot. The system parameter values are $d = 10$, $\delta d = \pi/4$, $\mathbf{\Phi} = \pi/2 = \mathbf{\Phi}_0/4$. For the particularly interesting case of full transparency at $k = 2$ the wave-packet scattering delays τ_{21} and τ_{12} differ. The phase of a coefficient may jump by π if the coefficient's absolute value is zero at that momentum, corresponding to perfect transparency or full reflection. The corresponding singularities in the phase's derivatives are removable, the wave-packet scattering delays are smooth functions of the momentum.

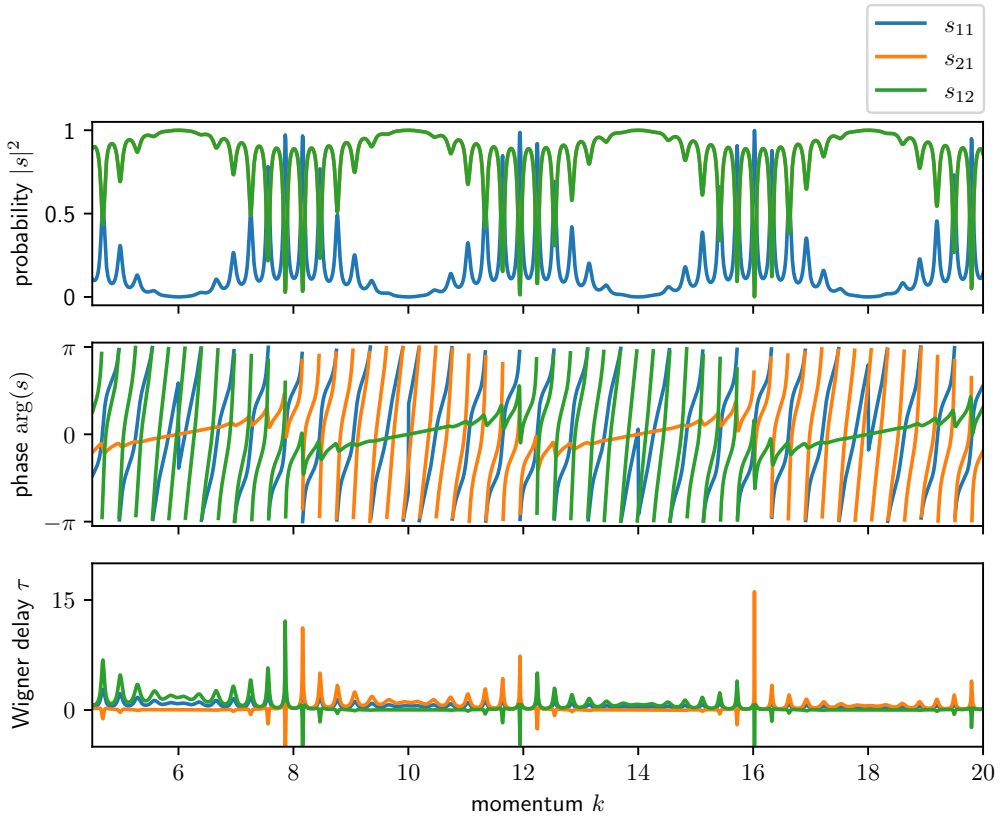


Figure 3.14: Plots showing the scattering coefficients in polar representation and wave-packet scattering delays of the asymmetric AB interferometer with the same parameters as presented in Fig. 3.13 for a larger range of k. As required by unitarity the transmission and reflection probabilities are always reciprocal, hence only two curves are visible in the probabilities plot. The plots show the quasi-periodic behavior of the transmission and reflection probabilities as a function of k and that the transmission coefficients' phases and thus the wave-packet scattering delays are nonreciprocal in general.

minimum at $\mathbf{\Phi} = 0$, a continuous shift of the oscillation pattern along the $\mathbf{\Phi}$ axis is impossible.

Importantly, the phases and thus the wave-packet scattering delays are not bound to these symmetries and therefore do not need to be phase rigid. Figure 3.15 shows the scattering coefficients in polar representation and the wave-packet scattering delays for the asymmetric AB interferometer. As expected, the probability (conductance) is strictly symmetric with respect to magnetic field reversal. In contrast, the wave-packet scattering delay has a significant $\mathbf{\Phi}$ asymmetric component.

To understand the scattering coefficients, it is helpful to follow the propagation of plane waves through the device. An incoming wave from lead 1 is split into two partial waves by the left beam splitter. These partial waves travel through the lower and upper interferometer arm and are finally rejoined at the right beam splitter. The definition of $\boldsymbol{S}_{\mathrm{BS}}$ shows that just after being split, the two partial waves are in phase. After traveling along the two interferometer arms a phase difference according to the different path lengths and according to the enclosed magnetic flux arises

$$\theta_{\mathrm{AB}} = k\delta d \pm 2\pi\mathbf{\Phi}/\mathbf{\Phi}_0 = k\delta d \pm \mathbf{\Phi}, \tag{3.67}$$

with the two-path AB phase difference θ_{AB} and the magnetic flux quantum $\mathbf{\Phi}_0 = h/q$, which equals to 2π in the chosen natural units ($\hbar = q = 2m = 1$). The plus sign applies if the waves propagate from the left to the right, the minus sign corresponds to the opposite direction. A particularly interesting case is

$$k\delta d = \pi/2 + 2\pi b, \quad \mathbf{\Phi} = \pi/2 + 2\pi b', \tag{3.68}$$

with arbitrary integer numbers b and b'. If the minus sign in Eq. 3.67 applies, the two-path AB phase difference θ_{AB} is divisible by 2π, leading to constructive interference and thus perfect transmission. In the left to right direction, the plus sign in Eq. 3.67 applies, $\theta_{\mathrm{AB}} = (2b + 2b' + 1)\pi$ and the two partial waves interfere destructively after being merged by the right beam splitter. Hence, the partial waves are reflected back into the two interferometer arms and travel back to the left beam splitter, acquiring an additional phase shift according to Eq. 3.68. Because of the left to right direction the minus sign in Eq. 3.67 applies again and the additional phase shift is a multiple of 2π. Therefore, the total phase shift is still an odd multiple of π and the two partial waves are reflected *again*. On the third transit through the interferometer the plus sign in Eq. 3.67 applies again adding another phase shift of $(2b + 2b' + 1)\pi$ to the two partial waves. Finally the total phase shift is an even multiple of π, the two partial waves interfere constructively at the right beam splitter and are fully transmitted into the outgoing lead. This interesting case is shown in Fig. 3.13 for $k = 2$. The transmission probability is one and the wave-packet scattering delay is direction-dependent.

The interpretation of the eigenfunctions in analogy to classical trajectories as above can be misleading in some cases. Comments and even calculations of this kind are found in [42]. Therefore, we do not want to rely on this picture and only use it as a readily understandable illustration to interpret the abstract results obtained with the Schrödinger equation.

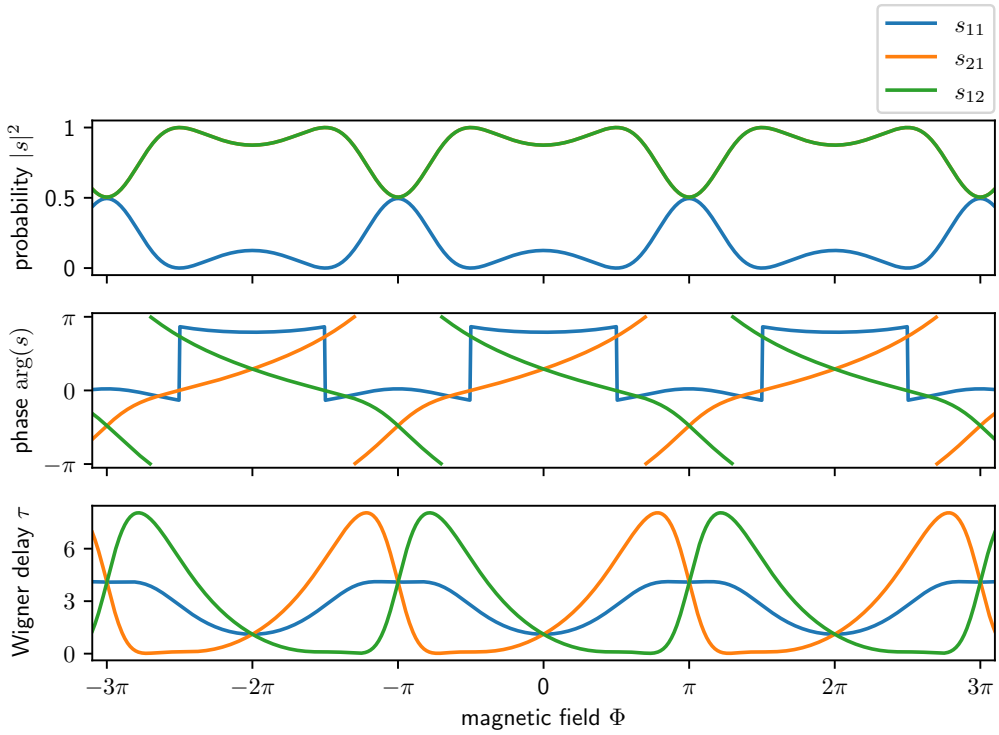
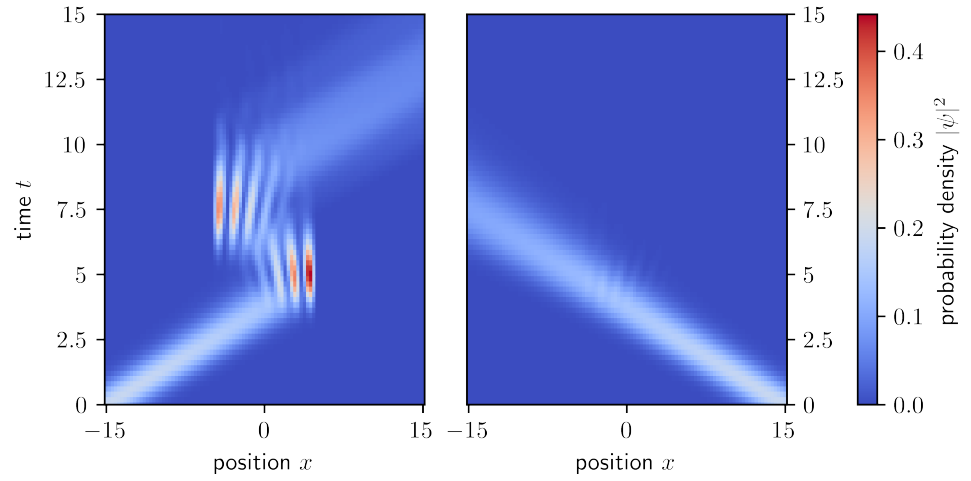


Figure 3.15: Plots of the scattering coefficients in polar representation and the wave-packet scattering delays for the asymmetric AB interferometer as a function of magnetic field. As required by unitarity the transmission and reflection probabilities are always reciprocal, hence only two curves are visible in the probabilities plot. The shown momentum is $k = 2$, the other parameters are identical to those used in Figs. 3.13 and 3.14. The transmission and reflection probabilities oscillate with a period of $\mathbf{\Phi}_0 = h/e = 2\pi$ (in natural units $\hbar = q = 2m = 1$). The phase rigidity of the probability (conductance) oscillations is clearly visible. In contrast, the transmission wave-packet scattering delays are not phase rigid.

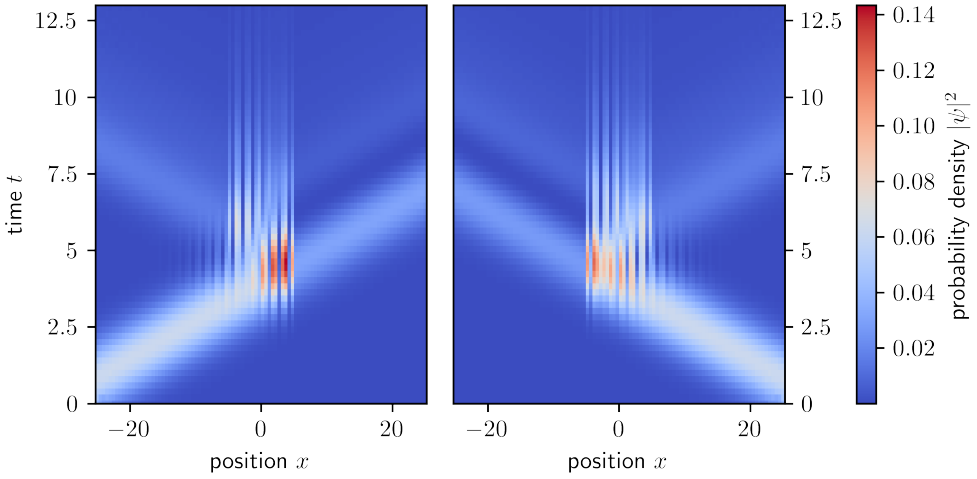
To convince ourselves that the simplified line of argumentation above is indeed correct we calculate the time evolutions of Gaussian wave packets. Figure 3.16 shows the probability density of the wave functions as a function of time for the same parameters as used in Figs. 3.13, 3.14 and 3.15. Figure 3.16a presents the evolution of a wave packet with a central momentum $k_0 = 2$, which is the momentum at which transparency is achieved. The result confirms what we found by naively counting the accumulated phases in the interferometer arms above. Upon approaching the system from the right side the wave packet easily passes through the interferometer. Upon approaching from the left side, however, the wave packet is completely reflected on the first traversal, bounces back, gets reflected a second time and then finally leaves the interferometer.

Another remarkable feature observed in Figs. 3.13 and 3.14 are the resonance-like peaks in the wave-packet scattering delays, for example in the range $k = 4 \ldots 5$. At these peaks the transmission wave-packet scattering delay in one direction has a maximum, whereas in the other direction it has a minimum. Figure 3.16b shows the time evolutions of wave packets that are centered around the momentum of one of these peaks. From the plots we see that the transmission of the wave packets is almost reciprocal, which is understandable from the fact that at the momenta with large nonreciprocal transmission delay, the transmission probability is small. Thus, the observed transmitted wave function mainly consists of the wave-packet components with momenta above and below the peak that are characterized by higher transmission probabilities but almost reciprocal transmission delays.

However, only a portion of the wave packet is transmitted or reflected within the first 5 time units after incidence. The probability density within the scattering region remains significant for around 10 time units after incidence and only slowly “leaks” out of the scattering region. The system is close to a so-called bound state, which is discussed in more detail in the following section.



(a)



(b)

Figure 3.16: Colormaps showing the time evolutions of wave packets incident on the asymmetric AB interferometer introduced in Fig. 3.12. In the scattering region the summed probability density of both interferometer arms is shown. To fit in the scattering region, the x coordinate of the upper arm is rescaled as $x \to (1 + \delta d/d)^{-1} x$. The system parameters are given by $d = 10$, $\delta d = \pi/4$ and $\mathbf{\Phi} = \mathbf{\Phi}_0/4 = \pi/2$. (a) Transparency is achieved at $\pm k_0 = 2$. Momentum space width and initial position of the wave packets are $\sigma_k = 1/3$ and $x_0 = \mp 15$. The nonreciprocal transmission delay is evident. Reprinted from [C]. (b) The wave-packet scattering delay shows resonance-like peaks with opposite sign for the two transmission directions as a function of k (Figs. 3.13 and 3.14). The wave packets here are centered around one of these peaks with $k_0 \approx \pm 4.1$, $\sigma_k = 1/9$ and $x_0 = \mp 32$.

3.6.3 Disordered Conductors

Next we want to take a look at a disordered two-lead 2D conductor, which is a well suited model to study universal conductance fluctuations (Section 2.2) in the Landauer-Büttiker picture. Disorder is implemented by adding an electrostatic potential that randomly varies in the scattering region. The random potential makes it difficult to diagonalize the continuum Hamiltonian, therefore we use a tight-binding Hamiltonian. An introduction to the tight-binding approach is given in Section 5.1.

Figure Fig. 3.17 shows the schematic view of the tight-binding system. The system is numerically solvable on desktop computers for virtually any choice of the electrostatic and vector potentials. The set of the site indices is called the tight-binding lattice Λ and the set of two-tuples containing the indices of every pair of nearest neighbors is given by $\mathrm{NN}(\Lambda)$. Then the tight-binding Hamiltonian in natural units $\hbar = q = 2m = 1$ is

$$\begin{aligned}\hat{\boldsymbol{H}}_{\mathrm{tb}} = &\left(\sum_{m\in\Lambda} \left(4 + \mathcal{V}_{\mathrm{dis}}(m)\right) |m\rangle\langle m| \right) \\ &- \left(\sum_{(m,n)\in \mathrm{NN}(\Lambda)} \exp\left(i \int_{\boldsymbol{l}(m,n)} \boldsymbol{A} \mathrm{d}\boldsymbol{r} \right) |m\rangle\langle n| \right)\end{aligned} \tag{3.69}$$

with the site m and n eigenvectors $|m\rangle$ and $|n\rangle$ and their dual vectors $\langle m|$ and $\langle n|$, the site-dependent disorder electrostatic potential $\mathcal{V}_{\mathrm{dis}}$, the electromagnetic vector potential $\boldsymbol{A}$ and the path $\boldsymbol{l}(m,n)$ connecting the sites m and n. The magnetic field is applied orthogonal to the xy-plane and is incorporated using the Peierls substitution (see Section 5.1). The chosen gauge for the electromagnetic vector potential $\boldsymbol{A}$ is $A_x = B_z y$, $A_y = A_z = 0$. The numerical procedure to find the scattering coefficients for this system is similar to the analytical method: The Schrödinger equation is solved independently for the different regions of the problem. The solutions in the leads yield the plane waves or scattering states, the solutions in the scattering region impose boundary conditions on these plane waves and allow to extract the scattering coefficients. A thorough discussion of the numerical methods involved is given in Section 5.1 and in the documentation of the software package `Kwant` [73].

The two leads are one-dimensional and we obtain the familiar 2×2 scattering matrix. Analog to the previous examples, Fig. 3.18 presents the scattering coefficients and the wave-packet scattering delays of the disordered wire. The energy dependence is not considered here, because the universal conductance fluctuations are most commonly of interest for their dependence on the magnetic field. The presented field range is chosen according to the wire size. At $B_z = 0.02$ the total flux through the disordered part of the wire equals approximately one flux quantum. The plots clearly show the aperiodic fluctutations of the probabilites, phases and wave-packet scattering delays which are the unique fingerprints of the random potential.

Whereas the probabilities shown are smooth functions of B_z, the reflection or transmission phases appear to have discontinuities at energies with a corresponding probability

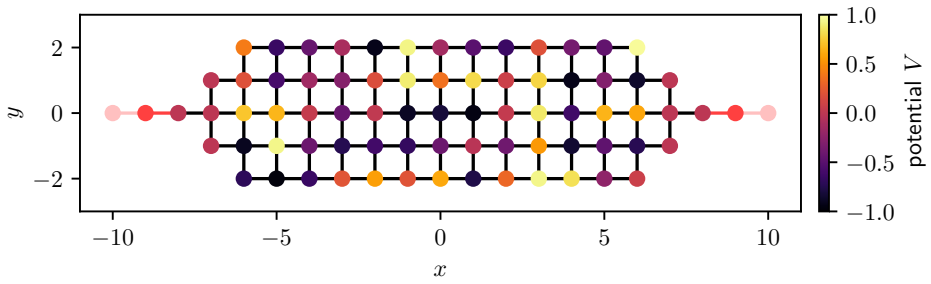


Figure 3.17: Plot of the 2D tight-binding wire geometry. The filled circles represent system sites, the lines connect nearest neighbors. The site color illustrates the local value of the electrostatic potential, with random values between -1 and 1 within the scattering region as displayed by the colorbar. The potential in the leads is zero. The faint sites in the left and right indicate the infinite continuation of the geometry. The plot was created with the `Kwant` software package [73].

close to zero. Suprisingly, the wave-packet scattering delays seem to diverge for certain B_z. Positive poles are principally allowed, indicating the occurrence of a bound state, negative poles are strictly forbidden to maintain causality [58]. To closer investigate the apparent poles, we "zoom in" on the interesting fields as shown in Fig. 3.19. This closer look reveals, in contrast to the apparent view, that the phases are in fact smooth functions of B_z (except for the apparent jumps of 2π due to the periodicity) and the wave-packet scattering delays are not singular, but bounded. At these three fields the system is close to a bound state and traps incoming particles for a long time.

The magnetic field (a)symmetries observed in Fig. 3.18 are readily understood by revisiting the symmetry transformations. The system is neither $\hat{\boldsymbol{\mathcal{P}}}$, nor $\hat{\boldsymbol{\mathcal{T}}}$, nor $\hat{\boldsymbol{\mathcal{P}}}\hat{\boldsymbol{\mathcal{T}}}$ symmetric, therefore all scattering phases and wave-packet scattering delays are nonreciprocal. Because the magnetic field reversal is equivalent to the reversal of time, the reflection coefficients are invariant under field reversal. The transmission coefficients for the two directions are exchanged under field reversal:

$$s_{\mathrm{tb},11}(B_z) = s_{\mathrm{tb},11}(-B_z), \tag{3.70}$$

$$s_{\mathrm{tb},22}(B_z) = s_{\mathrm{tb},22}(-B_z), \tag{3.71}$$

$$s_{\mathrm{tb},21}(B_z) = s_{\mathrm{tb},12}(-B_z). \tag{3.72}$$

As in all previous examples, the transmission and reflection probabilities are reciprocal and symmetric with respect to magnetic field reversal due to the unitarity of the scattering matrix, but the phases and delays are not. And once more, we will study the time evolutions of wave packets to find the consequences for the particle transport.

Unlike in the previous examples, the leads are no longer continuous one-dimensional wires. Instead, the leads are one-dimensional chains of tight-binding sites. In the pre-

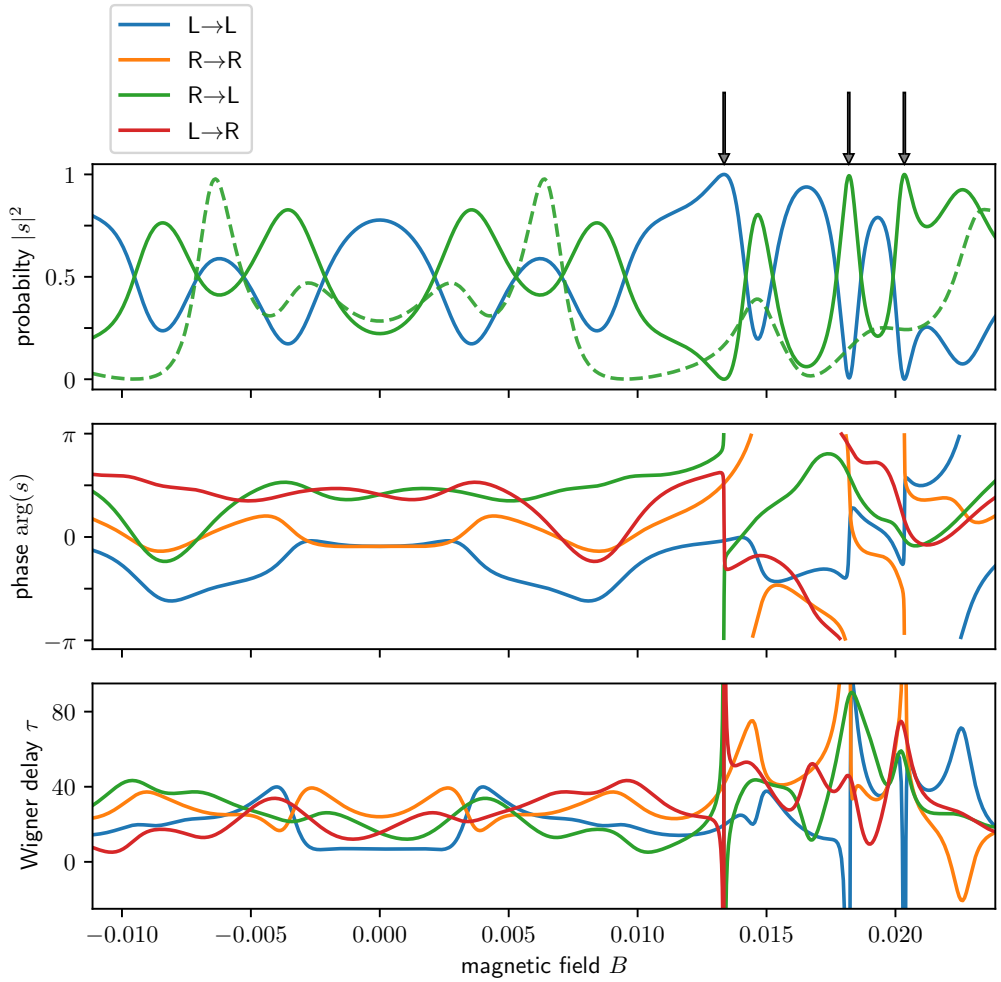


Figure 3.18: Plots showing the scattering coefficients in polar representation as well as the wave-packet scattering delays as a function of the applied magnetic field at the energy $E = 3$. As required by unitarity, the transmission and reflection probabilities are symmetric with respect to magnetic field reversal and reciprocal. Hence, only two curves are visible in the probabilities plot. The magnetic field is specified in units of flux quanta per unit area. The unit area is given by the squared nearest neighbor spacing. All quantities show the characteristic aperiodic fluctuations. The solid curves correspond to the potential shown in Fig. 3.17. The dashed curve is calculated with a different realization of the random potential leading to a completely different fluctuation pattern. At $B_z \approx 0.013$, the transmission probabilities are close to zero, at $B_z \approx 0.018$ and $B_z \approx 0.02$ the reflection probabilities are small (arrows). Zoomed views at the three fields are shown in Fig. 3.19.

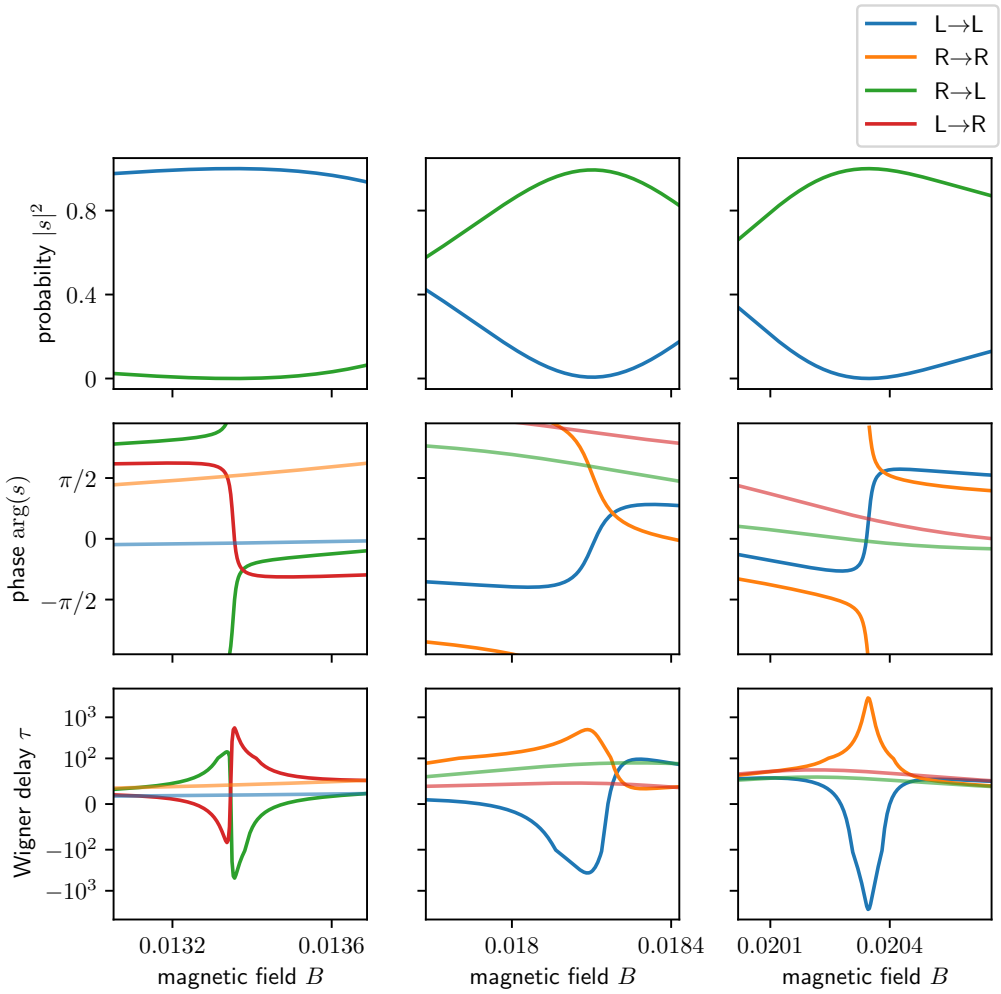


Figure 3.19: Plots of the probabilities, phases and the wave-packet scattering delays as a function of magnetic field around the three apparent singularities in Fig. 3.18. As required by unitarity the transmission and reflection probabilities are always reciprocal, hence only two curves are visible in the probabilities plot. The wave-packet scattering delay axis scaling is linear between -100 and 100 and logarithmic for larger values. All other axes use linear scaling. The field is specified in units of one flux quantum per unit area. As seen in Fig. 3.18, at all three fields step-like features in the phases and large (negative) delays occur. However, there are neither discontinuities in the phases nor poles in the delays, only steep but smooth steps in the phases and delays that are two orders of magnitude larger than for most other fields. Moreover, large reflection (transmission) delays are accompanied by small reflection (transmission) probabilities. Their effect on the transport is therefore small.

vious examples, the dispersion was given by a parabolic dependence $E = k^2$. Now, the dispersion is a periodic function $E = 4 - 2\cos(k)$. Therefore we need to avoid significant contributions of momenta $|k| \geq \pi$ in our wave packets, which would cause aliasing effects. In the following we will use a central momentum $k_0 = \pi/3$ and a momentum spread $\sigma_k = \pi/80$.

Moreover, we do not have exact expressions for the eigenfunctions anymore. Instead, a numerical solver is used that is able to find "numerically exact" eigenfunctions for a specified energy. From the definition of the Gaussian wave packet (Eq. 3.25), however, it is evident that the wave packets consist of superpositions of wave functions with all momenta. For the tight-binding wave packets we approximate this by a discrete sum over a dense grid of momenta, which can be evaluated numerically. For a more detailed explanation refer to Section 5.1.

Figures 3.20 and 3.21 show wave-packet evolutions for three different magnetic fields and for the energy $E = 3$ used in Figs. 3.18 and 3.19. The first magnetic field we choose is $\boldsymbol{B} = 1 \times 10^{-2}$ (Fig. 3.20), because transmission and reflection delays are significantly nonreciprocal and transmission probability is ≈ 0.5. The wave-packet evolution confirms that in the L $\rightarrow$ R direction ($\tau \approx 0$), most of the packet traverses the disordered wire as if it was freely propagating. In the R $\rightarrow$ L direction ($\tau \approx 40$) the transmitted packet leaves the scattering region around 40 time units later.

Interestingly, there are other, faint, features in the maps that are not part of the major reflected and transmitted wave packets. For example in the L $\rightarrow$ R direction a second wave packet is emitted to the left side. A similar small wave packet is emitted in the R $\rightarrow$ L direction. These features are due to the finite momentum width of the wave packet and indicate that the wave-packet scattering delays change rapidly with energy.

The wave-packet evolutions shown in Fig. 3.21 have been calculated for two of the magnetic fields with apparent poles in the transmission (Fig. 3.21a) and reflection (Fig. 3.21b) wave-packet scattering delays. In all four evolutions shown in Fig. 3.21 the wave packet dwells in the scattering region for a remarkably long time, which indicates the proximity to a bound state. We already saw in Fig. 3.19 that the parameter ranges with extremely large (negative) delays are accompanied by scattering probabilities close to zero. The wave-packet evolutions confirm that most of the incident packet is transmitted or reflected within ≈ 100 time units after incidence which confirms that the extreme delays do not significantly affect the wave-packet transport.

Despite the limited effect of the delay peaks, the high slopes and sign changes of the delays in the vicinity of the peaks do have an important impact. In all evolutions shown, the incoming wave packet is split not only into one reflected and one transmitted wave packet, but into multiple reflected and transmitted wave packets. The wave packets have a finite momentum spread σ_k, as already mentioned. If the wave-packet scattering delay varies strongly within this range, it may well be that different parts of the packets are subject to highly different delays and thus leave the system separately.

Finally, for all of the shown evolutions the reflected and transmitted wave-packet dynamics are nonreciprocal, that is, the shapes and delays of the transmitted and reflected wave functions differ for the two directions. In addition, the dynamics of the transmit-

ted wave function also changes under the reversal of field. The total transmission and reflection probabilities are of course fully reciprocal and symmetric with respect to a reversal of the magnetic field.

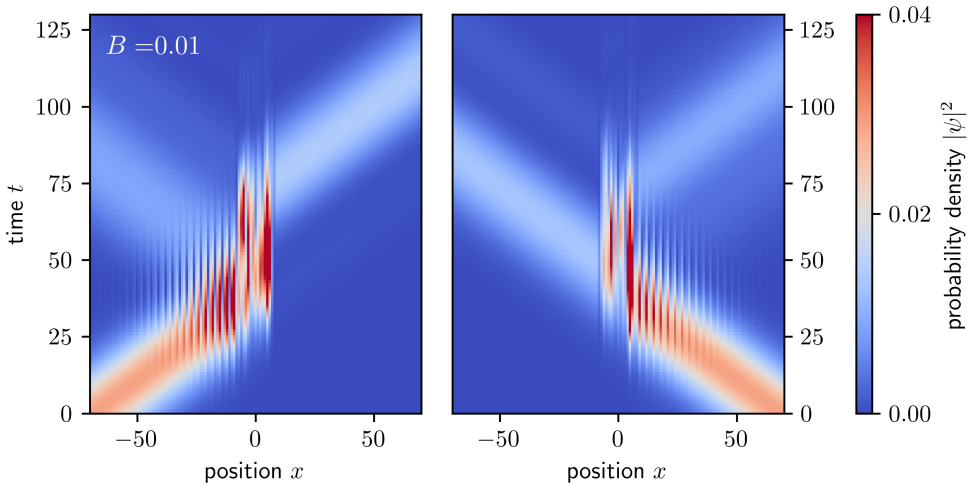
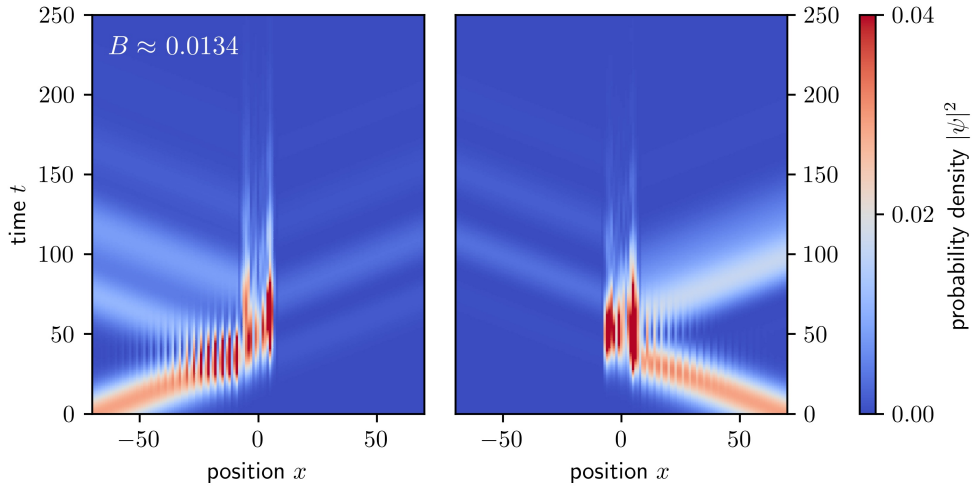
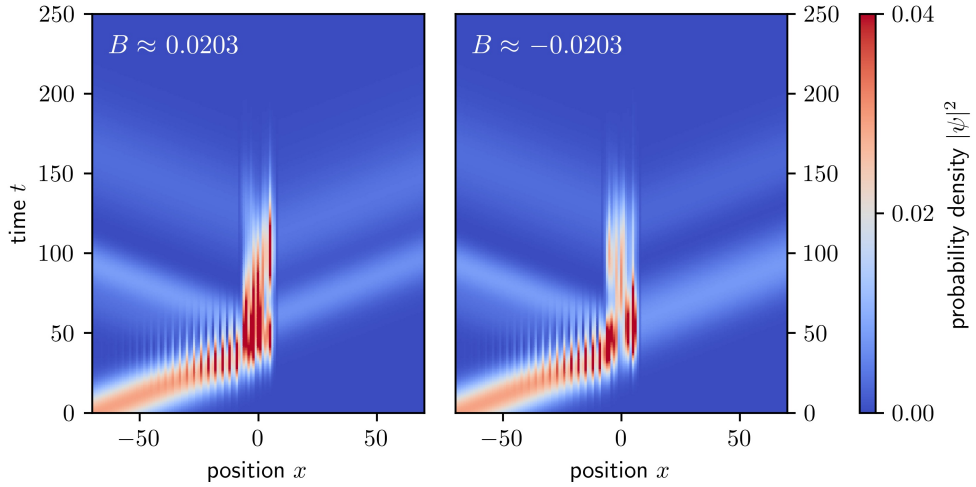


Figure 3.20: Maps showing the time evolutions of wave packets in the disordered wire introduced in Fig. 3.17. The wave-packet parameters are $k_0 = \pi/3$, $\sigma_k = \pi/80$ and $x_0 = 60$. The wave packets consist of 2000 eigenfunctions for evenly spaced momenta from $k_0 - 5\sigma_k$ to $k_0 + 5\sigma_k$ (k stepsize is $< 2 \times 10^{-4}$) with the eigenfunction weights given by Eq. 3.25. The dominant fractions of the transmitted and reflected wave functions follow the expectations gained from Fig. 3.18.



(a)



(b)

Figure 3.21: Maps showing the time evolutions of wave packets with the same parameters and system as in presented in Fig. 3.20 for the the magnetic field values corresponding to the apparent poles of the wave-packet scattering delays (Fig. 3.19). (a) At the first apparent pole at $B_z \approx 0.0134$ the transmission delays have large negative values for one direction only, and the transmission probability is close to zero. Accordingly, these delays are not visible in the wave-packet evolutions. The dynamics of all reflected and transmitted wave functions is nonreciprocal. (b) The other apparent pole, at $\boldsymbol{B} \approx 0.0203$, is present in the reflection delays. Here, the reflection probability is small, rendering the impact on the wave-packet evolution insignificant. Instead of the nonreciprocity the effect of the field reversal on the wave-packet evolution is here pointed out. Clearly, the dynamics of the transmitted wave function depends on the sign of the magnetic field.

3.7 Summary

This chapter introduced the Landauer-Büttiker picture of quantum transport and showed its application to typical quantum transport problems. The following statements summarize this chapter: The diagonalization of the Hamiltonian $\hat{\boldsymbol{H}}$ of a quantum mechanical problem yields the eigenvalues and eigenfunctions. With these, the time evolution of any wave function can be calculated (Section 3.1). Due to the periodic nature of the eigenfunctions within the leads of a scattering problem, the eigenfunctions can also be represented by the linear map of incoming to outgoing plane waves. This map is called the scattering matrix $\boldsymbol{S}$. It fully describes the weights of the eigenfunctions outside the scattering region (Section 3.2). The scattering matrix is a unitary matrix. For one-dimensional, two-lead systems, reciprocity of the transmission and reflection probabilities is therefore required. The reciprocity of the scattering coefficients' phases, however, is controlled by the systems symmetry with respect to the lead-exchange operator $\hat{\boldsymbol{\mathcal{P}}}$ and the time-reversal operator $\hat{\boldsymbol{\mathcal{T}}}$ (Section 3.2). The ballistic conductance is proportional to the transmission probability. Therefore, the unitarity of $\boldsymbol{S}$ implies reciprocity $G_{21} = G_{12} =: G$. If the system does not contain built-in magnetic moments, the unitarity of $\boldsymbol{S}$ also implies magnetic field symmetry $G(\boldsymbol{B}) = G(-\boldsymbol{B})$ (Section 3.3).

Eigenfunctions of scattering problems have an infinite extension and therefore are not suitable for the description of realistic particles. Normalizable wave packets are more realistic representations of single particle states. Due to the linearity of quantum mechanics, eigenfunctions and wave packets show the same transport behavior in the Landauer-Büttiker picture (Section 3.4). The scattering coefficients' phases control the dynamics of time-dependent wave functions (for example of wave packets), as exemplified by the wave-packet scattering delay (Section 3.5). Within the unitarity constraint of $\boldsymbol{S}$, there exists space for these phases to be nonreciprocal. The conductance of a one-dimensional channel with an embedded potential barrier ranges between 0 and G_0. The conductance is always symmetric with respect to the lead-exchange operator $\hat{\boldsymbol{\mathcal{P}}}$, even if the barrier is not. The phases of the reflection coefficients and thus the corresponding wave-packet scattering delays were found to generally share the asymmetries of the scattering potential (Section 3.6.1) [C]. The AB conductance oscillations in asymmetric AB interferometers are phase rigid due to $G(\boldsymbol{B}) = G(-\boldsymbol{B})$; the wave-packet scattering delays and the wave-packet dynamics are not (Section 3.6.2). The transmission and reflection probabilites, as well as the scattering phases and wave-packet scattering delays of disordered conductors fluctuate as a function of the magnetic field. The fluctuation pattern is a unique fingerprint of the disorder potential. For the conductance $G_{21} = G_{12}$ and $G(\boldsymbol{B}) = G(-\boldsymbol{B})$ hold again. This is, however, not the case for the wave-packet dynamics. (Section 3.6.3).

Theoretical Description of Decoherence

4

The previous chapter introduced the Landauer-Büttiker picture of quantum transport, which employs elastic scattering theory and is able to explain the phenomena introduced in Chapter 2. However, a phenomenon that is present in any experimental setup is neglected in the Landauer-Büttiker picture: The decoherence of quantum states within the device. According to the single-particle Schrödinger equation, the phase coherence of a quantum state is conserved eternally. The resulting time evolution implies that macroscopic Aharonov-Bohm (AB) interferometers still show AB oscillations. In reality, this is not the case. Characteristic phase coherence times and phase coherence lengths describe the time or length scales on which interference effects are observable. The single-particle Schrödinger equation that was used in the previous chapter is only applicable if this decoherence, which is induced by the environment, is negligible. This assumption is justified if the sample size or the average electron transit time is much smaller than the coherence length or coherence time, respectively. On longer time scales or across larger distances the inevitable coupling to the environment leads to decoherence. As the name implies, decoherence denotes the loss of phase coherence in a quantum system, which leads to a suppression of quantum mechanical interference effects [74, 75]. Strong decoherence leads to the crossover to classical dynamics in which quantum interference effects do not exist.

A key difference between the dynamics given by the Schrödinger equation and our experience from the macroscopic world is irreversibility. The unitary time evolution of quantum mechanics deterministically predicts the system state for any given time in the past or the future, if the system state is known at one single point in time. Reversing the time of a quantum-mechanical time evolution results in another physically sensible time evolution. The dynamics is fully reversible, because the Schrödinger equation preserves the von Neumann entropy of the system.

The dynamics of macroscopic objects, however, is irreversible. The milk shake in the blender will not be turned back into strawberries and milk if the blender's knifes rotate backwards, nor will a car produce fuel if it is pushed backwards. This irreversibility cannot be reproduced with unitary time evolutions. Apart from the time evolution, there is a second operation that dynamically alters the quantum state, namely the quantum measurement. Making an observation on a quantum state *irreversibly* alters the state, which is also known as the wave function collapse [76]. Looking at the corresponding mathematical operation, which is a projection, the irreversible nature of this process is evident: Projective maps are not invertible[1]. Further, the traditional quantum-mechanical measurement involves an entity called the observer, which leads to philosophical problems, for example to the Wigner's friend paradox or to the Schrödinger's cat problem.

[1] Except for the identity, which is the only invertible projection.

These philosophical questions will not bother us in this thesis. Rather, it will be argued that the coupling to a macroscopic environment can be modeled by treating the environment as a measurement device that disturbs the time evolution of the microscopic quantum system. The result of this disturbance is *decoherence* of this quantum system. With increasing decoherence rate, the quantum-mechanical dynamics crosses over to classical dynamics. A simplified sketch of this picture is shown in Fig. 4.1. A mesoscopic two-lead device, analog to those discussed in Chapter 3, couples to an environment or "bath" with a system-bath coupling strength Γ. The coupling allows energy exchange in both directions and influences the time evolution of the quantum state of the mesoscopic device.

If the mesoscopic system is assumed to be isolated from its environment, the quantum-mechanical time evolution can be calculated completely. If the mesoscopic system interacts with the environment, however, the environmental degrees of freedom have to be considered by the Schrödinger equation, which then becomes too large to solve. Fortunately, solving the full Schrödinger equation is not required, because the exact quantum state of the environment is not of interest for us. Instead, only the effective coupling between the bath and the system and the statistical properties of the bath, for example densities and temperature, are relevant. This description is sufficient to calculate to a good approximation the evolution of the quantum state of the mesoscopic system under the influence of the environment. The mathematical operation to remove the bath degrees of freedom is called the "partial trace", which averages the time evolution over all possible microscopic bath configurations.

The cut between system and bath is of course not physical. It is a calculational trick to limit the size of the quantum mechanical problem and still incorporate the effect of the macroscopic bath. This concept of splitting a problem into system and bath is a common approach. Indeed, several different methods have been developed to incorporate into the quantum mechanical calculations the coupling to an environment. This chapter presents three of these methods: Section 4.1 describes the decoherence model developed by Markus Büttiker [77], which models in an elastic scattering problem the coupling to an environment as an additional lead. In Section 4.2 a more general model is presented, in which a stochastic term is added to the quantum-mechanical time evolution. Section 4.3 discusses the Lindblad master equation approach. This method avoids the stochastic terms but requires use of density operators instead of wave functions. Finally, in Section 4.4 the close relation between the quantum trajectories and the Lindblad master equation is shown.

These models are introduced with regard to the central question of this thesis: Do the two-lead symmetries introduced in Chapter 3 still exist if decoherence is considered? In Section 3.6 we have seen that whereas the conductance of the two-lead devices is strictly reciprocal, the wave-packet scattering delays may well be nonreciprocal. However, the longer a particle dwells in the mesoscopic device, the stronger is the decoherence it is subjected to, which affects the transmission probability. Therefore, the question arises if the two-lead conductance reciprocity still holds [A, D, 5, 56].

A further method that should be briefly mentioned here, is the Kubo formula, which is

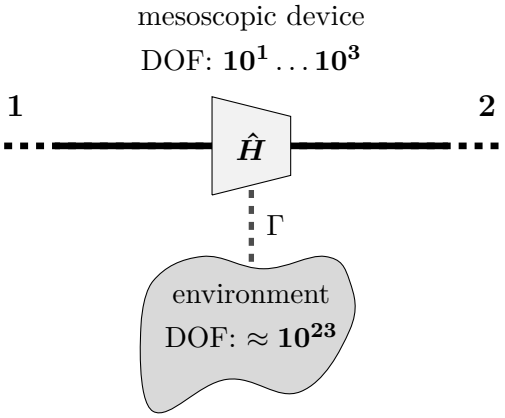


Figure 4.1: Sketch of a mesoscopic two-lead device with a microscopic number of DOF that couples to an environment characterized by a macroscopic number of DOF. The dynamics of the two-lead device without the environment is characterized by the Hermitian Hamiltonian $\hat{\boldsymbol{H}}$. The presence of the environment disturbs this unitary dynamics. In this simplified sketch the strength of the disturbance is characterized by the system-bath coupling strength Γ, which in a realistic model could, for example, be a scattering rate.

widely used to treat quantum transport and open quantum systems [53, 78]. The Kubo formula is a perturbation theory in the Hamiltonian $\hat{\boldsymbol{H}}$: This formalism permits the calculation of response and correlation functions of observables of a quantum mechanical system with respect to small perturbations of its Hamiltonian $\hat{\boldsymbol{H}}$. Permitivities and conductivities are among such responses, therefore the formalism is well suited to describe transport properties. However, Kubo states: "At a certain time t, we pick up a number of systems and observe B. [...] We shall not follow these systems after this observation [...] to avoid the quantum-mechanical disturbance of observation process. [...] We may, however, expect for most of macroscopic quantities which we observe this disturbance can be neglected. This is a condition for macroscopic observations. Unfortunately, exact conditions for the existence of such quantities are not known" [53]. The Kubo formalism deliberately ignores the effect of an observation of B on the system state to achieve microscopic reversibility. Because we want to study systems with a nonunitary, irreversible microscopic dynamics in this thesis, the Kubo formalism will not be further included in the discussion.

Finally, the literature also offers several more phenomenological approaches to model transport in open systems and the resulting decoherence [31, 74, 75, 79–81]. A number of these approaches excellently reproduce experimental data, however they are often developed particularly for certain mesoscopic systems, for example AB interferometers or quantum dots. Hence, these approaches tend to be difficult to generalize. These approaches will not be further discussed either.

4.1 Decoherence in the Landauer-Büttiker Model

The Landauer-Büttiker model of quantum transport successfully describes ballistic quantum transport by using elastic scattering theory. The best agreement between theory and experiment is achieved for extremely clean systems operated at very low temperatures. In samples with material purities $< 99.9\,\%$ or at "elevated" temperatures $> 1\,\mathrm{K}$, the inelastic interactions of electrons with lattice defects, phonons or other electrons render the description of the experimental observations with elastic scattering theory hopeless. M. Büttiker suggested to model these inelastic interactions by adding additional leads to the elastic scattering problem [77]. These leads do not represent real electrical contacts but serve in the model to incorporate the coupling of the system to the macroscopic baths. The terms "contact lead" and "decoherence lead" are used to distinguish both in the following. Particles that leave the system through a decoherence lead are automatically re-injected from the same lead with a random quantum mechanical phase-shift. This phase randomization causes the suppression of interference effects.

In [77], M. Büttiker applies this model to a sequence of potential barriers. Between each pair of barriers, a decoherence lead with variable coupling strength is attached. Without coupling to the environment, the conductance of the system scales exponentially with the number of barriers, as expected for quantum transport. With stronger coupling to the decoherence leads, the total conductance scales inversely with the barrier number. The barriers now behave as if they were classical resistors connected in series.

This approach has also been applied to AB rings. In this case, the decoherence lead is attached to one arm of the AB interferometer (Fig. 4.2), which results in the expected damping of the AB conductance oscillations [82]. When the electron enters the system from one of the contact leads it is split into a coherent superposition of traveling in the upper or lower arm of the ring. Before reaching the opposite side of the ring, where the two arms join again, the particle may leave the system through the decoherence lead. In this case, the partial wave function is immediately re-injected with a random phase, hence the interference condition with its partner in the other arm is randomized. Averaging over this random process causes a damping of the AB oscillation signal as expected [82].

The major advantage of this model is its calculational simplicity: The transport problem including decoherence is mapped onto an elastic scattering problem. A disadvantage is that the inelastic processes causing the decoherence can only happen in external baths that are coupled to the system through leads. A direct model for inelastic scattering centers inside the device is not implemented. Accordingly, the strength of the decoherence is not affected by the dwell time of the particle in the device. Instead, the transmission probabilities from the contact leads to the decoherence leads determine the decoherence strength. Hence, according to the Büttiker model, the nonreciprocal wave-packet scattering delays do not result in nonreciprocal decoherence strengths. Therefore, the conductance remains reciprocal for any two-lead device and any configuration of decoherence leads.

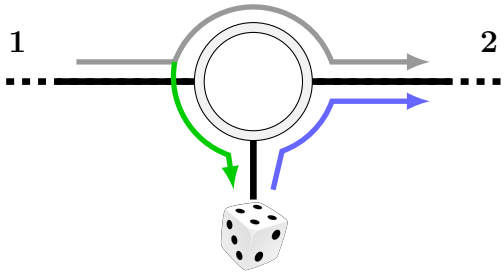


Figure 4.2: Sketch of an AB ring with decoherence included according to the Büttiker model. The two leads to the left and right are the standard electrical contacts, the third lead is used to model decoherence. Any particle that leaves through this lead (green arrow) is re-injected with a random phase (blue arrow). The interference between the partial waves in the upper and lower arm (grey and blue arrows) is suppressed by this phase randomization.

4.2 Quantum Trajectories

Instead of including additional leads to model decoherence, we can also modify the equation of motion to directly include decoherence into the dynamics of the system. In this approach, the coupling to the environment is modeled as quantum measurement that is performed at random intervals. In quantum optics, this method is established to model dissipative dynamics and is there known as the "quantum trajectories" or "Monte-Carlo wave function" method [83–89].

For this type of model, we need to specify the system Hamiltonian, one or more observables and the mean rate at which these observables are measured. For our AB interferometer, a reasonable choice for this observable is one that distinguishes if the electron is within one specific arm or whether it is located somewhere else. Figure 4.3 sketches an exemplary case for an electron that enters the ring from the left. The electron is split into a coherent superposition of partial waves traveling in the upper and lower interferometer arm. While the electron is in this superposition, a measurement occurs. Each eigenvalue of the observable corresponds to a possible outcome of the measurement. According to the Born rule, the probability of each of these outcomes is given by the squared absolute value of the overlap of the wave function with the respective eigenspace. The eigenspace is defined as the subspace of Hilbert space spanned by all eigenvectors having the specific eigenvalue. In this example the result "electron is in the lower arm" is measured, which corresponds to one of the eigenvalues of the measured observable. After the measurement, the wave function is projected onto the corresponding eigenspace. In this example, this space consists of wave functions localized in the lower arm only.

The dynamics that describes this idea is given by a combination of the Schrödinger equation and wave function projections. In the model used, the points in time at which a measurement occurs — the collapse times — are determined by a Poisson process with the mean time τ_c between two measurements. The standard Schrödinger equation

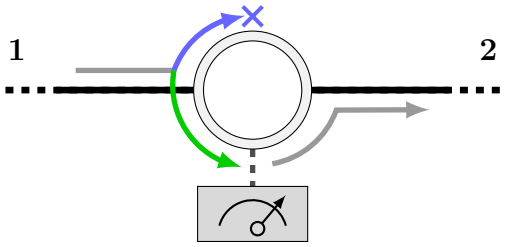


Figure 4.3: Sketch of an AB ring with decoherence as modeled by quantum trajectories. The two leads to the left and right are the electrical contacts. A measurement device checks at random time intervals the presence of the electron in the lower arm. An electron that enters from the left (grey line) is split into a coherent superposition of partial waves moving in the upper and lower arms (blue and green arrows). If a quantum measurement happens at a given time, the wave function collapses. In the case shown here, the result "electron is in the lower arm" is obtained. The partial wave function in the upper arm is then erased (blue cross) and the electron continues to travel in the lower arm only (grey arrow) preventing any two-path interference. The more frequent these measurements happen, the more the AB oscillations are suppressed.

applies in the time span between every pair of such neighboring points in time. At the collapse times, a wave function projection is applied. Figure 4.4 illustrates the resulting time-evolution of the system state.

At t_0, the system is prepared in the state $|\psi\rangle$. For $t_0 \leq t < t_1$, the time-evolution of $|\psi\rangle$ is described by to the unitary time-evolution operator $\hat{\boldsymbol{U}}$. At time t_1, the first quantum measurement occurs and the projection $\hat{\boldsymbol{P}}_1$ is applied to the system state. This projection is randomly selected at t_1 according to the outcome of the measurement. The resulting state evolves again unitarily, until time t_2, when the next measurement occurs and another projection $\hat{\boldsymbol{P}}_2$ is applied.

The stochastic time evolution described differs from the unitary time evolution determined by the Schrödinger equation: First, the time evolution from any $t < t_1$ to any $t > t_1$ is irreversible. Second, the evolution is now a stochastic process. As indicated in Fig. 4.4, the collapse times $t_1, t_2, t_3 \ldots$ are stochastic quantities, as generated by the Poisson process. Similarly, for every measurement the projection operators $\hat{\boldsymbol{P}}$ are randomly chosen. This implies that the time evolution of the expectation value $\langle\psi(t)|\,\hat{\boldsymbol{O}}\,|\psi(t)\rangle$ of an observable $\hat{\boldsymbol{O}}$, for example the particle position that we want to calculate, are also stochastic. Therefore, the expected particle position is found by calculating the statistical expectation value of many quantum mechanical expectation values, which is done by averaging over many realizations of the stochastic expression $\langle\psi(t)|\,\hat{\boldsymbol{O}}\,|\psi(t)\rangle$.

According to the Born rule, the probabilities involved in applying the projection operators $\hat{\boldsymbol{P}}$ depend on $|\psi(t)\rangle$ itself and the time evolution becomes nonlinear in $|\psi(t)\rangle$. Therefore, the definition of the scattering matrix introduced in Section 3.2, which required the linearity of the time evolution, is not applicable anymore. However, it is still

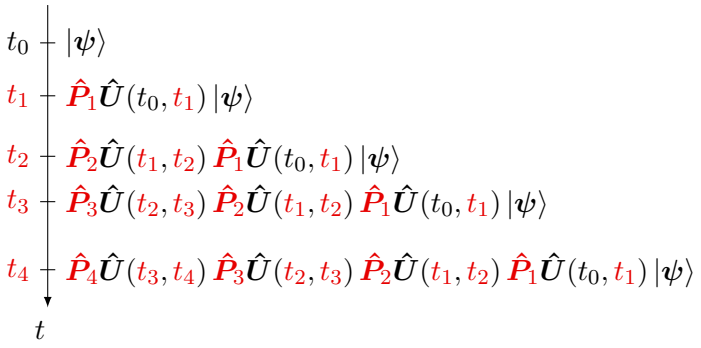


Figure 4.4: Illustration of a quantum trajectory given by the unitary time-evolution operator $\hat{\boldsymbol{U}}$ and the projection operators $\hat{\boldsymbol{P}}_m$. The state known at a time t_0 evolves unitarily until t_1, the first collapse time. At t_1, a measurement is performed which causes a projection according to $\hat{\boldsymbol{P}}_1$. The resulting state evolves again unitarily until t_2, when the next measurement occurs, and so on. Stochastic elements of this time-evolution are highlighted in red.

possible to define transmission and reflection probabilities. For this, a wave packet is prepared in one of the leads of the configuration with its momentum pointing towards the scattering region. Then the stochastic time evolution is run until the wave packet has left the system[2]. In the resulting final state, the probability to find the particle in each lead determines the corresponding transmission probability.

A disadvantage of this definition is that these transmission probabilities do not depend on the wave packet's central momentum only, but also on the initial position and the momentum spread of the packet. The conventional approach seems to suggest that these parameters are not physically sensible, because they can be arbitrarily chosen. However, the value of the wave-packet transmission probability depends on the wave-packet parameters. It is noteworthy that statements on symmetries that compare the response of the system and the symmetry-transformed system to wave packets with identical parameters, are able to avoid this dependence. Thus, the answer to the question if the transmission probability is even under magnetic field reversal, for example, does not necessarily depend on the wave-packet parameters.

Because the underlying time evolution is nonunitary, the previously discussed constraints related to the unitarity of the time-evolution operator and the scattering matrix do not necessarily apply anymore. The longer the wave packet dwells in the scattering region, the higher is the average number of measurements that occur during that time. The more measurements occur, the more often projections are applied to the wave function. It is therefore expected that the transmission probabilities for this stochastic time evolution inherit the symmetries of the wave-packet scattering delays. In Chapter 5 numerical results are presented that confirm this anticipation.

[2]Most wave packets never leave the system completely. The remaining wave function in the scattering region becomes exponentially small, however.

4.3 Lindblad Master Equation

The stochastic time evolutions of the quantum trajectories method discussed in Section 4.2 are equivalent to a (nonstochastic) Lindblad master equation. This correspondence is discussed in Section 4.4. The Lindblad master equation is thus suitable to model decoherence and is frequently used for this purpose [90–96]. Master equations describe the time-evolution of the density operator. Whereas wave functions can only represent pure states, the density operator is a description of the system state that is able to also represent mixed states. The following paragraphs quickly introduce the density operator formalism. A longer introduction can be found in standard quantum mechanics textbooks [50].

So far we used the wave function to describe the state of our quantum systems and evolved the state according to the Schrödinger equation. However, by using wave functions only, adding two wave functions always results in coherent superpositions, or "pure states". There is no convenient possibility to represent incoherent sums, or "mixed states". To be able to conveniently represent both pure states and mixed states in one formalism, it is necessary to replace the wave function with the density operator $\hat{\boldsymbol{\rho}}$. The density operator is frequently used in quantum optics. Especially for numerical calculations, the systems are modeled by finite dimensional Hilbert spaces and the density operator has a finite dimensional matrix representation. Therefore, it is often referred to as the density matrix. Here we will use the term density operator.

The density operator $\hat{\boldsymbol{\rho}}$ that represents the same state as a given wave function $|\boldsymbol{\psi}\rangle$ is simply the projection operator onto that wave function $|\boldsymbol{\psi}\rangle\langle\boldsymbol{\psi}|$. To incoherently add two wave functions $|\boldsymbol{\psi}_1\rangle$ and $|\boldsymbol{\psi}_2\rangle$, two density matrix representations are added:

$$\hat{\boldsymbol{\rho}}_{\text{mix}} = \frac{1}{2}|\boldsymbol{\psi}_1\rangle\langle\boldsymbol{\psi}_1| + \frac{1}{2}|\boldsymbol{\psi}_2\rangle\langle\boldsymbol{\psi}_2|. \tag{4.1}$$

For $|\boldsymbol{\psi}_1\rangle \neq |\boldsymbol{\psi}_2\rangle$, the operator $\hat{\boldsymbol{\rho}}_{\text{mix}}$ is not a projection operator, it is thus impossible to find a $|\boldsymbol{\psi}\rangle\langle\boldsymbol{\psi}|$ representation of $\hat{\boldsymbol{\rho}}_{\text{mix}}$. Wave functions cannot represent mixed states, as already stated above. The density operator corresponding to a coherent sum of wave functions is obtained by adding the two wave functions first and then forming the density operator:

$$\hat{\boldsymbol{\rho}}_{\text{pure}} = \frac{|\boldsymbol{\psi}_1 + \boldsymbol{\psi}_2\rangle\langle\boldsymbol{\psi}_1 + \boldsymbol{\psi}_2|}{|\boldsymbol{\psi}_1 + \boldsymbol{\psi}_2|^2}, \tag{4.2}$$

where $|\boldsymbol{\psi}|$ denotes the norm of the wave function $|\boldsymbol{\psi}\rangle$. Valid wave functions are normalized. The respective density operator norm is given by its trace, so $\text{tr}(\hat{\boldsymbol{\rho}}) = 1$ holds for a normalized $\hat{\boldsymbol{\rho}}$. To apply an operator $\hat{\boldsymbol{O}}$ to $\hat{\boldsymbol{\rho}}$, the product $\hat{\boldsymbol{O}}\hat{\boldsymbol{\rho}}\hat{\boldsymbol{O}}^\dagger$ is formed. The expectation value of an observable $\hat{\boldsymbol{O}}$ is given by $\text{tr}(\hat{\boldsymbol{O}}\hat{\boldsymbol{\rho}})$. The equation of motion for the density operator is given by the von Neumann equation

$$\delta_t\hat{\boldsymbol{\rho}} = -\frac{i}{\hbar}\left[\hat{\boldsymbol{H}}, \hat{\boldsymbol{\rho}}\right], \tag{4.3}$$

which is obtained, for example for a pure state, by inserting the definition of the density operator $\hat{\boldsymbol{\rho}} = |\boldsymbol{\psi}\rangle \langle\boldsymbol{\psi}|$ into the Schrödinger equation. The resulting time-evolution for $\hat{\boldsymbol{\rho}}$ is, analog to the wave function-time evolution, a unitary map:

$$\hat{\boldsymbol{\rho}}(t) = \hat{\boldsymbol{U}}(t_0, t)\hat{\boldsymbol{\rho}}(t_0)\hat{\boldsymbol{U}}(t_0, t)^\dagger \tag{4.4}$$

with the time-evolution operator $\hat{\boldsymbol{U}}$ and a given point in time t_0, at which $\hat{\boldsymbol{\rho}}$ is known.

This time evolution never transforms a pure into a mixed state and can therefore not be directly used to describe measurement processes or decoherence. Equation 4.4 conserves the purity of $\hat{\boldsymbol{\rho}}$, which is defined as $\mathrm{tr}(\hat{\boldsymbol{\rho}}^2)$. The purity of a pure state equals 1, mixed states are characterized by a purity below 1. The time evolution according to the von Neumann equation (Eq. 4.3) is equivalent to the Schrödinger time evolutions of all states that constitute the statistical mixture described by $\hat{\boldsymbol{\rho}}$. This time evolution is therefore fully reversible. To be able to describe irreversible processes, we need the equivalent of the irreversible wave function projections employed in Section 4.2. In the density operator formalism, these processes are characterized by a reduction of the purity $\mathrm{tr}(\hat{\boldsymbol{\rho}}^2)$.

In 1976, G. Lindblad [97], V. Gorini, A. Kossakowski, and E. C. G. Sudarshan [98] found that the most general form of a completely positive[3] and Markovian[4] master equation that is trace preserving $\delta_t \,\mathrm{tr}(\hat{\boldsymbol{\rho}}) = 0$ is given by

$$\delta_t \hat{\boldsymbol{\rho}} = -\frac{i}{\hbar}\left[\hat{\boldsymbol{H}}, \hat{\boldsymbol{\rho}}\right] + \sum_m \Gamma_m \left(\hat{\boldsymbol{C}}_m \hat{\boldsymbol{\rho}} \hat{\boldsymbol{C}}_m^\dagger - \frac{1}{2}\left(\hat{\boldsymbol{\rho}} \hat{\boldsymbol{C}}_m^\dagger \hat{\boldsymbol{C}}_m + \hat{\boldsymbol{C}}_m^\dagger \hat{\boldsymbol{C}}_m \hat{\boldsymbol{\rho}}\right)\right). \tag{4.5}$$

Here, the $\hat{\boldsymbol{C}}_m$ are the so-called jump operators if the Γ_m specify the corresponding rates. This equation is known as the Lindblad master equation or the master equation in Lindblad form. If the $\hat{\boldsymbol{C}}_m$ are chosen to be Hermitian, then the resulting time evolution always preserves or reduces the purity of the state $\delta_t \,\mathrm{tr}(\hat{\boldsymbol{\rho}}^2) \leq 0$. In Eq. 4.5 one immediately recognizes the commutator of $\hat{\boldsymbol{H}}$ and $\hat{\boldsymbol{\rho}}$ as given by the von Neumann equation (Eq. 4.3), which describes the reversible, unitary time evolution of $\hat{\boldsymbol{\rho}}$. In addition, terms containing the $\hat{\boldsymbol{C}}_m$ appear in the Lindblad equation, which describe the irreversible, nonunitary evolution of $\hat{\boldsymbol{\rho}}$. The jump operators $\hat{\boldsymbol{C}}_m$ describe the transitions between quantum states that are driven by the coupling to the environment. Generally, the jump operators $\hat{\boldsymbol{C}}_m$ are not necessarily Hermitian observables and are, therefore, not always straightforward to interpret.

Let us consider a typical example from quantum optics: An optical cavity is prepared in a state containing multiple photons. The finite temperature and imperfections of

[3] As the eigenvalues of $\hat{\boldsymbol{\rho}}$ can be interpreted as probabilities to find the system in a certain state, the eigenvalues have to be between zero and one, which guarantees the semipositivity of all physically sensible $\hat{\boldsymbol{\rho}}$. Thus, any physically sensible time evolution has to be completely positive to conserve this property of $\hat{\boldsymbol{\rho}}$.

[4] We are interested only in time evolutions, in which $\delta_t \hat{\boldsymbol{\rho}}(t)$ exclusively depends on the density operator at the same instance in time $\hat{\boldsymbol{\rho}}(t)$. Particularly, we want the time derivative of $\hat{\boldsymbol{\rho}}$ *not* to depend on the history of the system state. Such master equations are called time-local or *Markovian* master equations.

the mirrors lead to decoherence and photon loss. This is well described by the Lindblad equation with a single jump operator $\hat{\boldsymbol{C}} = \hat{\boldsymbol{a}}$ given by the bosonic annihilation operator $\hat{\boldsymbol{a}}$. Here the interpretation of $\hat{\boldsymbol{C}}$ is obvious, as $\hat{\boldsymbol{a}}$ describes the transition to a state with one photon removed. Therefore, the corresponding Γ can be interpreted as the rate of the photon removal process.

In the context of solid state physics, the Lindblad equation is relevant, wherever decoherence plays an important role and the single particle picture holds [93–96]. In quantum transport of electrons, it is unusual to lose particles to the environment. Therefore, in this thesis, the relevant jump operators are chosen to conserve the particle number in the system: The $\hat{\boldsymbol{C}}_m = \hat{\boldsymbol{P}}_m$ are given by the projection operators $\hat{\boldsymbol{P}}$ introduced in Section 4.2, and the sum of all projectors is equal to the identity $\sum_m \hat{\boldsymbol{P}}_m = \mathbb{1}$. The $\hat{\boldsymbol{C}}_m$ under these conditions correspond to the stochastic occurrence of quantum measurements, which of course conserve the electron number in the system. Section 4.4 illuminates this correspondence further.

The time evolution generated by Eq. 4.5 is not unitary for any $\Gamma_m \neq 0$ and $\hat{\boldsymbol{P}}_m \neq 0$. Thus, the previous definition of the scattering matrix cannot be applied. However, a scattering theory based on the Lindblad master equation formalism exists for certain conditions [99, 100]. In this thesis, we are interested in transmission probabilities. These can be calculated without a rigorous, formal scattering theory: We prepare wave packets in the system leads and evolve the system state until no significant interaction between wave packet and system remains. After this time evolution, the integrated probability densities in the system leads yield the desired transmission and reflection probabilities.

The symmetries presented in Section 3.2, which follow from the unitarity of the scattering matrix do not necessarily apply for the transmission probabilites obtained with Lindblad-type time evolution. The reasons are the same as for the case of quantum trajectories (Section 4.2). This is the case, because every quantum-trajectories time evolution corresponds to a Lindblad master equation, as will be elaborated in the following section.

4.4 Correspondence of Quantum Trajectories and the Lindblad Master Equation

For every stochastic Schrödinger equation used in the quantum trajectories method, there is a Lindblad master equation, such that the time evolution of the expectation value of any observable is identical at any time and any initial state. In fact, any physically sensible time evolution, that is, any evolution that conserves the norm $\delta_t \operatorname{tr}(\hat{\boldsymbol{\rho}}) = 0$ and is completely positive, has a unique Lindblad form [97]. In contrast, most time evolutions are accurately described by multiple different stochastic Schrödinger equations.

The equivalence of the Lindblad master equation and quantum trajectories is readily understood by rewriting the differential equation Eq. 4.5 as a finite-difference equation. In this example, we employ one jump operator $\hat{\boldsymbol{C}} = \sqrt{\Gamma}\hat{\boldsymbol{P}}$. The time evolution of the density operator according to the Lindblad equation for a small time step δt is then

given by

$$\hat{\boldsymbol{\rho}}(t+\delta t) = \underbrace{\hat{\boldsymbol{\rho}}(t)}_{\textbf{(III)}} + \delta t \Bigg(\underbrace{-\frac{i}{\hbar}\left[\hat{\boldsymbol{H}}, \hat{\boldsymbol{\rho}}(t)\right]}_{\textbf{(IV)}} + \underbrace{\Gamma \hat{\boldsymbol{P}} \hat{\boldsymbol{\rho}}(t) \hat{\boldsymbol{P}}}_{\textbf{(V)}} - \underbrace{\frac{\Gamma}{2}\left(\hat{\boldsymbol{\rho}}(t)\hat{\boldsymbol{P}} + \hat{\boldsymbol{P}}\hat{\boldsymbol{\rho}}(t)\right)}_{\textbf{(VI)}} \Bigg). \tag{4.6}$$

The overall equation describes how the density operator $\hat{\boldsymbol{\rho}}$ at time $t + \delta t$ is constructed from the density operator at the previous time t, neglecting δt^2 terms and higher orders. Three out of four terms in Eq. 4.6 are straightforward to interpret: Term (III) is the previous $\hat{\boldsymbol{\rho}}$, term (IV) is arising from the von Neumann evolution, and term (V) is the previous $\hat{\boldsymbol{\rho}}$ projected by $\hat{\boldsymbol{P}}$. Term (VI) is more difficult to grasp, because $\hat{\boldsymbol{P}}\hat{\boldsymbol{\rho}}$ and $\hat{\boldsymbol{\rho}}\hat{\boldsymbol{P}}$ are non-Hermitian and thus are no valid density operators by themselves. But without this term, the resulting time evolution is not norm preserving, because term (V) creates density in the subspace into which $\hat{\boldsymbol{P}}$ projects. Term (VI) removes density from $\hat{\boldsymbol{\rho}}$, to compensate for the density created by term (V). The role of term (VI) becomes more apparent, if we rearrange the equation and express it using proper[5] density operators only:

$$\hat{\boldsymbol{\rho}}(t+\delta t) = \underbrace{\left(1 - \frac{\delta t \Gamma}{2}\right)\hat{\boldsymbol{\rho}}(t)}_{\textbf{(VII)}} + \underbrace{\frac{\delta t \Gamma}{2}\hat{\boldsymbol{P}}_\perp \hat{\boldsymbol{\rho}}(t) \hat{\boldsymbol{P}}_\perp}_{\textbf{(VIII)}} + \underbrace{\frac{\delta t \Gamma}{2}\hat{\boldsymbol{P}}\hat{\boldsymbol{\rho}}(t)\hat{\boldsymbol{P}}}_{\textbf{(IX)}} \underbrace{-\delta t \frac{i}{\hbar}\left[\hat{\boldsymbol{H}}, \hat{\boldsymbol{\rho}}(t)\right]}_{\textbf{(X)}}, \tag{4.7}$$

with $\hat{\boldsymbol{P}}_\perp \coloneqq \mathbb{1} - \hat{\boldsymbol{P}}$ denoting the orthogonal complement of $\hat{\boldsymbol{P}}$. The characteristics of projection operators $\hat{\boldsymbol{P}} = \hat{\boldsymbol{P}}^\dagger$ and $\hat{\boldsymbol{P}}^2 = \hat{\boldsymbol{P}}$ have been used and the two improper density operators in term (VI) from Eq. 4.6 have been rewritten using the identity

$$\hat{\boldsymbol{\rho}}\hat{\boldsymbol{P}} + \hat{\boldsymbol{P}}\hat{\boldsymbol{\rho}} = \hat{\boldsymbol{\rho}} - \hat{\boldsymbol{P}}_\perp \hat{\boldsymbol{\rho}} \hat{\boldsymbol{P}}_\perp + \hat{\boldsymbol{P}}\hat{\boldsymbol{\rho}}\hat{\boldsymbol{P}}. \tag{4.8}$$

Doing so, term (III) and term (VI) yield together term (VII) and term (VIII). Now, it becomes apparent how the stochastic occurrence of quantum measurements is embedded in the equation: After the interval δt, the probability that a measurement occured is $\delta t \Gamma / 2$. The previous density operator is intermixed with the two possible outcomes of a quantum measurement given by term (VIII) and by term (IX). Note that the two projected density matrices are not renormalized. Their norm is given by the respective probability of the result of the quantum measurement. Term (X) again describes the unitary propagation of $\hat{\boldsymbol{\rho}}$.

Such a stochastic process that is equivalent to a Lindblad equation is called a stochastic unraveling of the Lindblad equation [86, 87, 89]. As mentioned, such a stochastic unraveling is not unique, as the following example illustrates. Rearranging Eq. 4.6 yields

$$\hat{\boldsymbol{\rho}}(t+\delta t) = \left(1 - \frac{\delta t \Gamma}{2}\right)\hat{\boldsymbol{\rho}}(t) + \frac{\delta t \Gamma}{2}\hat{\boldsymbol{P}}\hat{\boldsymbol{\rho}}(t)\hat{\boldsymbol{P}} \underbrace{- \delta t \frac{i}{\hbar}\left(\hat{\boldsymbol{H}}_{\mathrm{nh}}\hat{\boldsymbol{\rho}}(t) - \hat{\boldsymbol{\rho}}(t)\hat{\boldsymbol{H}}_{\mathrm{nh}}^\dagger\right)}_{\textbf{(XI)}}, \tag{4.9}$$

$$\hat{\boldsymbol{H}}_{\mathrm{nh}} = \hat{\boldsymbol{H}} - \frac{i \delta t \Gamma}{2}\hat{\boldsymbol{P}}, \tag{4.10}$$

[5] Here, a proper density operator is one that represents a physically sensible state after being normalized.

with the non-Hermitian Hamiltonian $\hat{\boldsymbol{H}}_{\mathrm{nh}}$. Comparing this equation to Eq. 4.6 reveals that both feature a process that projects $\hat{\boldsymbol{\rho}}$ according to $\hat{\boldsymbol{P}}$ with a rate of $\Gamma/2$. However, the process that projects onto the orthogonal complement $\hat{\boldsymbol{P}}_{\perp}$ is not present in Eq. 4.9. Instead, this term is incorporated in the part of the equation representing the von Neumann time-evolution, given now by term (XI). This von Neumann evolution is no longer generated by the Hermitian system Hamiltonian $\hat{\boldsymbol{H}}$, but by the non-Hermitian effective Hamiltonian $\hat{\boldsymbol{H}}_{\mathrm{nh}}$ which depends on the coupling to the environment[6]. Originating from term (VI) in Eq. 4.6, this non-Hermiticity again introduces loss of density to compensate for the density created by the projector term.

This simple example demonstrates the freedom to choose between stochastic processes or non-Hermitian terms in the effective Hamiltonian, when unraveling the Lindblad master equation. Different unravelings of the same master equation cannot be distinguished by any measurable property. This general rule holds for any choice of the jump operators, which do not need to be limited to projection operators, as presented here.

For the rest of this thesis, situations in which all jump operators are provided by projection operators will be discussed. Further, it will be required that the Hamiltonian of the unraveled time evolution is Hermitian, which for every Lindblad master equation allows an unraveling similar to Eq. 4.6. This is preferable, because it allows for an intuitive interpretation of the time evolution as a Schrödinger-like time evolution interrupted by the stochastic occurrence of quantum measurements.

4.5 Summary

Because it is impossible to perfectly isolate quantum systems from their environment, decoherence is present in any laboratory setup. The unitary time evolution of an isolated quantum system is deterministic and fully reversible. Inevitable coupling to the environment leads to an irreversible time evolution and usually suppresses quantum effects.

If one wishes to calculate the time evolution of a quantum system in the presence of decoherence due to coupling to an environment, it is usually not feasible to solve the Schrödinger equation for the full system including the environmental degrees of freedom. It is therefore mandatory to introduce an artificial cut between the quantum system and its environment, such that the quantum system contains all degrees of freedom that are of interest. This reduces the amount of degrees of freedom of the quantum mechanical problem to an acceptable value, such that at least a numerical treatment it possible.

Markus Büttiker developed a method to apply this concept to transport problems. In his model, the coupling to the environment is incorporated via one or more additional leads. Alternatively, equation for the quantum mechanical time evolution can be modified to incorporate the coupling to the environment, which leads to a nonunitary equation. The generalized and unique form of such an equation is given by the Lindblad

[6] Term (XI) reflects the time evolution according to the von Neumann equation with a non-Hermitian Hamiltonian. Because $\hat{\boldsymbol{H}}_{\mathrm{nh}}$ is non-Hermitian, term (XI) cannot be rewritten as a commutator.

master equation. Like other master equation do, the Lindblad equation describes the time evolution of a density operator.

For any Lindblad master equation, a stochastic Schrödinger equation can be found that is indistinguishable from the corresponding Lindblad equation with regard to any physically observable quantity. Such a stochastic Schrödinger equation describes quantum trajectories and is called an unraveling of the Lindblad equation. Generally, such an unraveling is not unique for a given master equation. This ambiguity can be avoided by requiring that all jump operators are projection operators and that the time evolution between quantum jumps is unitary. This requirement will be obeyed in the rest of this thesis. This kind of unraveling is chosen here, because its interpretation is particularly easy: The time evolution is equivalent to the evolution according to the ordinary Schrödinger equation of a closed quantum system, but containing interruptions by quantum measurements at random time intervals as given by a Poisson process with a rate that is proportional to the system-environment coupling.

Numerical Implementation of Stochastic Tight-Binding Schrödinger Equations

5

Chapter 3 presented the symmetry requirements for two-lead devices imposed by the unitarity of the corresponding scattering matrix. This unitarity enforces full reciprocity and magnetic field inversion symmetry of the transmission and reflection probabilities. Further, it was shown that the scattering phases and wave-packet scattering delays are nonreciprocal and asymmetric with respect to magnetic field inversion if the Hamiltonian of the system breaks appropriate symmetries. However, the description via the scattering matrix neglects decoherence, which is present in any real-world setup. As shown in Chapter 4, numerous theoretical methods are available to describe decoherence. In this chapter, one of these methods, namely the stochastic Schrödinger equation, is applied to the systems discussed in Chapter 3.6. The most important finding is the violation of the two-lead reciprocity and magnetic field inversion symmetry of the transmission probabilities if the system breaks appropriate symmetries, and if the decoherence rate is comparable to the inverse wave-packet scattering delays. The stochastic solver employed for the corresponding calculations was developed as part of this thesis and was run on the institute's high performance computing infrastructure.

Whereas Section 3.6 mostly discussed continuum systems, this chapter considers discrete tight-binding systems. On tight-binding systems, the calculation of the dynamics not exact in the analytical sense, but "numerically exact", that is, the maximum numerical error is close to the precision of the floating point numbers and does not accumulate for large times. Section 5.1 briefly introduces the basics of tight-binding systems. The above statements concerning the numerical advantages of tight-binding systems compared to continuum systems are limited to systems of finite size. In fact, the full matrix representation of the quantum mechanical operators has to fit into the computer's memory. However, the scattering problems discussed in Chapter 3.6 have infinite leads. To nevertheless benefit from the numerical advantages, these infinite systems are approximated here by finite, but sufficiently large systems.

For a system with N_s sites, the memory necessary to store operators, which are given by square matrices, is proportional to N_s^2. It is thus reasonable to expect that the memory requirement for evolving single particle wave functions in time, which requires to compute the time-evolution operator, also grows with $\mathcal{O}(N_s^2)$. Section 5.2 presents a new method which allows to calculate the time evolution with memory usage that grows only as $\mathcal{O}(N_s)$. This method is thus well suited to treat large systems that may be used to approximate infinite systems. As Section 4.2 shows, the ability to evolve wave functions on an (approximately) infinite system together with stochastic processes enables the calculation of transmission and reflection probabilities of wave packets incorporating decoherence. To validate the implementation, Section 5.4 presents a comparison of results obtained with the solver developed in this thesis with results obtained with

existing solvers available online. Section 5.5 discusses a series of example systems similar to the systems shown in Section 3.6. The central result of these calculations is given by violations of the two-lead symmetries of the transmission probabilities, in case the decoherence rate matches the inverse wave-packet scattering delay.

5.1 Tight-Binding Models

Tight-binding models are powerful approximations for quantum mechanical problems in which the total Hilbert space can be seen as an arrangement of weakly overlapping localized degrees of freedom [101]. These localized degrees of freedom are the so-called sites. In this thesis, each site is given by a spinless s-orbital with thus one complex degree of freedom. Generally, several orbitals, spins or other degrees of freedom per site are also possible. A quantum mechanical problem with continuous space coordinates is characterized by an infinite dimensional Hilbert space, even if the geometry under consideration has a finite extension. In contrast, the Hilbert space dimension of a tight-binding problem is given by the number of sites. For a finite geometric size, the number of sites is also finite, hence the tight-binding wave functions and operators have vector and matrix representations of finite size.

To solve the Schrödinger equation it is necessary to find the eigenvectors and eigenvalues of the Hamiltonian. In the space-continuous case, these exact solutions are given by analytical expressions, for which closed forms only exist in simple low-dimensional cases (Section 3.6). For a tight-binding problem with a finite system size, however, the Hamiltonian is a finite-dimensional Hermitian matrix. The eigendecomposition is straightforward for any given Hermitian matrix. Virtually any numerical linear algebra package offers such eigendecomposition routines. This makes the formulation as a tight-binding problem very appealing from a numerical point of view. The name "tight-binding" originates from the fact that every site usually interacts only with itself and with its nearest neighbors. Hence, the Hamiltonian matrix contains nonzero entries H_{mn} only on the diagonal $m = n$, for $m \neq n$ only if sites m and n are direct neighbors. The nearest neighbor terms are termed the hopping energy.

Regarding quantitative modeling, the tight-binding method is frequently used for electronic band structure calculations of crystals or molecules, where the nearest-neighbor coupling of localized orbitals is often a well-justified approximation. Examples for such materials are transition metal oxides with partially filled d-shells or insulators [101]. For literature on tight-binding models see [73, 101–103] or the `Kwant` online tutorial[1].

The numerical procedures to calculate time evolutions in tight-binding systems are readily explained using the example of a minimal system. Figure 5.1a sketches a chain of three sites. The left and the central site are direct neighbors as well as the central

[1] `Kwant` is a python package for tight-binding calculations containing routines to create and visualize models as well as several solvers: `https://kwant-project.org/doc/`

and the right site. The system Hamiltonian of this system in the site basis is given by

$$\hat{\boldsymbol{H}} = \left(\sum_{m \in \Lambda} 2|m\rangle\langle m| \right) - \left(\sum_{(m,n) \in \mathrm{NN}(\Lambda)} |m\rangle\langle n| \right), \tag{5.1}$$

with the set of all sites Λ, the set of all next nearest neighbors $\mathrm{NN}(\Lambda)$, the site m and n eigenvectors $|m\rangle$ and $|n\rangle$ and their dual vectors $\langle m|$ and $\langle n|$. Due to the finite number of sites, this Hamiltonian can be conveniently written in matrix representation

$$\hat{\boldsymbol{H}} = \begin{pmatrix} 2 & -1 & 0 \\ -1 & 2 & -1 \\ 0 & -1 & 2 \end{pmatrix}. \tag{5.2}$$

To evolve wave functions in time, we have to find the eigendecomposition of $\hat{\boldsymbol{H}}$. The three normalized eigenvectors $\boldsymbol{\phi}_1$, $\boldsymbol{\phi}_2$ and $\boldsymbol{\phi}_3$ and eigenvalues E_1, E_2 and E_3 are

$$E_1 = 2 - \sqrt{2}, \quad \boldsymbol{\phi}_1 = \begin{pmatrix} \frac{1}{2} \\ \frac{1}{\sqrt{2}} \\ \frac{1}{2} \end{pmatrix} \tag{5.3}$$

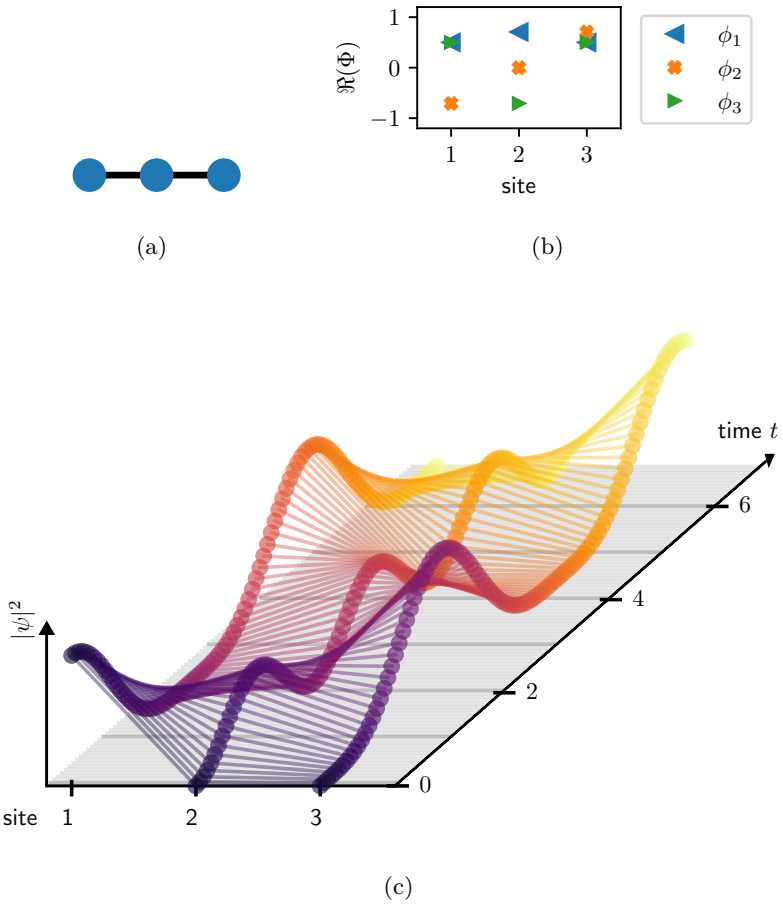
$$E_2 = 2, \quad \boldsymbol{\phi}_2 = \begin{pmatrix} -\frac{1}{\sqrt{2}} \\ 0 \\ \frac{1}{\sqrt{2}} \end{pmatrix} \tag{5.4}$$

$$E_3 = 2 + \sqrt{2}, \quad \boldsymbol{\phi}_3 = \begin{pmatrix} \frac{1}{2} \\ -\frac{1}{\sqrt{2}} \\ \frac{1}{2} \end{pmatrix} \tag{5.5}$$

Because $\hat{\boldsymbol{H}}$ is Hermitian, its eigenvectors span an orthogonal basis of the Hilbert space, which is called the eigenbasis. Figure 5.1b shows a plot of the eigenfunctions. If the three eigenvectors are written as a matrix one obtains

$$\boldsymbol{T} = \begin{pmatrix} \frac{1}{2} & -\frac{1}{\sqrt{2}} & \frac{1}{2} \\ \frac{1}{\sqrt{2}} & 0 & -\frac{1}{\sqrt{2}} \\ \frac{1}{2} & \frac{1}{\sqrt{2}} & \frac{1}{2} \end{pmatrix}. \tag{5.6}$$

The matrix $\boldsymbol{T}$ transforms a wave function given in the eigenbasis representation into the site-basis representation. Due the Hermiticity of $\hat{\boldsymbol{H}}$, the transformation implied by $\boldsymbol{T}$ is unitary, hence the inverse transform is given by $\boldsymbol{T}^\dagger$. The eigenbasis and site-basis representations will be frequently used in this chapter. For better readability, wave functions and operators will be given in the site basis by default. Wave functions and



(a) (b)

(c)

Figure 5.1: (a) Schematic of a small tight-binding system, a chain of three sites. The Hamiltonian $\hat{\boldsymbol{H}}$ of this system is given by Equation 5.2. (b) Plot showing the real part of the eigenvectors $\boldsymbol{\phi}_1$, $\boldsymbol{\phi}_2$ and $\boldsymbol{\phi}_3$ of $\hat{\boldsymbol{H}}$ in the site basis. The three eigenvectors are unique except for a global complex phase. Due to the completely real Hamiltonian, this global phase can be chosen such that the imaginary part of the eigenvectors is zero, which is the choice made here. (c) Plot of the time evolution of the probability density $|\boldsymbol{\psi}|^2$ with the initial wave function given by $\boldsymbol{\psi}(t=0) = (1,0,0)$ in the site basis. The time-evoluton resembles the classical motion of a particle bouncing between the left and right side of the system. Starting completely localized at site 1, the particle is mostly localized at site 2 at $t = 1$, then mostly localized at site 3 at $t = 2$ and then travels back in a similar fashion.

operators given in the energy-eigenbasis (called the eigenbasis in the following) representation will be marked with an additional index E. For example $\boldsymbol{\phi}_1 = (1/2, 1/\sqrt{2}, 1/2)$ specifies a wave function given in the site-basis representation, $\boldsymbol{\phi}_{\mathrm{E},1} = (1, 0, 0)$ denotes the same wave function in the eigenbasis representation.

Wave functions in the site-basis representation are advantageous if one wishes to calculate position-like properties. The major advantage of the eigenbasis representation is that the calculating the time evolution is straightforward, because the time-evolution operator $\hat{\boldsymbol{U}}$ is diagonal in the eigenbasis representation:

$$\hat{\boldsymbol{U}}_{\mathrm{E}}(t_1, t_2) = \begin{pmatrix} e^{iE_1(t_2-t_1)} & 0 & 0 \\ 0 & e^{iE_2(t_2-t_1)} & 0 \\ 0 & 0 & e^{iE_3(t_2-t_1)} \end{pmatrix}. \tag{5.7}$$

To calculate the time evolution $\boldsymbol{\psi}(t)$ of a given wave function $\boldsymbol{\psi}_0$ given in the site-basis representation, we transform the eigenbasis time evolution operator using the site-basis-to-eigenbasis transformation matrix $\boldsymbol{T}$:

$$\boldsymbol{\psi}(t) = \boldsymbol{T}^\dagger \hat{\boldsymbol{U}}_{\mathrm{E}}(t_1, t_2) \boldsymbol{T} \boldsymbol{\psi}_0. \tag{5.8}$$

Figure 5.1c shows the time evolution of a wave function that is initially localized at the left site $\boldsymbol{\psi} = (1, 0, 0)$. With time, the wave function spreads over the central site, then becomes mostly localized on the right site, to later move back to the left site in the same fashion.

This recipe to find the time evolution of arbitrary site-basis wave functions is obviously also applicable to larger systems. The only difference for larger systems is that it may not be possible to find the exact expressions for the eigendecomposition of $\hat{\boldsymbol{H}}$, because finding exact roots of the characteristic polynomial becomes increasingly difficult with system size. However, a numerically exact eigendecomposition can always be found. The resulting numerical errors are of the order of the resolution of the used floating-point format. In many cases, these errors amplify during further computation and finally cause significant deviations of the final results from the exact values. Fortunately, the time evolution operator is a unitary transformation, which thus always features a condition number of one [104]. This implies that numerical errors are not amplified by this transformation. The numerical error of the entire time evolution of $\boldsymbol{\psi}$ therefore remains comparable to the floating point precision (IEEE-754 "double precision", ≈ 15 significant digits). The eigendecomposition is a very common operation and virtually any numerical algebra software offers highly optimized routines. As long as the entire Hamiltonian fits into the memory, the difficulty scales with the number of sites squared. With the `scipy.linalg.eigh`[2] solver, systems comprising 1000 sites are solved within a few seconds on a standard desktop computer.

Even much larger systems can be partially diagonalized, by benefiting from the fact that most of the entries of the Hamiltonian are zero. Such matrices are so-called sparse matrices, which can be stored in memory in several compressed formats. Specialized sparse-matrix algorithms are capable of finding eigenvalues and eigenvectors

[2] `https://docs.scipy.org/doc/scipy/reference/generated/scipy.linalg.eigsh.html`

much faster than the equivalent algorithms for general matrices. The python package `scipy.sparse.linalg.eigh`[3] offers such sparse-matrix solvers. These solvers are usually extremely fast in finding a limited number of small eigenvalues and the corresponding eigenvectors even for huge matrices. However, if one wishes to find *all* eigenvalues and eigenvectors to completely diagonalize the matrix with a sparse-matrix solver, the cost to diagonalize a $N \times N$ matrix again scales with $\mathcal{O}(N^2)$. In this thesis, we restrict ourselves to small systems that can be fully kept in memory. Thus, the calculation of the full diagonalization of $\hat{\boldsymbol{H}}$ is possible without the need for sparse-matrix solvers.

The Hamiltonian given by Eq. 5.2 needs to be extended for our purposes: We wish to apply a magnetic field perpendicular to the plane of sites and to locally modulate the electrostatic potential. The electrostatic potential at a site m is modulated by changing the respective diagonal element of the Hamiltonian. The magnetic field is incorporated by the Peierls substitution [105], which rotates the complex phase of every hopping-term H_{mn} according to the path integral of the electromagnetic vector potential between the two sites m and n. The Hamiltonian is then given by

$$\hat{\boldsymbol{H}} = \left(\sum_{m \in \Lambda} \left(4 + \mathcal{V}(m)\right) |m\rangle\langle m| \right) - \left(\sum_{(m,n) \in \mathrm{NN}(\Lambda)} \exp\left(i \int_{\boldsymbol{l}(m,n)} \boldsymbol{A} \mathrm{d}\boldsymbol{r} \right) |m\rangle\langle n| \right), \quad (5.9)$$

with the site-dependent electrostatic potential $\mathcal{V}(m)$ and the vector potential $\boldsymbol{A}$. In this chapter, the sites are located on the xy-plane in a square lattice with lattice constant 1 and we apply a perpendicular magnetic field specified by the resulting z-component of the magnetic flux density B_z. Nearest neighbors are either connected by paths in x or in y direction. With the gauge chosen as $A_x = yB_z$, $A_y = A_z = 0$, the Hamiltonian is simplified to

$$\begin{aligned} \hat{\boldsymbol{H}} = & \left(\sum_{m \in \Lambda} \left(4 + \mathcal{V}(m)\right) |m\rangle\langle m| \right) \\ & - \left(\sum_{(m,n) \in \mathrm{NN}_x(\Lambda)} \exp\Big(iy(m,n) B_z \Big) |m\rangle\langle n| \right) \\ & - \left(\sum_{(m,n) \in \mathrm{NN}_y(\Lambda)} |m\rangle\langle n| \right), \end{aligned} \quad (5.10)$$

where $\mathrm{NN}_x(\Lambda)$ and $\mathrm{NN}_y(\Lambda)$ are the sets of nearest neighbors only in x or y direction and $y(m,n)$ specifies the mean value of the y coordinates of the two sites m and n. For neighbors in x direction, this integral is given by the average y coordinates of both sites and the z-component of the magnetic flux density B_z. For neighbors in y direction, the integral in Eq. 5.9 vanishes because $A_y = 0$. This is the Hamiltonian that will be used in the rest of this chapter.

[3] `https://docs.scipy.org/doc/scipy/reference/generated/scipy.sparse.linalg.eigsh.html`

In the Hamiltonian given by Eq. 5.10 the weight of the diagonal elements is $4 + \mathcal{V}$, whereas in the Hamiltonian given by Eq. 5.2 the diagonal elements have a value of 2. Generally, adding an arbitrary real number to all diagonal elements of $\hat{\boldsymbol{H}}$ leaves the system dynamics unchanged, because it is equivalent to changing the electrostatic potential globally. Such a gauge transformation must not affect measurable quantities. We choose this gauge here for $\hat{\boldsymbol{H}}$ to have a completely positive spectrum. For a one-dimensional chain of sites (Eq. 5.2) this amounts to diagonal elements greater or equal to 2, for a two-dimensional lattice of sites the diagonal elements have to be greater or equal to 4.

This section briefly introduced how to set up the tight-binding Hamiltonian for a given lattice and potentials. Further it was shown how to calculate the time evolutions of wave functions on such systems. However, the presented numerical methods are directly applicable only to systems with a finite number of sites. As our main interest is the treatment of scattering problems, we need to extend the methods to infinite systems.

5.2 Time Evolutions of Infinite Systems

As discussed in Section 3.1, the Schrödinger equation describing scattering problems can be solved with the help of Bloch waves: Due to the periodicity of the Hamiltonian in the infinite leads, the differential equation has to be solved for one finite period of the lead only. The solution for the infinite lead is then given by a plane wave term multiplied with the solution of the finite lead period.

This also works for tight-binding systems. The `Kwant` software package offers a toolbox to set up a scattering problem and solvers to find the eigenfunctions of the problem for a given eigenvalue (= energy). In principle we can use these eigenfunctions to calculate the time evolutions of wave functions as described in Section 5.1. However, there is an infinite number of eigenfunctions in any energy interval, of which we have to sample a finite subset if we want to perform numerical calculations. Importantly, the numerics have to be designed such that the unitarity of the calculated $\hat{\boldsymbol{U}}$ does not suffer from numerical errors. This is because the overall aim of the method presented in this chapter is to analyze the symmetries of scattering processes, especially the symmetries imposed by the unitarity of the time-evolution operator $\hat{\boldsymbol{U}}$ (and thus the scattering matrix). Because, the site-basis-to-eigenbasis transformation matrix $\boldsymbol{T}$ is used to calculate the site-basis representation of $\hat{\boldsymbol{U}}$, the unitarity of $\boldsymbol{T}$ important as well. However, numerically the unitarity of $\boldsymbol{T}$ and therefore of $\hat{\boldsymbol{U}}$ is difficult to achieve. The matrix $\boldsymbol{T}$ is unitary only if it is constructed using *all* eigenfunctions of the system. This can of course not be realized on a finite computer, because an infinite number of eigenfunctions exists. If a finite subset of the eigenfunctions is used, the method is prone to induce asymmetries in the time evolutions caused by the resulting numerical errors. This would make it difficult to distinguish between real asymmetries and numerical artifacts. For this reason, this method is not further used in this thesis.

To obtain a time-evolution operator $\hat{\boldsymbol{U}}$ that is unitary to floating point precision, we completely avoid the eigenfunctions of the infinite systems and only consider finite systems. The key is to approximate the infinite system by a very large, but finite

system. Such a system can be fully diagonalized and we can obtain all eigenfunctions to construct a unitary site-basis-to-eigenbasis transformation matrix $\boldsymbol{T}$. An important question concerns the size required for the system to be "approximately infinite". The answer depends on the initial wave function, the maximum time span for which one would like to evolve the wave function, and the size of the region in which the precise value of the wave function is of interest.

A wave packet starting somewhere in the region of interest will reach the leads at some point in time. In the infinite system, these leads do of course extend infinitely. However, in the approximated finite system this is not the case (Figure 5.2). If the wave packet reaches the lead ends it will be reflected. Therefore, the system size has to be chosen large enough, such that during the desired time span of the evolution these reflections of the lead ends do not return to the region of interest. Under this condition, the resulting dynamics of the finite system is identical to the dynamics of the infinite system *and* the unitarity of $\boldsymbol{T}$ is guaranteed. By this, we have achieved a proper foundation to study the symmetries of the scattering process.

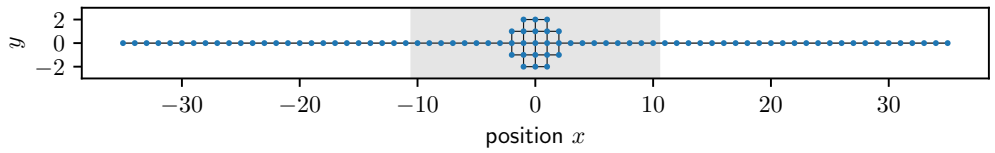
5.2.1 Algorithm with Linear Scaling

If the naive implementation of calculating time evolutions, directly as given by Eq. 5.8, is combined with the method of increasing the system size until it approximates the infinite system, the numerics quickly runs into memory issues. Therefore, it is worthwhile to optimize the algorithms for large systems, particularly for systems with very long leads. The first step, which is the full diagonalization of $\hat{\boldsymbol{H}}$, cannot be avoided, because we need to obtain the complete orthogonal basis. However, the result of the diagonalization contains unneeded information. Because we are only interested in the wave functions in a well defined, small region, it is possible to simplify the calculation of Eq. 5.8 substantially, as will be shown in the following.

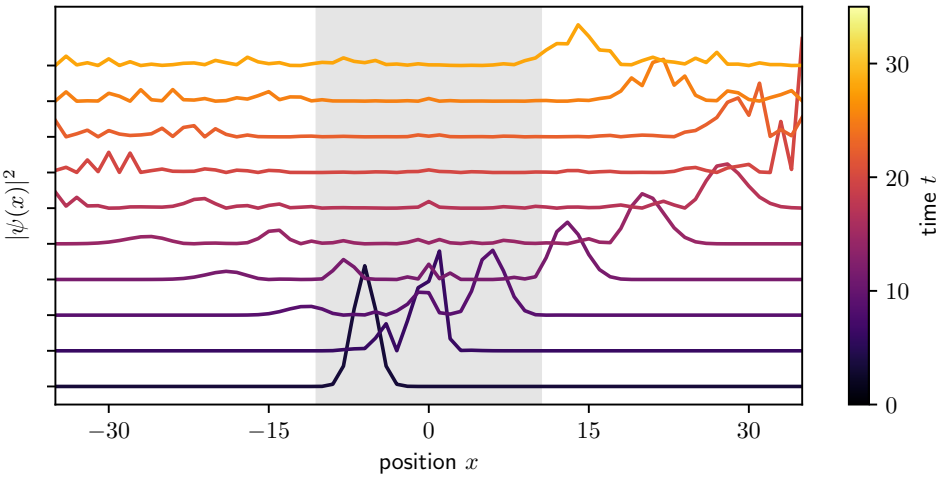
The memory size of the full site-basis-to-eigenbasis transformation matrix $\boldsymbol{T}$ scales with the square of the number of sites N_s. From this matrix $\boldsymbol{T}$, we do need all eigenspace basis vectors, because, as discussed above, the completeness of the eigenspace basis is essential to conserve the unitarity of the time evolution. However, only a subset of the position space basis vectors is of interest for our problem. To compute the transmission and reflection probabilities of wave packets, we need to calculate the total probability of finding the particle within a given lead. The straightforward implementation would be to calculate the site-basis time evolution according to Eq. 5.8, and to integrate the resulting probability densities over the respective lead region. However, instead of spatial integration of the probability density in the lead, we can time-integrate the probability current flowing into this lead (see Section 5.2.2)

$$\mathcal{Q}_\alpha(t) = \int_{t_0}^{t} \mathcal{I}(\tau)\mathrm{d}\tau, \tag{5.11}$$

with the integrated probability current $\mathcal{Q}_\alpha(t)$, the lead index α, and a time t_0 at which the probability distribution of the full wave function is known. This is for example the case for a wave packet that is localized to a specific lead.



(a)



(b)

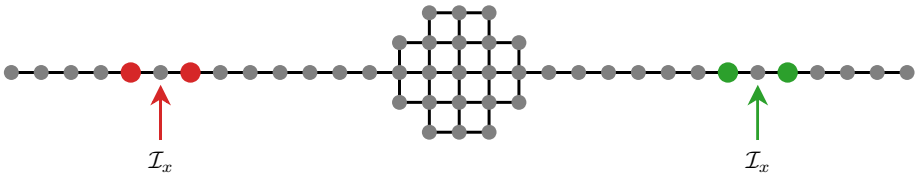
Figure 5.2: Illustration of the approximation of infinite systems by large systems. (a) A tight-binding system is sketched by the set of sites (blue dots) and the nearest-neighbor interaction (lines between dots). The region of interest (gray) is located around the structure in the center. (b) The time evolution of a wave packet illustrates the effect of the finite length of the leads. Each curve represents the probability densitity $|\psi(x)|^2$ of the wave function at a given time according to the color code. The curves are vertically shifted for clarity. The wave packet starts in the left of the region of interest at $t = 0$, encounters the boundary of the structure at $t = 10$ and is then partially transmitted and partially reflected. In the infinite system, the transmitted and reflected fractions never return to the region of interest in the center. However, with the finite lead length shown here, these fractions of the wave packet eventually reach the lead ends and are reflected back to the region of interest. For the shown system size, the dynamics of the infinite system and the dynamics of the finite system are identical until $t \approx 15$.

This calculation only requires the site-basis representation of the wave function around the system-lead boundaries. As Fig. 5.3 illustrates, the columns of the matrix $\boldsymbol{T}$ are given by the eigenvectors of the system in site-basis representation. Therefore, each row of $\boldsymbol{T}$ corresponds to one site basis vector. For the probability current integral method, we only need to keep those rows of $\boldsymbol{T}$, which are required for the calculation of the currents. This drastically reduces the memory size of the matrix and speeds up matrix multiplications.

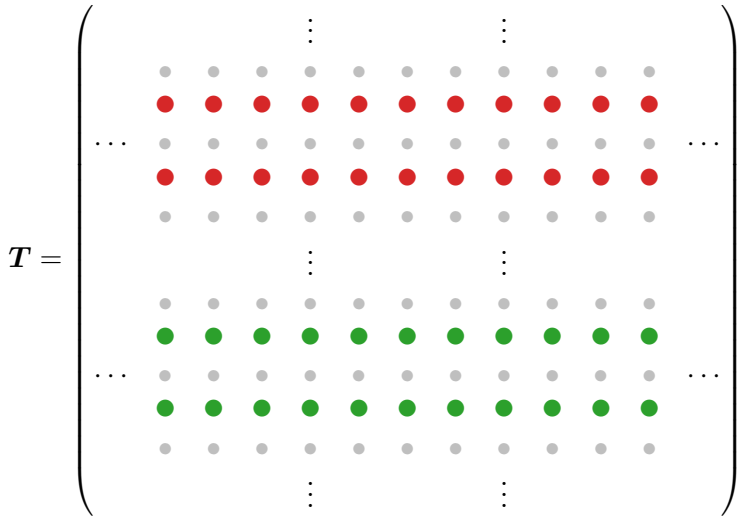
The example of the structure with 87 sites shown in Fig. 5.2 is first calculated by using the full $\boldsymbol{T}$ with 87×87 entries. The transmission and reflection probabilities can be extracted from the time evolution by integrating the probability density over the sites with $x \geq 10$ and $x \leq -10$ at a suitable time. This time has to be late enough, such that the interaction of the wave packet with the structure in the center has decayed, but early enough such that the reflections from the lead ends did not return to what we defined to be the structure boundaries, $x = -10$ and $x = 10$. Figure 5.4a shows the summed probability densities for $x \leq -10$ and $x \geq 10$ as a function of time. After $t = 20$ the wave packet has completely left the region of interest and the probabilities do not change with time anymore. However, at $t = 30$ the wave-packet reflections of the lead ends enter the region of interest, causing the probabilities to again change with time. From this plot we can see that $t = 25$ is a suitable point in time to evaluate the transmission and reflection probabilities.

Alternatively, we can calculate the transmission and reflection probability employing the probability current integral method. To calculate the current at $x = -10$ and at $x = 10$, we need to calculate the site basis wave functions only for the four sites located at $x = -11$, $x = -9$, $x = 9$ and $x = 11$. The details on how to calculate this probability current and why two sites are required to determine one current will be discussed at the end of this section. From of the total 87×87 elements of $\boldsymbol{T}$, we now only need 4×87 elements. The results obtained with the numerical current integration are shown in Fig. 5.4b. They are in good agreement with the results obtained by calculating the full time evolution shown in Fig. 5.4a. The relative difference of the probabilities calculated with the two methods at $t = 25$ is less than 2×10^{-3}. The value of the transmission probability is 0.71, the reflection probability equals 0.26. The remaining 3 % of the wave packet are still within the structure in the center. To improve the accuracy of the calculation, we would need to run the time evolution for longer times, which leads to artifacts using the shown lead length. Increasing the lead length allows to prolong the artifact-free time span and to improve the accuracy of the calculated transmission and reflection probabilities.

This example system with a lead length of 30 sites shown in Figs. 5.2 and 5.4 is sufficiently small to readily reveal some of the possible error sources of the numerical method. The nonreciprocity that we want to analyze in this chapter has a typical magnitude of a few percent. Therefore, the systems in the rest of this chapter will typically use lead lengths of 500 to 2000 sites to keep the numerical errors as small as desired.



(a)



(b)



(c)

Figure 5.3: Illustration of the size reduction of the matrix $\boldsymbol{T}$ enabled by the probability-current integral method. (a) Sketch of a tight-binding device with two leads, in which the probability current $\mathcal{I}_x$ in x-direction is calculated at the two sites indicated by the red and green arrows. The sites colored in red and green are the only sites at which the wave function needs to be known to calculate $\mathcal{I}_x$ (see Section 5.2.2). (b) Illustration of the matrix $\boldsymbol{T}$. The matrix elements are represented by gray, red or green dots. The $\cdots$ indicate skipped lines or columns. Each line of $\boldsymbol{T}$ corresponds to one site. The two red (green) lines correspond to the two sites needed to calculate the probability current in the left (right) lead. The gray dots correspond to other sites. (c) To calculate the probability current, the reduced matrix $\boldsymbol{T}_r$ suffices. This matrix consists only of the four red and green rows of the matrix $\boldsymbol{T}$.

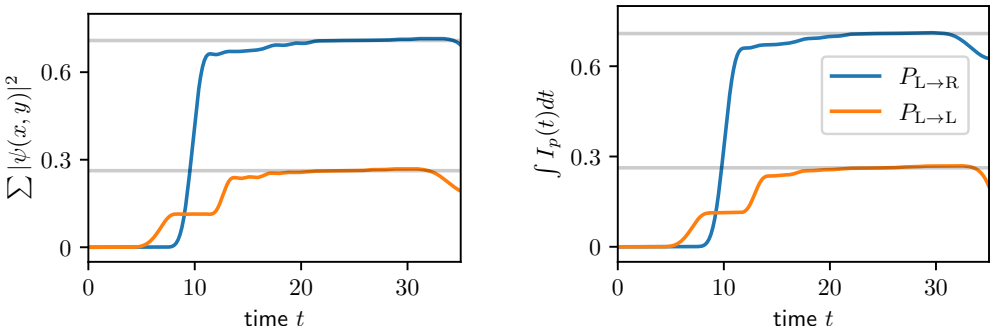


Figure 5.4: Plot of the integrated probability density of the transmitted and reflected wave-packet fractions as a function of time. The value of the probabilities for $20 < t < 30$ (grey lines) is stationary and describes the transmission or reflection probability of the wave packet. After $t = 30$ the probabilities drop, because the reflections from the leads' ends re-enter the region of interest. (a) The left plot shows the probabilities obtained from the sum of the site basis probability density $|\boldsymbol{\psi}(x, y)|^2$ over the region $x \leq -10$ or $x \geq 10$, respectively. (b) The right plot shows the probabilities obtained with the time-integrated probability current $\mathcal{I}(t)$ at the region edge $x = -10$ or $x = 10$, respectively.

5.2.2 The Probability Current in Tight-Binding Systems

The previous paragraphs introduced the probability current, which, when integrated over time, yields the transported probability. This subsection describes how the probability current is calculated for the tight-binding systems considered here. For this, we start with the general definition of the probability current for a quantum mechanical system. As any current, the probability current is defined by the corresponding continuity equation, which leads to the following expression for the current [50]

$$\mathcal{I} = -\frac{i\hbar}{2m}\left(\boldsymbol{\psi}^\dagger \nabla \boldsymbol{\psi} - \boldsymbol{\psi} \nabla \boldsymbol{\psi}^\dagger\right) \tag{5.12}$$

$$= \frac{1}{2m}\left(\boldsymbol{\psi}^\dagger \hat{\boldsymbol{p}} \boldsymbol{\psi} - \boldsymbol{\psi} \hat{\boldsymbol{p}} \boldsymbol{\psi}^\dagger\right), \tag{5.13}$$

with the reduced Planck constant $\hbar$, the particle mass m and the wave function $\boldsymbol{\psi}$. Because we exclusively calculate the probability current in the two leads of the system which are located parallel to the x-axis at $y = 0$, the electromagnetic vector potential $\boldsymbol{A}$ is always zero in the chosen gauge (Eq. 5.10). Further, the electrostatic potential $\mathcal{V}$ in the leads always equals zero. Equation 5.13 and the following steps can be generalized to the case of $\boldsymbol{A} \neq 0$ and $\mathcal{V} \neq 0$. However, this generalization is not needed here. For simplicity, we therefore proceed with $\boldsymbol{A} = 0$. Because the leads are always aligned parallel to the x-axis, we are interested in the x component of the probability current. Therefore, we

will replace $\hat{\boldsymbol{p}}$ with the momentum operator x-component $\hat{\boldsymbol{p}}_x$. The momentum operator x-component $\hat{\boldsymbol{p}}_x$ can be written as the commutator of the x-position operator $\hat{\boldsymbol{X}}$ and the Hamiltonian $\hat{\boldsymbol{H}}$:

$$\frac{m}{i\hbar}\left[\hat{\boldsymbol{X}},\hat{\boldsymbol{H}}\right] = \frac{1}{2i\hbar}\left[\hat{\boldsymbol{X}},\hat{\boldsymbol{p}}^2\right] = \hat{\boldsymbol{p}}_x. \tag{5.14}$$

The matrix representation of the Hamiltonian $\hat{\boldsymbol{H}}$ was discussed in Section 5.1. The matrix representation of the x-position operator $\hat{\boldsymbol{X}}$ is given by a diagonal matrix in the site basis, in which the m-th diagonal element is given by the x coordinate of that site. For example, $\hat{\boldsymbol{X}}$ and its commutator with $\hat{\boldsymbol{H}}$ of the system shown in Fig. 5.1 are given by

$$\hat{\boldsymbol{X}} = \begin{pmatrix} -1 & 0 & 0 \\ 0 & 0 & 0 \\ 0 & 0 & 1 \end{pmatrix}, \quad \left[\hat{\boldsymbol{X}},\hat{\boldsymbol{H}}\right] = \begin{pmatrix} 0 & 1 & 0 \\ -1 & 0 & 1 \\ 0 & -1 & 0 \end{pmatrix}. \tag{5.15}$$

Inserting Eq. 5.14 into Eq. 5.13 yields an expression for $\mathcal{I}$ that we can numerically evaluate. Expanding and rearranging the commutators allows us to simplify the expression further.

$$\mathcal{I} = \frac{1}{2i\hbar}\left(\boldsymbol{\psi}^\dagger\left[\hat{\boldsymbol{X}},\hat{\boldsymbol{H}}\right]\boldsymbol{\psi} - \boldsymbol{\psi}\left[\hat{\boldsymbol{X}},\hat{\boldsymbol{H}}\right]\boldsymbol{\psi}^\dagger\right) \tag{5.16}$$

$$= \frac{1}{2i\hbar}\left(\boldsymbol{\psi}^\dagger\hat{\boldsymbol{X}}\hat{\boldsymbol{H}}\boldsymbol{\psi} - \left(\boldsymbol{\psi}^\dagger\hat{\boldsymbol{X}}\hat{\boldsymbol{H}}\boldsymbol{\psi}\right)^\dagger + \boldsymbol{\psi}\hat{\boldsymbol{H}}\hat{\boldsymbol{X}}\boldsymbol{\psi}^\dagger - \left(\boldsymbol{\psi}\hat{\boldsymbol{H}}\hat{\boldsymbol{X}}\boldsymbol{\psi}^\dagger\right)^\dagger\right) \tag{5.17}$$

$$= \frac{1}{\hbar}\left(\Im\left(\boldsymbol{\psi}^\dagger\hat{\boldsymbol{X}}\hat{\boldsymbol{H}}\boldsymbol{\psi} + \boldsymbol{\psi}\hat{\boldsymbol{H}}\hat{\boldsymbol{X}}\boldsymbol{\psi}^\dagger\right)\right), \tag{5.18}$$

with the imaginary part $\Im(\dots)$. The obtained expression resembles an (anti-) commutator, except that in one term of Eq. 5.18 $\boldsymbol{\psi}^\dagger$ appears on the left and in the other case on the right hand side of the product. Fortunately, the whole expression is wrapped by the $\Im$ function. The imaginary part of the transposal of an operator is equal to the imaginary part of the adjoint operator multiplied by minus one. This allows us to rearrange the expression to a commutator, which then is identified with the x-component $\hat{\boldsymbol{p}}_x$ of the momentum operator

$$\mathcal{I} = \frac{1}{\hbar}\left(\Im\left(\boldsymbol{\psi}^\dagger\hat{\boldsymbol{X}}\hat{\boldsymbol{H}}\boldsymbol{\psi} + \boldsymbol{\psi}\hat{\boldsymbol{H}}\hat{\boldsymbol{X}}\boldsymbol{\psi}^\dagger\right)\right) \tag{5.19}$$

$$= \frac{1}{\hbar}\Im\left(\boldsymbol{\psi}^\dagger\left[\hat{\boldsymbol{X}},\hat{\boldsymbol{H}}\right]\boldsymbol{\psi}\right) \tag{5.20}$$

$$= \frac{1}{m}\Im\left(\boldsymbol{\psi}^\dagger i\hat{\boldsymbol{p}}_x\boldsymbol{\psi}\right) \tag{5.21}$$

$$= -\frac{1}{m}\Re\left(\boldsymbol{\psi}^\dagger\hat{\boldsymbol{p}}_x\boldsymbol{\psi}\right), \tag{5.22}$$

with the real part $\Re(\dots)$. For the numerics, Eq. 5.20 is the crucial equation. We know the site basis matrix representations of $\hat{\boldsymbol{X}}$ and $\hat{\boldsymbol{H}}$ of our problem, and the site basis wave function $\boldsymbol{\psi}$ is given by the corresponding time step of the wave function's evolution. Equation 5.20 then allows to calculate the probability current in x-direction for that wave function (or point in time) at every site.

As discussed in the previous paragraphs, we only need to calculate the probability current flowing through the system-lead boundaries to keep track of the transported probability. Notably, we are not required to calculate the full site-basis representation of the wave function $\boldsymbol{\psi}$. However, if we are interested in the probability current $\mathcal{I}$ at site m, the wave function element at site m alone is not sufficient. Additionally, we do need the wave function element at all sites, at which the m-th column or the m-th row of the matrix $[\hat{\boldsymbol{X}}, \hat{\boldsymbol{H}}]$ contains nonzero elements. As implied previously, in the case of a 1D chain these are the direct neighbors of the site m in the chain. On a 2D grid these are the 4 nearest neighbors. Therefore, to measure the probability current at a specific site, our effective region of interest has to be a small environment around that site.

5.2.3 Summary

The presented method allows to numerically calculate the transmission and reflection probabilities of a tight-binding system maintaining with high accuracy the unitarity of the time-evolution operator $\hat{\boldsymbol{U}}$. First, we need to find all eigenvectors of the system. From the eigenvectors we then only keep a reduced site-basis representation given by our region of interest. The transmission and reflection probabilities for wave packets are obtained by time integration of the probability currents flowing into the leads. These few sites in the leads where we need to measure the probability current are for now our region of interest. From the full N_s^2 entries of the site-basis-to-eigenbasis transformation matrix $\boldsymbol{T}$, we then need only $N_s N_r$ elements. Here, N_r is the number of sites in the region of interest and usually $N_s \gg N_r$. Using the reduced site-basis-to-eigenbasis transformation matrix $\boldsymbol{T}_r$ to calculate the strictly unitary time evolution according to Eq. 5.8 is a factor of N_s cheaper in cpu time and memory cost, than using the full matrix $\boldsymbol{T}$. Initially, however, the full $\boldsymbol{T}$ has to be calculated by diagonalization of $\hat{\boldsymbol{H}}$ to obtain a complete and orthogonal basis, which guarantees unitarity of the time evolution with floating point precision. After the initial diagonalization the unneeded rows of the matrix are discarded to speed up the subsequent calculations of time evolutions. Therefore, this method is well suited to treat systems with large leads, which is important to approximate infinite systems.

5.3 Stochastic Dynamics

To implement the stochastic Schrödinger equation introduced in Section 4.2, it is necessary to extend the unitary time evolution presented in the previous section by the stochastic occurrence of quantum measurements. Therefore, we need the numerical tools to model quantum measurements using the tight-binding wave functions. To mea-

sure an observable $\hat{\boldsymbol{O}}$ with respect to a given wave function $\boldsymbol{\psi}$, we need to calculate the probabilities of the possible measurement outcomes and the respective projection operators that are applied to the wave function as a side effect of acquiring the measurement result.

In the geometries discussed in this chapter, the superposition of multiple particle paths is crucial in determining the total transmission probability. This superposition is suppressed if the observer gathers which-way information. In our case, the environment, which couples to the quantum system and induces decoherence, acts as the observer. Which-way information is gathered by measuring observables $\hat{\boldsymbol{O}}$ that feature the same set of eigenvectors as the position operators $\hat{\boldsymbol{X}}$ and $\hat{\boldsymbol{Y}}$, thus, $[\hat{\boldsymbol{O}}, \hat{\boldsymbol{X}}] = 0$ and $[\hat{\boldsymbol{O}}, \hat{\boldsymbol{Y}}] = 0$. This class of observables measure whether the particle is located within a certain region or measure the position itself. Because $\hat{\boldsymbol{X}}$ and $\hat{\boldsymbol{Y}}$ obviously commute with each other and with themselves, they are also part of this class. To model decoherence in a two-path interferometer, for example, a suitable observable measures in which of the two arms of the interferometer the particle is located.

In the scenarios considered here, the measured value is actually not of interest, it is only the effect of the post-measurement projection on the time evolution is important. Therefore, the precise value of the eigenvalues of the observable $\hat{\boldsymbol{O}}$ are not relevant. However, the degeneracies are of importance. If all eigenvalues are distinct, then all possible post-measurement projection operators are given by single site basis vectors, which project onto one-dimensional, maximally localized subspaces. This measurement corresponds to a complete erasure of phase and momentum information. If several eigenvalues of $\hat{\boldsymbol{O}}$ are degenerate, the post-measurement projector projects onto the space spanned by the corresponding site basis vectors. In this case, phase and momentum information is partially preserved. If all eigenvalues are degenerate, then $\hat{\boldsymbol{O}}$ must be proportional to the identity. Then only one post-measurement projection operator exists, which is also given by the identity. As the probabilities of the measurement outcomes are solely defined by the projection operators, for our purpose an observable $\hat{\boldsymbol{O}}$ is completely defined, if its degeneracies are known and if it commutes with $\hat{\boldsymbol{X}}$ and $\hat{\boldsymbol{Y}}$.

To perform a quantum measurement of such an observable $\hat{\boldsymbol{O}}$ on a wave function $\boldsymbol{\psi}$, we first need to calculate the post-measurement projection operators $\hat{\boldsymbol{P}}_m$ of $\hat{\boldsymbol{O}}$. There is one $\hat{\boldsymbol{P}}_m$ for every distinct eigenvalue λ_m of $\hat{\boldsymbol{O}}$. In the site basis, the diagonal entries of $\hat{\boldsymbol{P}}_m$ corresponding to sites with the eigenvalue λ_m are one, all other entries are zero. The probability p_m to measure the result λ_m is then given by

$$p_m = \boldsymbol{\psi}^\dagger \hat{\boldsymbol{P}}_m \boldsymbol{\psi}. \tag{5.23}$$

Due to $\sum_m \hat{\boldsymbol{P}}_m = \mathbb{1}$ these probabilities sum to one $\sum_m p_m = 1$. With the time evolution given by Eq. 5.8, we do not have numerical access to the full position space representation of wave functions. This imposes a limitation on the choice of the projection operator $\hat{\boldsymbol{P}}_m$. To still be able to perform quantum measurements numerically, there must be only one $\hat{\boldsymbol{P}}_m$ that projects onto the space outside the region of interest. In the following, this will be the projector $\hat{\boldsymbol{P}}_0$. The probability of the respective measurement outcome λ_0 is given by one minus the sum of the remaining probabilities, $1 - \sum_{m>0} p_m$.

This implies that in terms of quantum measurements, we can only measure if the particle is located *anywhere* outside the region of interest, no further details on the location are derivable. This is not surprising, as we deliberately dropped this information from the site-basis-to-eigenbasis transformation matrix $\boldsymbol{T}$ to speed up the calculation of time evolutions. Figure 5.5 sketches an example for projectors and the corresponding subspaces fulfilling the above criteria.

In the numerical implementation, a random number generator determines the outcome of the measurement. Assuming that the result λ_m was selected by the random number generator, the wave function is replaced by the projected, normalized wave function

$$\boldsymbol{\psi} \to \frac{\hat{\boldsymbol{P}}_m \boldsymbol{\psi}}{\sqrt{\boldsymbol{\psi}^\dagger \hat{\boldsymbol{P}}_m \boldsymbol{\psi}}}. \tag{5.24}$$

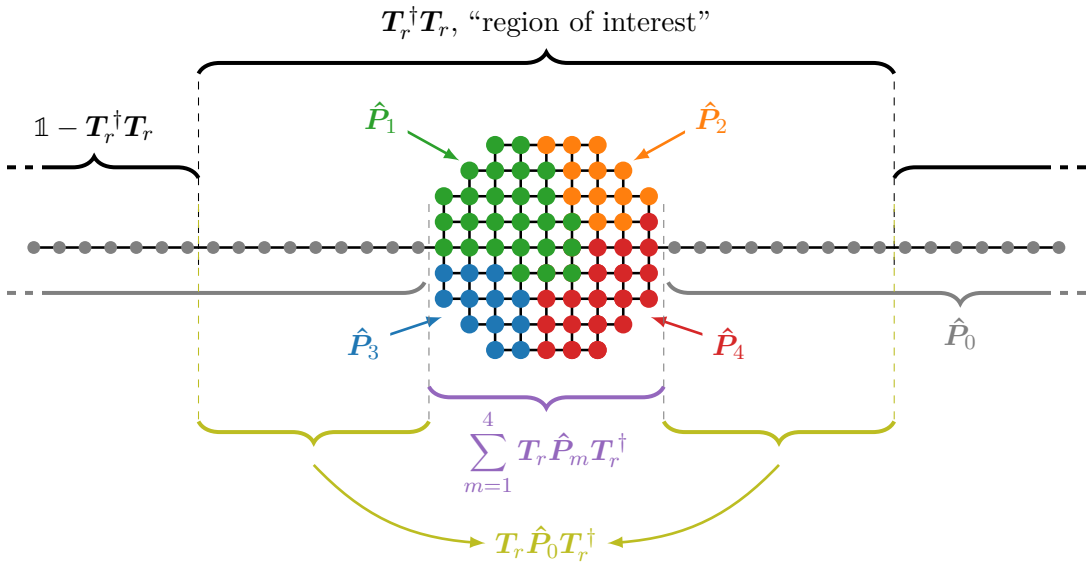
Again we have to evaluate this expression in the reduced site-basis representation. We already constrained the $\hat{\boldsymbol{P}}_m$ such that only one of them projects onto the subspace lying outside the region of interest. For all other $\hat{\boldsymbol{P}}_m$ — those that project onto subspaces lying within the region of interest — it is straightforward to evaluate Eq. 5.24 because the reduced site-basis representation is an exact description of the wave function within the region of interest.

However, for applying $\hat{\boldsymbol{P}}_0$, the reduced site-basis representation does not suffice, because the projected wave function does not necessarily vanish outside the region of interest. The information about the wave function outside of the region of interest is not part of the reduced site-basis representation $\boldsymbol{\psi}$. However, it is contained in its eigenbasis representation $\boldsymbol{\psi}_\mathrm{E}$. The correspondence of Eq. 5.24 given in the energy basis is

$$\boldsymbol{\psi}_\mathrm{E} \to \frac{\left(\mathbb{1} - \boldsymbol{T}_r^\dagger \boldsymbol{T}_r\right) \boldsymbol{\psi}_\mathrm{E} + \boldsymbol{T}_r^\dagger \hat{\boldsymbol{P}}_0 \boldsymbol{T}_r \boldsymbol{\psi}_\mathrm{E}}{\sqrt{1 - \boldsymbol{\psi}_\mathrm{E}^\dagger \left(\sum_{n>0} \boldsymbol{T}_r^\dagger \hat{\boldsymbol{P}}_n \boldsymbol{T}_r\right) \boldsymbol{\psi}_\mathrm{E}}}. \tag{5.25}$$

The projection operators of Eq. 5.24 and 5.25 are visualized in Fig. 5.5. The operator $\mathbb{1} - \boldsymbol{T}_r^\dagger \boldsymbol{T}_r$ performs a projection onto everything but the region of interest, leaving only the information that we cannot access in the reduced site basis. If we then add the result of the projection in the reduced site basis $\boldsymbol{T}_r^\dagger \hat{\boldsymbol{P}}_0 \boldsymbol{T}_r \boldsymbol{\psi}_\mathrm{E}$, we obtain the full energy basis representation of the projected wave function. For the denominator of Eq. 5.25 we apply the same trick we already applied for the probability p_0 and exploit that we can easily calculate all p_m with $m > 0$ and that the sum of all probabilitys equals one.

This allows us to calculate with our tight-binding framework the probabilities of measurement outcomes and the post-measurement projections. To incorporate these quantum measurements into the time evolution introduced in Section 5.2, we need to also analyze the implications of a quantum measurement for the current integrals. During the smooth unitary time evolution these integrals (Eq. 5.11) are well defined. However, when a quantum measurement happens, the wave function changes abruptly. The integral does not capture this change. In the cases in which the projection operators $\hat{\boldsymbol{P}}_m$ with $m > 0$ operate, the effect on the probabilities in the leads is obvious (see Fig. 5.5).



$$\boldsymbol{\psi}_\mathrm{E} \to \frac{\left(\mathbb{1} - \boldsymbol{T}_r^\dagger\boldsymbol{T}_r\right)\boldsymbol{\psi}_\mathrm{E} + \boldsymbol{T}_r^\dagger\hat{\boldsymbol{P}}_0\boldsymbol{T}_r\boldsymbol{\psi}_\mathrm{E}}{\sqrt{1 - \boldsymbol{\psi}_\mathrm{E}^\dagger\left(\sum_{m>0}\boldsymbol{T}_r^\dagger\hat{\boldsymbol{P}}_m\boldsymbol{T}_r\right)\boldsymbol{\psi}_\mathrm{E}}} \qquad \text{(see Eq. 5.25)}$$

Figure 5.5: Overview of the projection operators used to calculate the post-measurement wave function in the reduced site basis for an example system. The operator $\boldsymbol{T}_r\boldsymbol{T}_r^\dagger$ projects onto the reduced site basis: the region of interest; $\mathbb{1} - \boldsymbol{T}_r\boldsymbol{T}_r^\dagger$ projects onto the remaining Hilbert space. The projectors $\hat{\boldsymbol{P}}_{1\ldots4}$ correspond to the possible measurement outcomes and project onto the subspace spanned by the sites drawn in the same color as the operator. Their sum $\sum_{m=1}^{4}\boldsymbol{T}_r\hat{\boldsymbol{P}}_m\boldsymbol{T}_r^\dagger$, therefore, is a projector onto the entire dot. The operator $\boldsymbol{T}_r\hat{\boldsymbol{P}}_0\boldsymbol{T}_r^\dagger$ projects onto the overlap of the region of interest and the space into which $\hat{\boldsymbol{P}}_0$ projects. At the bottom, Eq. 5.25 is reprinted with individual terms highlighted in the respective colors as shown in the sketch.

After the projection, the entire wave function is localized within a region that is part of the region of interest. Thus, when such a measurement result occurs the probability to find the particle in the leads is zero afterwards and the value $\mathcal{Q}_\alpha(t)$ of the current integral has to be discarded. After the measurement, the lower integration bound has to be set to the time of the measurement, such that the integral is zero after the measurement.

In case $\hat{\boldsymbol{P}}_0$ is applied, the wave function is not localized to the region of interest and we know that applying $\hat{\boldsymbol{P}}_0$ does not change the wave function outside of the region of interest (see Fig. 5.5). The charges that have flown into the leads before the projection, as measured by the current integrals, are still meaningful, and have to be properly renormalized. The projection $\hat{\boldsymbol{P}}_0$ preserves the wave function in all leads (see Fig. 5.5) and thus does not affect the ratios of the probabilities to find the particle in different leads. Therefore, the same renormalization factor has to be applied to all current integrals. Because this factor is a normalization factor, it has to be applied also to the wave function in the region of interest. Further, the factor has to be chosen such that before and after the projection, the total probability equals 1,

$$\boldsymbol{\psi}^\dagger\boldsymbol{\psi} + \sum_\alpha \mathcal{Q}_\alpha = a\left(\boldsymbol{\psi}^\dagger\hat{\boldsymbol{P}}_0\boldsymbol{\psi} + \sum_\alpha \mathcal{Q}_\alpha\right) = 1, \tag{5.26}$$

where $\mathcal{Q}_\alpha$ is the integrated probability current of lead α just before the measurement occured, which is the probability to find the particle in lead α. The sums run over all leads and a is the normalization factor to be applied after the projection. The wave function $\boldsymbol{\psi}$ here is a vector in the reduced position basis representation, therefore $\boldsymbol{\psi}^\dagger\boldsymbol{\psi}$ is the probability to find the particle within the region of interest before projection and $\boldsymbol{\psi}^\dagger\hat{\boldsymbol{P}}_0\boldsymbol{\psi}$ is the unnormalized probability to find it there after the projection.

In the numerical framework discussed in this chapter, there is only one unknown variable a in Eq. 5.26. Therefore, we can rearrange the two equations to obtain two different expressions to calculate a:

$$a = \frac{1}{\boldsymbol{\psi}^\dagger\hat{\boldsymbol{P}}_0\boldsymbol{\psi} + \sum_\alpha \mathcal{Q}_\alpha} \tag{5.27}$$

$$= \frac{1}{\boldsymbol{\psi}^\dagger\hat{\boldsymbol{P}}_0\boldsymbol{\psi} + 1 - \boldsymbol{\psi}^\dagger\boldsymbol{\psi}}. \tag{5.28}$$

Analytically, both expressions are of course identical. In a numerical context, however, they are *not*. Importantly, Eq. 5.27 contains the integrated probability currents $\mathcal{Q}_\alpha$, whereas Eq. 5.28 completely avoids using $\mathcal{Q}_\alpha$ for the calculation of a, which makes a significant difference for the propagation of numerical errors. The numerical time integration, which is necessary to calculate the $\mathcal{Q}_\alpha$, leads to an integration error which depends on the size of the time steps. Using smaller time steps improves the accuracy of the numerical integrals at the cost of a longer calculation such that a trade-off has to be chosen. Employing Eq. 5.28 for renormalization well conserves the total probability, no matter how large the numerical integration errors are. However, this procedure simply covers up these errors and makes it difficult to track them. In contrast, Eq. 5.27 accumulates the

integration errors of the total probability that are caused by the renormalization step. The resulting deviation of the total probability from 1 therefore measures the total error introduced by the numerical integrals. Thus, checking for the probability conservation allows to evaluate the numerical accuracy of the calculated time evolution. The solver developed in this thesis offers both methods via the `renormalizationRule` parameter. The use of Eq. 5.27 corresponds to `renormalizationRule='strict'`, and the behavior given by Eq. 5.28 is selected with `renormalizationRule='damp␣errors'`. For the calculations shown in this chapter, it is particularly important to monitor the numerical errors, the rule `'strict'` is therefore employed in all calculations.

Figure 5.6 shows results obtained for quantum states that evolve by the combination of unitary time evolution and stochastic occurrence of quantum measurements. The plots show the probabilities and the probability conservation errors calculated with the previously described algorithms. Initially, the wave packet is placed within the region of interest. After the time evolution, the wave packet resides within the two leads. The probability to find it in the region of interest is small. As explained previously, the deviation of the total probability from unity is an important quantity that captures numerical errors introduced by the numerical diagonalization of $\hat{\boldsymbol{H}}$, the numerical current integrals and the numerical implementation of the quantum measurement. The numerical diagonalization causes a negligible error, close to the floating point resolution. Figure 5.6 reveals that, as anticipated, the numerical integration errors and their effect on the renormalization dominate the total error; especially, if the time axis is discretized too coarsely. With sufficiently fine time steps, however, the total error can be reduced to well below 10^{-4}.

To conclude, this section presented how to numerically evaluate quantum measurements, given the eigenbasis and the reduced site-basis representation of a wave function and the probabilities and projection operators corresponding to an observable. Required conditions imposed on the observable are that it measures a position-like quantity, that is, that it commutes with the position operators, and that all its eigenvalues corresponding to sites that are not located within the region of interest are degenerate. In other words, among the projectors that are applied after a measurement of $\hat{\boldsymbol{O}}$ there must be only one that projects onto the subspace outside of the region of interest. Interrupting the unitary time evolution (Section 5.2) with quantum measurements in random time intervals allows us to calculate the transmission and reflection probabilities of wave packets under the influence of decoherence.

5.4 Benchmarking the Stochastic Model Against the Master Equation

As mentioned in Section 4.3, for any stochastic Schrödinger equation there is an equivalent Lindblad master equation. For the stochastic Schrödinger equations described in

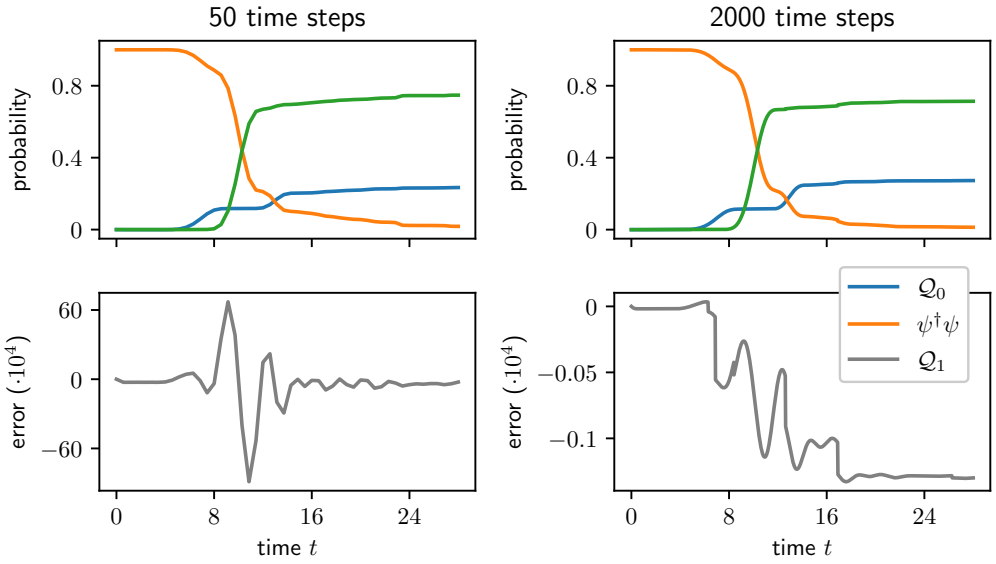


Figure 5.6: Time evolutions of the probabilities (upper row) and the probability conservation error (lower row) calculated with two different time step sizes (left and right column). The system and wave-packet parameters are identical to those presented in Fig. 5.2. During the evolution, an observable is measured at random times with a mean interval of 3.5 time units. The observable has two eigenvalues, one corresponding to a projection onto the site at $x = y = 0$, the other one corresponding to a projection onto all other sites. The integrated probability currents $\mathcal{Q}_0$ and $\mathcal{Q}_1$ reflect the probability to find the particle in the left or the right lead, respectively. The probability to find the particle in the structure in the center is $\boldsymbol{\psi}^\dagger\boldsymbol{\psi}$, with $\boldsymbol{\psi}$ given in the reduced site basis. In the results of the numerical calculation, the sum of these three probabilities deviates from 1. This difference, multiplied by 1×10^4, is plotted in the lower row.

this chapter it reads

$$\delta_t \hat{\boldsymbol{\rho}} = -\frac{i}{\hbar}\left[\hat{\boldsymbol{H}}, \hat{\boldsymbol{\rho}}\right] + \Gamma \sum_m \left(\hat{\boldsymbol{P}}_m \hat{\boldsymbol{\rho}} \hat{\boldsymbol{P}}_m^\dagger - \frac{1}{2}\left(\hat{\boldsymbol{\rho}} \hat{\boldsymbol{P}}_m^\dagger \hat{\boldsymbol{P}}_m + \hat{\boldsymbol{P}}_m^\dagger \hat{\boldsymbol{P}}_m \hat{\boldsymbol{\rho}} \right) \right), \tag{5.29}$$

with the Hamiltonian $\hat{\boldsymbol{H}}$ the projection operators $\hat{\boldsymbol{P}}_m$ and the system-bath coupling rate Γ. Whereas the stochastic Schrödinger equation describes the time evolution of a wave function, a master equation describes the time evolution of the density operator. On a tight-binding lattice with N_s sites, wave functions are given by vectors of size N_s. Density operators, represented by matrices with N_s^2 entries, require a computer memory that is by a factor of N_s larger than that required by wave functions. Further, the optimizations shown in the previous sections are not applicable to the Lindblad master equation. The solution of the master equation therefore requires the treatment of the full geometry, including the extremely long leads. This limits the applicability of the Lindblad master equation to small systems and moderate time scales.

The well tested and commonly used solvers for the Lindblad master equation offered, for example, by the `QuTiP` python package, are valuable benchmark tests for the solver developed in this thesis. The results of such benchmark calculations are shown in Fig. 5.7. The figure presents transmission probabilities calculated for three different systems using both the stochastic Schrödinger equation solver developed in this thesis, and the Lindblad master equation solver of the `QuTiP` python package. The error bars indicate the deviation of the sum of the transmission and reflection probabilities from unity. For the Lindblad calculations, each of the leads was chosen to be 150 sites long, which limits the maximum evolution time to 250 time units before reflections from the lead ends occur. Especially for the system shown in Fig. 5.7e, the wave packet dwells in the structure in the center for a comparably long time and has not completely left the structure after the 250 time units. This leads to the large error bars in the Lindblad calculation of this geometry.

Because the calculation costs of the the new stochastic Schrödinger equation solver scales better with the system size than the costs of the Lindblad equation solver, the treatment of systems with much longer leads is now feasible. For the systems shown in Figs. 5.7a and 5.7c, the leads were 2500 sites long, for the system shown in Fig. 5.7e length was 1000 sites. With these leads, the time evolution was run for over 900 time units without any reflections occurring at the lead ends. Error bars are plotted for the stochastic Schrödinger equation data in the same way as for the Lindblad data. However, they are not visible because the errors are $<0.3\,\%$ for the systems shown in Figs. 5.7a and 5.7c and $<1\,\%$ in the system shown in Fig. 5.7e.

The examples shown here demonstrate that results obtained with the newly implemented solver accurately agree with the results obtained by direct integration of the Lindblad master equation. The examples demonstrate this agreement for various geometries and for decoherence strengths covering multiple orders of magnitude.

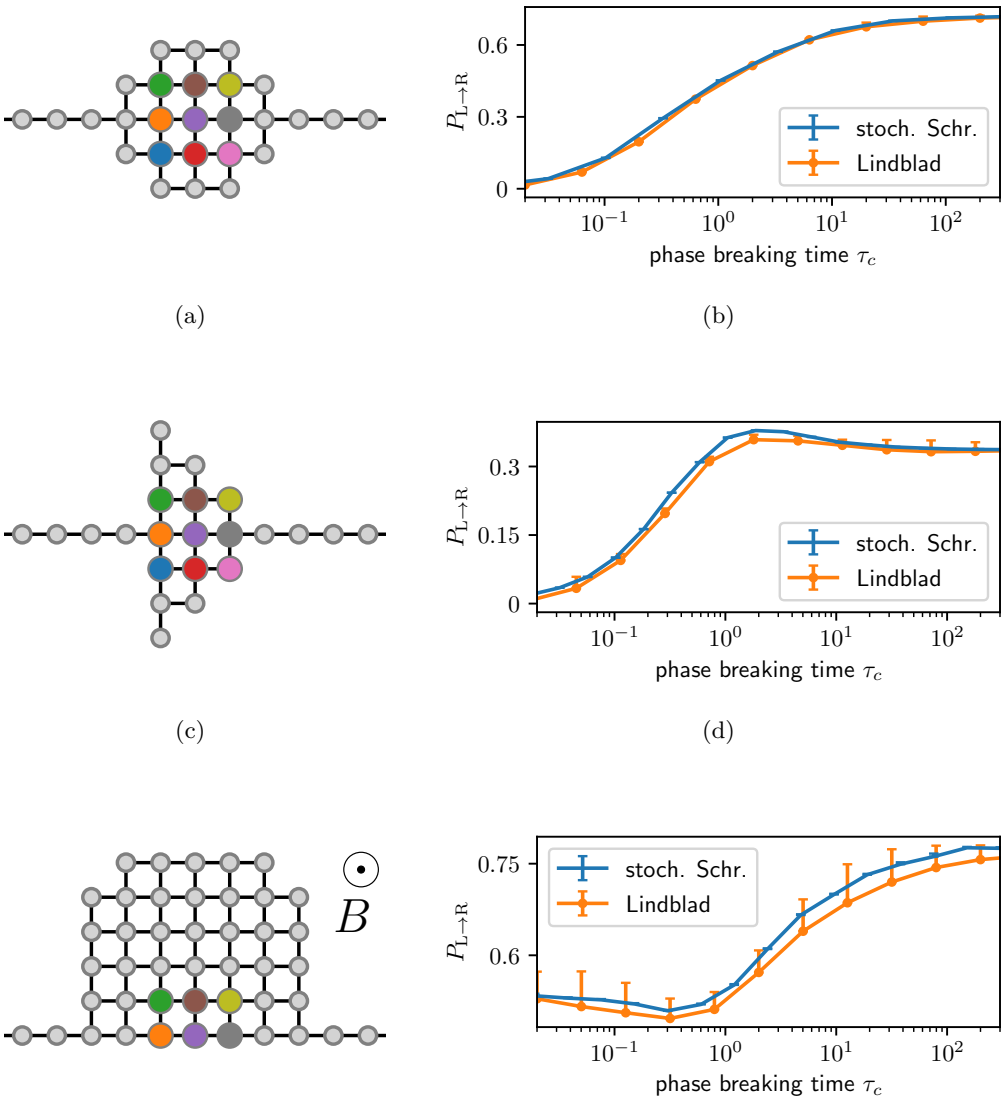


Figure 5.7: Plots of the transmission probabilities of three two-lead devices calculated as a function of decoherence time with both the stochastic Schrödinger equation and the Lindblad equation. The leads continue infinitely to the left and right. Each color of the colored sites represents a distinct eigenvalue of the observable used to model the decoherence. All the remaining sites (grey), including the infinite leads, correspond to a common eigenvalue. The shown systems are (a,b) a symmetric quantum dot, (c,d) an asymmetric quantum dot and (e,f) an asymmetric quantum dot with an applied magnetic field. (b,d,f) The transmission probabilities calculated with the two methods agree well within the numerical errors.

5.5 Decoherence-Induced Nonreciprocal Transmission Probabilities

The previous sections of this chapter presented a method to efficiently calculate the transmission and reflection probabilities for wave packets in the presence of decoherence effects. In this section, this method will be applied to show that the two-terminal conductance reciprocity and magnetic field symmetry presented in Chapter 3 do not necessarily apply if the dynamics is nonunitary. If the wave-packet scattering delays τ_{mn} are nonreciprocal, and if the decoherence rate is comparable to $1/\tau_{mn}$, then the wave packet transmission probability is also nonreciprocal. The following examples demonstrate this nonreciprocity, which is found in a well defined window of the decoherence strength.

5.5.1 Potential Barriers

Figure 5.8 presents an asymmetric potential barrier comparable to those discussed earlier. However, instead of the continuum systems discussed in Chapter 3, this potential barrier is implemented in a tight-binding model, so that the stochastic Schrödinger equation can be readily evaluated. The tight-binding lattice is given by a chain of sites. The electrostatic potential is zero everywhere except for the three sites at $x = -1$, $x = 0$ and $x = 1$ that form the barrier (Fig. 5.8a). As Fig. 5.8b shows, the dispersion relation of the infinite chain of sites is given by a cosine-shaped function instead of the parabola known from the continuum case. Because the dispersion relation is 2π periodic and an even function of k, all information is contained within the $[0, \pi)$ interval shown in the plots.

Figures 5.8c and 5.8d show the properties of the potential barrier derived from the scattering matrix, namely the transmission and reflection probabilities and the wave-packet scattering delays. The probabilities are strictly reciprocal as required by unitarity. Similarly to the continuum case, the transmission probability is low for small energies and increases with energy until it is finally close to unity for high energies. However, due to the nonparabolic dispersion, the transmission probability decreases again for momenta close to the Brillouin-zone boundary $k = \pi$. Because the barrier is time-reversal symmetric but asymmetric with respect to lead-exchange operator $\hat{\boldsymbol{\mathcal{P}}}$, the transmission wave-packet scattering delays are identical. The reflection delays are nonreciprocal, however: $\tau_{21} = \tau_{12}$ and $\tau_{11} \neq \tau_{22}$.

To calculate the transmission probabilities in the presence of decoherence, we calculate time evolutions of gaussian wave packets, which requires to specify the wave-packet parameters: the central momentum k_0, the momentum spread σ_k and the initial position x_0. For this first example, the parameters are chosen as $k_0 = \pm\pi/3$, $\sigma_k = 1/6$ and $x_0 = \pm 14$. The parameters are not fine tuned and virtually any other choice of the wave-packet parameters yields similar results, which is shown in later examples.

In Fig. 5.8, the k-range highlighted in green indicates the range that is significant for wave packets with the specified parameters. The solid green lines mark $k_0 = \pi/3$ and the corresponding energy $E_0 = 3$. The green highlight spans $k_0 \pm \sigma_k$. We therefore estimate such wave packets to be transmitted by $\approx 60\,\%$ and expect the wave-packet reflection

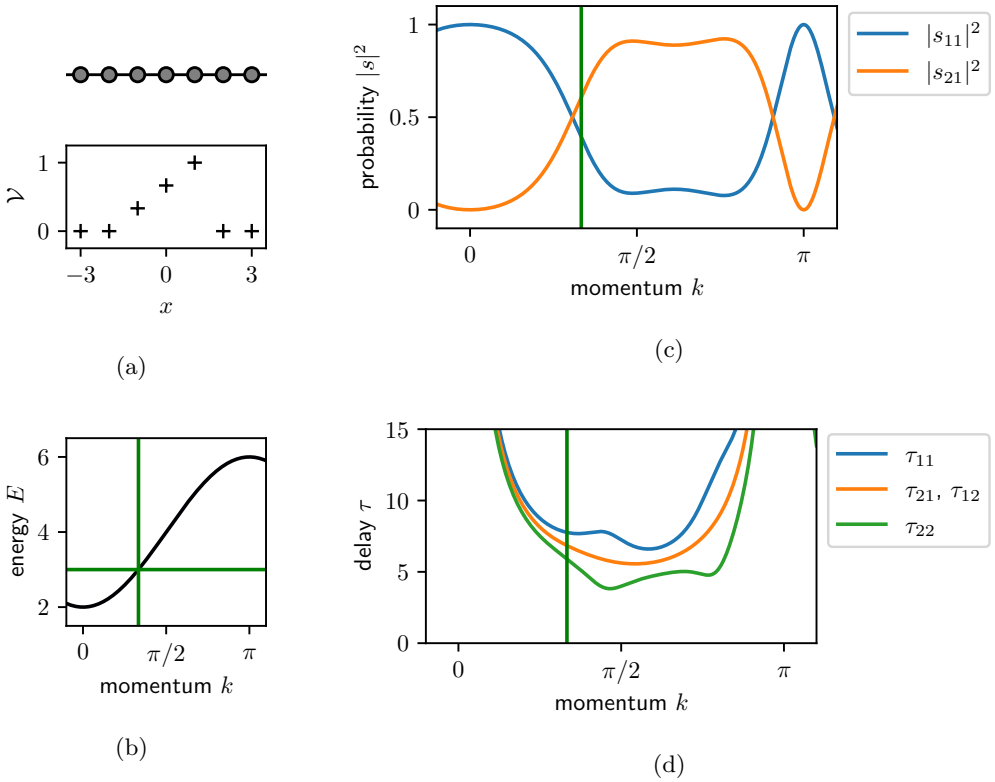


Figure 5.8: Properties of the tight-binding model of the asymmetric potential barrier. The green cursor lines indicate the parameter range relevant for the wave-packet calculations described later in this section. (a) The lattice of the system is given by an one-dimensional chain of sites. The electrostatic potential is shown in the plot. (b) The calculated dispersion relation of the system is given by a cosine function. (c) Plots of the transmission and reflection probabilities as a function of k. (d) Three distinct wave-packet scattering delays τ exist for this system. The reflection delays are nonreciprocal due to the asymmetry of the barrier.

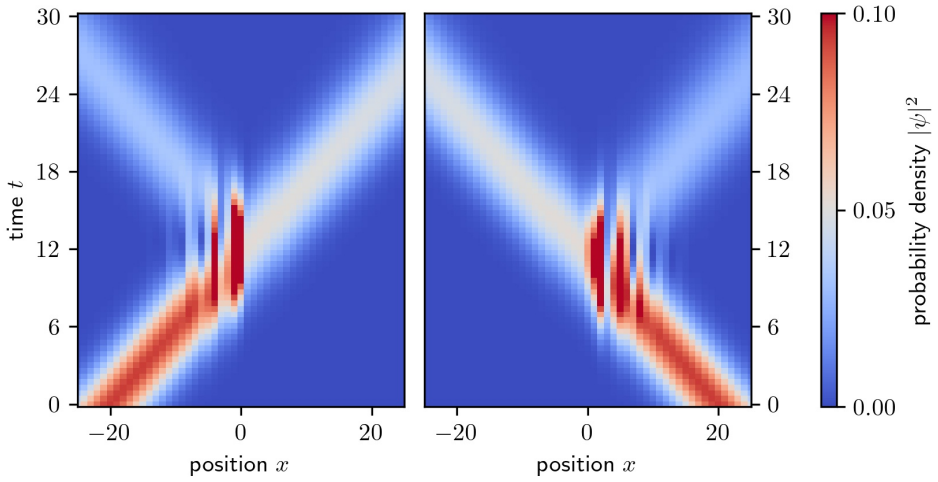
time delays to differ by a few time units. Figure 5.9 shows the time evolutions of the probability density of such a wave packet incident from the left (lead 1) and from the right (lead 2) of the barrier. Plotting the total reflected probability as a function of time (Fig. 5.9b) confirms that the reflected wave packet on the left side is $\delta t \approx 2$ time units delayed, as compared to the wave packet reflected on the right side.

Up to this point, all results are obtained with the unitary time evolution generated by the ordinary Schrödinger equation, completely analog to Chapter 3. Next, the stochastic Schrödinger equation is employed to study the effect of decoherence on the transport in this system. For this, an observable with four eigenvalues is used; three eigenvalues corresponding to the measurement results "particle found at $x = -1$", "found at $x = 0$" and "found at $x = 1$". The fourth eigenvalue corresponds to the result "particle is somewhere else". The corresponding projectors are given by the three projection operator $\hat{\boldsymbol{P}}_{1\ldots3}$ that project onto the respective one of the three sites and a fourth projector $\hat{\boldsymbol{P}}_0$ that projects onto the entire remaining Hilbert space. The measurement outcomes corresponding to the projectors projection operator $\hat{\boldsymbol{P}}_{1\ldots3}$ localize the particle, completely erase the momentum information, and break any coherent superposition. The decoherence strength is parametrized by the mean time between two measurements τ_c.

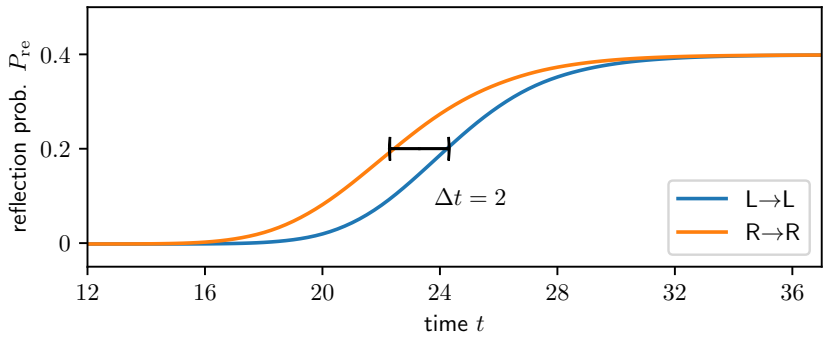
With the resulting stochastic Schrödinger equation, every calculated time evolution is a realization of the underlying stochastic process. Two time evolutions starting with the same wave packet state may therefore end up in completely different final states. To determine the transmission probability of a wave packet, we therefore have to calculate many realizations of the time evolution and average the results. However, not only the average transmission probability of the multitude of time evolutions is of interest for us, the full statistics of possible final states for individual wave packets also contains valuable information about the dynamics. To illustrate this point, Fig. 5.10 shows normalized histograms of the transmission probabilities for the two transmission directions $P_{\mathrm{R}\to\mathrm{L}}$ and $P_{\mathrm{L}\to\mathrm{R}}$ as a function of the mean time between to measurements τ_c, which is a measure of the inverse of the decoherence strength. For each value of τ_c, the time evolution was run 3000 to 5000 times.

Let us first look at the two limits of very large and small τ_c, for which the histograms have a simple structure: For $\tau_\mathrm{c} > 10^3$, the quantum measurements occur so rarely that they hardly affect the transport. Almost all time evolutions end with a transmission probability of $P_{\mathrm{R}\to\mathrm{L}} = P_{\mathrm{L}\to\mathrm{R}} \approx 0.6$, which reproduces the standard unitary behavior. For $\tau_\mathrm{c} < 10^{-1}$ the histograms for both $P_{\mathrm{R}\to\mathrm{L}}$ and $P_{\mathrm{L}\to\mathrm{R}}$ are peaked exclusively at the probabilities 0 and 1. This implies that all time evolutions end with the wave packet either being completely transmitted or completely reflected, which is the behavior of a classical particle.

In the limit of $\tau_\mathrm{c} \to 0$, the transmission probabilities for both directions tend to zero. For very small τ_c, the quantum measurements are so frequent that only a vanishing fraction of the wave packet can enter one of the three sites $x = -1$, $x = 0$ or $x = 1$ between two measurements. If a quantum measurement occurs, the probability to find the particle at one of these sites is therefore negligibly small and the measurements never find the particle at these sites. The resulting projection nulls the value of the



(a)



(b)

Figure 5.9: (a) Colormaps showing the unitary time evolution of the probability density for a wave packet starting on the left and on the right of the barrier presented in Fig. 5.8. The transmission and reflection probabilities, as well as the slightly time-shifted reflected wave packets match the expectations based on the scattering matrix (Fig. 5.8). (b) Plot of the total reflected probability P_{re} as a function of time highlights the time shift between the two reflected wave packets.

post-measurement wave function at these sites. This effect resembles the quantum Zeno effect [106], which captures that frequent measurements prevent a quantum state from transitioning to another state. Here, the sites $x = -1$, $x = 0$ and $x = 1$ can never be populated if the measurement of the site population is sufficiently frequent. Vice versa, the particle would not be able to leave the sites, if it was initially prepared being localized on one of these sites. For our transport calculation, this of course implies that the particle cannot cross the barrier and is always reflected into the lead from which it came, which causes $P_{\mathrm{L}\to\mathrm{R}}$ and $P_{\mathrm{R}\to\mathrm{L}}$ to vanish for small τ_c.

Between these two regimes of very large and small τ_c, in which the histograms are peaked at only one or two probabilities, there is a transition regime in which the histograms display a rich structure. In the range $10^{-1} < \tau_\mathrm{c} < 10^3$, several peak-like features in the histograms are observed, which change their shape with τ_c. The distribution of $P_{\mathrm{L}\to\mathrm{R}}$ and $P_{\mathrm{R}\to\mathrm{L}}$ now comprises almost the full range between 0 and 1. The newly appearing histogram peaks originate from time evolutions in which a measurement localized the particle onto one of the three sites. This transition regime occurs when the mean time between two measurements τ_c is comparable to the wave-packet scattering delay (Fig. 5.8d). During the time span that the wave packet needs to pass the barrier, only a few quantum measurements occur. In this case, the fine structure of the histogram in the transition regime for the $\mathrm{L} \to \mathrm{R}$ direction differs much from the features appearing in the $\mathrm{R} \to \mathrm{L}$ direction. This can be understood by recalling that the wave-packet scattering delays differ for the two directions. Therefore, the condition that τ_c is comparable to the wave-packet scattering delay is direction dependent.

Beyond the histograms being different, also the averaged transmission probabilities differ depending on the transmission direction. This may be difficult to discern from the red curves in Fig. 5.10. Figure 5.11 therefore presents the difference of these two red curves as a function of τ_c. Clearly, the transmission probabilities for both directions are identical for very large and very small τ_c, indicating that the transport is reciprocal. In the transition regime, however, the transport is nonreciprocal, the $\mathrm{L} \to \mathrm{R}$ direction has a higher transmission probability than the $\mathrm{R} \to \mathrm{L}$ direction. This is a central result of this thesis.

To demonstrate that this effect is indeed not a numerical artifact of the model or the algorithm, Fig. 5.11 also shows the results obtained with a symmetric potential barrier but otherwise identical parameters. In the case of the symmetric barrier, the transmission probability is reciprocal within the stochastic noise margin for all τ_c, revealing that the observed nonreciprocity for the other system is in fact induced by the barrier asymmetry.

This occurrence of nonreciprocal transmission probabilities if the inverse decoherence rate is comparable to the time scale of wave-packet scattering is not limited to the potential barrier presented in this section. It is a general property of systems with appropriately broken symmetries. To illustrate this astounding behavior, the following sections will discuss results obtained for other geometries and parameter choices.

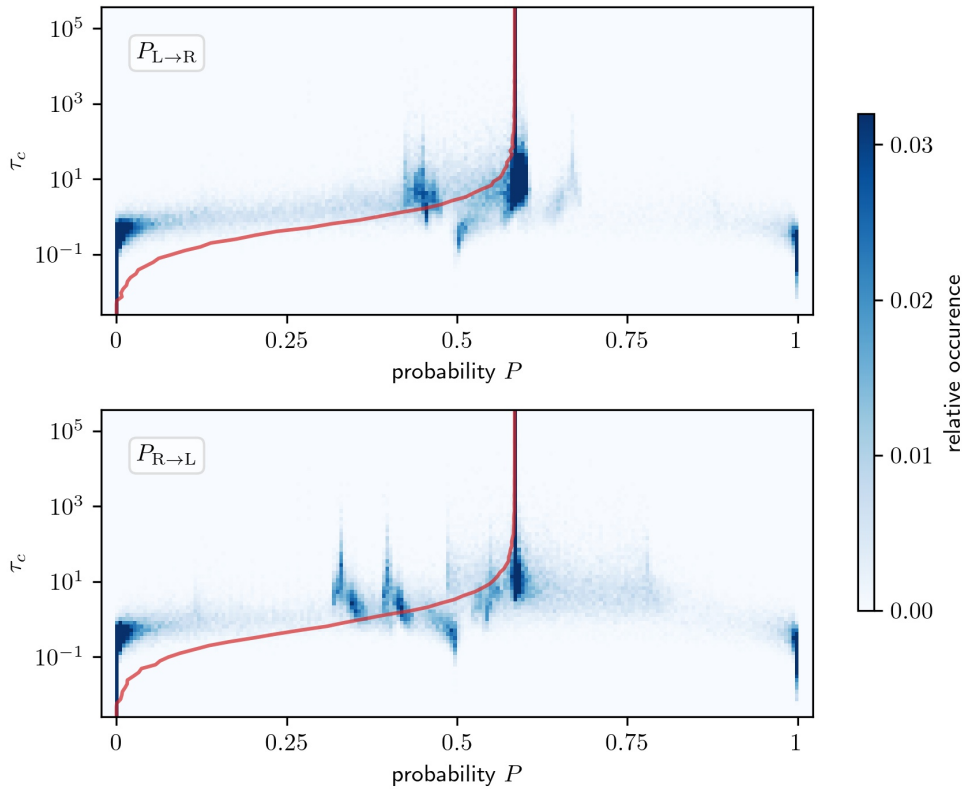


Figure 5.10: Colormap representation of the transmission probability histograms for both transmission directions as a function of the mean time between two measurements τ_c. Generally, wave packets end in coherent superpositions of being transmitted and reflected after their time evolution. This ratio is plotted on the abscissa. The color indicates the statistical occurrence of each superposition ratio. The total average taken for a given τ_c yields the overall expectation value of the transmission probability, which is shown by the red curves.

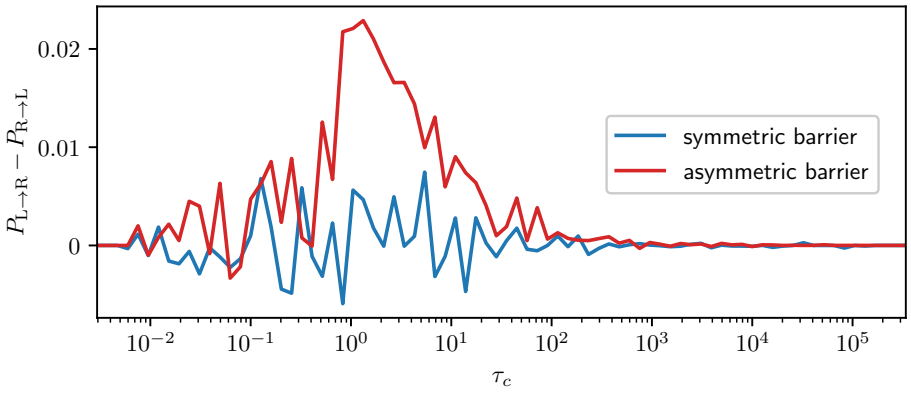


Figure 5.11: Plots showing calculated differences of the averaged transmission probabilities as a function of the decoherence strength parameter τ_c. This difference is genereally zero for small or large enough values of τ_c. For the asymmetric barrier, the wave-packet scattering delays of both directions differ (see Fig. 5.8d). If τ_c is comparable to this difference, the transmission probabilites for both directions are not anymore equal. A comparison with the symmetric barrier confirms that this is indeed caused by the barrier asymmetry.

5.5.2 Quantum Dots

Numerous transport experiments involving quantum dots made from various materials in a variety of geometries are reported in the literature. Many of these studies are interested in the symmetries of the transport coefficients [27, 28, 107–111]. In the devices used in those experiments, typically two or more leads are attached to the so-called "quantum dot". Strictly speaking, the underlying concept of a quantum dot — a zero-dimensional structure featuring sharp, quantized energy levels — does then not apply anymore. A quantum dot with attached leads has eigenstates at any given energy. To avoid the association with zero-dimensionality, these devices are also called electron billiards. In the following, the term quantum dot will refer to structures with sizes comparable to the particle wavelength with leads attached to them. The quantum dots described here are not meant to quantitatively reproduce experimental results, but to investigate whether the results obtained in the previous section also apply to these 2D geometries.

This section will discuss three different geometries of quantum dots. First, a quantum dot that is symmetric with respect to lead exchange and time reversal ("symmetric quantum dot", Figs. 5.12a and 5.12b). Second, a dot that is asymmetric with respect to lead exchange but time-reversal symmetric ("$\hat{\boldsymbol{\mathcal{P}}}$-asymmetric dot", Figs. 5.12c and 5.12d). Third, a structure that is symmetric with respect to lead exchange but time-reversal asymmetric ("$\hat{\boldsymbol{\mathcal{T}}}$-asymmetric dot", Figs. 5.12e and 5.12f). These three quantum dot geometries have already been shown in Figs. 5.7a, 5.7c and 5.7e, where the systems

served as benchmarks to compare the stochastic Schrödinger equation and the Lindblad master equation. The properties of these quantum dots as unitary systems without decoherence are displayed in Figure 5.12. The transmission and reflection probabilities, as well as the wave-packet scattering delays follow the anticipated symmetries.

Owing to the nonreciprocal wave-packet scattering delays for the asymmetric dots, we again expect nonreciprocal wave-packet transmission probabilities at appropriate decoherence strengths. To investigate whether this is indeed the case, the transmission and reflection probabilities for wave packets were calculated as a function of the decoherence strength employing the stochastic Schrödinger equation. The observable used in these calculations to model decoherence is identical to the observable described in Section 5.4: It features nine eigenvalues corresponding to the particle being located at the site in the origin $x = 0$, $y = 0$ or at one of the eight sites surrounding the origin. The tenth eigenvalue corresponds to the particle residing at any of the remaining sites. The expected nonreciprocity is indeed obtained in a well defined window of τ_c. The results of the calculation shown in Fig. 5.13. As the figure clearly reveals, for the $\hat{\boldsymbol{\mathcal{P}}}$-asymmetric dot, the nonreciprocity is comparable to the behavior of the asymmetric potential barrier. For the $\hat{\boldsymbol{\mathcal{T}}}$-asymmetric dot, however, the nonreciprocity flips sign at $\tau_\mathrm{c} \approx 5 \cdot 10^{-1}$. At $\tau_\mathrm{c} \approx 10^{-1}$, the R $\to$ L transmission probability is larger than the L $\to$ R transmission probability, at $\tau_\mathrm{c} \approx 10^{1}$ it is vice versa.

The calculations therefore provide evidence that asymmetry of the devices manifests itself as a difference of the transmission probabilities $P_{\mathrm{L}\to\mathrm{R}} - P_{\mathrm{R}\to\mathrm{L}}$. This is a remarkable result. Comparing these transmission probabilities $P_{\mathrm{L}\to\mathrm{R}}$ and $P_{\mathrm{R}\to\mathrm{L}}$ for wave packets to the transmission probabilities $|s_{12}|^2$ and $|s_{21}|^2$ of plane waves in unitary transport, two important differences stand out: First of all, finite values of the transmission probability difference $P_{\mathrm{L}\to\mathrm{R}} - P_{\mathrm{R}\to\mathrm{L}}$ for the two transmission directions are not allowed in the case of unitary transport, where $|s_{12}| = |s_{21}|$ must hold. Additionally, the second fundamental symmetry of unitary transport, $|s_{12}(\boldsymbol{B})| = |s_{12}(-\boldsymbol{B})|$, does not apply for wave packets. Due to the geometry of the $\hat{\boldsymbol{\mathcal{T}}}$-asymmetric dot (Figs. 5.7e and 5.12e), the effect of a lead exchange on the transport properties is identical to the effect caused by a reversal of the magnetic field. Hence, the behavior of $P_{\mathrm{L}\to\mathrm{R}} - P_{\mathrm{R}\to\mathrm{L}}$ is equivalent to the behavior of $P_{\mathrm{L}\to\mathrm{R}}(\boldsymbol{B}) - P_{\mathrm{L}\to\mathrm{R}}(-\boldsymbol{B})$. Therefore, both, the two-lead conductance reciprocity, as well as the two-lead magnetic field symmetry are not obeyed in nonunitary wave-packet transport.

To elucidate whether the nonreciprocity found is caused by the special choice of the observable used to model decoherence, Fig. 5.13 also shows data that has been calculated using an alternative observable. The blue, orange and red curves were calculated employing the observable mentioned above, with up to nine single-site projection operators and a further projector onto the remaining Hilbert space. The green curve was calculated using only two projection operators, employing an observable characterized by two eigenvalues: One eigenvalue corresponds to the measurement result "particle is found at either of the nine sites with $x \in \{-1, 0, 1\}$, $y \in \{-1, 0, 1\}$", the other eigenvalue corresponds to the result "particle is somewhere else". According to the two eigenvalues, the quantum measurement implied by this observable uses two projection operators.

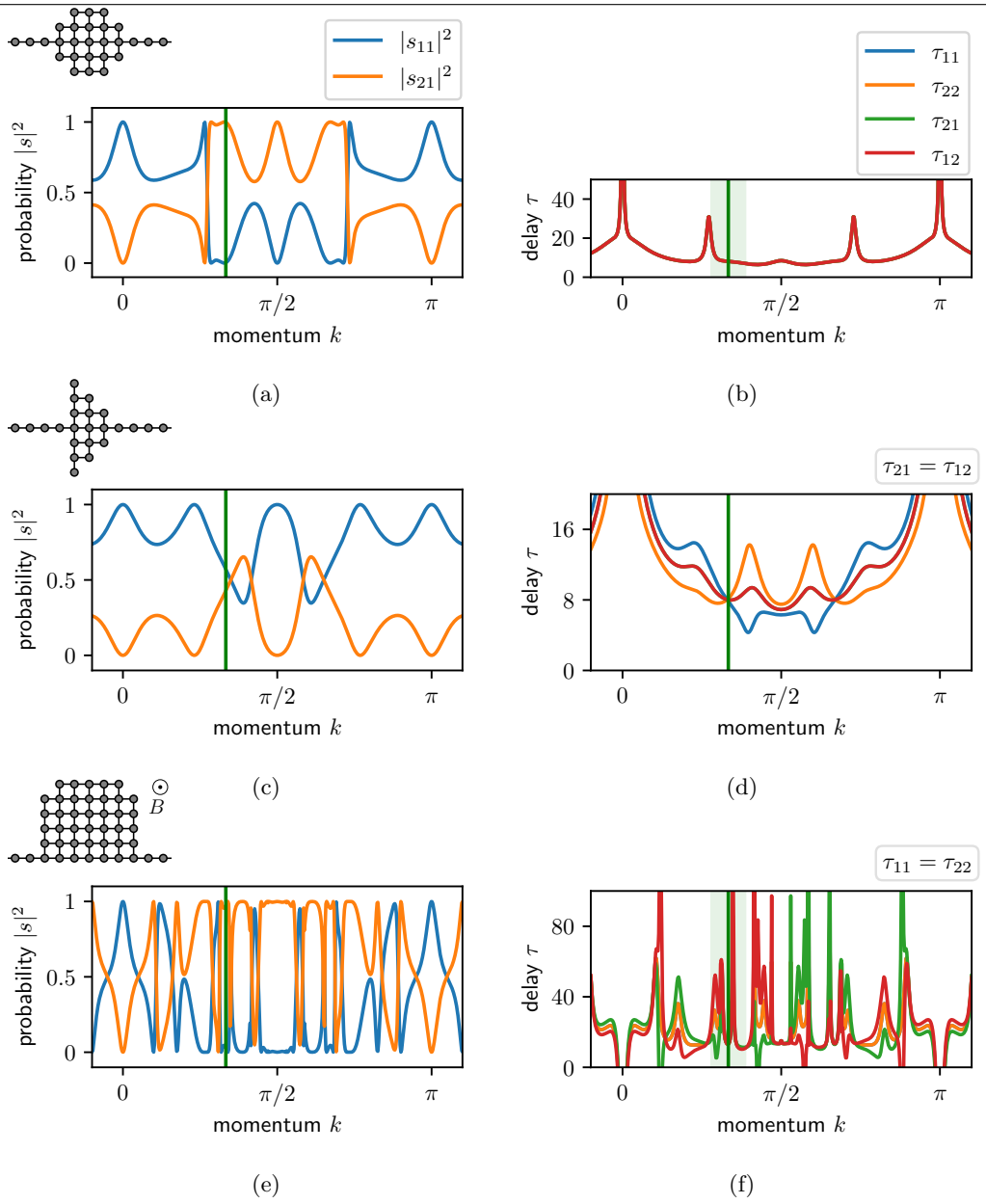


Figure 5.12: Plots of the calculated transmission and reflection probabilities $|s_{mn}|^2$ and the wave-packet scattering delays τ_{mn} as a function of momentum for three quantum dot geometries. Sketches of the quantum dots are given in the upper left corner of the probability plots; larger versions of the sketches are shown in Fig. 5.7. The k-range highlighted in green indicates the range that is relevant for the wave packets considered in the following. (a,b) For the symmetric quantum dot only one graph is visible in the delay plot, because all four delays are identical (see Eq. 3.50). (c,d) The $\hat{\boldsymbol{\mathcal{P}}}$-asymmetric quantum dot is characterized by nonreciprocal reflection delays. (e,f) Similarly, the $\hat{\boldsymbol{\mathcal{T}}}$-asymmetric dot features nonreciprocal transmission delays.

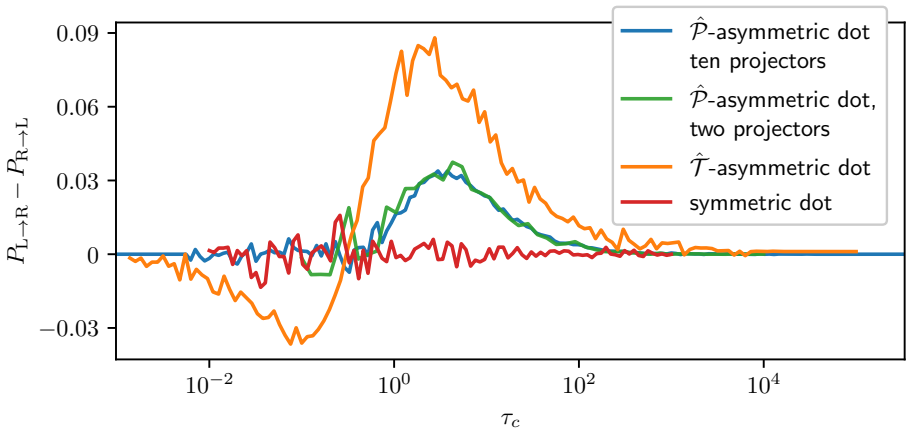


Figure 5.13: Plots showing calculated differences of the averaged transmission probabilities as a function of the decoherence strength parameter τ_c for the quantum dots presented in Fig. 5.12. This difference is zero for sufficiently small or large values of τ_c. For the $\hat{\boldsymbol{\mathcal{P}}}$ and $\hat{\boldsymbol{\mathcal{T}}}$ asymmetric dots, the transmission probabilities for both directions differ for certain τ_c. For the symmetric dot, the transmission probabilities in both directions are equal within the statistical error. The terms "ten projectors" and "two projectors" indicate two different observables used for modeling decoherence.

One operator projects onto the subspace spanned by the nine central sites, the other operator projects onto the entire remaining subspace of the total Hilbert space.

This observable provides a "weaker" position measurement than the observables featuring projectors onto single sites. If the quantum measurement finds the particle in one of the central sites, it still causes a localization of the particle, but here the momentum and phase information is only partially erased. In the site-basis representation of wave functions, the momentum is encoded in the phase relation of the wave function at neighboring sites. The projection onto a single site therefore completely erases any existing momentum information. The projection onto subspaces spanned by multiple sites leaves the phase relation of neighboring sites intact within this subspace. Correspondingly, the extracted position information is less sharp, the result only reports that the particle is located in a space that is several sites large. As the green and blue curves in Fig. 5.13 show, however, applying this "weaker" measurement does not induce a notable difference for the nonreciprocity of the wave packet transport. Apparently the exact degree of the localization is not important in the shown example.

Another key question to be answered is whether the nonreciprocal transmission probabilities found hinge on the specific wave packet parameters used, namely the central momentum k_0 and the momentum spread σ_k. Is the observed nonreciprocal transport canceled if the results are averaged over various choices of these parameters? To answer this question, Fig. 5.14 presents the averaged nonreciprocity for the $\hat{\boldsymbol{\mathcal{P}}}$-asymmetric dot

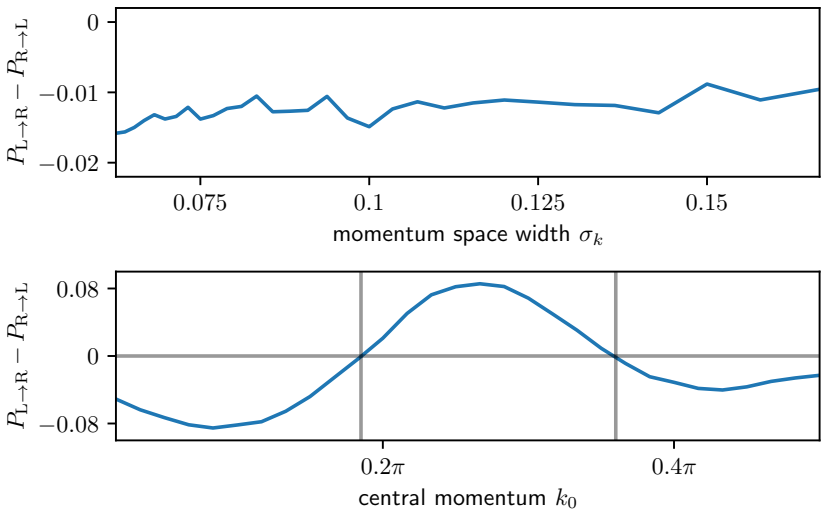


Figure 5.14: Plots showing the averaged nonreciprocity of the wave-packet transport as a function of σ_k and k_0 for the $\hat{\boldsymbol{\mathcal{P}}}$ asymmetric dot. The data underlying these plots has been calculated with the following parameters being varied in the specified ranges: $1 < \tau_\mathrm{c} < 10$, $0 < k_0 < \pi/2$ and $0.06 < \sigma_k < 0.17$. The upper plot shows the results averaged over τ_c and k_0, the lower plot presents the same data averaged over τ_c and σ_k. Remarkably, the sign change of the nonreciprocity at $k_0 \approx 0.36\pi$ coincides with the crossover of $\tau_{11}(k)$ and $\tau_{22}(k)$ (Fig. 5.12d). However, it is not completely clear from this data, if this is causally related or a coincidence, because the second sign change of the nonreciprocity at $k_0 \approx 0.19\pi$ does not correspond to an intersection of the wave-packet scattering delays.

calculated for various τ_c, k_0 and σ_k. Whereas the precise value of $P_{\mathrm{L}\to\mathrm{R}} - P_{\mathrm{R}\to\mathrm{L}}$ obviously depends on the wave packet parameters, finite values of $P_{\mathrm{L}\to\mathrm{R}} - P_{\mathrm{R}\to\mathrm{L}}$ occur for virtually any choice of these parameters.

We also observe a remarkable similarity to the behavior of the wave-packet scattering delays of the $\hat{\boldsymbol{\mathcal{P}}}$-asymmetric dot. The nonreciprocity $P_{\mathrm{L}\to\mathrm{R}} - P_{\mathrm{R}\to\mathrm{L}}$ changes its sign at $k_0 \approx 0.4\pi$ and $k_0 \approx 0.6\pi$, the same momenta at which the two reflection delays of the $\hat{\boldsymbol{\mathcal{P}}}$-asymmetric dot intersect (Fig. 5.12d). This is compatible with the suggested mechanism that the nonreciprocal transmission probabilities are caused by combining nonreciprocal wave-packet scattering delays with decoherence of a suitable strength.

5.5.3 Asymmetric Aharonov-Bohm Interferometer

The nonreciprocity of the wave packet transport in the asymmetric Aharonov-Bohm (AB) interferometer [56] is particularly illustrative. As shown by the model calculations in Chapter 3.6.2, the wave packets pass straight through the interferometer when approaching from one lead, whereas two internal reflections occur within the interferometer when the wave packet approaches from the other one. This behavior is observed if the interferometer arms enclose a quarter of the magnetic flux quantum $h/(4q)$ and for momenta at which the arm-length difference provides for a phase shift of $\pi/2$. In this section, the decoherence model will be applied to such an asymmetric AB interferometer.

The first required step is to find a tight-binding lattice that approximates the continuum system discussed in Section 3.6.2. For this purpose, a generalized interferometer geometry was described via parametric curves, which were piece-wise defined using Gaussian error functions and straight lines. In defining this curve, 9 parameters were left free, allowing for the independent tuning of widths, lengths and curve radii of different parts of the interferometer. For any set of these parameters, the resulting curve can be overlayed with a square lattice of tight-binding sites, which then results in a tight-binding lattice for an interferometer candidate. Given the knowledge that the interferometer that we look for is fully transparent (Section 3.6.2), we can use the transparency of the resulting tight-binding lattice as a fitness function for an iterative optimizer. For this, the set of parameters was varied by a genetic optimizer, which converged to a structure providing for $\approx 90\,\%$ transparency at a momentum of $k = 0.88$ and a magnetic flux density of $\boldsymbol{B} = 10^{-3}$. The lattice of this system is shown in Fig. 5.15. To model decoherence in the interferometers, an observable was applied that acquires which-way information by measuring whether the particle is located in the lower interferometer arm. The corresponding projection operator projects onto the subspace spanned by all sites highlighted blue in Fig. 5.15.

Figure 5.16 summarizes properties of the asymmetric interferometer as derived from the scattering matrix. In contrast to the previous examples, the leads of this system are three sites wide. Correspondingly, a transverse momentum quantum number and multiple channels exist within each lead. As Fig. 5.16a shows, there are three bands in each of the leads, the maximum size of the scattering matrix is therefore 6×6. However, by limiting ourselves to the low energy regime $E < 2$, we effectively use a single band model, which is described by a 2×2 scattering matrix. At these low energies the upper two bands cannot be populated, the single-band description is therefore accurate. All momenta mentioned in this section thus refer to the lowest of the bands shown in Fig. 5.16a.

The transmission and reflection probabilities in this low energy range are shown in Fig. 5.16b. At zero momentum, the transmission probability is zero. With increasing momentum, the transmission probability increases to reach almost unity, to then drop back in an oscillatory fashion to smaller values. Around $k \approx 0.88$ (Fig. 5.16b, green highlight), the transmission probability is close to unity for a comparably large k-range. This behavior is in good qualitative agreement with the continuum interferometer discussed in Section 3.6.2 (compare Fig. 3.13).

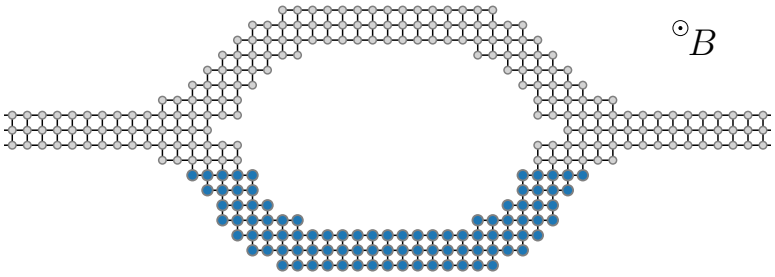
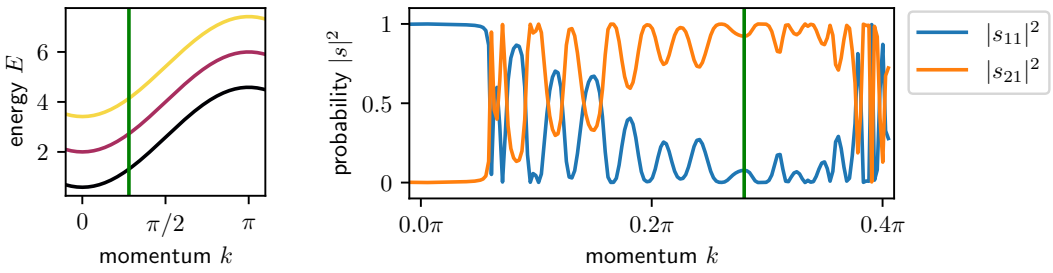


Figure 5.15: Sketch of the tight-binding lattice of the asymmetric AB interferometer. The lower interferometer arm is by one row of sites longer than the upper arm. The structure was found by a genetic optimizer, which varied 9 geometrical parameters to optimize the transparency of the interferometer. The two leads of the device are three sites wide and continue to the left and to the right. The observable used to model decoherence measures if the particle is located on one of the sites highlighted in blue.



(a) (b)

Figure 5.16: Overview of the unitary transport properties of the asymmetric AB interferometer. The wave packet parameters $k_0 = 0.88$ and $\sigma_k = 0.1$ are highlighted by the green region, in analogy to Figs. 5.8 and 5.12. (a) Due to the finite width, each lead supports three bands. By restricting ourselves to the low energy range $E < 2$, the single-band description suffices. (b) The transmission and reflection probabilities of this lower band are in good qualitative agreement with those of the asymmetric AB interferometer discussed in Section 3.6.2.

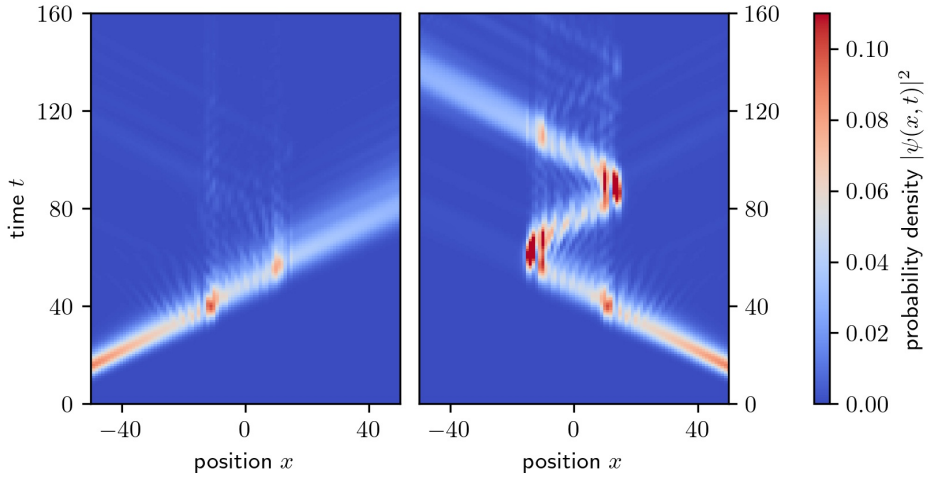
As Fig. 5.17 illustrates, the wave-packet transport also nicely matches the behavior of the continuum system. In the R $\rightarrow$ L direction, the majority of the wave packet easily passes through the interferometer as if it was propagating freely. Minor back reflections occur at $x \approx \pm 10$, where the two interferometer arms split and are rejoined, respectively. These regions, which represent the beam splitters in the system discussed in Section 3.6.2, are obviously not represented by the ideal beam-splitter scattering matrix, nevertheless they approximate this behavior sufficiently well. In the L $\rightarrow$ R direction, the majority of the wave packet is reflected twice within the interferometer before leaving the system, as originally suggested in [56]. Again, deviations from the ideal beam-splitter behavior of the regions around $x \approx \pm 10$ lead to minor back reflections.

Figure 5.17b points out the time delay between the wave packet transmitted in L $\rightarrow$ R and R $\rightarrow$ L directions. The plotted transmission probability is obtained by integrating the probability density $|\psi(x,t)|^2$ of the wave packet time evolution along all $x > 20$ or $x < -20$, respectively. Except for the small additional steps at $t \approx 120$ and $t \approx 220$ observed in the slower R $\rightarrow$ L direction, the time-dependent transmission probability in the slower direction is a time-shifted twin of the faster direction.

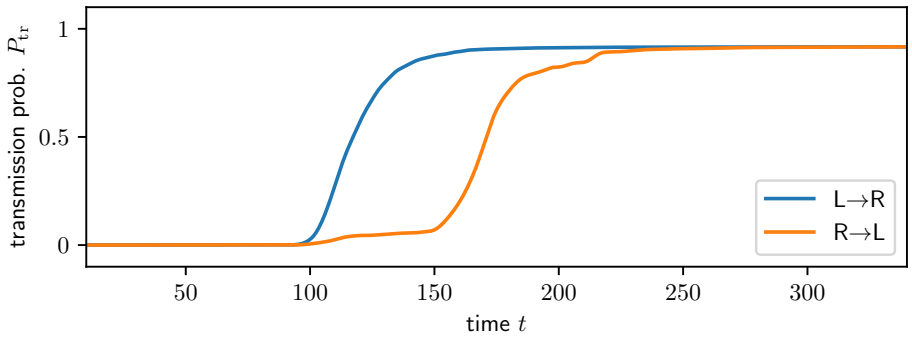
The transmission probability of AB interferferomers is of course characterized by the two-path interference. Obtaining which-path information suppresses the interference and therefore is expected to have a large effect on the total transmission probabiltiy. For this reason, the observable that is used to model decoherence in this example is chosen to distinguish between the two interference paths (Fig. 5.15). The observable features two distinct eigenalues, thus the quantum measurement has two different outcomes: either the particle is found in the lower interferometer arm, or somewhere else.

Owing to the dwell-time difference for the two transmission directions, the probability that a quantum measurement occurs while the wave packet is in a fragile superposition state between upper and lower arm is expected to be direction dependent. In the slower R $\rightarrow$ L direction, the wave packet is more sensitive to decoherence and the effects on the total transmission probability are hence expected to set in at larger mean time between two measurements τ_c, than for the faster L $\rightarrow$ R direction. In Fig. 5.18a, the transmission probability histograms are shown as a function of τ_c. For further explanations of the fine structure displayed in the figure, see the analogous Fig. 5.10 and the related text.

For large τ_c, the unitary quantum limit is observed. Here, the transmission probability is independent of τ_c. For $\tau_c < 10^3$, the effects of decoherence in the transmission of wave packets become evident. As observed before in Section 5.5.1, the histograms in the unitary limit are peaked at one sharp probability, in the transition regime this peak broadens accompanied by the possible formation of side peaks. In this example, the total transmission probabilities of both directions decrease monotonously as the decoherence sets in. This is anticipated, as the interferometer is designed to have a high transmission probability in the unitary limit and any suppression of coherent transmission is likely to reduce the transmission probability. Also in line with the expectations, this effect of decoherence is stronger in the slow R $\rightarrow$ L direction than in the fast L $\rightarrow$ R direction at a given τ_c. Figure 5.18b shows the difference of the two transmission probabilities. In the transition regime the transition probability in the L $\rightarrow$ R is higher than in the

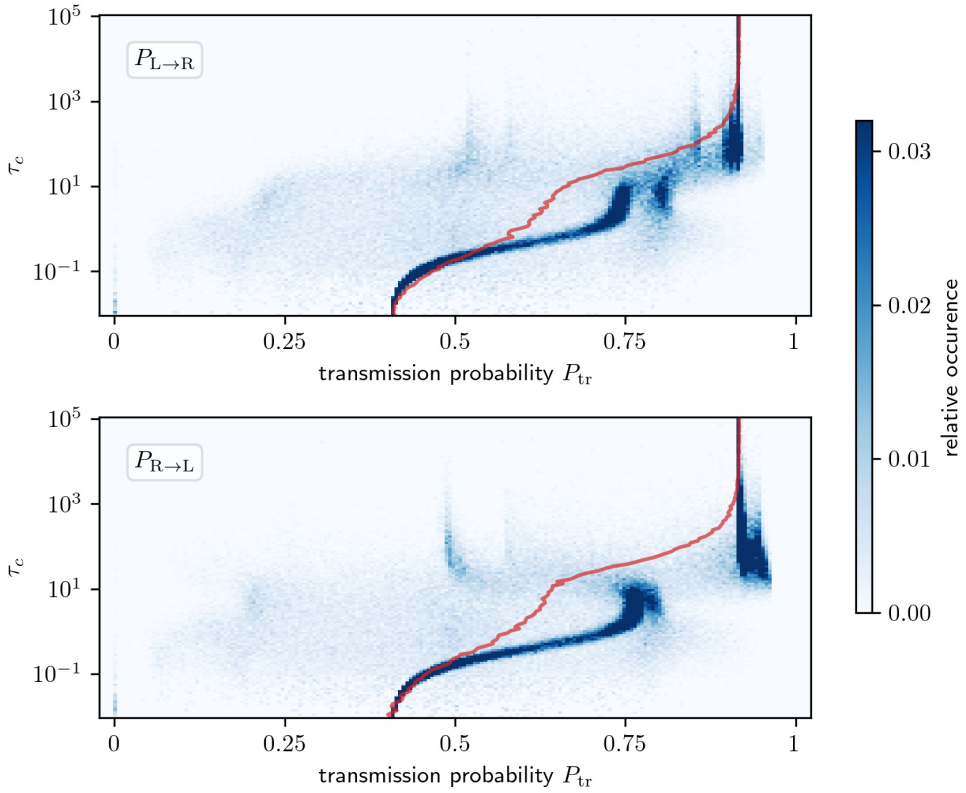


(a)

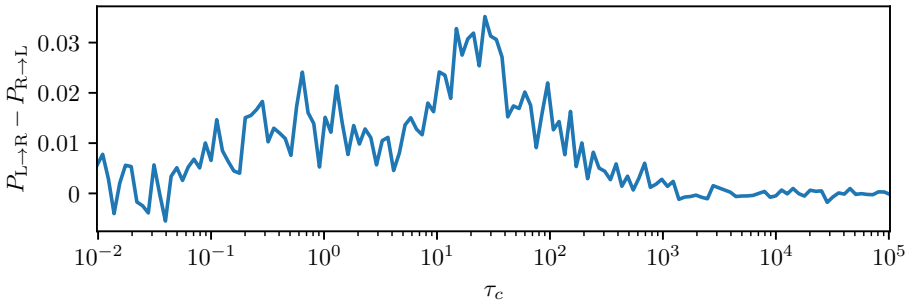


(b)

Figure 5.17: Visualization of the wave packet transport in the tight-binding model of the asymmetric AB interferometer. (a) The wave packet approaching from the left simply passes through the interferometer, the wave packet approaching from the right is subject to two internal reflections before leaving. The probability density shown has been integrated along the y-direction. (b) Plot of the transmission probability as a function of time, revealing a transmission time difference of ≈50 time units for the two directions.



(a)



(b)

Figure 5.18: Transmission probability histograms and averaged nonreciprocity of the asymmetric AB interferometer as a function of the average time between inelastic scattering events τ_{c}. (a) Colormaps showing the histograms of the transmission probabilities of wave packets. The average transmission probability is indicated by the red lines. (b) The nonreciprocity, that is, the difference of the wave packet transmission probabilities for both directions, again vanishes in the limit of large and small τ_{c} and peaks in the transition regime.

R → L direction. This indicates a weaker effect of the decoherence in the faster L → R direction, again as anticipated.

In the limit of small τ_c, the transmission probabilities also seem to become independent of τ_c as expected. Here, the quantum-Zeno [106] like effect already described in Section 5.5.1 prevents the wave packet from entering the lower interferometer arm. In the limit of small τ_c, the transmission probabilities are therefore expected to equal $\approx 50\,\%$ and to become independent of τ_c. The data shown in Fig. 5.18a is compatible with this expecation, however calculations with even smaller τ_c would be necessary to proof this. Because the calculations become increasingly expensive with smaller τ_c, these results are not available here.

These data extend to τ_c so small that the reciprocity of the transmission probabilities is restored. This reproduces the characteristic peak already observed in the previous examples and further supports the claim that this peak is a universal characteristic of asymmetric systems. Again, the largest nonreciprocity occurs when τ_c matches the wave-packet scattering delay difference for the two directions, which is around 50 time units in this example. Analog to the $\hat{\boldsymbol{\mathcal{T}}}$-asymmetric dot, the $\hat{\boldsymbol{\mathcal{P}}}$ and $\hat{\boldsymbol{\mathcal{T}}}$ symmetry transformations for the asymmetric AB interferometer are equivalent. Therefore, the observed nonreciprocity does not only correspond to the breakdown of the $|s_{12}| = |s_{21}|$ symmetry of unitary transport, but also to the breakdown of the respective magnetic field symmetry $|s_{12}(\boldsymbol{B})| = |s_{12}(-\boldsymbol{B})|$.

5.6 Summary

This chapter introduced the basic concepts of tight-binding models. Due to their discrete Hilbert spaces, the Schrödinger equation is easily solved by diagonalization of the finite matrix representing the Hamiltonian of the system. Nonunitary extensions of the Schrödinger equation, namely the Lindblad equation and the stochastic Schrödinger equation are straightforward to implement for tight-binding models. For the scattering problems this thesis is concerned with, it is desired to calculate the time evolution on systems with extensively long leads.

The size of the computer memory to describe the time-evolution operator in a naive implementation scales with the square of the number of sites N_s^2, which limits the maximum system size. An algorithm was developed to calculate the time-evolution operator which scales linearly with N_s and is therefore capable of treating much larger systems. This algorithm is further extended to solve stochastic Schrödinger equations, which makes it possible to incorporate decoherence effects into quantum transport calculations. To assure the correct implementation of this new solver, it has been benchmarked against the solver from the `QuTiP` Python package that solves the equivalent Lindblad equation. Both solvers yield the same results within the numerical errors.

With the developed solver we can study quantum transport in the presence of decoherence. We can investigate whether the combination of nonreciprocal wave-packet scattering delays and decoherence yields nonreciprocal transmission probabilities. The example systems studied here are potential barriers, a series of symmetric and asym-

metric quantum dots and an asymmetric AB interferometer. The symmetries of unitary transport $|s_{12}| = |s_{21}|$ and $|s_{12}(\boldsymbol{B})| = |s_{12}(-\boldsymbol{B})|$ enforce reciprocity and magnetic field inversion symmetry of the transmission probabilities under all circumstances. For the nonunitary transport studied here, we found that the transmission probabilities are nonreciprocal if the decoherence strength is comparable to the difference of the wave-packet scattering delays for the two directions. Nonreciprocal transport unter these conditions is shown to occur for different geometries, in presence of vector and/or scalar potentials, for various choices of wave packet parameters, and for different types of observables used to model the decoherence. This nonreciprocal transport is therefore not a special case confined to specific fine-tuned systems. Instead, it is a general behavior shown by systems with appropriately broken symmetries at appropriate decoherence strengths, as originally suggested in [56].

Comparison of the Novel Nonreciprocal Transport With the Transport Behavior Known Before

6

The calculations presented in Chapter 5 suggest that decoherence is capable of inducing nonreciprocal transport in two-lead devices. This possibility has not been reported in the literature so far. Also the resulting nonreciprocal transport cannot be identified with published nonreciprocal transport effects. This chapter presented a brief overview of such known effects. In a recent review [112], nonreciprocal transport effects are grouped by whether they occur in linear or in nonlinear response and if they require broken time-reversal symmetry or not. The well-known pn-junction, for example, does not require time-reversal symmetry breaking and operates in the nonlinear response regime only. The effect discussed in this thesis occurs in the linear response and requires time-reversal symmetry breaking. Importantly, this time-reversal symmetry breaking does not have to be introduced by a magnetic fields or similar means, but is introduced by the irreversible decoherence processes. Within the category of linear response and time-reversal asymmetry, the review [112] only presents effects that require magnetic order, which the effect reported here does obviously not require.

Regarding nonreciprocal transport and/or recitification effects in mesoscopic electronic devices, a broad range of literature on nonlinear effects exists [108, 113–117]. In these cases, the applied bias is usually large enough to distort the confinement potential which defines the mesoscopic device. In the range of such bias voltages, the bias direction thus affects the Hamiltonian describing the device, which then allows nonreciprocal transmission probabilities to occur. In contrast to these nonlinear transport phenomena, the effect discussed in this thesis does occur in the linear response as well, because it does not rely on a distortion of the confinement potential. Instead, the nonlinear effects and the effect reported here both are related to the wave-packet scattering delay. The wave-packet scattering delay is related to a partial density of states [64], which again is well known to play an important role in nonlinear and AC transport [60–63].

There is also literature on wave packet transport using various forms of nonlinear Schrödinger equations to break the magnetic field symmetry or the reciprocity in two-lead transport [118–120]. In these publications, the nonreciprocity was again introduced by considering charges accumulated by the applied bias current. These charges then lead to a change in the effective potential seen by the carriers, which again affected the dynamics in a nonlinear manner. Although being based on a nonlinear microscopic dynamics, as e.g. generated by the Lindblad equation, the nonreciprocity discussed in this thesis does not require a bias current or voltage to be applied. It is therefore a linear-response effect.

The idea of nonreciprocal wave-packet scattering delays in systems with adequately broken systems is described in a straightforward manner by using the example of the asymmetric Aharonov-Bohm (AB) interferometer (see Fig. 3.16, Section 3.6.2). Aside

from literature related to this work [56], [A, C–E], I am only aware of two other publications that are using the asymmetric transmission delays of the asymmetric AB interferometers to achieve nonreciprocal or magnetic-field asymmetric transmission [71, 72]. Interestingly, in [71], the transmission delays for different transmission directions are not addressed by the authors. In [72], a ring arranged with the chiral edge modes of a Dirac material in a transversal electric field has been proposed. The remarkable properties of the wave packets in this setup are in the focus of attention of [72]. It therefore seems that the importance of the asymmetric wave-packet scattering delay of ordinary asymmetric Aharonov-Bohm interferometers was not recognized previously.

More literature on nonreciprocal transport is found in the field of quantum optics. Similarly to the mesoscopic devices discussed here, the transmission of optical elements is determined by the quantum mechanical transmission probabilities of photons. An important ingredient for the analogy to the mesoscopic AB rings is however missing for photons: There is no Lorentz force for the particles of light, they are usually not affected by a vector potential. Nevertheless, an effective vector potential for photons can be realized using phonon-photon coupling [121] or a photonic Ramsey interferometer [122]. As an advantage over electronic setups, the quantum measurement is straightforward to integrate in a photonic setup. For a proposal of the optical effect that corresponds to the electronic effect discussed in this work, see [123].

In summary, the effect revealed by the numerical results of Chapter 5.1 differs twofold from known nonreciprocal transport effects: First, the effect is expected to occur in the linear response, therefore the nonreciprocity is expected to persist at arbitrarily small bias currents or voltages. Second, the nonreciprocity is expected to vanish in the limits of very large and very small decoherence strengths. Regarding experiments, the first characteristic is challenging to test, because the measurement of the transmission coefficients always requires a finite bias. One may therefore always argue that the applied bias suffices for nonlinear transport to occur. The second characteristic, however, is a robust prediction that is straightforward to test in an experiment, in case the decoherence strength can be tuned over a sufficient range. In this respect, transport experiments are promising, because materials with large low temperature electronic coherence lengths are available and because temperature is a convenient handle to increase the decoherence strength induced by inelastic electron-phonon scattering to values that completely suppress quantum effects. Thus, the study of the symmetries of magnetoconductance curves measured at low bias currents and over a broad temperature range is a promising approach to explore the nonreciprocal transport proposed by Chapter 5 experimentally. The experimental approach based on mesoscopic transport is further motivated by reports of unexpected asymmetries in the literature that have not been fully understood until today [124–127].

Magnetotransport Studies of Mesoscopic Gold Structures

7

The previous chapters of this thesis report how the reciprocity of wave-packet transmission probabilities in mesoscopic two-lead devices may be violated if the device geometry breaks appropriate symmetries and if the decoherence time scale is comparable to the traversal time of electrons passing through the device [A, D, 5, 56]. This chapter documents the current status of the experimental search for this effect in mesoscopic gold structures.

The nonreciprocal wave packet transmission probabilities are expected to result in nonreciprocal resistance of asymmetric mesoscopic devices for a suitable decoherence strength. Importantly, this nonreciprocity is expected to vanish in the limit of large and small decoherence strengths. The decoherence length depends on the temperature. Measurements of the differential resistance of asymmetric mesoscopic devices at a small forward and reverse bias have to yield identical values if the transport is reciprocal. Deviating differential resistances for forward and reverse bias are thus fingerprints of nonreciprocal transport and are expected to occur in a specific, experiment-dependent temperature window. For lower or higher temperatures, this nonreciprocal is expected to vanish.

In a transport experiment it is usually difficult to attribute uniquely a certain measured feature, for example a kink or a dip in the magnetoresistance curve, to a microscopic origin. Most measured features have a multitude of possible explanations and the discussion of the transport measurement results can easily become challenging. However, there is a feature that is perfectly unique and thus can be identified with a microscopic mechanism: The Aharonov-Bohm (AB) resistance oscillations in mesoscopic ring structures. A periodic oscillation pattern in the magnetoresistance is a unique fingerprint of two-path interference in the device. Therefore, asymmetric AB rings are the geometry of choice for the experimental investigations considered here. Alternatively, the observation of universal conductance fluctuations (UCF) is a second clear indicator of quantum coherent transport. However, the UCF signal is not as unambiguous to analyze as the AB oscillations, because it only shows that quantum coherent transport happens *somewhere* in the sample. In samples with ring structures, it is possible to identify the location of interfering paths, if AB oscillations of the expected periodicity are observed.

Due to these arguments, asymmetric AB rings are the preferred geometry for the experiments reported here. Regarding the choice of the material, we wish to obtain electron coherence lengths that are as large as possible. Coherence lengths up to the 100 µm range are achieved in the two-dimensional electron gas (2DEG) formed in AlGaAs/GaAs heterostructures[18, 38, 39]. However, the use of the requires recipes and technology to grow such heterostructures are beyond the scope of this PhD thesis. Historically, the AB effect in mesoscopic devices was first observed in high-purity gold films [24]. Nowadays

such gold films are straightforward to grow with a wide range of deposition techniques, which are available in the institute. Therefore, gold films were chosen as a material for these first samples. The following sections describe the sample preparation and measurement setup and then discuss the experimental results. The images and measurement data in the following sections were obtained with four different samples, which are named samples $\mathbb{A}$, $\mathbb{B}$, $\mathbb{C}$ and $\mathbb{D}$. A detailed description of each sample's fabrication procedure is found in Appendix C.

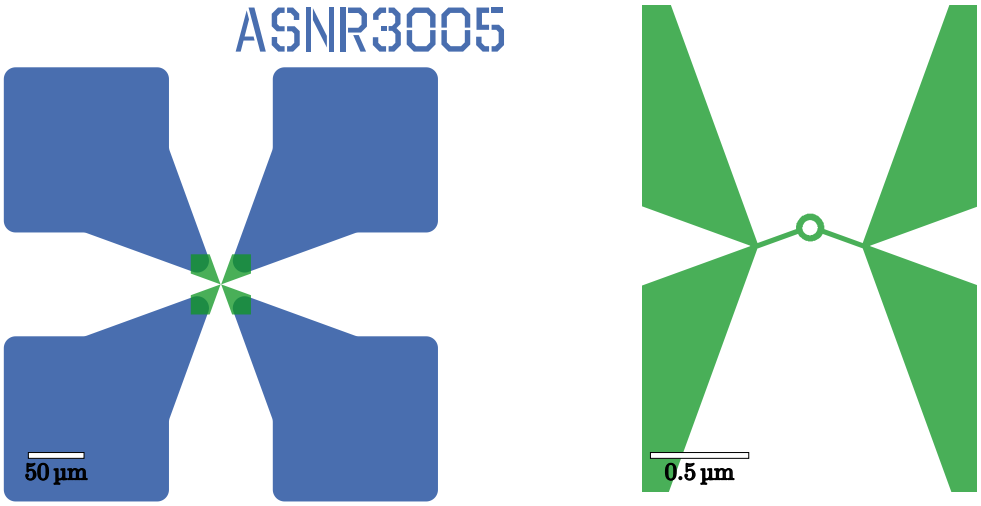
7.1 Sample Preparation

This section presents an overview of the sample preparation process, focusing on the most important fabrication steps and concepts. This section does *not* go through the sample fabrication steps as applied in their chronological sequence, instead it is ordered by importance. For a chronological step-by-step recipe of the sample preparation, see Appendix C.

The samples were prepared on $\approx 0.5\,\mathrm{mm}$ thick $5\,\mathrm{mm} \times 5\,\mathrm{mm}$ pieces of oxidized undoped silicon substrates. Two separate electron beam lithography steps with lift-off pattern transfer were employed. First, the bond pads, labels, markers and other large metal structures were structured using a thick AuPd film ($\approx 100\,\mathrm{nm}$) grown on either a thin film (5 nm) of Cr or Ti that serves as adhesion promoter. Robust bond pads with good adhesion are important to electrically contact the sample after the fabriction is done. Moreover, good adhesion of the metal layers is crucial for the lift-off process. In the second step, the mesoscopic devices were patterned using a much thinner high-purity Au film ($\approx 20\,\mathrm{nm}$) without any adhesion promoter. The adhesion promoter was avoided because its presence would reduce the purity and thus the coherence length of the Au film. Accordingly, this lift-off was more difficult to do and required an optimized choice of solvent, temperatures and sonication power (see Appendix C).

Figure 7.1 shows the two lithography layers of a typical device. Along with the asymmetric AB rings, also nanowires and symmetric rings in various sizes were fabricated. Figure 7.2 gives an overview of sample $\mathbb{A}$ after fabrication. As shown, the developed patterning process is capable of transferring the ring pattern with line widths as narrow as 30 nm to the weakly adhering gold film.

Both patterning steps were done using the lift-off technique to avoid contamination and structure damage possibly caused by etchants. For the first lithography step a layer of 100 nm (50 nm for sample $\mathbb{D}$) of AuPd 60/40 was evaporated on top of 5 nm of Cr (Ti for sample $\mathbb{B}$) on the patterned resist. This evaporation step was done in an automatic Oerlikon Leybold Univex 350 thermal evaporation system. During deposition, the typical chamber pressure was $1 \times 10^{-5}\,\mathrm{mbar}$. In the second lithography step, 20 nm of pure Au were deposited via electron beam evaporation (EBE) under extremely clean conditions in a chamber originally designed for molecular beam epitaxy (MBE) growth. The evaporation material was 5N (99.999 %) pure gold. This evaporation chamber was kept permanently evacuated and samples were (un)loaded using a series of load lock chambers. To minimize sample contamination, the evaporation source was ramped to



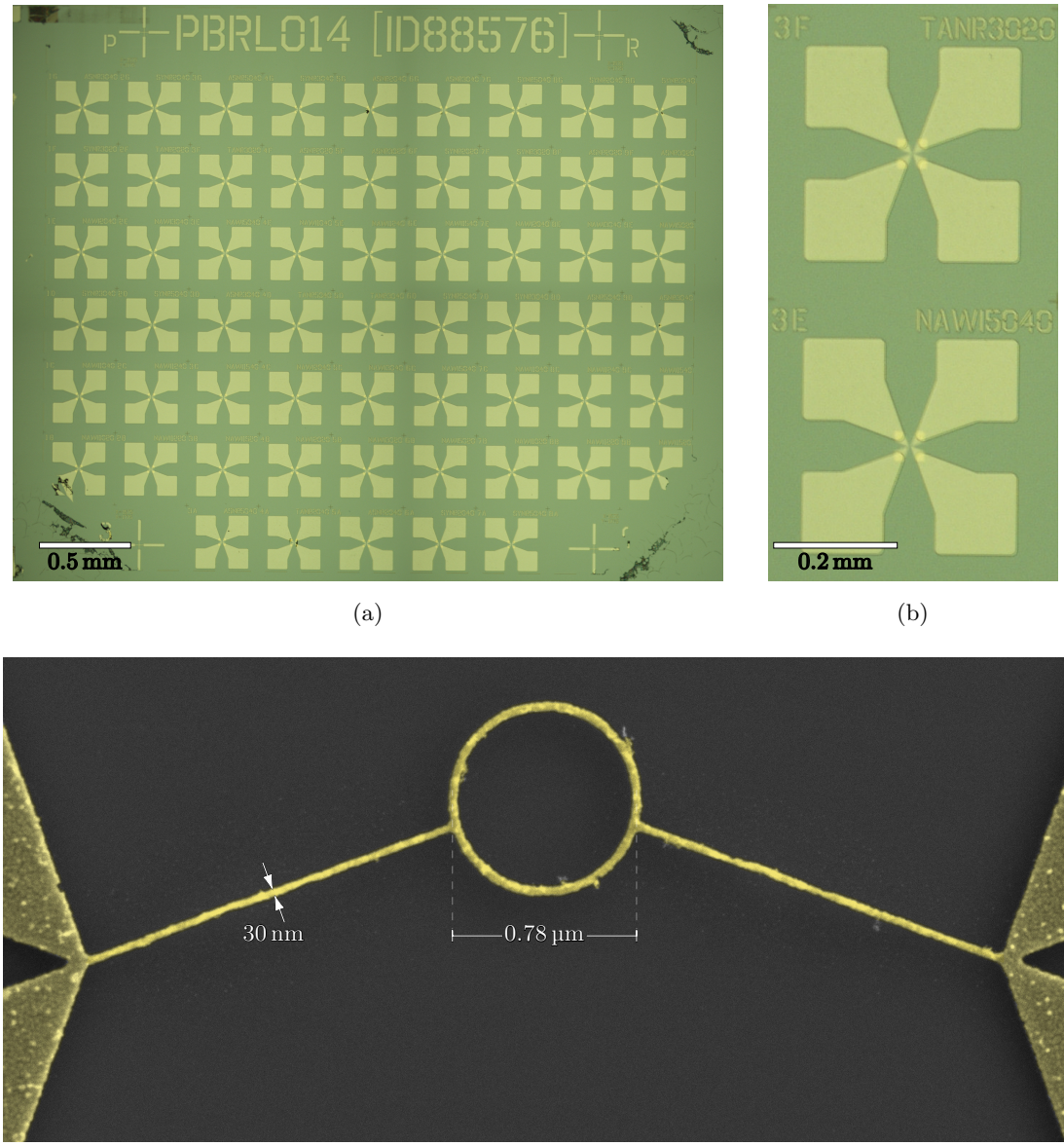
(a) (b)

Figure 7.1: (a) Dual layer electron beam lithography layout. The blue layer defines the labels and bondpads, the green layer defines the mesoscopic device, which is located in the very center of the shown layout, but too small to be resolved in this picture. (b) In the 100× magnified view of the layout, the mesoscopic ring interferometer with asymmetric contacts are visible.

operating power before the sample entered the chamber. Only after reaching and stabilizing the operating point, the sample was transferred into the evaporation chamber. Further, the cryopanels of the chamber were filled with liquid nitrogen to trap contaminants and thus reduce the chamber pressure during operation. With these measures, the pressure during evaporation was 1×10^{-8} mbar. To have a reference for a film deposited under less careful conditions, for sample $\mathbb{A}$ both deposition steps were performed in the Univex system at a pressure of 1×10^{-5} mbar.

7.2 Measurement Setup

The goal of the measurements is to find unexpected asymmetries in the differential resistance $\partial V/\partial I$ of the device. Therefore, $\partial V/\partial I$ was measured as a function of the magnetic flux density $\boldsymbol{B}$ and the DC bias current I_{bias}. The results were then analyzed for asymmetries with respect to $\boldsymbol{B}$ and I_{bias}. The temperature T served as a handle to control the decoherence strength. The samples were first tested in a Quantum Design PPMS cryostat with a base temperature of 1.8 K. To observe quantum transport phenomena such as UCF or AB oscillations, the samples were then transferred to a dilution refrigerator, which was able to stabilize temperatures between 50 mK and 1.5 K. As shown in Fig. 7.2, the fabricated devices feature four bond pads. This permits to measure $\partial V/\partial I$ in a standard four-wire measurement scheme: Two pads are used to source



(a) (b)

(c)

Figure 7.2: (a) Microscopy picture showing sample 𝔸 after processing. 59 electrically independent devices are placed on one sample. (b) In a close-up view the second metal layer is visible in the center of the device. (c) The false-color SEM image of the mesoscopic structure in the center of the device. The four contacts that are connected to the four bond pads are visible in the left and right of the image.

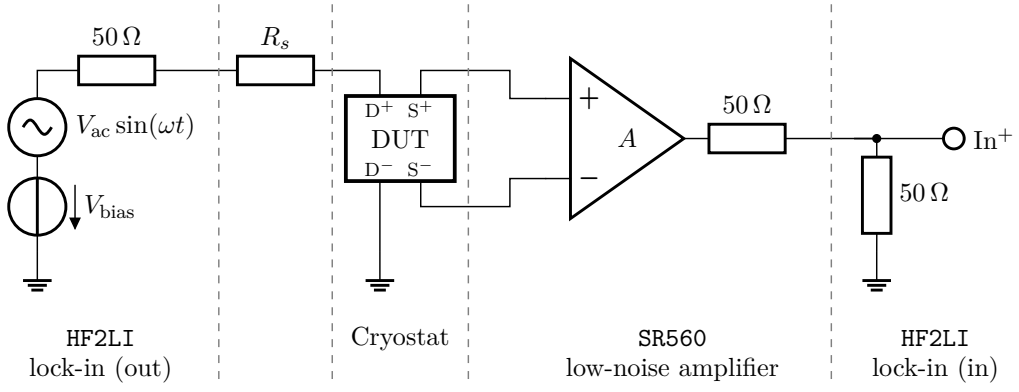
a current through the device, the other two are used to measure the voltage across the device. Despite four wires being used for the measurement, the setup corresponds to a two-lead device in the sense of Landauer and Büttiker. This is because the two leads split into four with more than the coherence length distance to the ring. Therefore, coherent superpositions of a carrier being located in the device and multiple contacts are very unlikely and the description as a two-lead Landauer-Büttiker device is accurate.

As discussed in Chapter 6, an important characteristic of the nonreciprocal transport effect that we are looking for, is its existence at small bias currents. Most known nonreciprocal transport effects vanish at small bias. Therefore, trying to find the effect in the regime of small currents is a promising strategy. All measurements discussed here were conducted with lock-in amplifiers, which offer high signal-to-noise ratios even with the small signal amplitudes that are required.

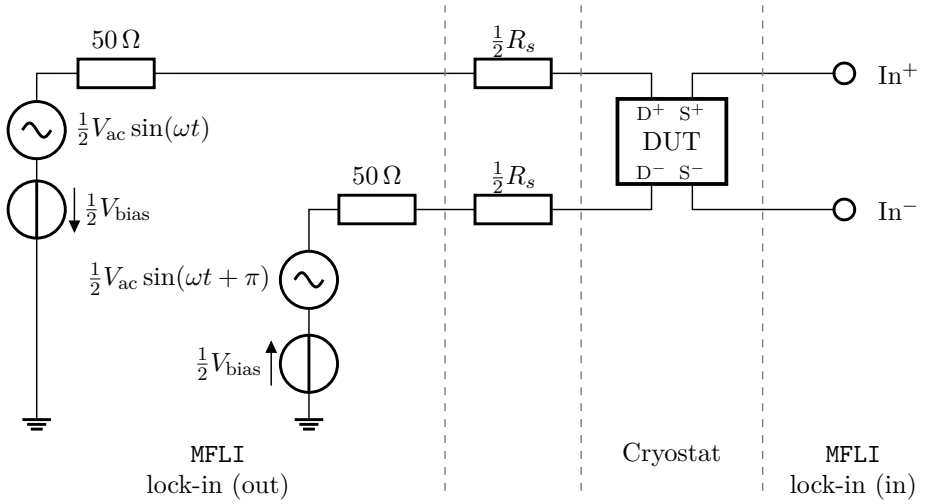
For the initial measurements, the most suited lock-in amplifier was the Zurich Instruments `HF2LI`. This device is optimized for high frequency operation $f > 10\,\mathrm{kHz}$. However, the transport experiments discussed here require frequencies $f < 50\,\mathrm{Hz}$, to avoid capacitive responses. To improve the noise level at these low frequencies, an external preamplifier, the Stanford Research Systems `SR560`, was used. Figure 7.3a sketches the setup schematics. In the following, this setup is called the "`HF2LI` based setup".

To improve the overall noise performance of the setup, the Zurich Instruments `MFLI` lock-in amplifier was used for later measurements. This lock-in amplifier is specialized on the low frequency range. With this lock-in, no external preamplifier was needed. Moreover, the `MFLI` features a differential output option. In the differential output mode, one output generates the desired sine signal with half the selected amplitude and bias. The second output generates the same signal with opposite sign (π phase shift). Thus, the sum of the two signals is zero at any time; the difference yields the desired sine wave. With this, a fully differential measurement setup was implemented. This setup is less sensitive to noise on the ground lines and greatly improved the overall noise levels in the setup. Figure 7.3b sketches the schematics. In the following, this setup is termed the "`MFLI` based setup".

In both setups, the signal generated by the lock-in amplifier is given by a sine wave with amplitude V_{ac}, superimposed on a DC bias of V_{bias}. This voltage signal is converted to a current by the series resistor R_s. This resistor is typically chosen to be $1\,\mathrm{M\Omega}$ or $10\,\mathrm{M\Omega}$, much larger than the average device resistance of $<1\,\mathrm{k\Omega}$. Therefore, changes in the device resistance do not affect the current that is flowing through the device, which to a good approximation is given by $I(t) = V(t)/R_s$. The lock-in then measures the AC component of the response voltage signal that oscillates at the same frequency as the drive signal generated by the lock-in. In the measurements shown here, this frequency was chosen to be in the range of $10\,\mathrm{Hz}$ to $40\,\mathrm{Hz}$, which results in an in-phase, ohmic response signal. From this measured AC voltage amplitude V_{in} at the lock-in input, the differential resistance is deduced via $\partial V/\partial I \approx V_{\mathrm{in}}/I_{\mathrm{ac}} = R_s V_{\mathrm{in}}/(V_{\mathrm{ac}} A)$ with the preamp gain A effectively being 1 in the `MFLI` based setup. In the `HF2LI` based setup, the preamp gain A was chosen in the range from $10^2 - 10^4$, optimizing the noise performance of the setup. The following results have been obtained from such $\partial V/\partial I$ measurements as a



(a)



(b)

Figure 7.3: Schematics showing the measurement setup based on the HF2LI and the MFLI lock-in amplifiers. The device under test (DUT) is connected via four wires, two wires for driving (D^+ and D^-, lower left and lower right in Fig. 7.2c) and two wires for sensing (S^+ and S^-, upper left and upper right in Fig. 7.2c). (a) In the single-ended driving circuit used with the HF2LI lock-in amplifier, one wire of the sample is directly connected to ground. An external SR560 preamplifier with a gain of A is used. (b) The MFLI lock-in amplifier features a differential output option, making a fully differential measurement scheme possible. In this configuration, no device wire is connected to ground.

function of the DC bias current I_{bias}, the magnetic flux density $\boldsymbol{B}$ and the temperature T.

7.3 Experimental Results

The following sections present the results of the measurements done with the fabricated mesoscopic gold structures. First, the measurements of the residual resistance ratio are presented as a first indicator of the material quality. Further the results from the measurements in the dilution refrigerator, namely UCF and the AB oscillations are shown, as well as evidence for nonreciprocal transport.

7.3.1 Residual Resistance Ratio

The residual resistance ratio is defined as the ratio of the resistance at 300 K and the resistance at 0 K. In most samples, the resistance becomes temperature independent at low temperatures, therefore the value at 0 K is approximated with the value at a low-enough temperature. Here, we use the value measured at 2 K. At high temperatures, the inelastic electron scattering is dominated by electron-phonon collisions. At low temperatures, however, scattering at lattice defects such as grain boundaries is dominant. Therefore the residual resistance ratio (RRR) is an indicator of the defect density in the material. Figure 7.4 shows the RRR measurements of the four samples. These values of the RRR are very small compared to the values observed in bulk metal, which is close to 100 [128]. However, the RRR of metallic thin films is known to be strongly thickness dependent due to scattering at grain boundaries and film interfaces [129]. As expected, the devices fabricated from the film deposited at 1×10^{-5} mbar show the lowest RRR, whereas the devices fabricated from films that were deposited at 1×10^{-8} mbar show better residual resistance ratios.

7.3.2 Universal Conductance Fluctuations

The occurrence of UCF in the measured $\partial V/\partial I$ as a function of the magnetic flux density $\boldsymbol{B}$ is a characteristic of quantum transport. The aperiodic modulation pattern occurs in small samples in which disorder affects the coherent transport [32, 42]. UCF were observed in sample sample $\mathbb{B}$ and sample $\mathbb{C}$, which where measured <1 K. Figures 7.5 and 7.6 show the magnetoresistance curves obtained at a series of temperatures. For each temperature, two curves are shown. One of these curves is plotted in color and corresponds to the case of a positive DC bias current I_{bias}. The second curve for each temperature is plotted in grey and corresponds to a negative I_{bias}. The color of the forward bias curve indicates the temperature at which the curve pair was measured.

Figures 7.5 and 7.6 show that the differential resistance at ≈ 1 K is less dependent on $\boldsymbol{B}$ than at lower temperatures. With decreasing temperature, a random fluctuation pattern in the differential resistance appears. This fluctuation pattern extends over the entire accesible magnetic field range. For sample $\mathbb{C}$ (Fig. 7.5), the amplitude of the pattern is $\approx 0.3\,\Omega$ peak-to-peak or 0.25 % of the average device resistance, which is 25 % of the estimated maximum amplitude $G_0 R^2 = 1.2\,\Omega$. Here, G_0 is the conductance quantum

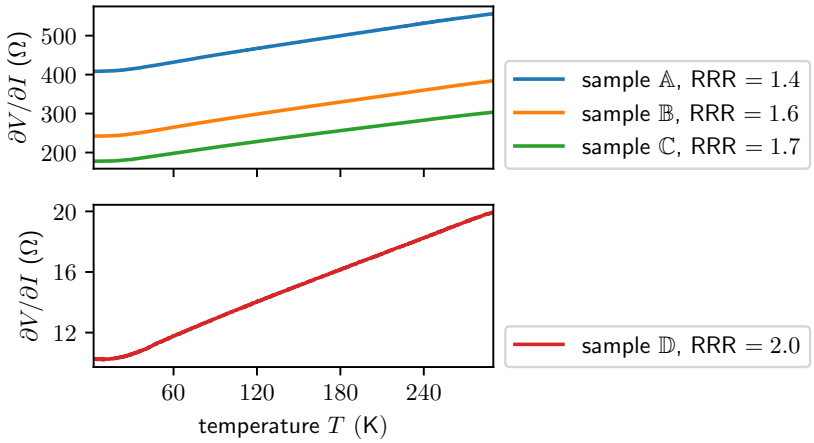


Figure 7.4: Plots of the differential resistance $\partial V/\partial I$ measured as a function of temperature during cool down. The `HF2LI` based setup was used in the measurements. For all four samples, the $\partial V/\partial I$ drops linearly with temperature and saturates at $\approx 20\,\mathrm{K}$. Sample 𝔸, deposited in the Univex chamber, shows the highest average resistance and the smallest residual resistance ratio (RRR). The device layouts of sample 𝔻 differs a lot from the other samples, the device resistance is therefore much lower.

and R is the mean device resistance (see Eq. 2.1 in Section 2.2). For sample 𝔹 (Fig. 7.6), the amplitude also equals $\approx 0.3\,\Omega$, which only corresponds to 0.1 % of the mean device resistance and is well below the estimated maximum amplitude $G_0 R^2 = 7.7\,\Omega$. This suggests that the coherence length of sample 𝔹 is smaller than that of sample ℂ.

The lower the temperature, the finer the features in the fluctuation pattern become. This well known property of UCF originates from the coherence length increase at lower temperatures [33, 41]. The fact that the fluctuations of sample ℂ (Fig. 7.5) are generally finer than the fluctuations of sample 𝔹 (Fig. 7.6) is an additional indication that the coherence length of sample ℂ is larger than the coherence length of sample 𝔹.

The central question of this thesis is if the two-lead symmetries are violated in the presence of decoherence. In the context of this measurement the question is whether the UCF pattern is independent of the bias direction, as the Landauer-Büttiker picture of quantum transport predicts. In Figs. 7.5 and 7.6, it is evident that this is only the case at elevated temperatures. At low temperatures, the details of the UCF features of the two bias directions generally differ. This is a direct indication that at specific values of $\boldsymbol{B}$, the differential resistance $\partial V/\partial I$ in forward bias direction is different from the $\partial V/\partial I$ in reverse bias direction. In the measurements shown for sample ℂ, the applied current corresponds to a voltage drop of 5.5 µV across the sample, which is below the thermal energy scale $k_\mathrm{B}T = 6\,\mu\mathrm{eV}$ at 70 mK. Thus, the applied voltage distorts the potential seen by the carriers by less than typical thermal activation energies. Therefore, it is unlikely that nonlinear transport effects cause the observed asymmetry of $\partial V/\partial I$ with

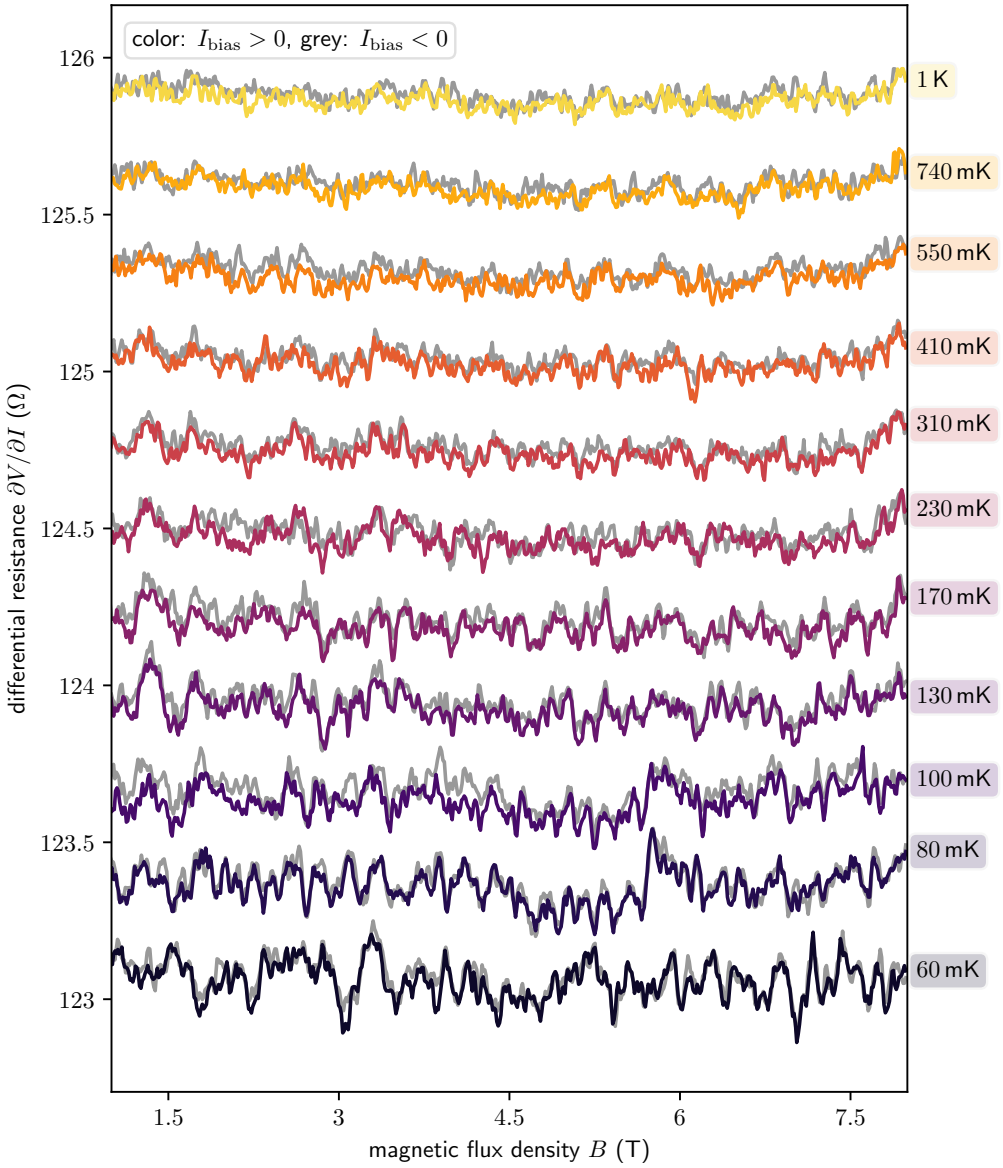


Figure 7.5: Measured differential resistance of sample ℂ as a function of the magnetic flux density $\boldsymbol{B}$ and the temperature T for forward and reverse bias direction using the `MFLI` based setup. The applied AC excitation current I_{ac} was 20 nA, the applied DC bias current I_{bias} was ±25 nA. The lowest temperature sweeps are unshifted, all other curves are shifted in the y-direction by 0.3 Ω per temperature step. For each temperature, there is one colored curve, corresponding to forward bias, plotted on top of a grey curve, which corresponds to the reverse bias. The color of the forward bias curve indicates the temperature for both curves.

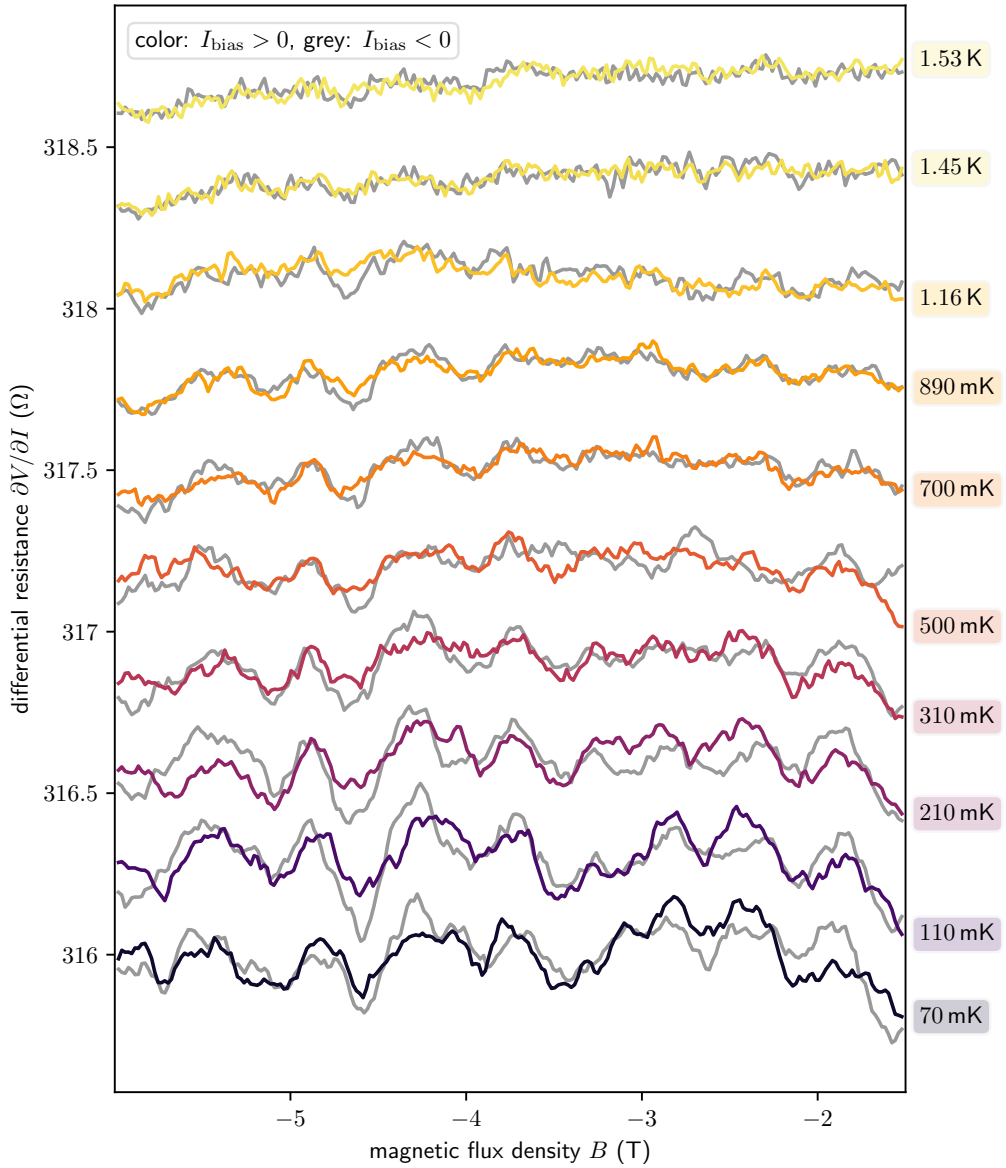


Figure 7.6: Measured differential resistance of sample 𝔹 as a function of the magnetic flux density $\boldsymbol{B}$ and the temperature T for forward and reverse bias direction using the `HF2LI` based setup. The applied AC excitation current I_{ac} was 100 nA, the applied DC bias current I_{bias} was ±150 nA. The plot structure is completely analogous to Fig. 7.5.

respect to I_{bias}.

In the plots shown in Figs. 7.5 and 7.6, one might suspect that differences of the $\partial V/\partial I(\boldsymbol{B})$ between the two bias directions are caused by noise or drift. This is not the case, as many of the nonreciprocal features are reproducible (Fig. 7.7). In the two field regions shaded in grey, the differential resistance under reverse bias (blue and orange curves) shows a distinct dip or peak, respectively. The dip and the peak are clearly reproduced in the $2\,\mathrm{T} \rightarrow 7\,\mathrm{T}$ and the $7\,\mathrm{T} \rightarrow 2\,\mathrm{T}$ sweep. In contrast, both forward-bias curves lack the dip or the peak in the regions shaded in grey, which gives evidence for a reproducibly nonreciprocal differential resistance of the device.

7.3.3 Aharonov-Bohm Oscillations

Aharonov-Bohm (AB) resistance oscillations were shown by both AB ring devices on sample ℂ measured at low temperature. One ring structure on sample 𝔹 was measured at low temperature as well but did not exhibit AB osciallations. In Section 7.3.2, the electron coherence length in sample ℂ was shown to be larger than the coherence length in sample 𝔹, which is a possible explanation for the absence of AB oscillations in sample 𝔹.

The oscillation pattern was observed in the entire examined magnetic field range from $-8\,\mathrm{T}$ to $8\,\mathrm{T}$. Figure 7.8 shows an extract of the magnetoresistance of a ring with a middle radius of $r = 200\,\mathrm{nm}$. The magnetic flux density that corresponds to one magnetic flux quantum $\boldsymbol{\Phi}_0 = h/q$ enclosed within this ring is given by $\boldsymbol{\Phi}_0/(\pi r^2) \approx 30\,\mathrm{mT}$. Thus, the expected fundamental period of the oscillation signal is anticipated to be $30\,\mathrm{mT}$, which is indeed observed in the measurements. Further, the Fourier spectrum of the entire magnetoresistance curve yields a pronounced peak at the expected fundamental frequency $(30\,\mathrm{mT})^{-1}$, which emphasizes the fact that the oscillations have a harmonic component over the entire magnetic field range. As shown by Eq. 3.65 and 3.65 (Section 3.6.2), the transmission probability of the simplified 1D model of the AB interferometer contains terms periodic with the magnetic flux quantum $\boldsymbol{\Phi}_0$ and $2\boldsymbol{\Phi}_0$. Since the denominator of these expressions also contains terms periodic with $\boldsymbol{\Phi}_0$, $2\boldsymbol{\Phi}_0$ and terms independent of the magnetic flux, the Fourier expansion of the transmission probability contains components periodic with all harmonics of the fundamental periodicity $\boldsymbol{\Phi}_0$. For the AB ring measured here it is therefore not surprising that peaks corresponding to the second, and possibly to the third, harmonics are visible in the Fourier spectrum of the magnetoresistance (Fig. 7.8). The amplitude of the oscillations is $\approx 0.1\,\Omega$ with an average device resistance of $120\,\Omega$, in accordance with values from the literature reported for metallic AB rings [24–26, 31, 45].

These observations clarify that the measurement results are indeed caused by the two-path interference of electrons traveling through both arms of the ring simultaneously. Next, we analyze the symmetry of the AB oscillation signal with respect to a reversal of the bias-current direction. Figure 7.9 presents a series of magnetoresistance measurements taken at different temperatures and in both bias directions. The plot is structured analogous to Figs. 7.5 and 7.6, with the curves corresponding to forward bias being colored according to the temperature and the curves in reverse bias direction being grey.

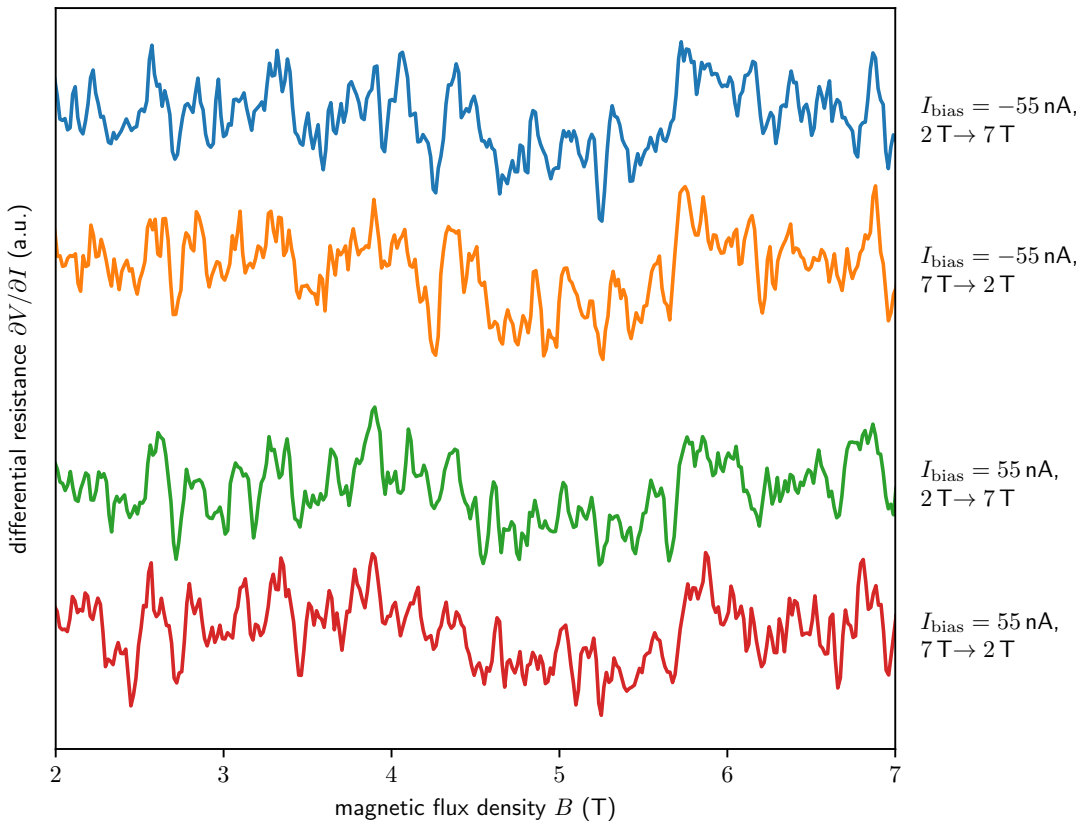


Figure 7.7: Measured differential resistance of sample ℂ as a function of the magnetic flux density $\boldsymbol{B}$ for forward and reverse bias direction and two independent field sweeps. The curves are y-shifted for clarity. The shown data corresponds to the second pair of curves from below in Fig. 7.5, measured at 70 mK. The blue and the orange plots show the results for two independent magnetic field sweeps with a negative bias current applied. The red and the green plots show two analogous measurements with a positive bias current applied. The grey shadows highlight nonreciprocal features of the differential resistance curves, which clearly appear on all four magnetic field sweeps.

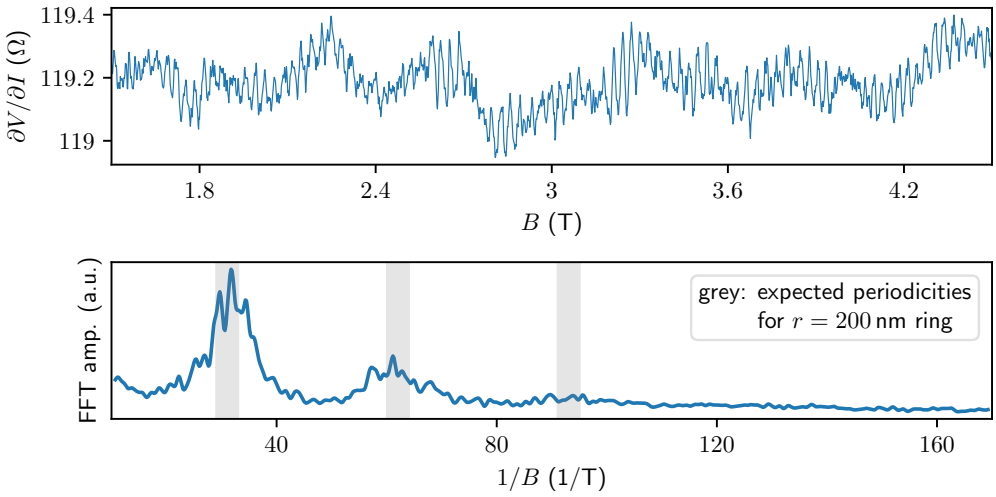


Figure 7.8: Measured differential resistance of sample ℂ as a function of the magnetic flux density $\boldsymbol{B}$ and corresponding Fourier spectrum for a ring structure with a radius of 200 nm at 60 mK. Pronounced AB oscillations with a period of 30 mT are observed in the magnetoresistance, superimposed by the aperiodic UCF. The Fourier spectrum shows peaks around the expected AB frequency and its harmonics.

The curve pair corresponding to the lowest temperature is unshifted, all other curves are shifted by 0.15 Ω per temperature step.

Similar to the UCF measurements, the measured magnetoresistance curves in forward and the reverse bias direction deviate at well-defined fields, especially at lower temperatures. In Fig. 7.9, three of such deviations are highlighted by the blue and green ovals. In all three cases, the AB oscillations are more pronounced in one bias direction than in the other. From the data as shown in Fig. 7.9, it is not possible to judge if these deviations from reciprocity are reproducible or random. Therefore, Fig. 7.10 shows the magnetoresistance measured in two different magnetic field sweeps magnified around the region corresponding to the blue ellipse in Fig. 7.9.

In the parameter window shown in Fig. 7.10, the bias direction dependence of the AB oscillation pattern is present in both shown magnetic field sweeps. Just as for the UCF signal anlyzed in the previous section, many of the nonreciprocal features in the magnetoresistance curves show this reproducibility.

The observed bias-current direction dependence of the AB is strong evidence for the occurrence of nonreciprocal transport: At a given magnetic field the differential resistance in forward bias direction is different from the differential resistance in reverse bias direction, which is compatible with the picture put forward by Fig. 5.17 (Section 5.5.3): In one direction, the interference is more sensitive to decoherence than in the other direction, because the dwell time of carriers in the interferometer differs for the two

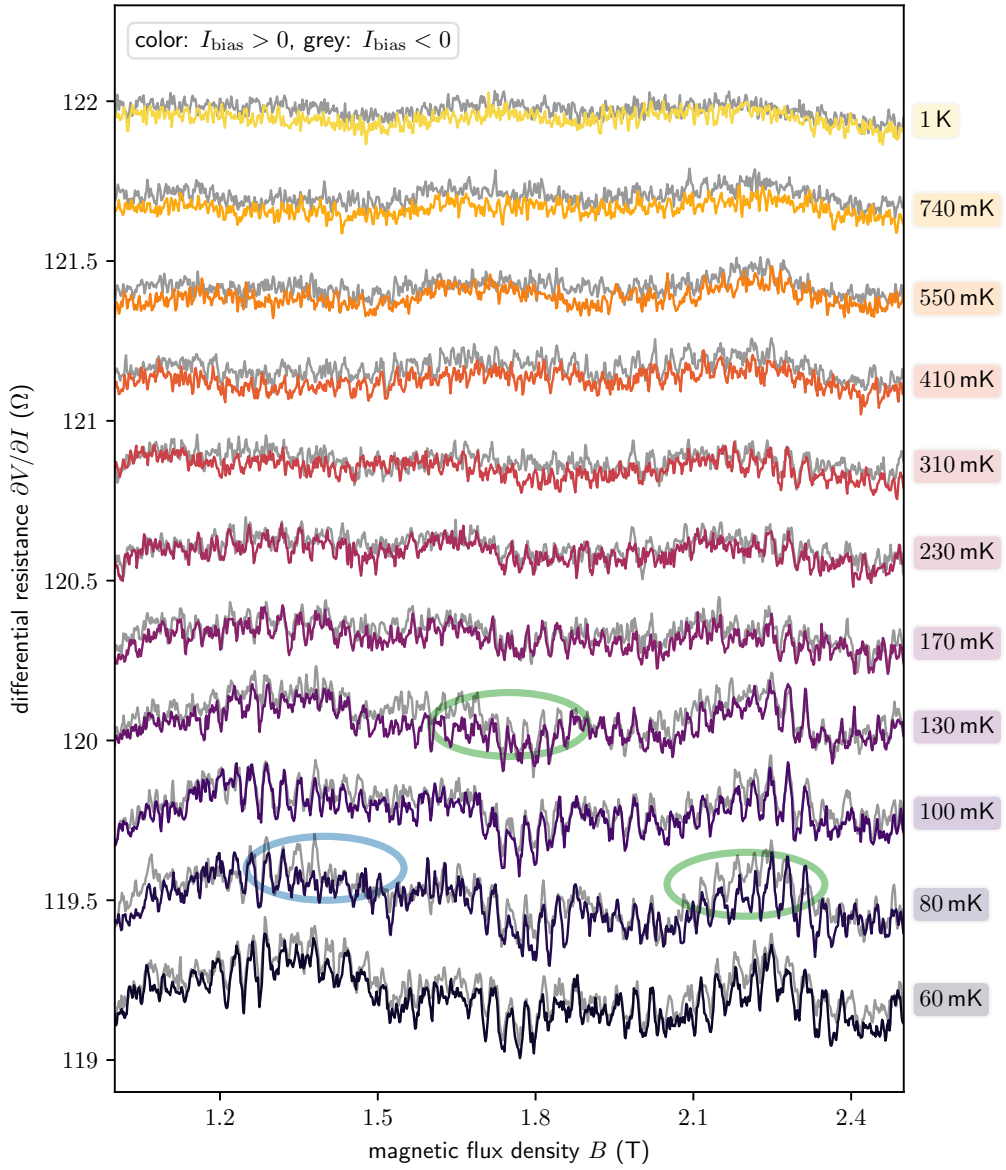


Figure 7.9: Measured differential resistance of sample ℂ for a ring structure with a radius of 200 nm as a function of the magnetic flux density $\boldsymbol{B}$ and the temperature T for forward and reverse bias direction. The plot structure is completely analogous to Fig. 7.5. Pronounced AB oscillations are observed at low temperature. Certain low temperature features of the $\partial V/\partial I$ curves differ for the two bias directions, three examples are highlighted by the ovals. The applied AC excitation current I_{ac} is 40 nA, the applied DC bias current I_{bias} is ±55 nA.

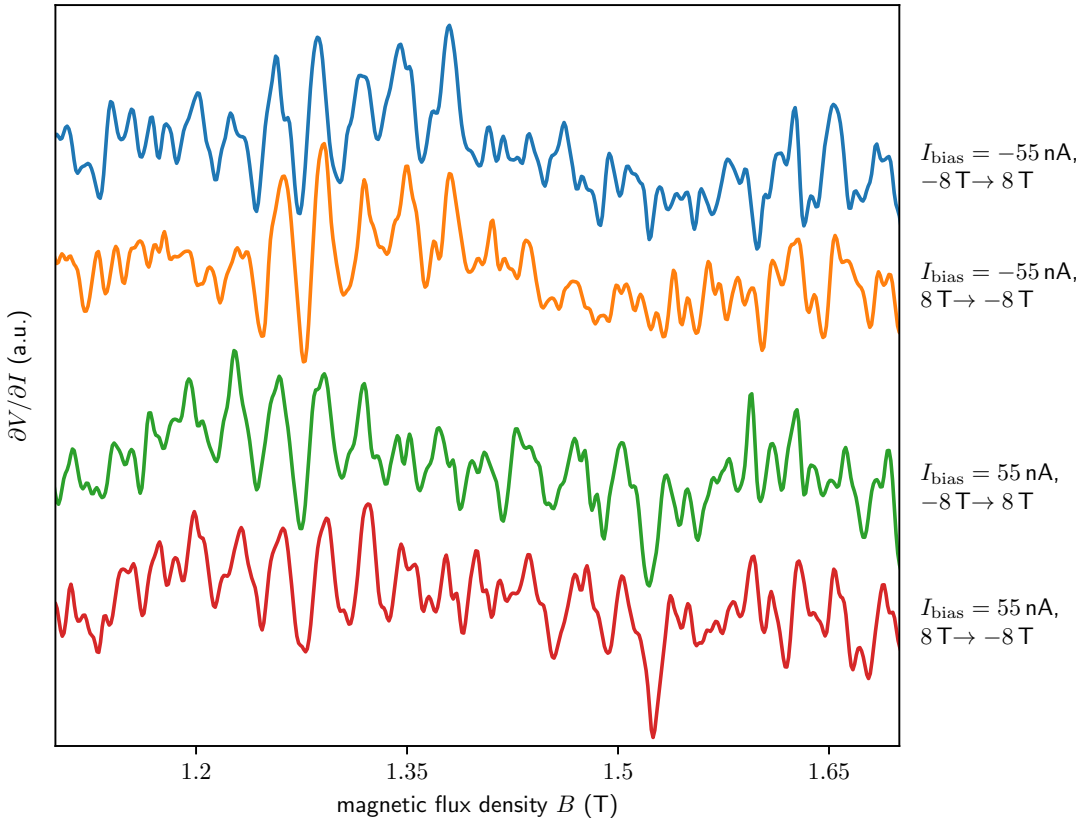


Figure 7.10: Measured differential resistance of sample ℂ as a function of the magnetic flux density $\boldsymbol{B}$ for forward and reverse bias direction and two independent field sweeps. The curves are y-shifted for clarity. The shown data correspond to the second pair of curves from below in Fig. 7.9, measured at 70 mK. The blue and the orange plots show two retraces under reverse bias. The red and the green plots show two retraces under forward bias. In the shaded region round 1.35 T, both reverse bias curves show stronger AB oscillations than the two forward bias curves, in the shaded region at 1.5 T it is vice versa.

directions. This is a possible explanation for the magnitude of the oscillation patterns to depend on the bias direction.

7.4 Discussion and Summary

The numerical results obtained Chapter 5 suggest a breakdown of two-lead symmetries of transport for suitably broken device symmetries and appropriate decoherence strengths. One way to search for this effect in experiments is to study the magnetotransport of mesoscopic devices, using the temperature to control the decoherence strength. Here, mesoscopic gold rings were fabricated and analyzed. This framework was chosen, because of the straightforward sample preparation and the clear fingerprints of quantum transport at low temperatures reported in the literature [17, 24, 32]. The samples were fabricated using a two-layer electron-beam lithography (EBL) layout and standard lift-off pattern transfer processes. To observe quantum transport phenomena, the devices were fabricated from high purity materials. The Au film was deposited in a permanently evacuated evaporation chamber from source material with 99.999 % purity, and using cryopanels to further reduce the pressure. A comparison with a standard film deposited as reference under less careful conditions showed a superior RRR of the high-purity films. The film thickness was 20 nm and the minimum line width used for devices was 30 nm. The fabricated devices were nanowires and nanorings with various sizes.

In the low temperature measurements in the dilution refrigerator, UCF and AB oscillations were observed in multiple devices. To test the predictions of Chapter 5, the dependence of the differential resistance on the direction of the bias current was measured with high precision. Even for the smallest accessible bias currents, it was still possible to find magnetic fields at which the differential resistance was different in forward and reverse bias direction, which is evidence for nonreciprocal transport. The bias currents were small enough to be comparable with the thermal energy scale, therefore it is unlikely that nonlinear transport effects, caused by the distortion of the confinement potential by the bias, were causing the nonreciprocity.

However, to be clearly separable from other effects, it would be necessary to observe the peak-like visibility of nonreciprocal transport effects as a function of the decoherence strength, as suggested by Figs. 5.11, 5.13 and 5.18 (Section 5.5). For the measurements, this would require the restoration of reciprocal transport at very low and very high decoherence rates, that is, at low and high temperatures. Whereas this restoration is in fact observed at high temperatures, the lowest accessible temperatures are not low enough to reach the other side of the predicted peak. For this, the coherence length has to become much larger than the device dimensions. This could possibly be achieved in future experiments by using materials with intrinsically larger coherence lengths, for example semiconductor heterostructures, or by fabricating smaller devices, for example by using special patterning techniques such as sidewall deposition [130] or self organization [131].

8 Discussion and Outlook

This thesis presents a numerical and experimental exploration of nonreciprocal transport in two-lead devices. This nonreciprocal transport is predicted to occur at the transition between classical and quantum physics, where the frequency of irreversible processes is comparable to the inverse transit time of quantum mechanical wave packets. As Chapter 3 shows, in the quantum mechanical unitary transport regime, the linear transport is fully determined by the absolute values of the scattering matrix elements. Due to the unitarity of the scattering matrix, nonreciprocal transport is excluded in unitary quantum transport. However, the dynamics of wave packets is not subject to this constraint. Dwell times and scattering delays are generally nonreciprocal if the Hamiltonian breaks appropriate symmetries. Chapter 4 introduced methods to model decoherence, namely the Lindblad master equation and the stochastic Schrödinger equation. These generate a nonunitary time evolution, where the transport is no longer governed by the unitary scattering matrix. Chapter 5 shows that the nonreciprocal dynamics, combined with decoherence of appropriate strength, leads to nonreciprocal wave-packet transmission probabilities. These nonreciprocal probabilities are always observed if the Hamiltonian breaks suitable symmetries and if the phase-breaking time scale is comparable to the wave-packet scattering delay. Whereas the magnitude of this nonreciprocity may depend on model parameters other than the decoherence strength, its presence does not. Importantly, the reciprocity of the transport is restored in the limits of weak and strong decoherence, in agreement with the expected behavior in the unitary and the classical transport regimes. This characteristic makes it possible to distinguish the effect from known nonreciprocal transport effects. Chapter 6 provides a comparison with similar effects known from the literature. Chapter 7 shows encouraging preliminary experimental results obtained with quantum transport measurements of mesoscopic normal-metal rings. In the following sections of this chapter, open questions and perspectives for further work are discussed.

8.1 Model Calculations

From the model calculations, the nonreciprocal transport is predicted to occur for arbitrarily small bias values, which does not match the Onsager-Casimir reciprocal relations [132]. However, this apparent conflict is not a contradiction, because the nonreciprocal transport effect discussed in this thesis is generated by irreversible microscopic time evolutions: the initial states are given by wave packets, the final states are not. The Onsager-Casimir reciprocal relations only hold if the underlying microscopic dynamics is reversible. Therefore, it seems that whenever a description with wave packets is appropriate, we cannot safely assume microscopic reversibility. Thinking along this direction,

it seems interesting to identify processes in nature that generate these wave packets. The spontaneous photoemission, detrapping or tunneling of electrons are candidates for such processes. The spatio-temporal resolution required to measure the properties of such electron wave packets is experimentally achievable [67].

A further route for improvements of the model calculations concerns the fermionic character of electrons. The electrons in a conductor are described by the many-body state of the Fermi sea. The single particle picture for transport is motivated by the fact that the excitations of this Fermi sea behave as if they were single particles with an effective mass. This allows the use of the single particle picture in unitary transport. Importantly, due to the Pauli exclusion principle, state transitions of these single particle excitations only occur from occupied to unoccupied states. The single particle stochastic Schrödinger equations and the equivalent Lindblad master equations cannot guarantee a behavior in accordance with this restriction. The state transitions given by the nonunitary terms of the Lindblad master equation occur with a constant rate, independent of the occupation of the target state. This assumption is well justified for small electron densities, for which only one or a few electrons are located within the device at a given time. If only one electron is present, the possible target states for state transitions cannot be blocked by other electrons. In this case, the single particle Lindblad equation therefore provides an accurate description and does not provoke forbidden state transitions. To generalize this concept to arbitrary carrier densities, it is required to revisit the full many-body description of the Fermi sea and to derive an effective single particle dynamics from the full fermionic many-body Lindblad equation. One example of such a derivation is given in [133]. Using such a single-particle dynamics would make it possible to explore how the carrier concentration and the resulting Pauli exclusion repulsion affect the suggested nonreciprocal transport. Whether this leads to an amplification or attenuation of the effect is unclear; a full cancellation is very unlikely, however.

Alternatively, a scattering theory for the Lindblad master equations could be employed to derive the symmetries of transport in the presence of decoherence. This approach may lead to very general conclusions. The respective scattering theory is, however, considerably more convoluted than the scattering theory implied by the unitary Schrödinger dynamics [99].

8.2 Experiments

The quantum transport experiments performed on mesoscopic metallic structures described in this thesis indicate that nonreciprocal features exist in the magnetoresistance curves even at the lowest bias currents. This nonreciprocal transport is related to quantum transport properties, namely the universal conductance fluctuations (UCF) or the Aharonov-Bohm (AB) oscillations. In these experiments, the temperature served as a control parameter for the decoherence strength. At large decoherence strength, that is, at high temperature, reciprocal transport is restored. However, the experiments did not yet succeed to observe the restoration of reciprocity at small decoherence strength, that is, at low temperature. At the lowest available temperature, the coherence length is still on the same scale as the device dimensions, and purely unitary transport is not achieved. Several approaches for the next generation of experiments are conceivable:

Firstly, measuring the same devices at even lower temperatures, to possibly reach the unitary limit. However, with the currently available technology it is not feasible to cool solid state samples below temperatures of a few millikelvin, which is not far from the $\approx 50\,\mathrm{mK}$ reported in this thesis. It seems unlikely that this is enough to observe the restoration of reciprocal transport.

Secondly, smaller devices fabricated from the same material have a larger coherence-length to device-size ratio at any temperature. Reducing the device size therefore obviously help in achieving unitary quantum transport. Thus, further shrinking of the nanodevices could help to reach the unitary transport regime. In scaling the devices, it remains important that the fabrication process ensures a very high material purity. Increased defect densities, and thus a reduced coherence length, would cancel the improvements due to smaller device sizes.

Thirdly, it is possible to choose a different material with a larger coherence length than Au. For example, high-mobility AlGaAs/GaAs heterostructures achieve momentum-relaxation lengths in the 100 µm range at low temperature [38, 39]. Employing such a two-dimensional electron gas (2DEG) introduces additional challenges for the design of the experiment, because these 2DEG are very sensitive to electrostatic gating. Comparing the conductance of such samples for forward and reverse bias is challenging, because the bias reversal also shifts the electrostatic potentials and thus effectively gates the device. However, these challenges can be met by careful design of the device and measurement setup.

Apart from elemental metals and the semiconductor heterostructures, there are candidates for large electronic coherence lengths among the complex oxides. An example is given by the metallic delafossite $PdCoO_2$, for which bulk crystals with mean free paths of $\approx 20\,\mu\mathrm{m}$ have been reported [134–136]. The fabrication of conducting $PdCoO_2$ thin films was recently achieved [137]. UCF were observed in these films at much higher temperatures than for samples fabricated from elemental metals [B].

One of these approaches will hopefully lead to the observation of a restoration of reciprocity at low temperatures. The observation of nonreciprocal transport at intermediate temperatures, with reciprocity being restored at both large and very small temperatures,

would constitute a clear confirmation of the effect suggested in this thesis. Finally, it is also possible to conceive of experimental approaches that do not use the temperature to control the coherence length. For example, the proximity of a superconductor to a carbon nanotube can act as a switchable measurement device that prevents coherent quantum transport if active [138].

The experimental demonstration of the effect proposed in this thesis remains an interesting task for the future. The preliminary experimental results presented in this thesis are an encouraging starting point for further studies on the route towards novel electronic devices. These novel devices are characterized by functions that are impossible to achieve if the electrons are seen as purely quantum mechanical or purely classical particles, but possible only if both quantum and classical aspects are combined.

9 Literature

List of own Publications

[A] J. Mannhart, H. Boschker, and P. Bredol, "Non-unitary quantum electronics: Novel functions from the edge of the quantum world", Nano Express **2**, 014008 (2021, invited contribution).

[B] T. Harada, P. Bredol, H. Inoue, S. Ito, J. Mannhart, and A. Tsukazaki, "Determination of the phase coherence length of $PdCoO_2$ nanostructures by conductance fluctuation analysis", Phys. Rev. B **103**, 045123 (2021).

[C] P. Bredol, "Nonreciprocity of the wave-packet scattering delay in ballistic two-terminal devices", Phys. Rev. B **103**, 035404 (2021).

[D] P. Bredol, H. Boschker, D. Braak, and J. Mannhart, "Decoherence effects break reciprocity in matter transport", Phys. Rev. B **104**, 115413 (2021).

[E] J. Mannhart, P. Bredol, and D. Braak, "Phase filters for a novel kind of asymmetric transport — scientific prospects and opportunities for possible applications", Physica E, Low Dimens. Syst. Nanostruct. **109**, 198–200 (2019).

References

[1] A. Hirohata, K. Yamada, Y. Nakatani, I.-L. Prejbeanu, B. Diény, P. Pirro, and B. Hillebrands, "Review on spintronics: principles and device applications", J. Magn. Magn. Mater. **509**, 166711 (2020).

[2] C. Nayak, S. H. Simon, A. Stern, M. Freedman, and S. Das Sarma, "Non-abelian anyons and topological quantum computation", Rev. Mod. Phys. **80**, 1083–1159 (2008).

[3] X. Zhang, G. P. Zhao, H. Fangohr, J. P. Liu, W. X. Xia, J. Xia, and F. J. Morvan, "Skyrmion-skyrmion and skyrmion-edge repulsions in skyrmion-based racetrack memory", Sci. Rep. **5**, 7643 (2015).

[4] L. Gyongyosi and S. Imre, "A survey on quantum computing technology", Comput. Sci. Rev. **31**, 51–71 (2019).

[5] C. L. Degen, F. Reinhard, and P. Cappellaro, "Quantum sensing", Rev. Mod. Phys. **89**, 035002 (2017).

[6] M. Arndt, O. Nairz, J. Vos-Andreae, C. Keller, G. van der Zouw, and A. Zeilinger, "Wave-particle duality of C_{60} molecules", Nature **401**, 680–682 (1999).

[7] N. Bohr, "Can quantum-mechanical description of physical reality be considered complete?", Phys. Rev. **48**, 696–702 (1935).

[8] H. Everett, "Relative state formulation of quantum mechanics", Rev. Mod. Phys. **29**, 454–462 (1957).

[9] H. D. Zeh, "On the interpretation of measurement in quantum theory", Found. Phys. **1**, 69–76 (1970).

[10] G. C. Ghirardi, A. Rimini, and T. Weber, "Unified dynamics for microscopic and macroscopic systems", Phys. Rev. D **34**, 470–491 (1986).

[11] W. H. Zurek, "Decoherence, einselection, and the quantum origins of the classical", Rev. Mod. Phys. **75**, 715–775 (2003).

[12] A. J. Leggett, "The quantum measurement problem", Science **307**, 871–872 (2005).

[13] E. Joos, H. D. Zeh, C. Kiefer, D. J. Giulini, J. Kupsch, and I.-O. Stamatescu, *Decoherence and the appearance of a classical world in quantum theory* (Springer Science & Business Media, 2013).

[14] C. W. J. Beenakker and H. van Houten, "Quantum transport in semiconductor nanostructures", arXiv cond-mat/0412664 (2004).

[15] A. N. Broers, "High resolution electron beam fabrication: a brief review of experimental studies that began at Cambridge University in 1962", J. Microsc. **139**, 139–152 (1985).

[16] D. W. Carr and R. C. Tiberio, "Direct-write electron beam lithography: history and state of the art", Mater. Res. Soc. Symp. Proc. **584**, 33 (1999).

[17] R. Laibowitz and A. Broers, "Fabrication and physical properties of ultrasmall structures", in *Preparation and properties of thin films*, Vol. 24, edited by K. TU and R. Rosenberg, Treatise on Materials Science & Technology (Elsevier, 1982), pp. 285–311.

[18] L. Pfeiffer and K. West, "The role of MBE in recent quantum Hall effect physics discoveries", Physica E, Low Dimens. Syst. Nanostruct. **20**, 57–64 (2003).

[19] B. J. Hiley, "The early history of the Aharonov-Bohm effect", arXiv 1304.4736 (2013).

[20] Y. Aharonov and D. Bohm, "Significance of electromagnetic potentials in the quantum theory", Phys. Rev. **115**, 485–491 (1959).

[21] G. Möllenstedt and H. Düker, "Beobachtungen und Messungen an Biprisma-Interferenzen mit Elektronenwellen", Z. Angew. Phys. **145**, 377–397 (1956).

[22] G. Möllenstedt and W. Bayh, "Kontinuierliche Phasenschiebung von Elektronenwellen im kraftfeldfreien Raum durch das magnetische Vektorpotential eines Solenoids", Phys. Bl. **18**, 299–305 (1962).

[23] A. Tonomura, N. Osakabe, T. Matsuda, T. Kawasaki, J. Endo, S. Yano, and H. Yamada, "Evidence for Aharonov-Bohm effect with magnetic field completely shielded from electron wave", Phys. Rev. Lett. **56**, 792–795 (1986).

[24] R. A. Webb, S. Washburn, C. P. Umbach, and R. B. Laibowitz, "Observation of h/e Aharonov-Bohm oscillations in normal-metal rings", Phys. Rev. Lett. **54**, 2696–2699 (1985).

[25] R. Webb, S. Washburn, C. Umbach, F. Milliken, R. Laibowitz, and A. Benoit, "The Aharonov-Bohm effect in normal metals-non-ensemble averaged quantum transport", Physica A **140**, 175–182 (1986).

[26] R. Webb, S. Washburn, C. Umbach, and R. Laibowitz, "h/e Aharonov-Bohm effect in gold rings", J. Magn. Magn. Mater. **54-57**, 1423–1427 (1986).

[27] U. F. Keyser, C. Fühner, S. Borck, R. J. Haug, M. Bichler, G. Abstreiter, and W. Wegscheider, "Kondo effect in a few-electron quantum ring", Phys. Rev. Lett. **90**, 196601 (2003).

[28] Y. Ji, M. Heiblum, and H. Shtrikman, "Transmission phase of a quantum dot with Kondo correlation near the unitary limit", Phys. Rev. Lett. **88**, 076601 (2002).

[29] S. Takada, C. Bäuerle, M. Yamamoto, K. Watanabe, S. Hermelin, T. Meunier, A. Alex, A. Weichselbaum, J. von Delft, A. Ludwig, A. D. Wieck, and S. Tarucha, "Transmission phase in the Kondo regime revealed in a two-path interferometer", Phys. Rev. Lett. **113**, 126601 (2014).

[30] S. S. Buchholz, S. F. Fischer, U. Kunze, M. Bell, D. Reuter, and A. D. Wieck, "Control of the transmission phase in an asymmetric four-terminal Aharonov-Bohm interferometer", Phys. Rev. B **82**, 045432 (2010).

[31] S. Washburn and R. A. Webb, "Quantum transport in small disordered samples from the diffusive to the ballistic regime", Rep. Prog. Phys. **55**, 1311–1383 (1992).

[32] P. A. Lee and A. D. Stone, "Universal conductance fluctuations in metals", Phys. Rev. Lett. **55**, 1622–1625 (1985).

[33] P. A. Lee, A. D. Stone, and H. Fukuyama, "Universal conductance fluctuations in metals: effects of finite temperature, interactions, and magnetic field", Phys. Rev. B **35**, 1039–1070 (1987).

[34] M. Büttiker, Y. Imry, R. Landauer, and S. Pinhas, "Generalized many-channel conductance formula with application to small rings", Phys. Rev. B **31**, 6207–6215 (1985).

[35] V. Rodrigues, T. Fuhrer, and D. Ugarte, "Signature of atomic structure in the quantum conductance of gold nanowires", Phys. Rev. Lett. **85**, 4124–4127 (2000).

[36] V. V. Fisun and Y. I. Yanson, "Conductance quantization in metal nanowires produced by chemical anodization", J. Low Temp. Phys. **27**, 935–937 (2001).

[37] B. J. van Wees, H. van Houten, C. W. J. Beenakker, J. G. Williamson, L. P. Kouwenhoven, D. van der Marel, and C. T. Foxon, "Quantized conductance of point contacts in a two-dimensional electron gas", Phys. Rev. Lett. **60**, 848–850 (1988).

[38] V. Umansky, R. de-Picciotto, and M. Heiblum, "Extremely high-mobility two dimensional electron gas: evaluation of scattering mechanisms", Appl. Phys. Lett. **71**, 683–685 (1997).

[39] Y. J. Chung, K. A. Villegas Rosales, K. W. Baldwin, P. T. Madathil, K. W. West, M. Shayegan, and L. N. Pfeiffer, "Ultra-high-quality two-dimensional electron systems", Nat. Mater. **20**, 632–637 (2021).

[40] B. J. van Wees, L. P. Kouwenhoven, E. M. M. Willems, C. J. P. M. Harmans, J. E. Mooij, H. van Houten, C. W. J. Beenakker, J. G. Williamson, and C. T. Foxon, "Quantum ballistic and adiabatic electron transport studied with quantum point contacts", Phys. Rev. B **43**, 12431–12453 (1991).

[41] V. Chandrasekhar, P. Santhanam, and D. E. Prober, "Weak localization and conductance fluctuations in complex mesoscopic geometries", Phys. Rev. B **44**, 11203–11220 (1991).

[42] Y. V. Nazarov and Y. M. Blanter, *Quantum transport, Introduction to nanoscience* (Cambridge university press, 2009).

[43] B. Reulet, H. Bouchiat, and D. Mailly, "Magnetoconductance, weak localization and electron-electron interactions in semi-ballistic quantum wires", EPL **31**, 305 (1995).

[44] A. Carl, G. Dumpich, and E. Wassermann, "Determination of electrons scattering lengths in thin discontinuous gold-films", Physica A **157**, 177–180 (1989).

[45] J. J. Lin and J. P. Bird, "Recent experimental studies of electron dephasing in metal and semiconductor mesoscopic structures", J. Phys. Condens. Matter **14**, R501–R596 (2002).

[46] M. Büttiker, "Time-dependent transport in mesoscopic structures", J. Low Temp. Phys. **118**, 519–542 (2000).

[47] G. Bergmann, "Weak localization in thin films: a time-of-flight experiment with conduction electrons", Phys. Rep. **107**, 1–58 (1984).

[48] Y. Imry, "Delocalization, inelastic scattering and transport due to interactions", in *Mesoscopic electron transport*, edited by L. L. Sohn, L. P. Kouwenhoven, and G. Schön (Springer Netherlands, Dordrecht, 1997), pp. 83–103.

[49] S. Hikami, A. I. Larkin, and Y. Nagaoka, "Spin-orbit interaction and magnetoresistance in the two dimensional random system", Prog. Theor. Phys. **63**, 707–710 (1980).

[50] F. Schwabl, *Quantenmechanik (QM I)* (Springer-Verlag Berlin Heidelberg, 2007).

[51] R. Landauer, "Spatial variation of currents and fields due to localized scatterers in metallic conduction", IBM J. Res. Dev. **1**, 223–231 (1957).

[52] R. Landauer, "Residual resistivity dipoles", Z. Phys. B: Condens. Matter **21**, 247–254 (1975).

[53] R. Kubo, "Statistical-mechanical theory of irreversible processes. I. General theory and simple applications to magnetic and conduction problems", J. Phys. Soc. Japan **12**, 570–586 (1957).

[54] R. Landauer, "Electrical transport in open and closed systems", Z. Phys. B: Condens. Matter **68**, 217–228 (1987).

[55] E. N. Economou and C. M. Soukoulis, "Static conductance and scaling theory of localization in one dimension", Phys. Rev. Lett. **46**, 618–621 (1981).

[56] J. Mannhart, "Non-reciprocal interferometers for matter waves", J. Supercond. Nov. Magn. **31**, 1649–1657 (2018).

[57] E. P. Wigner and L. Eisenbud, "Higher angular momenta and long range interaction in resonance reactions", Phys. Rev. **72**, 29–41 (1947).

[58] E. P. Wigner, "Lower limit for the energy derivative of the scattering phase shift", Phys. Rev. **98**, 145–147 (1955).

[59] F. T. Smith, "Lifetime matrix in collision theory", Phys. Rev. **118**, 349–356 (1960).

[60] D. Sánchez and M. Büttiker, "Magnetic-field asymmetry of nonlinear mesoscopic transport", Phys. Rev. Lett. **93**, 106802 (2004).

[61] M. L. Polianski and M. Büttiker, "Mesoscopic fluctuations of nonlinear conductance of chaotic quantum dots", Phys. Rev. Lett. **96**, 156804 (2006).

[62] M. Büttiker, A. Prêtre, and H. Thomas, "Dynamic conductance and the scattering matrix of small conductors", Phys. Rev. Lett. **70**, 4114–4117 (1993).

[63] M. Buttiker, “Capacitance, admittance, and rectification properties of small conductors”, J. Condens. Matter Phys. **5**, 9361–9378 (1993).

[64] V. Gasparian, T. Christen, and M. Büttiker, “Partial densities of states, scattering matrices, and Green’s functions”, Phys. Rev. A **54**, 4022–4031 (1996).

[65] D. Chauvat, O. Emile, F. Bretenaker, and A. Le Floch, “Direct measurement of the Wigner delay associated with the Goos-Hänchen effect”, Phys. Rev. Lett. **84**, 71–74 (2000).

[66] R. Bourgain, J. Pellegrino, S. Jennewein, Y. R. P. Sortais, and A. Browaeys, “Direct measurement of the Wigner time delay for the scattering of light by a single atom”, Opt. Lett. **38**, 1963–1965 (2013).

[67] G. Yamahata, S. Ryu, N. Johnson, H.-S. Sim, A. Fujiwara, and M. Kataoka, “Picosecond coherent electron motion in a silicon single-electron source”, Nature Nanotechnol. **14**, 1019–1023 (2019).

[68] Z. Ringel, Y. Imry, and O. Entin-Wohlman, “Delayed currents and interaction effects in mesoscopic capacitors”, Phys. Rev. B **78**, 165304 (2008).

[69] M. Yamamoto, S. Takada, C. Bäuerle, K. Watanabe, A. D. Wieck, and S. Tarucha, “Electrical control of a solid-state flying qubit”, Nat. Nanotechnol. **7**, 247– (2012).

[70] M. Strauß, A. Carmele, J. Schleibner, M. Hohn, C. Schneider, S. Höfling, J. Wolters, and S. Reitzenstein, “Wigner time delay induced by a single quantum dot”, Phys. Rev. Lett. **122**, 107401 (2019).

[71] Y. Li, J. Zhou, F. Marchesoni, and B. Li, “Wave-packet rectification in nonlinear electronic systems: a tunable Aharonov-Bohm diode”, Sci. Rep. **4**, 4566– (2014).

[72] B. Szafran, B. Rzeszotarski, and A. Mreńca-Kolasińska, “Topologically protected wave packets and quantum rings in silicene”, Phys. Rev. B **100**, 085306 (2019).

[73] C. W. Groth, M. Wimmer, A. R. Akhmerov, and X. Waintal, “Kwant: a software package for quantum transport”, New J. Phys. **16**, 063065 (2014).

[74] A. Stern, Y. Aharonov, and Y. Imry, “Phase uncertainty and loss of interference: a general picture”, Phys. Rev. A **41**, 3436–3448 (1990).

[75] A. E. Hansen, A. Kristensen, S. Pedersen, C. B. Sørensen, and P. E. Lindelof, “Mesoscopic decoherence in Aharonov-Bohm rings”, Phys. Rev. B **64**, 045327 (2001).

[76] J. v. Neumann, “Beweis des Ergodensatzes und des H-Theorems in der neuen Mechanik”, Z. Phys. **57**, 30–70 (1929).

[77] M. Büttiker, “Role of quantum coherence in series resistors”, Phys. Rev. B **33**, 3020–3026 (1986).

[78] R. Kubo, M. Yokota, and S. Nakajima, "Statistical-mechanical theory of irreversible processes. II. Response to thermal disturbance", J. Phys. Soc. Japan **12**, 1203–1211 (1957).

[79] Y. Gefen, Y. Imry, and M. Y. Azbel, "Quantum oscillations and the Aharonov-Bohm effect for parallel resistors", Phys. Rev. Lett. **52**, 129–132 (1984).

[80] Y. Blanter and M. Büttiker, "Shot noise in mesoscopic conductors", Phys. Rep. **336**, 1–166 (2000).

[81] S. Feng, "Quantum transport in the presence of phase-breaking scattering: generalized landauer formula", Physica A **168**, 439–446 (1990).

[82] C. Benjamin and A. M. Jayannavar, "Dephasing via stochastic absorption: a case study in Aharonov-Bohm oscillations", Phys. Rev. B **65**, 153309 (2002).

[83] A. J. Daley, "Quantum trajectories and open many-body quantum systems", Advances in Physics **63**, 77–149 (2014).

[84] H. Carmichael, *An open systems approach to quantum optics*, Vol. 18 (Springer Science & Business Media, 2009).

[85] N. Gisin and I. C. Percival, "The quantum-state diffusion model applied to open systems", Journal of Physics A: Mathematical and General **25**, 5677–5691 (1992).

[86] R. Dum, P. Zoller, and H. Ritsch, "Monte Carlo simulation of the atomic master equation for spontaneous emission", Phys. Rev. A **45**, 4879–4887 (1992).

[87] R. Dum, A. S. Parkins, P. Zoller, and C. W. Gardiner, "Monte Carlo simulation of master equations in quantum optics for vacuum, thermal, and squeezed reservoirs", Phys. Rev. A **46**, 4382–4396 (1992).

[88] M. B. Plenio and P. L. Knight, "The quantum-jump approach to dissipative dynamics in quantum optics", Rev. Mod. Phys. **70**, 101–144 (1998).

[89] K. Mølmer, Y. Castin, and J. Dalibard, "Monte Carlo wave-function method in quantum optics", J. Opt. Soc. Am. B **10**, 524–538 (1993).

[90] F. Rossi, *Theory of semiconductor quantum devices, Microscopic modeling and simulation strategies* (Springer Science & Business Media, 2011).

[91] F. Dolcini, R. C. Iotti, and F. Rossi, "Interplay between energy dissipation and reservoir-induced thermalization in nonequilibrium quantum nanodevices", Phys. Rev. B **88**, 115421 (2013).

[92] P. R. Eastham, A. O. Spracklen, and J. Keeling, "Lindblad theory of dynamical decoherence of quantum-dot excitons", Phys. Rev. B **87**, 195306 (2013).

[93] O. Sauret, D. Feinberg, and T. Martin, "Quantum master equations for the superconductor–quantum dot entangler", Phys. Rev. B **70**, 245313 (2004).

[94] F. Brange, O. Malkoc, and P. Samuelsson, "Subdecoherence time generation and detection of orbital entanglement in quantum dots", Phys. Rev. Lett. **114**, 176803 (2015).

[95] L. D. Contreras-Pulido and R. Aguado, "Entanglement between charge qubits induced by a common dissipative environment", Phys. Rev. B **77**, 155420 (2008).

[96] N. Lambert and F. Nori, "Detecting quantum-coherent nanomechanical oscillations using the current-noise spectrum of a double quantum dot", Phys. Rev. B **78**, 214302 (2008).

[97] G. Lindblad, "On the generators of quantum dynamical semigroups", Commun. Math. Phys. **48**, 119–130 (1976).

[98] V. Gorini, A. Kossakowski, and E. C. G. Sudarshan, "Completely positive dynamical semigroups of n-level systems", J. Math. Phys. **17**, 821–825 (1976).

[99] M. Falconi, J. Faupin, J. Fröhlich, and B. Schubnel, "Scattering theory for Lindblad master equations", Commun. Math. Phys. **350**, 1185–1218 (2017).

[100] V. V. Albert and L. Jiang, "Symmetries and conserved quantities in Lindblad master equations", Phys. Rev. A **89**, 022118 (2014).

[101] N. Ashcroft and N. Mermin, *Solid state physics* (Saunders College Publishing, 1976).

[102] C. M. Goringe, D. R. Bowler, and E. Hernández, "Tight-binding modelling of materials", Rep. Prog. Phys **60**, 1447–1512 (1997).

[103] A. García-Cristóbal and A. Molina-Sánchez, "Tight-binding simulations of nanowires", in *Encyclopedia of nanotechnology*, edited by B. Bhushan (Springer Netherlands, Dordrecht, 2016), pp. 4178–4189.

[104] E. Cheney and D. Kincaid, *Numerical mathematics and computing* (Brooks/Cole Publishing Company, 2007).

[105] R. Peierls, "Zur Theorie des Diamagnetismus von Leitungselektronen", Z. Phys. **80**, 763–791 (1933).

[106] B. Misra and E. C. G. Sudarshan, "The Zeno's paradox in quantum theory", J. Math. Phys. **18**, 756–763 (1977).

[107] D. Sánchez and K. Kang, "Validity and breakdown of Onsager symmetry in mesoscopic conductors interacting with environments", Phys. Rev. Lett. **100**, 036806, 036806 (2008).

[108] D. M. Zumbühl, C. M. Marcus, M. P. Hanson, and A. C. Gossard, "Asymmetry of nonlinear transport and electron interactions in quantum dots", Phys. Rev. Lett. **96**, 206802 (2006).

[109] M. Brotons-Gisbert, A. Branny, S. Kumar, R. Picard, R. Proux, M. Gray, K. S. Burch, K. Watanabe, T. Taniguchi, and B. D. Gerardot, "Coulomb blockade in an atomically thin quantum dot coupled to a tunable Fermi reservoir", Nat. Nanotechnol. **14**, 442–446 (2019).

[110] C. A. Marlow, R. P. Taylor, M. Fairbanks, I. Shorubalko, and H. Linke, "Experimental investigation of the breakdown of the Onsager-Casimir relations", Phys. Rev. Lett. **96**, 116801 (2006).

[111] M. Josefsson, A. Svilans, A. M. Burke, E. A. Hoffmann, S. Fahlvik, C. Thelander, M. Leijnse, and H. Linke, "A quantum-dot heat engine operating close to the thermodynamic efficiency limits", Nat. Nanotechnol. **13**, 920–924 (2018).

[112] Y. Tokura and N. Nagaosa, "Nonreciprocal responses from non-centrosymmetric quantum materials", Nat. Commun. **9** (2018).

[113] R. Leturcq, D. Sánchez, G. Götz, T. Ihn, K. Ensslin, D. C. Driscoll, and A. C. Gossard, "Magnetic field symmetry and phase rigidity of the nonlinear conductance in a ring", Phys. Rev. Lett. **96**, 126801 (2006).

[114] L. Angers, E. Zakka-Bajjani, R. Deblock, S. Guéron, H. Bouchiat, A. Cavanna, U. Gennser, and M. Polianski, "Magnetic-field asymmetry of mesoscopic *dc* rectification in Aharonov-Bohm rings", Phys. Rev. B **75**, 115309 (2007).

[115] A. Yacoby, R. Schuster, and M. Heiblum, "Phase rigidity and $h/2e$ oscillations in a single-ring Aharonov-Bohm experiment", Phys. Rev. B **53**, 9583–9586 (1996).

[116] R. Leturcq, R. Bianchetti, G. Götz, T. Ihn, K. Ensslin, D. Driscoll, and A. Gossard, "Coherent nonlinear transport in quantum rings", Physica E, Low Dimens. Syst. Nanostruct. **35**, 327–331 (2006).

[117] R. Wakatsuki, Y. Saito, S. Hoshino, Y. M. Itahashi, T. Ideue, M. Ezawa, Y. Iwasa, and N. Nagaosa, "Nonreciprocal charge transport in noncentrosymmetric superconductors", Sci. Adv. **3**, 3740 (2017).

[118] R. Kalina, B. Szafran, S. Bednarek, and F. M. Peeters, "Magnetic-field asymmetry of electron wave packet transmission in bent channels capacitively coupled to a metal gate", Phys. Rev. Lett. **102**, 066807 (2009).

[119] B. Szafran and F. M. Peeters, "Time-dependent simulations of electron transport through a quantum ring: effect of the Lorentz force", Phys. Rev. B **72**, 165301 (2005).

[120] B. Szafran, M. R. Poniedziałek, and F. M. Peeters, "Violation of Onsager symmetry for a ballistic channel Coulomb coupled to a quantum ring", EPL **87**, 47002 (2009).

[121] E. Li, B. J. Eggleton, K. Fang, and S. Fan, "Photonic Aharonov-Bohm effect in photon-phonon interactions", Nat. Commun. **5**, 3225 (2014).

[122] L. D. Tzuang, K. Fang, P. Nussenzveig, S. Fan, and M. Lipson, "Non-reciprocal phase shift induced by an effective magnetic flux for light", Nat. Photonics **8**, 701 (2014).

[123] D. Braak and J. Mannhart, "Fermi's golden rule and the second law of thermodynamics", Found. Phys. **50**, 1509–1540 (2020).

[124] R. Taboryski, A. K. Geim, M. Persson, and P. E. Lindelof, "Nonlinear conductance at small driving voltages in quantum point contacts", Phys. Rev. B **49**, 7813–7816 (1994).

[125] P. H. M. van Loosdrecht, C. W. J. Beenakker, H. van Houten, J. G. Williamson, B. J. van Wees, J. E. Mooij, C. T. Foxon, and J. J. Harris, "Aharonov-Bohm effect in a singly connected point contact", Phys. Rev. B **38**, 10162–10165 (1988).

[126] P. G. N. de Vegvar, G. Timp, P. M. Mankiewich, J. E. Cunningham, R. Behringer, and R. E. Howard, "Second-harmonic generation in submicrometer GaAs$-$Al$_x$Ga$_{1-x}$As wires and rings", Phys. Rev. B **38**, 4326–4328 (1988).

[127] C. Beenakker and H. van Houten, "Quantum transport in semiconductor nanostructures", in *Semiconductor heterostructures and nanostructures*, Vol. 44, edited by H. Ehrenreich and D. Turnbull, Solid State Physics (Academic Press, 1991), pp. 1–228.

[128] R. A. Matula, "Electrical resistivity of copper, gold, palladium, and silver", J. Phys. Chem. Ref. Data **8**, 1147–1298 (1979).

[129] J. De Vries, "Temperature and thickness dependence of the resistivity of thin polycrystalline aluminium, cobalt, nickel, palladium, silver and gold films", Thin Solid Films **167**, 25–32 (1988).

[130] S. Pi, C. Li, H. Jiang, W. Xia, H. Xin, J. J. Yang, and Q. Xia, "Memristor crossbar arrays with 6-nm half-pitch and 2-nm critical dimension", Nat. Nanotechnol. **14**, 35–39 (2018).

[131] B. Kuiper, J. L. Blok, H. J.W. Zandvliet, D. Blank, G. Rijnders, and G. Koster, "Self-organization of $SrRuO_3$ nanowires on ordered oxide surface terminations", MRS Commun. **1**, 17–21 (2011).

[132] H. B. G. Casimir, "Reciprocity theorems and irreversible processes", Proc. IEEE **51**, 1570–1573 (1963).

[133] R. Rosati, R. C. Iotti, F. Dolcini, and F. Rossi, "Derivation of nonlinear single-particle equations via many-body Lindblad superoperators: a density-matrix approach", Phys. Rev. B **90**, 125140 (2014).

[134] C. W. Hicks, A. S. Gibbs, A. P. Mackenzie, H. Takatsu, Y. Maeno, and E. A. Yelland, "Quantum oscillations and high carrier mobility in the delafossite $PdCoO_2$", Phys. Rev. Lett. **109**, 116401 (2012).

[135] H. Takatsu, S. Yonezawa, S. Mouri, S. Nakatsuji, K. Tanaka, and Y. Maeno, "Roles of high-frequency optical phonons in the physical properties of the conductive delafossite $PdCoO_2$", J. Phys. Soc. Japan **76**, 104701 (2007).

[136] M. D. Bachmann, A. L. Sharpe, A. W. Barnard, C. Putzke, M. König, S. Khim, D. Goldhaber-Gordon, A. P. Mackenzie, and P. J. W. Moll, "Super-geometric electron focusing on the hexagonal Fermi surface of $PdCoO_2$", Nat. Commun. **10**, 5081 (2019).

[137] T. Harada, K. Fujiwara, and A. Tsukazaki, "Highly conductive $PdCoO_2$ ultrathin films for transparent electrodes", APL Mater. **6**, 046107 (2018).

[138] Y.-F. Chen, T. Dirks, G. Al-Zoubi, N. O. Birge, and N. Mason, "Nonequilibrium tunneling spectroscopy in carbon nanotubes", Phys. Rev. Lett. **102**, 036804 (2009).

Acronyms

2DEG two-dimensional electron gas

AB Aharonov-Bohm

DOF degrees of freedom

DUT device under test

EBE electron beam evaporation

EBL electron-beam lithography

MBE molecular beam epitaxy

RRR residual resistance ratio

SEM scanning electron microscope

UCF universal conductance fluctuations

Symbols

i imaginary unit

$\arg(z)$ complex argument of z

A^{T} transpose of A

A^* complex conjugate of A

A^{-1} inverse of A

$A^\dagger$ conjugated transpose of A, adjoint of A

$\left[\hat{\boldsymbol{A}}, \hat{\boldsymbol{B}}\right]$ commutator of $\hat{\boldsymbol{A}}$ and $\hat{\boldsymbol{B}}$: $\hat{\boldsymbol{A}}\hat{\boldsymbol{B}} - \hat{\boldsymbol{B}}\hat{\boldsymbol{A}}$

$\left\{\hat{\boldsymbol{A}}, \hat{\boldsymbol{B}}\right\}$ anti-commutator of $\hat{\boldsymbol{A}}$ and $\hat{\boldsymbol{B}}$: $\hat{\boldsymbol{A}}\hat{\boldsymbol{B}} + \hat{\boldsymbol{B}}\hat{\boldsymbol{A}}$

∂_a derivation with respect to a

∇ Nabla operator, derivative with respect to the three directions in space $(\partial_x, \partial_y, \partial_z)^{\mathrm{T}}$

$\mathrm{Ai}(x), \mathrm{Bi}(x), \mathrm{Ai'}(x), \mathrm{Bi'}(x)$ Airy functions of first and second kind and their derivatives

$\boldsymbol{A} \times \boldsymbol{B}$ vector product of vectors $\boldsymbol{A}$ and $\boldsymbol{B}$

a eigenbasis coefficient

$\hat{\boldsymbol{a}}$ annihilation operator

$\boldsymbol{A}$ electromagnetic vector potential

A preamp gain

$\mathcal{A}_{\mathrm{CA}}$ amplitude of the Ai function

$\mathcal{A}_{\mathrm{CB}}$ amplitude of the Bi function

$\mathcal{A}_{\mathrm{CL}}$ amplitude of the left moving plane wave in the central region

$\mathcal{A}_{\mathrm{CR}}$ amplitude of the right moving plane wave in the central region

$\mathcal{A}_{\mathrm{DL}}$ amplitude of the left moving plane wave in the central region

$\mathcal{A}_{\mathrm{DR}}$ amplitude of the right moving plane wave in the central region

$\mathcal{A}^{-}$ amplitude of the outgoing plane wave

$\mathcal{A}^{-}_{\mathrm{L}}$ amplitude of the plane wave leaving to the left

$\mathcal{A}^{-}_{\mathrm{R}}$ amplitude of the plane wave leaving to the right

$\mathcal{A}^{+}$ amplitude of the incoming plane wave

$\mathcal{A}^{+}_{\mathrm{L}}$ amplitude of the plane wave arriving from the left

$\mathcal{A}^{+}_{\mathrm{R}}$ amplitude of the plane wave arriving from the right

A_x x-component of $\boldsymbol{A}$

A_y y-component of $\boldsymbol{A}$

A_z z-component of $\boldsymbol{A}$

b integer number

b' integer number

$\boldsymbol{B}$ magnetic flux density

B_z z-component of the magnetic flux density

$\hat{\boldsymbol{C}}$ jump operator

d path length

δd path length difference

θ_{AB} two-path Aharonov-Bohm (AB) phase difference

$\delta \boldsymbol{r}$ lattice vector of a periodic lead

E energy

G conductance

G_0 conductance quantum

γ Airy function argument

Γ system-bath coupling rate

$\hat{\boldsymbol{H}}$ Hamiltonian

$\hat{\boldsymbol{H}}_{\mathrm{nh}}$ non-Hermitian Hamiltonian

H Hamiltonian element

$\boldsymbol{H}$ magnetic field

h Planck constant

$\hbar$ reduced Planck constant

I current

I_{ac} AC excitation current

I_{bias} DC bias current

$\mathcal{I}$ probability current

$\boldsymbol{k}$ wave vector

k momentum

k_0 central momentum

κ propagation constant

κ_{i} imaginary part of the propagation constant

κ_{r} real part of the propagation constant

k_{B} Boltzmann constant

k_{L} left moving plane wave momentum

k_{R} right moving plane wave momentum

k_x wave vector x-component

k_y wave vector y-component

$\boldsymbol{l}$ path

λ eigenvalue

Λ tight-binding lattice

l_Φ phase coherence length

L_x scattering region length

m mass

M number of scattering channels

μ Fermi level

$|m\rangle$ site m basis vector

$\langle m|$ site m basis vector

n density

N_l number of leads

N_s number of sites

N_r number of sites in the region of interest

$|n\rangle$ site n basis vector

$\langle n|$ site n basis vector

$\mathrm{NN}\,(\Lambda)$ next nearest neighbors

$\mathrm{NN}_x\,(\Lambda)$ nearest neighbors in x direction

$\mathrm{NN}_y\,(\Lambda)$ nearest neighbors in y direction

$\hat{\boldsymbol{O}}$ observable

ω lock-in frequency

p probability

$\hat{\boldsymbol{\mathcal{P}}}$ lead-exchange operator

Φ scattering phase

$\boldsymbol{\Phi}$ magnetic flux

$\boldsymbol{\Phi}_0$ magnetic flux quantum

$\boldsymbol{\phi}$ eigenfunction

$\boldsymbol{\phi}^-$ wave front of the outgoing plane wave

$\boldsymbol{\phi}^+$ wave front of the incoming plane wave

$\hat{\boldsymbol{P}}$ projection operator

$\hat{\boldsymbol{P}}_\perp$ orthogonal complement of $\hat{\boldsymbol{P}}$

$\boldsymbol{\psi}$ wave function

P_{tr} transmission probability

$P_{\mathrm{L}\to\mathrm{R}}$ transmission probability from left to right side

$P_{\mathrm{R}\to\mathrm{L}}$ transmission probability from right to left side

P_{re} reflection probability

$\hat{\boldsymbol{p}}$ momentum operator

$\hat{\boldsymbol{p}}_x$ momentum operator x-component

q elementary charge

$\mathcal{Q}$ integrated probability current

$\boldsymbol{r}$ position

r radius

$\hat{\boldsymbol{\rho}}$ density operator

R resistance

R_s series resistor

$\boldsymbol{S}$ scattering matrix

s scattering coefficient

$\boldsymbol{S}_{\mathrm{BS}}$ ideal beam-splitter scattering matrix

σ_k momentum spread

σ_x position spread

t time

$\hat{\boldsymbol{\mathcal{T}}}$ time-reversal operator

T temperature

τ wave-packet scattering delay

τ_{c} mean time between two measurements

δt time difference

$\boldsymbol{T}$ site-basis-to-eigenbasis transformation matrix

$\boldsymbol{T}^\dagger$ eigenbasis-to-site-basis transformation matrix

$\boldsymbol{T}_r$ reduced site-basis-to-eigenbasis transformation matrix

$\boldsymbol{T}_r^\dagger$ eigenbasis-to-reduced-site-basis transformation matrix

$\hat{\boldsymbol{U}}$ time-evolution operator

V voltage

V_{ac} AC excitation voltage

V_{bias} DC bias voltage

V_{in} measured AC voltage amplitude

$\partial V/\partial I$ differential resistance

$\mathcal{V}$ electrostatic potential

$\mathcal{V}_{\mathrm{L}}$ left side potential

$\mathcal{V}_{\mathrm{R}}$ right side potential

$\mathcal{W}$ region

$\mathcal{W}_\alpha$ region of lead α

$\mathcal{W}_s$ scattering region

$\hat{\boldsymbol{X}}$ x-position operator

x_0 central position

$\hat{\boldsymbol{Y}}$ y-position operator

Acknowledgements

I would like to kindly thank all the helpful and friendly people that I met during my time in Stuttgart. First of all, I would like to thank Prof. Jochen Mannhart for the initial idea and for entrusting me with this project. I would further like to deeply thank him, Daniel Braak and Hans Boschker for their efforts spent on this project and for the countless discussions. I would like to thank Hans for sharing his experience with quantum transport and for the valuable advice on pitfalls of transport experiments and data analysis. Without Daniel's help, none of theoretical results presented in Chapters 3, 4 and 5 would have been possible. I deeply acknowledge Prof. Regina Dittmann for the friendly supervision despite the the long distance to Aachen and for her visits in February 2019 and for the Ringberg meeting 2019.

Further, I would like to express my gratitude towards the staff of our institute's Nanostructuring Lab, who do an excellent job running and maintaining an outstanding cleanroom infrastructure. I would like to thank Jürgen Weis for the organization and continuous improvement of the equipment. I would like to thank Achim Güth, Thomas Reindl and Ulrike Waizmann for introducing me to lithography, thin-film deposition, and the countless other machines and tools in the cleanroom. I would also like to thank them for sharing their nanostructuring expertise and for patiently answering my questions. I would like to also kindly thank Gennadii Laskin, a former PhD student of the group, for sharing his process recipes and for recommending my nowadays favorite e-beam resist to me. I would like to thank Wolfgang Braun for his advice on how to achieve clean gold films, for pushing me to use the cryopanels of the deposition chamber and for the countless inspiring scientific and nonscientific discussions.

Many of the numerical results shown in this work would not have been possible without the institute's HPC cluster. Therefore, I kindly thank Armin Burkhardt and Armin Schuhmacher for helping me with converting my programs to the massively parallelized versions necessary in a cluster environment and for general advice on good practice for long running calculations.

Moreover, I would like to thank Sabine Seiffert, Wolfgang Winter, Ingo Hagel, Konrad Lazarus and Manfred Schmid for their amazing support with the low temperature experiments. Especially in 2019, when it was not possible for me to look after the cryostat, Sabine, Ingo and Wolfgang stood in and took over all the required tasks.

I kindly thank Prof. Mannhart, Daniel Braak, Hans Boschker, Max Brucker, Tom

Whittles, my girlfriend Shirin and my father Michael for proofreading of this manuscript.

Also, I kindly thank Takayuki Harada for an equally busy and fun week filled with nanostructuring, electron microscopy and dinners at da Franco.

I greatly appreciate everyone that helps to make the institute this friendly place that it is. I would like to thank Hans Boschker, Fabian Felden, Evangelos Fillis-Tsirakis, Dong-Yeong Kim, Wilson Lin, Prosper Ngabonziza, Rezgar Osman, Arnaud Pastel Nono, Iman Rastegar, Thomas Smart, Sander Smink, Ali Teker, Wolfgang Voesch, Robin Wanke, Thomas Whittles and Pascal Wittlich for the inspiring discussions and fun times we had in coffee corners, offices, laboratories, Bärenschlössle, Sonnenuhrhütte and the Auld Rogue.

I owe very special thanks to my family, to Shirin and to my close friends from Münster that each contributed their share to where I am today and for their support during 2019.

Finally, I would like to thank all the maintainers and contributors of scientific open-source projects and open-source projects in general. Simulation, data analysis and visualization are greatly simplified by the Python data science ecosystem including `numpy`, `scipy` and `matplotlib`. There is no question hard enough not be be answered on one of the countless boards of the stackexchange network. For this work, the packages `Kwant` and `QuTiP` were of great value, both to produce numerical results and to learn about quantum mechanics.

Importable Expressions

A

The following code blocks were generated using SymPy's export functionality and can be imported by package or program given in the title of the block with the respective import routine. The evaluation of the code block yields the analytic expression object for the entries of the scattering matrix of the scattering problems described in Chapter 3. If you have problems importing these expressions, feel free to write an email to philipp.bredol@rwth-aachen.de.

A.1 Symmetric Potential Barrier

A.1.1 Reflection Coefficient $s_{11} = s_{22}$

Expression for Python's SymPy package:

```
(kappa**2*exp(2*I*L_x*kappa) - kappa**2 - k**2*exp(2*I*L_x*kappa) + k**2)*exp(-I*L_x*k)/(-kappa
    **2*exp(2*I*L_x*kappa) + kappa**2 + 2*kappa*k*exp(2*I*L_x*kappa) + 2*kappa*k - k**2*exp(2*
    I*L_x*kappa) + k**2)
```

Expression for Matlab and Octave:

```
(kappa.^2.*exp(2*1i*L_x.*kappa) - kappa.^2 - k.^2.*exp(2*1i*L_x.*kappa) + k.^2).*exp(-1i*L_x.*k
    )./(-kappa.^2.*exp(2*1i*L_x.*kappa) + kappa.^2 + 2*kappa.*k.*exp(2*1i*L_x.*kappa) + 2*
    kappa.*k - k.^2.*exp(2*1i*L_x.*kappa) + k.^2)
```

Expression for Mathematica:

```
(kappa^2*Exp[2*I*L_x*kappa] - kappa^2 - k^2*Exp[2*I*L_x*kappa] + k^2)*Exp[-I*L_x*k]/(-kappa^2*
    Exp[2*I*L_x*kappa] + kappa^2 + 2*kappa*k*Exp[2*I*L_x*kappa] + 2*kappa*k - k^2*Exp[2*I*L_x*
    kappa] + k^2)
```

Expression for Maple:

```
(kappa^2*exp(2*I*L_x*kappa) - kappa^2 - k^2*exp(2*I*L_x*kappa) + k^2)*exp(-I*L_x*k)/(-kappa^2*
    exp(2*I*L_x*kappa) + kappa^2 + 2*kappa*k*exp(2*I*L_x*kappa) + 2*kappa*k - k^2*exp(2*I*L_x*
    kappa) + k^2)
```

A.1.2 Transmission Coefficient $s_{12} = s_{21}$

Expression for Python's SymPy package:

```
4*kappa*k*exp(I*L_x*(kappa - k))/(-kappa**2*exp(2*I*L_x*kappa) + kappa**2 + 2*kappa*k*exp(2*I*
    L_x*kappa) + 2*kappa*k - k**2*exp(2*I*L_x*kappa) + k**2)
```

Expression for Matlab and Octave:

```
4*kappa.*k.*exp(1i*L_x.*(kappa - k))./(-kappa.^2.*exp(2*1i*L_x.*kappa) + kappa.^2 + 2*kappa.*k
    .*exp(2*1i*L_x.*kappa) + 2*kappa.*k - k.^2.*exp(2*1i*L_x.*kappa) + k.^2)
```

Expression for Mathematica:

```
4*kappa*k*Exp[I*L_x*(kappa - k)]/(-kappa^2*Exp[2*I*L_x*kappa] + kappa^2 + 2*kappa*k*Exp[2*I*L_x
    *kappa] + 2*kappa*k - k^2*Exp[2*I*L_x*kappa] + k^2)
```

Expression for Maple:

```
4*kappa*k*exp(I*L_x*(kappa - k))/(-kappa^2*exp(2*I*L_x*kappa) + kappa^2 + 2*kappa*k*exp(2*I*L_x
    *kappa) + 2*kappa*k - k^2*exp(2*I*L_x*kappa) + k^2)
```

A.2 Asymmetric Potential Barrier

A.2.1 Left Side Reflection Coefficient s_{11}

Expression for Python's SymPy package:

```
(2**(1/3)*L_x**(2/3)*k**2*airyai(L_x**(2/3)*(-E + V_l)/(-V_l + V_r)**(2/3))*airybi(L_x**(2/3)
    *(-E + V_r)/(-V_l + V_r)**(2/3)) - 2**(1/3)*L_x**(2/3)*k**2*airyai(L_x**(2/3)*(-E + V_r)
    /(-V_l + V_r)**(2/3))*airybi(L_x**(2/3)*(-E + V_l)/(-V_l + V_r)**(2/3)) + 2**(1/3)*I*L_x
    **(1/3)*k*(-V_l + V_r)**(1/3)*airyai(L_x**(2/3)*(-E + V_l)/(-V_l + V_r)**(2/3))*
    airybiprime(L_x**(2/3)*(-E + V_r)/(-V_l + V_r)**(2/3)) - 2**(1/3)*I*L_x**(1/3)*k*(-V_l +
    V_r)**(1/3)*airyai(L_x**(2/3)*(-E + V_r)/(-V_l + V_r)**(2/3))*airybiprime(L_x**(2/3)*(-E +
     V_l)/(-V_l + V_r)**(2/3)) + 2**(1/3)*I*L_x**(1/3)*k*(-V_l + V_r)**(1/3)*airyaiprime(L_x
    **(2/3)*(-E + V_l)/(-V_l + V_r)**(2/3))*airybi(L_x**(2/3)*(-E + V_r)/(-V_l + V_r)**(2/3))
    - 2**(1/3)*I*L_x**(1/3)*k*(-V_l + V_r)**(1/3)*airyaiprime(L_x**(2/3)*(-E + V_r)/(-V_l +
    V_r)**(2/3))*airybi(L_x**(2/3)*(-E + V_l)/(-V_l + V_r)**(2/3)) - 2**(1/3)*(-V_l + V_r)
    **(2/3)*airyaiprime(L_x**(2/3)*(-E + V_l)/(-V_l + V_r)**(2/3))*airybiprime(L_x**(2/3)*(-E
    + V_r)/(-V_l + V_r)**(2/3)) + 2**(1/3)*(-V_l + V_r)**(2/3)*airyaiprime(L_x**(2/3)*(-E +
    V_r)/(-V_l + V_r)**(2/3))*airybiprime(L_x**(2/3)*(-E + V_l)/(-V_l + V_r)**(2/3)))*exp(-I*
    L_x*k)/(2**(1/3)*L_x**(2/3)*k**2*airyai(L_x**(2/3)*(-E + V_l)/(-V_l + V_r)**(2/3))*airybi(
    L_x**(2/3)*(-E + V_r)/(-V_l + V_r)**(2/3)) - 2**(1/3)*L_x**(2/3)*k**2*airyai(L_x**(2/3)*(-
    E + V_r)/(-V_l + V_r)**(2/3))*airybi(L_x**(2/3)*(-E + V_l)/(-V_l + V_r)**(2/3)) + 2**(1/3)
    *I*L_x**(1/3)*k*(-V_l + V_r)**(1/3)*airyai(L_x**(2/3)*(-E + V_l)/(-V_l + V_r)**(2/3))*
    airybiprime(L_x**(2/3)*(-E + V_r)/(-V_l + V_r)**(2/3)) + 2**(1/3)*I*L_x**(1/3)*k*(-V_l +
    V_r)**(1/3)*airyai(L_x**(2/3)*(-E + V_r)/(-V_l + V_r)**(2/3))*airybiprime(L_x**(2/3)*(-E +
     V_l)/(-V_l + V_r)**(2/3)) - 2**(1/3)*I*L_x**(1/3)*k*(-V_l + V_r)**(1/3)*airyaiprime(L_x
    **(2/3)*(-E + V_l)/(-V_l + V_r)**(2/3))*airybi(L_x**(2/3)*(-E + V_r)/(-V_l + V_r)**(2/3))
    - 2**(1/3)*I*L_x**(1/3)*k*(-V_l + V_r)**(1/3)*airyaiprime(L_x**(2/3)*(-E + V_r)/(-V_l +
    V_r)**(2/3))*airybi(L_x**(2/3)*(-E + V_l)/(-V_l + V_r)**(2/3)) + 2**(1/3)*(-V_l + V_r)
    **(2/3)*airyaiprime(L_x**(2/3)*(-E + V_l)/(-V_l + V_r)**(2/3))*airybiprime(L_x**(2/3)*(-E
    + V_r)/(-V_l + V_r)**(2/3)) - 2**(1/3)*(-V_l + V_r)**(2/3)*airyaiprime(L_x**(2/3)*(-E +
    V_r)/(-V_l + V_r)**(2/3))*airybiprime(L_x**(2/3)*(-E + V_l)/(-V_l + V_r)**(2/3)))
```

Expression for Matlab and Octave:

```
(2^(1/3)*L_x.^(2/3).*k.^2.*airy(0, L_x.^(2/3).*(-E + V_l)./(-V_l + V_r).^(2/3)).*airy(2, L_x
    .^(2/3).*(-E + V_r)./(-V_l + V_r).^(2/3)) - 2^(1/3)*L_x.^(2/3).*k.^2.*airy(0, L_x.^(2/3)
    .*(-E + V_r)./(-V_l + V_r).^(2/3)).*airy(2, L_x.^(2/3).*(-E + V_l)./(-V_l + V_r).^(2/3)) +
     2^(1/3)*1i*L_x.^(1/3).*k.*(-V_l + V_r).^(1/3).*airy(0, L_x.^(2/3).*(-E + V_l)./(-V_l +
    V_r).^(2/3)).*airy(3, L_x.^(2/3).*(-E + V_r)./(-V_l + V_r).^(2/3)) - 2^(1/3)*1i*L_x.^(1/3)
    .*k.*(-V_l + V_r).^(1/3).*airy(0, L_x.^(2/3).*(-E + V_r)./(-V_l + V_r).^(2/3)).*airy(3,
    L_x.^(2/3).*(-E + V_l)./(-V_l + V_r).^(2/3)) + 2^(1/3)*1i*L_x.^(1/3).*k.*(-V_l + V_r)
    .^(1/3).*airy(1, L_x.^(2/3).*(-E + V_l)./(-V_l + V_r).^(2/3)).*airy(2, L_x.^(2/3).*(-E +
    V_r)./(-V_l + V_r).^(2/3)) - 2^(1/3)*1i*L_x.^(1/3).*k.*(-V_l + V_r).^(1/3).*airy(1, L_x
    .^(2/3).*(-E + V_r)./(-V_l + V_r).^(2/3)).*airy(2, L_x.^(2/3).*(-E + V_l)./(-V_l + V_r)
    .^(2/3)) - 2^(1/3)*(-V_l + V_r).^(2/3).*airy(1, L_x.^(2/3).*(-E + V_l)./(-V_l + V_r)
    .^(2/3)).*airy(3, L_x.^(2/3).*(-E + V_r)./(-V_l + V_r).^(2/3)) + 2^(1/3)*(-V_l + V_r)
    .^(2/3).*airy(1, L_x.^(2/3).*(-E + V_r)./(-V_l + V_r).^(2/3)).*airy(3, L_x.^(2/3).*(-E +
    V_l)./(-V_l + V_r).^(2/3)).*exp(-1i*L_x.*k)./(2^(1/3)*L_x.^(2/3).*k.^2.*airy(0, L_x
    .^(2/3).*(-E + V_l)./(-V_l + V_r).^(2/3)).*airy(2, L_x.^(2/3).*(-E + V_r)./(-V_l + V_r)
    .^(2/3)) - 2^(1/3)*L_x.^(2/3).*k.^2.*airy(0, L_x.^(2/3).*(-E + V_r)./(-V_l + V_r).^(2/3))
    .*airy(2, L_x.^(2/3).*(-E + V_l)./(-V_l + V_r).^(2/3)) + 2^(1/3)*1i*L_x.^(1/3).*k.*(-V_l +
     V_r).^(1/3).*airy(0, L_x.^(2/3).*(-E + V_l)./(-V_l + V_r).^(2/3)).*airy(3, L_x.^(2/3).*(-
    E + V_r)./(-V_l + V_r).^(2/3)) + 2^(1/3)*1i*L_x.^(1/3).*k.*(-V_l + V_r).^(1/3).*airy(0,
    L_x.^(2/3).*(-E + V_r)./(-V_l + V_r).^(2/3)).*airy(3, L_x.^(2/3).*(-E + V_l)./(-V_l + V_r)
    .^(2/3)) - 2^(1/3)*1i*L_x.^(1/3).*k.*(-V_l + V_r).^(1/3).*airy(1, L_x.^(2/3).*(-E + V_l)
    ./(-V_l + V_r).^(2/3)).*airy(2, L_x.^(2/3).*(-E + V_r)./(-V_l + V_r).^(2/3)) - 2^(1/3)*1i*
    L_x.^(1/3).*k.*(-V_l + V_r).^(1/3).*airy(1, L_x.^(2/3).*(-E + V_r)./(-V_l + V_r).^(2/3)).*
    airy(2, L_x.^(2/3).*(-E + V_l)./(-V_l + V_r).^(2/3)) + 2^(1/3)*(-V_l + V_r).^(2/3).*airy
    (1, L_x.^(2/3).*(-E + V_l)./(-V_l + V_r).^(2/3)).*airy(3, L_x.^(2/3).*(-E + V_r)./(-V_l +
    V_r).^(2/3)) - 2^(1/3)*(-V_l + V_r).^(2/3).*airy(1, L_x.^(2/3).*(-E + V_r)./(-V_l + V_r)
    .^(2/3)).*airy(3, L_x.^(2/3).*(-E + V_l)./(-V_l + V_r).^(2/3)))
```

Expression for Mathematica:

```
(2^(1/3)*L_x^(2/3)*k^2*AiryAi[L_x^(2/3)*(-E + V_l)/(-V_l + V_r)^(2/3)]*AiryBi[L_x^(2/3)*(-E +
    V_r)/(-V_l + V_r)^(2/3)] - 2^(1/3)*L_x^(2/3)*k^2*AiryAi[L_x^(2/3)*(-E + V_r)/(-V_l + V_r)
    ^(2/3)]*AiryBi[L_x^(2/3)*(-E + V_l)/(-V_l + V_r)^(2/3)] + 2^(1/3)*I*L_x^(1/3)*k*(-V_l +
    V_r)^(1/3)*AiryAi[L_x^(2/3)*(-E + V_l)/(-V_l + V_r)^(2/3)]*AiryBiPrime[L_x^(2/3)*(-E + V_r
    )/(-V_l + V_r)^(2/3)] - 2^(1/3)*I*L_x^(1/3)*k*(-V_l + V_r)^(1/3)*AiryAi[L_x^(2/3)*(-E +
    V_r)/(-V_l + V_r)^(2/3)]*AiryBiPrime[L_x^(2/3)*(-E + V_l)/(-V_l + V_r)^(2/3)] + 2^(1/3)*I*
    L_x^(1/3)*k*(-V_l + V_r)^(1/3)*AiryAiPrime[L_x^(2/3)*(-E + V_l)/(-V_l + V_r)^(2/3)]*AiryBi
    [L_x^(2/3)*(-E + V_r)/(-V_l + V_r)^(2/3)] - 2^(1/3)*I*L_x^(1/3)*k*(-V_l + V_r)^(1/3)*
    AiryAiPrime[L_x^(2/3)*(-E + V_r)/(-V_l + V_r)^(2/3)]*AiryBi[L_x^(2/3)*(-E + V_l)/(-V_l +
    V_r)^(2/3)] - 2^(1/3)*(-V_l + V_r)^(2/3)*AiryAiPrime[L_x^(2/3)*(-E + V_l)/(-V_l + V_r)
    ^(2/3)]*AiryBiPrime[L_x^(2/3)*(-E + V_r)/(-V_l + V_r)^(2/3)] + 2^(1/3)*(-V_l + V_r)^(2/3)*
    AiryAiPrime[L_x^(2/3)*(-E + V_r)/(-V_l + V_r)^(2/3)]*AiryBiPrime[L_x^(2/3)*(-E + V_l)/(-
    V_l + V_r)^(2/3)])*Exp[-I*L_x*k]/(2^(1/3)*L_x^(2/3)*k^2*AiryAi[L_x^(2/3)*(-E + V_l)/(-V_l
    + V_r)^(2/3)]*AiryBi[L_x^(2/3)*(-E + V_r)/(-V_l + V_r)^(2/3)] - 2^(1/3)*L_x^(2/3)*k^2*
    AiryAi[L_x^(2/3)*(-E + V_r)/(-V_l + V_r)^(2/3)]*AiryBi[L_x^(2/3)*(-E + V_l)/(-V_l + V_r)
    ^(2/3)] + 2^(1/3)*I*L_x^(1/3)*k*(-V_l + V_r)^(1/3)*AiryAi[L_x^(2/3)*(-E + V_l)/(-V_l + V_r
    )^(2/3)]*AiryBiPrime[L_x^(2/3)*(-E + V_r)/(-V_l + V_r)^(2/3)] + 2^(1/3)*I*L_x^(1/3)*k*(-
    V_l + V_r)^(1/3)*AiryAi[L_x^(2/3)*(-E + V_r)/(-V_l + V_r)^(2/3)]*AiryBiPrime[L_x^(2/3)*(-E
     + V_l)/(-V_l + V_r)^(2/3)] - 2^(1/3)*I*L_x^(1/3)*k*(-V_l + V_r)^(1/3)*AiryAiPrime[L_x
    ^(2/3)*(-E + V_l)/(-V_l + V_r)^(2/3)]*AiryBi[L_x^(2/3)*(-E + V_r)/(-V_l + V_r)^(2/3)] -
    2^(1/3)*I*L_x^(1/3)*k*(-V_l + V_r)^(1/3)*AiryAiPrime[L_x^(2/3)*(-E + V_r)/(-V_l + V_r)
    ^(2/3)]*AiryBi[L_x^(2/3)*(-E + V_l)/(-V_l + V_r)^(2/3)] + 2^(1/3)*(-V_l + V_r)^(2/3)*
    AiryAiPrime[L_x^(2/3)*(-E + V_l)/(-V_l + V_r)^(2/3)]*AiryBiPrime[L_x^(2/3)*(-E + V_r)/(-
    V_l + V_r)^(2/3)] - 2^(1/3)*(-V_l + V_r)^(2/3)*AiryAiPrime[L_x^(2/3)*(-E + V_r)/(-V_l +
    V_r)^(2/3)]*AiryBiPrime[L_x^(2/3)*(-E + V_l)/(-V_l + V_r)^(2/3)])
```

Expression for Maple:

```
(2^(1/3)*L_x^(2/3)*k^2*AiryAi(L_x^(2/3)*(-E + V_l)/(-V_l + V_r)^(2/3))*AiryBi(L_x^(2/3)*(-E +
    V_r)/(-V_l + V_r)^(2/3)) - 2^(1/3)*L_x^(2/3)*k^2*AiryAi(L_x^(2/3)*(-E + V_r)/(-V_l + V_r)
    ^(2/3))*AiryBi(L_x^(2/3)*(-E + V_l)/(-V_l + V_r)^(2/3)) + 2^(1/3)*I*L_x^(1/3)*k*(-V_l +
    V_r)^(1/3)*AiryAi(L_x^(2/3)*(-E + V_l)/(-V_l + V_r)^(2/3))*airybiprime(L_x^(2/3)*(-E + V_r
    )/(-V_l + V_r)^(2/3)) - 2^(1/3)*I*L_x^(1/3)*k*(-V_l + V_r)^(1/3)*AiryAi(L_x^(2/3)*(-E +
    V_r)/(-V_l + V_r)^(2/3))*airybiprime(L_x^(2/3)*(-E + V_l)/(-V_l + V_r)^(2/3)) + 2^(1/3)*I*
    L_x^(1/3)*k*(-V_l + V_r)^(1/3)*airyaiprime(L_x^(2/3)*(-E + V_l)/(-V_l + V_r)^(2/3))*AiryBi
    (L_x^(2/3)*(-E + V_r)/(-V_l + V_r)^(2/3)) - 2^(1/3)*I*L_x^(1/3)*k*(-V_l + V_r)^(1/3)*
    airyaiprime(L_x^(2/3)*(-E + V_r)/(-V_l + V_r)^(2/3))*AiryBi(L_x^(2/3)*(-E + V_l)/(-V_l +
    V_r)^(2/3)) - 2^(1/3)*(-V_l + V_r)^(2/3)*airyaiprime(L_x^(2/3)*(-E + V_l)/(-V_l + V_r)
    ^(2/3))*airybiprime(L_x^(2/3)*(-E + V_r)/(-V_l + V_r)^(2/3)) + 2^(1/3)*(-V_l + V_r)^(2/3)*
    airyaiprime(L_x^(2/3)*(-E + V_r)/(-V_l + V_r)^(2/3))*airybiprime(L_x^(2/3)*(-E + V_l)/(-
    V_l + V_r)^(2/3))*exp(-I*L_x*k)/(2^(1/3)*L_x^(2/3)*k^2*AiryAi(L_x^(2/3)*(-E + V_l)/(-V_l
    + V_r)^(2/3))*AiryBi(L_x^(2/3)*(-E + V_r)/(-V_l + V_r)^(2/3)) - 2^(1/3)*L_x^(2/3)*k^2*
    AiryAi(L_x^(2/3)*(-E + V_r)/(-V_l + V_r)^(2/3))*AiryBi(L_x^(2/3)*(-E + V_l)/(-V_l + V_r)
    ^(2/3)) + 2^(1/3)*I*L_x^(1/3)*k*(-V_l + V_r)^(1/3)*AiryAi(L_x^(2/3)*(-E + V_l)/(-V_l + V_r
    )^(2/3))*airybiprime(L_x^(2/3)*(-E + V_r)/(-V_l + V_r)^(2/3)) + 2^(1/3)*I*L_x^(1/3)*k*(-
    V_l + V_r)^(1/3)*AiryAi(L_x^(2/3)*(-E + V_r)/(-V_l + V_r)^(2/3))*airybiprime(L_x^(2/3)*(-E
     + V_l)/(-V_l + V_r)^(2/3)) - 2^(1/3)*I*L_x^(1/3)*k*(-V_l + V_r)^(1/3)*airyaiprime(L_x
    ^(2/3)*(-E + V_l)/(-V_l + V_r)^(2/3))*AiryBi(L_x^(2/3)*(-E + V_r)/(-V_l + V_r)^(2/3)) -
    2^(1/3)*I*L_x^(1/3)*k*(-V_l + V_r)^(1/3)*airyaiprime(L_x^(2/3)*(-E + V_r)/(-V_l + V_r)
    ^(2/3))*AiryBi(L_x^(2/3)*(-E + V_l)/(-V_l + V_r)^(2/3)) + 2^(1/3)*(-V_l + V_r)^(2/3)*
    airyaiprime(L_x^(2/3)*(-E + V_l)/(-V_l + V_r)^(2/3))*airybiprime(L_x^(2/3)*(-E + V_r)/(-
    V_l + V_r)^(2/3)) - 2^(1/3)*(-V_l + V_r)^(2/3)*airyaiprime(L_x^(2/3)*(-E + V_r)/(-V_l +
    V_r)^(2/3))*airybiprime(L_x^(2/3)*(-E + V_l)/(-V_l + V_r)^(2/3)))
```

A.2.2 Right Side Reflection Coefficient s_{22}

Expression for Python's SymPy package:

```
(2**(1/3)*L_x**(2/3)*k**2*airyai(L_x**(2/3)*(-E + V_l)/(-V_l + V_r)**(2/3))*airybi(L_x**(2/3)
    *(-E + V_r)/(-V_l + V_r)**(2/3)) - 2**(1/3)*L_x**(2/3)*k**2*airyai(L_x**(2/3)*(-E + V_r)
    /(-V_l + V_r)**(2/3))*airybi(L_x**(2/3)*(-E + V_l)/(-V_l + V_r)**(2/3)) - 2**(1/3)*I*L_x
    **(1/3)*k*(-V_l + V_r)**(1/3)*airyai(L_x**(2/3)*(-E + V_l)/(-V_l + V_r)**(2/3))*
    airybiprime(L_x**(2/3)*(-E + V_r)/(-V_l + V_r)**(2/3)) + 2**(1/3)*I*L_x**(1/3)*k*(-V_l +
    V_r)**(1/3)*airyai(L_x**(2/3)*(-E + V_r)/(-V_l + V_r)**(2/3))*airybiprime(L_x**(2/3)*(-E +
     V_l)/(-V_l + V_r)**(2/3)) - 2**(1/3)*I*L_x**(1/3)*k*(-V_l + V_r)**(1/3)*airyaiprime(L_x
    **(2/3)*(-E + V_l)/(-V_l + V_r)**(2/3))*airybi(L_x**(2/3)*(-E + V_r)/(-V_l + V_r)**(2/3))
    + 2**(1/3)*I*L_x**(1/3)*k*(-V_l + V_r)**(1/3)*airyaiprime(L_x**(2/3)*(-E + V_r)/(-V_l +
    V_r)**(2/3))*airybi(L_x**(2/3)*(-E + V_l)/(-V_l + V_r)**(2/3)) - 2**(1/3)*(-V_l + V_r)
    **(2/3)*airyaiprime(L_x**(2/3)*(-E + V_l)/(-V_l + V_r)**(2/3))*airybiprime(L_x**(2/3)*(-E
    + V_r)/(-V_l + V_r)**(2/3)) + 2**(1/3)*(-V_l + V_r)**(2/3)*airyaiprime(L_x**(2/3)*(-E +
    V_r)/(-V_l + V_r)**(2/3))*airybiprime(L_x**(2/3)*(-E + V_l)/(-V_l + V_r)**(2/3)))*exp(-I*
    L_x*k)/(2**(1/3)*L_x**(2/3)*k**2*airyai(L_x**(2/3)*(-E + V_l)/(-V_l + V_r)**(2/3))*airybi(
    L_x**(2/3)*(-E + V_r)/(-V_l + V_r)**(2/3)) - 2**(1/3)*L_x**(2/3)*k**2*airyai(L_x**(2/3)*(-
    E + V_r)/(-V_l + V_r)**(2/3))*airybi(L_x**(2/3)*(-E + V_l)/(-V_l + V_r)**(2/3)) + 2**(1/3)
    *I*L_x**(1/3)*k*(-V_l + V_r)**(1/3)*airyai(L_x**(2/3)*(-E + V_l)/(-V_l + V_r)**(2/3))*
    airybiprime(L_x**(2/3)*(-E + V_r)/(-V_l + V_r)**(2/3)) + 2**(1/3)*I*L_x**(1/3)*k*(-V_l +
    V_r)**(1/3)*airyai(L_x**(2/3)*(-E + V_r)/(-V_l + V_r)**(2/3))*airybiprime(L_x**(2/3)*(-E +
     V_l)/(-V_l + V_r)**(2/3)) - 2**(1/3)*I*L_x**(1/3)*k*(-V_l + V_r)**(1/3)*airyaiprime(L_x
    **(2/3)*(-E + V_l)/(-V_l + V_r)**(2/3))*airybi(L_x**(2/3)*(-E + V_r)/(-V_l + V_r)**(2/3))
    - 2**(1/3)*I*L_x**(1/3)*k*(-V_l + V_r)**(1/3)*airyaiprime(L_x**(2/3)*(-E + V_r)/(-V_l +
    V_r)**(2/3))*airybi(L_x**(2/3)*(-E + V_l)/(-V_l + V_r)**(2/3)) + 2**(1/3)*(-V_l + V_r)
    **(2/3)*airyaiprime(L_x**(2/3)*(-E + V_l)/(-V_l + V_r)**(2/3))*airybiprime(L_x**(2/3)*(-E
    + V_r)/(-V_l + V_r)**(2/3)) - 2**(1/3)*(-V_l + V_r)**(2/3)*airyaiprime(L_x**(2/3)*(-E +
    V_r)/(-V_l + V_r)**(2/3))*airybiprime(L_x**(2/3)*(-E + V_l)/(-V_l + V_r)**(2/3)))
```

Expression for Matlab and Octave:

```
(2^(1/3)*L_x.^(2/3).*k.^2.*airy(0, L_x.^(2/3).*(-E + V_l)./(-V_l + V_r).^(2/3)).*airy(2, L_x
    .^(2/3).*(-E + V_r)./(-V_l + V_r).^(2/3)) - 2^(1/3)*L_x.^(2/3).*k.^2.*airy(0, L_x.^(2/3)
    .*(-E + V_r)./(-V_l + V_r).^(2/3)).*airy(2, L_x.^(2/3).*(-E + V_l)./(-V_l + V_r).^(2/3)) -
     2^(1/3)*1i*L_x.^(1/3).*k.*(-V_l + V_r).^(1/3).*airy(0, L_x.^(2/3).*(-E + V_l)./(-V_l +
    V_r).^(2/3)).*airy(3, L_x.^(2/3).*(-E + V_r)./(-V_l + V_r).^(2/3)) + 2^(1/3)*1i*L_x.^(1/3)
    .*k.*(-V_l + V_r).^(1/3).*airy(0, L_x.^(2/3).*(-E + V_r)./(-V_l + V_r).^(2/3)).*airy(3,
    L_x.^(2/3).*(-E + V_l)./(-V_l + V_r).^(2/3)) - 2^(1/3)*1i*L_x.^(1/3).*k.*(-V_l + V_r)
    .^(1/3).*airy(1, L_x.^(2/3).*(-E + V_l)./(-V_l + V_r).^(2/3)).*airy(2, L_x.^(2/3).*(-E +
    V_r)./(-V_l + V_r).^(2/3)) + 2^(1/3)*1i*L_x.^(1/3).*k.*(-V_l + V_r).^(1/3).*airy(1, L_x
    .^(2/3).*(-E + V_r)./(-V_l + V_r).^(2/3)).*airy(2, L_x.^(2/3).*(-E + V_l)./(-V_l + V_r)
    .^(2/3)) - 2^(1/3)*(-V_l + V_r).^(2/3).*airy(1, L_x.^(2/3).*(-E + V_l)./(-V_l + V_r)
    .^(2/3)).*airy(3, L_x.^(2/3).*(-E + V_r)./(-V_l + V_r).^(2/3)) + 2^(1/3)*(-V_l + V_r)
    .^(2/3).*airy(1, L_x.^(2/3).*(-E + V_r)./(-V_l + V_r).^(2/3)).*airy(3, L_x.^(2/3).*(-E +
    V_l)./(-V_l + V_r).^(2/3))).*exp(-1i*L_x.*k)./(2^(1/3)*L_x.^(2/3).*k.^2.*airy(0, L_x
    .^(2/3).*(-E + V_l)./(-V_l + V_r).^(2/3)).*airy(2, L_x.^(2/3).*(-E + V_r)./(-V_l + V_r)
    .^(2/3)) - 2^(1/3)*L_x.^(2/3).*k.^2.*airy(0, L_x.^(2/3).*(-E + V_r)./(-V_l + V_r).^(2/3))
    .*airy(2, L_x.^(2/3).*(-E + V_l)./(-V_l + V_r).^(2/3)) + 2^(1/3)*1i*L_x.^(1/3).*k.*(-V_l +
     V_r).^(1/3).*airy(0, L_x.^(2/3).*(-E + V_l)./(-V_l + V_r).^(2/3)).*airy(3, L_x.^(2/3).*(-
    E + V_r)./(-V_l + V_r).^(2/3)) + 2^(1/3)*1i*L_x.^(1/3).*k.*(-V_l + V_r).^(1/3).*airy(0,
    L_x.^(2/3).*(-E + V_r)./(-V_l + V_r).^(2/3)).*airy(3, L_x.^(2/3).*(-E + V_l)./(-V_l + V_r)
    .^(2/3)) - 2^(1/3)*1i*L_x.^(1/3).*k.*(-V_l + V_r).^(1/3).*airy(1, L_x.^(2/3).*(-E + V_l)
    ./(-V_l + V_r).^(2/3)).*airy(2, L_x.^(2/3).*(-E + V_r)./(-V_l + V_r).^(2/3)) - 2^(1/3)*1i*
    L_x.^(1/3).*k.*(-V_l + V_r).^(1/3).*airy(1, L_x.^(2/3).*(-E + V_r)./(-V_l + V_r).^(2/3)).*
    airy(2, L_x.^(2/3).*(-E + V_l)./(-V_l + V_r).^(2/3)) + 2^(1/3)*(-V_l + V_r).^(2/3).*airy
    (1, L_x.^(2/3).*(-E + V_l)./(-V_l + V_r).^(2/3)).*airy(3, L_x.^(2/3).*(-E + V_r)./(-V_l +
    V_r).^(2/3)) - 2^(1/3)*(-V_l + V_r).^(2/3).*airy(1, L_x.^(2/3).*(-E + V_r)./(-V_l + V_r)
    .^(2/3)).*airy(3, L_x.^(2/3).*(-E + V_l)./(-V_l + V_r).^(2/3)))
```

Expression for Mathematica:

```
(2^(1/3)*L_x^(2/3)*k^2*AiryAi[L_x^(2/3)*(-E + V_l)/(-V_l + V_r)^(2/3)]*AiryBi[L_x^(2/3)*(-E +
    V_r)/(-V_l + V_r)^(2/3)] - 2^(1/3)*L_x^(2/3)*k^2*AiryAi[L_x^(2/3)*(-E + V_r)/(-V_l + V_r)
    ^(2/3)]*AiryBi[L_x^(2/3)*(-E + V_l)/(-V_l + V_r)^(2/3)] - 2^(1/3)*I*L_x^(1/3)*k*(-V_l +
    V_r)^(1/3)*AiryAi[L_x^(2/3)*(-E + V_l)/(-V_l + V_r)^(2/3)]*AiryBiPrime[L_x^(2/3)*(-E + V_r
    )/(-V_l + V_r)^(2/3)] + 2^(1/3)*I*L_x^(1/3)*k*(-V_l + V_r)^(1/3)*AiryAi[L_x^(2/3)*(-E +
    V_r)/(-V_l + V_r)^(2/3)]*AiryBiPrime[L_x^(2/3)*(-E + V_l)/(-V_l + V_r)^(2/3)] - 2^(1/3)*I*
    L_x^(1/3)*k*(-V_l + V_r)^(1/3)*AiryAiPrime[L_x^(2/3)*(-E + V_l)/(-V_l + V_r)^(2/3)]*AiryBi
    [L_x^(2/3)*(-E + V_r)/(-V_l + V_r)^(2/3)] + 2^(1/3)*I*L_x^(1/3)*k*(-V_l + V_r)^(1/3)*
    AiryAiPrime[L_x^(2/3)*(-E + V_r)/(-V_l + V_r)^(2/3)]*AiryBi[L_x^(2/3)*(-E + V_l)/(-V_l +
    V_r)^(2/3)] - 2^(1/3)*(-V_l + V_r)^(2/3)*AiryAiPrime[L_x^(2/3)*(-E + V_l)/(-V_l + V_r)
    ^(2/3)]*AiryBiPrime[L_x^(2/3)*(-E + V_r)/(-V_l + V_r)^(2/3)] + 2^(1/3)*(-V_l + V_r)^(2/3)*
    AiryAiPrime[L_x^(2/3)*(-E + V_r)/(-V_l + V_r)^(2/3)]*AiryBiPrime[L_x^(2/3)*(-E + V_l)/(-
    V_l + V_r)^(2/3)])*Exp[-I*L_x*k]/(2^(1/3)*L_x^(2/3)*k^2*AiryAi[L_x^(2/3)*(-E + V_l)/(-V_l
    + V_r)^(2/3)]*AiryBi[L_x^(2/3)*(-E + V_r)/(-V_l + V_r)^(2/3)] - 2^(1/3)*L_x^(2/3)*k^2*
    AiryAi[L_x^(2/3)*(-E + V_r)/(-V_l + V_r)^(2/3)]*AiryBi[L_x^(2/3)*(-E + V_l)/(-V_l + V_r)
    ^(2/3)] + 2^(1/3)*I*L_x^(1/3)*k*(-V_l + V_r)^(1/3)*AiryAi[L_x^(2/3)*(-E + V_l)/(-V_l + V_r
    )^(2/3)]*AiryBiPrime[L_x^(2/3)*(-E + V_r)/(-V_l + V_r)^(2/3)] + 2^(1/3)*I*L_x^(1/3)*k*(-
    V_l + V_r)^(1/3)*AiryAi[L_x^(2/3)*(-E + V_r)/(-V_l + V_r)^(2/3)]*AiryBiPrime[L_x^(2/3)*(-E
     + V_l)/(-V_l + V_r)^(2/3)] - 2^(1/3)*I*L_x^(1/3)*k*(-V_l + V_r)^(1/3)*AiryAiPrime[L_x
    ^(2/3)*(-E + V_l)/(-V_l + V_r)^(2/3)]*AiryBi[L_x^(2/3)*(-E + V_r)/(-V_l + V_r)^(2/3)] -
    2^(1/3)*I*L_x^(1/3)*k*(-V_l + V_r)^(1/3)*AiryAiPrime[L_x^(2/3)*(-E + V_r)/(-V_l + V_r)
    ^(2/3)]*AiryBi[L_x^(2/3)*(-E + V_l)/(-V_l + V_r)^(2/3)] + 2^(1/3)*(-V_l + V_r)^(2/3)*
    AiryAiPrime[L_x^(2/3)*(-E + V_l)/(-V_l + V_r)^(2/3)]*AiryBiPrime[L_x^(2/3)*(-E + V_r)/(-
    V_l + V_r)^(2/3)] - 2^(1/3)*(-V_l + V_r)^(2/3)*AiryAiPrime[L_x^(2/3)*(-E + V_r)/(-V_l +
    V_r)^(2/3)]*AiryBiPrime[L_x^(2/3)*(-E + V_l)/(-V_l + V_r)^(2/3)])
```

Expression for Maple:

```
(2^(1/3)*L_x^(2/3)*k^2*AiryAi(L_x^(2/3)*(-E + V_l)/(-V_l + V_r)^(2/3))*AiryBi(L_x^(2/3)*(-E +
    V_r)/(-V_l + V_r)^(2/3)) - 2^(1/3)*L_x^(2/3)*k^2*AiryAi(L_x^(2/3)*(-E + V_r)/(-V_l + V_r)
    ^(2/3))*AiryBi(L_x^(2/3)*(-E + V_l)/(-V_l + V_r)^(2/3)) - 2^(1/3)*I*L_x^(1/3)*k*(-V_l +
    V_r)^(1/3)*AiryAi(L_x^(2/3)*(-E + V_l)/(-V_l + V_r)^(2/3))*airybiprime(L_x^(2/3)*(-E + V_r
    )/(-V_l + V_r)^(2/3)) + 2^(1/3)*I*L_x^(1/3)*k*(-V_l + V_r)^(1/3)*AiryAi(L_x^(2/3)*(-E +
    V_r)/(-V_l + V_r)^(2/3))*airybiprime(L_x^(2/3)*(-E + V_l)/(-V_l + V_r)^(2/3)) - 2^(1/3)*I*
    L_x^(1/3)*k*(-V_l + V_r)^(1/3)*airyaiprime(L_x^(2/3)*(-E + V_l)/(-V_l + V_r)^(2/3))*AiryBi
    (L_x^(2/3)*(-E + V_r)/(-V_l + V_r)^(2/3)) + 2^(1/3)*I*L_x^(1/3)*k*(-V_l + V_r)^(1/3)*
    airyaiprime(L_x^(2/3)*(-E + V_r)/(-V_l + V_r)^(2/3))*AiryBi(L_x^(2/3)*(-E + V_l)/(-V_l +
    V_r)^(2/3)) - 2^(1/3)*(-V_l + V_r)^(2/3)*airyaiprime(L_x^(2/3)*(-E + V_l)/(-V_l + V_r)
    ^(2/3))*airybiprime(L_x^(2/3)*(-E + V_r)/(-V_l + V_r)^(2/3)) + 2^(1/3)*(-V_l + V_r)^(2/3)*
    airyaiprime(L_x^(2/3)*(-E + V_r)/(-V_l + V_r)^(2/3))*airybiprime(L_x^(2/3)*(-E + V_l)/(-
    V_l + V_r)^(2/3))*exp(-I*L_x*k)/(2^(1/3)*L_x^(2/3)*k^2*AiryAi(L_x^(2/3)*(-E + V_l)/(-V_l
    + V_r)^(2/3))*AiryBi(L_x^(2/3)*(-E + V_r)/(-V_l + V_r)^(2/3)) - 2^(1/3)*L_x^(2/3)*k^2*
    AiryAi(L_x^(2/3)*(-E + V_r)/(-V_l + V_r)^(2/3))*AiryBi(L_x^(2/3)*(-E + V_l)/(-V_l + V_r)
    ^(2/3)) + 2^(1/3)*I*L_x^(1/3)*k*(-V_l + V_r)^(1/3)*AiryAi(L_x^(2/3)*(-E + V_l)/(-V_l + V_r
    )^(2/3))*airybiprime(L_x^(2/3)*(-E + V_r)/(-V_l + V_r)^(2/3)) + 2^(1/3)*I*L_x^(1/3)*k*(-
    V_l + V_r)^(1/3)*AiryAi(L_x^(2/3)*(-E + V_r)/(-V_l + V_r)^(2/3))*airybiprime(L_x^(2/3)*(-E
     + V_l)/(-V_l + V_r)^(2/3)) - 2^(1/3)*I*L_x^(1/3)*k*(-V_l + V_r)^(1/3)*airyaiprime(L_x
    ^(2/3)*(-E + V_l)/(-V_l + V_r)^(2/3))*AiryBi(L_x^(2/3)*(-E + V_r)/(-V_l + V_r)^(2/3)) -
    2^(1/3)*I*L_x^(1/3)*k*(-V_l + V_r)^(1/3)*airyaiprime(L_x^(2/3)*(-E + V_r)/(-V_l + V_r)
    ^(2/3))*AiryBi(L_x^(2/3)*(-E + V_l)/(-V_l + V_r)^(2/3)) + 2^(1/3)*(-V_l + V_r)^(2/3)*
    airyaiprime(L_x^(2/3)*(-E + V_l)/(-V_l + V_r)^(2/3))*airybiprime(L_x^(2/3)*(-E + V_r)/(-
    V_l + V_r)^(2/3)) - 2^(1/3)*(-V_l + V_r)^(2/3)*airyaiprime(L_x^(2/3)*(-E + V_r)/(-V_l +
    V_r)^(2/3))*airybiprime(L_x^(2/3)*(-E + V_l)/(-V_l + V_r)^(2/3)))
```

A.2.3 Transmission Coefficient $s_{12} = s_{21}$

Expression for Python's SymPy package:

```
2*2**(1/3)*I*L_x**(1/3)*k*(-V_l + V_r)**(1/3)*(airyai(L_x**(2/3)*(-E + V_l)/(-V_l + V_r)**(2/3)
    )*airybiprime(L_x**(2/3)*(-E + V_l)/(-V_l + V_r)**(2/3)) - airyaiprime(L_x**(2/3)*(-E +
    V_l)/(-V_l + V_r)**(2/3))*airybi(L_x**(2/3)*(-E + V_l)/(-V_l + V_r)**(2/3)))*exp(-I*L_x*k)
    /(2**(1/3)*L_x**(2/3)*k**2*airyai(L_x**(2/3)*(-E + V_l)/(-V_l + V_r)**(2/3))*airybi(L_x
    **(2/3)*(-E + V_r)/(-V_l + V_r)**(2/3)) - 2**(1/3)*L_x**(2/3)*k**2*airyai(L_x**(2/3)*(-E +
     V_r)/(-V_l + V_r)**(2/3))*airybi(L_x**(2/3)*(-E + V_l)/(-V_l + V_r)**(2/3)) + 2**(1/3)*I*
    L_x**(1/3)*k*(-V_l + V_r)**(1/3)*airyai(L_x**(2/3)*(-E + V_l)/(-V_l + V_r)**(2/3))*
    airybiprime(L_x**(2/3)*(-E + V_r)/(-V_l + V_r)**(2/3)) + 2**(1/3)*I*L_x**(1/3)*k*(-V_l +
    V_r)**(1/3)*airyai(L_x**(2/3)*(-E + V_r)/(-V_l + V_r)**(2/3))*airybiprime(L_x**(2/3)*(-E +
     V_l)/(-V_l + V_r)**(2/3)) - 2**(1/3)*I*L_x**(1/3)*k*(-V_l + V_r)**(1/3)*airyaiprime(L_x
    **(2/3)*(-E + V_l)/(-V_l + V_r)**(2/3))*airybi(L_x**(2/3)*(-E + V_r)/(-V_l + V_r)**(2/3))
    - 2**(1/3)*I*L_x**(1/3)*k*(-V_l + V_r)**(1/3)*airyaiprime(L_x**(2/3)*(-E + V_r)/(-V_l +
    V_r)**(2/3))*airybi(L_x**(2/3)*(-E + V_l)/(-V_l + V_r)**(2/3)) + 2**(1/3)*(-V_l + V_r)
    **(2/3)*airyaiprime(L_x**(2/3)*(-E + V_l)/(-V_l + V_r)**(2/3))*airybiprime(L_x**(2/3)*(-E
    + V_r)/(-V_l + V_r)**(2/3)) - 2**(1/3)*(-V_l + V_r)**(2/3)*airyaiprime(L_x**(2/3)*(-E +
    V_r)/(-V_l + V_r)**(2/3))*airybiprime(L_x**(2/3)*(-E + V_l)/(-V_l + V_r)**(2/3)))
```

Expression for Matlab and Octave:

```
2*2^(1/3)*1i*L_x.^(1/3).*k.*(-V_l + V_r).^(1/3).*(airy(0, L_x.^(2/3).*(-E + V_l)./(-V_l + V_r)
    .^(2/3)).*airy(3, L_x.^(2/3).*(-E + V_l)./(-V_l + V_r).^(2/3)) - airy(1, L_x.^(2/3).*(-E +
     V_l)./(-V_l + V_r).^(2/3)).*airy(2, L_x.^(2/3).*(-E + V_l)./(-V_l + V_r).^(2/3))).*exp(-1
    i*L_x.*k)./(2^(1/3)*L_x.^(2/3).*k.^2.*airy(0, L_x.^(2/3).*(-E + V_l)./(-V_l + V_r).^(2/3))
    .*airy(2, L_x.^(2/3).*(-E + V_r)./(-V_l + V_r).^(2/3)) - 2^(1/3)*L_x.^(2/3).*k.^2.*airy(0,
     L_x.^(2/3).*(-E + V_r)./(-V_l + V_r).^(2/3)).*airy(2, L_x.^(2/3).*(-E + V_l)./(-V_l + V_r
    ).^(2/3)) + 2^(1/3)*1i*L_x.^(1/3).*k.*(-V_l + V_r).^(1/3).*airy(0, L_x.^(2/3).*(-E + V_l)
    ./(-V_l + V_r).^(2/3)).*airy(3, L_x.^(2/3).*(-E + V_r)./(-V_l + V_r).^(2/3)) + 2^(1/3)*1i*
    L_x.^(1/3).*k.*(-V_l + V_r).^(1/3).*airy(0, L_x.^(2/3).*(-E + V_r)./(-V_l + V_r).^(2/3)).*
    airy(3, L_x.^(2/3).*(-E + V_l)./(-V_l + V_r).^(2/3)) - 2^(1/3)*1i*L_x.^(1/3).*k.*(-V_l +
    V_r).^(1/3).*airy(1, L_x.^(2/3).*(-E + V_l)./(-V_l + V_r).^(2/3)).*airy(2, L_x.^(2/3).*(-E
     + V_r)./(-V_l + V_r).^(2/3)) - 2^(1/3)*1i*L_x.^(1/3).*k.*(-V_l + V_r).^(1/3).*airy(1, L_x
    .^(2/3).*(-E + V_r)./(-V_l + V_r).^(2/3)).*airy(2, L_x.^(2/3).*(-E + V_l)./(-V_l + V_r)
    .^(2/3)) + 2^(1/3)*(-V_l + V_r).^(2/3).*airy(1, L_x.^(2/3).*(-E + V_l)./(-V_l + V_r)
    .^(2/3)).*airy(3, L_x.^(2/3).*(-E + V_r)./(-V_l + V_r).^(2/3)) - 2^(1/3)*(-V_l + V_r)
    .^(2/3).*airy(1, L_x.^(2/3).*(-E + V_r)./(-V_l + V_r).^(2/3)).*airy(3, L_x.^(2/3).*(-E +
    V_l)./(-V_l + V_r).^(2/3)))
```

Expression for Mathematica:

```
2*2^(1/3)*I*L_x^(1/3)*k*(-V_l + V_r)^(1/3)*(AiryAi[L_x^(2/3)*(-E + V_l)/(-V_l + V_r)^(2/3)]*
    AiryBiPrime[L_x^(2/3)*(-E + V_l)/(-V_l + V_r)^(2/3)] - AiryAiPrime[L_x^(2/3)*(-E + V_l)/(-
    V_l + V_r)^(2/3)]*AiryBi[L_x^(2/3)*(-E + V_l)/(-V_l + V_r)^(2/3)])*Exp[-I*L_x*k]/(2^(1/3)*
    L_x^(2/3)*k^2*AiryAi[L_x^(2/3)*(-E + V_l)/(-V_l + V_r)^(2/3)]*AiryBi[L_x^(2/3)*(-E + V_r)
    /(-V_l + V_r)^(2/3)] - 2^(1/3)*L_x^(2/3)*k^2*AiryAi[L_x^(2/3)*(-E + V_r)/(-V_l + V_r)
    ^(2/3)]*AiryBi[L_x^(2/3)*(-E + V_l)/(-V_l + V_r)^(2/3)] + 2^(1/3)*I*L_x^(1/3)*k*(-V_l +
    V_r)^(1/3)*AiryAi[L_x^(2/3)*(-E + V_l)/(-V_l + V_r)^(2/3)]*AiryBiPrime[L_x^(2/3)*(-E + V_r
    )/(-V_l + V_r)^(2/3)]*AiryBiPrime[L_x^(2/3)*(-E + V_l)/(-V_l + V_r)^(2/3)] - 2^(1/3)*I*
    L_x^(1/3)*k*(-V_l + V_r)^(1/3)*AiryAiPrime[L_x^(2/3)*(-E + V_l)/(-V_l + V_r)^(2/3)]*AiryBi
    [L_x^(2/3)*(-E + V_r)/(-V_l + V_r)^(2/3)] - 2^(1/3)*I*L_x^(1/3)*k*(-V_l + V_r)^(1/3)*
    AiryAiPrime[L_x^(2/3)*(-E + V_r)/(-V_l + V_r)^(2/3)]*AiryBi[L_x^(2/3)*(-E + V_l)/(-V_l +
    V_r)^(2/3)] + 2^(1/3)*(-V_l + V_r)^(2/3)*AiryAiPrime[L_x^(2/3)*(-E + V_l)/(-V_l + V_r)
    ^(2/3)]*AiryBiPrime[L_x^(2/3)*(-E + V_r)/(-V_l + V_r)^(2/3)] - 2^(1/3)*(-V_l + V_r)^(2/3)*
    AiryAiPrime[L_x^(2/3)*(-E + V_r)/(-V_l + V_r)^(2/3)]*AiryBiPrime[L_x^(2/3)*(-E + V_l)/(-
    V_l + V_r)^(2/3)])
```

Expression for Maple:

```
2*2^(1/3)*I*L_x^(1/3)*k*(-V_l + V_r)^(1/3)*(AiryAi(L_x^(2/3)*(-E + V_l)/(-V_l + V_r)^(2/3))*
    airybiprime(L_x^(2/3)*(-E + V_l)/(-V_l + V_r)^(2/3)) - airyaiprime(L_x^(2/3)*(-E + V_l)/(-
    V_l + V_r)^(2/3))*AiryBi(L_x^(2/3)*(-E + V_l)/(-V_l + V_r)^(2/3)))*exp(-I*L_x*k)/(2^(1/3)*
    L_x^(2/3)*k^2*AiryAi(L_x^(2/3)*(-E + V_l)/(-V_l + V_r)^(2/3))*AiryBi(L_x^(2/3)*(-E + V_r)
    /(-V_l + V_r)^(2/3)) - 2^(1/3)*L_x^(2/3)*k^2*AiryAi(L_x^(2/3)*(-E + V_r)/(-V_l + V_r)
    ^(2/3))*AiryBi(L_x^(2/3)*(-E + V_l)/(-V_l + V_r)^(2/3)) + 2^(1/3)*I*L_x^(1/3)*k*(-V_l +
    V_r)^(1/3)*AiryAi(L_x^(2/3)*(-E + V_l)/(-V_l + V_r)^(2/3))*airybiprime(L_x^(2/3)*(-E + V_r
    )/(-V_l + V_r)^(2/3)) + 2^(1/3)*I*L_x^(1/3)*k*(-V_l + V_r)^(1/3)*AiryAi(L_x^(2/3)*(-E +
    V_r)/(-V_l + V_r)^(2/3))*airybiprime(L_x^(2/3)*(-E + V_l)/(-V_l + V_r)^(2/3)) - 2^(1/3)*I*
    L_x^(1/3)*k*(-V_l + V_r)^(1/3)*airyaiprime(L_x^(2/3)*(-E + V_l)/(-V_l + V_r)^(2/3))*AiryBi
    (L_x^(2/3)*(-E + V_r)/(-V_l + V_r)^(2/3)) - 2^(1/3)*I*L_x^(1/3)*k*(-V_l + V_r)^(1/3)*
    airyaiprime(L_x^(2/3)*(-E + V_r)/(-V_l + V_r)^(2/3))*AiryBi(L_x^(2/3)*(-E + V_l)/(-V_l +
    V_r)^(2/3)) + 2^(1/3)*(-V_l + V_r)^(2/3)*airyaiprime(L_x^(2/3)*(-E + V_l)/(-V_l + V_r)
    ^(2/3))*airybiprime(L_x^(2/3)*(-E + V_r)/(-V_l + V_r)^(2/3)) - 2^(1/3)*(-V_l + V_r)^(2/3)*
    airyaiprime(L_x^(2/3)*(-E + V_r)/(-V_l + V_r)^(2/3))*airybiprime(L_x^(2/3)*(-E + V_l)/(-
    V_l + V_r)^(2/3)))
```

A.3 Aharonov-Bohm Interferometer

A.3.1 Reflection Coefficient $s_{11} = s_{22}$

Expression for Python's SymPy package:

```
-(-exp(I*Phi) + exp(I*(sqrt(E)*delta d + 2*Phi)) - exp(I*(2*sqrt(E)*delta d + Phi)) + exp(I*
    sqrt(E)*delta d))*exp(I*sqrt(E)*d_{})/(-4*exp(I*Phi) + exp(I*(2*sqrt(E)*d_{} + Phi)) + exp
    (I*(sqrt(E)*delta d + 2*sqrt(E)*d_{} + 2*Phi)) + exp(I*(2*sqrt(E)*delta d + 2*sqrt(E)*d_{}
     + Phi)) + exp(I*sqrt(E)*(delta d + 2*d_{})))
```

Expression for Matlab and Octave:

```
-(-exp(1i*Phi) + exp(1i*(sqrt(E).*delta d + 2*Phi)) - exp(1i*(2*sqrt(E).*delta d + Phi)) + exp
    (1i*sqrt(E).*delta d)).*exp(1i*sqrt(E).*d_{})./(-4*exp(1i*Phi) + exp(1i*(2*sqrt(E).*d_{} +
     Phi)) + exp(1i*(sqrt(E).*delta d + 2*sqrt(E).*d_{} + 2*Phi)) + exp(1i*(2*sqrt(E).*delta d
     + 2*sqrt(E).*d_{} + Phi)) + exp(1i*sqrt(E).*(delta d + 2*d_{})))
```

Expression for Mathematica:

```
-(-Exp[I*Phi] + Exp[I*(E^(1/2)*delta d + 2*Phi)] - Exp[I*(2*E^(1/2)*delta d + Phi)] + Exp[I*E
    ^(1/2)*delta d])*Exp[I*E^(1/2)*d_{}]/(-4*Exp[I*Phi] + Exp[I*(2*E^(1/2)*d_{} + Phi)] + Exp[
    I*(E^(1/2)*delta d + 2*E^(1/2)*d_{} + 2*Phi)] + Exp[I*(2*E^(1/2)*delta d + 2*E^(1/2)*d_{}
    + Phi)] + Exp[I*E^(1/2)*(delta d + 2*d_{})])
```

Expression for Maple:

```
-(-exp(I*Phi) + exp(I*(sqrt(E)*delta d + 2*Phi)) - exp(I*(2*sqrt(E)*delta d + Phi)) + exp(I*
    sqrt(E)*delta d))*exp(I*sqrt(E)*d_{})/(-4*exp(I*Phi) + exp(I*(2*sqrt(E)*d_{} + Phi)) + exp
    (I*(sqrt(E)*delta d + 2*sqrt(E)*d_{} + 2*Phi)) + exp(I*(2*sqrt(E)*delta d + 2*sqrt(E)*d_{}
     + Phi)) + exp(I*sqrt(E)*(delta d + 2*d_{})))
```

A.3.2 Left to Right Transmission Coefficient s_{21}

Expression for Python's SymPy package:

```
2*(-exp(I*(sqrt(E)*delta d + Phi)) + exp(I*(sqrt(E)*delta d + 2*sqrt(E)*d_{} + Phi)) + exp(2*I*
    sqrt(E)*(delta d + d_{})) - 1)*exp(I*Phi)/(-4*exp(I*Phi) + exp(I*(2*sqrt(E)*d_{} + Phi)) +
     exp(I*(sqrt(E)*delta d + 2*sqrt(E)*d_{} + 2*Phi)) + exp(I*(2*sqrt(E)*delta d + 2*sqrt(E)*
    d_{} + Phi)) + exp(I*sqrt(E)*(delta d + 2*d_{})))
```

Expression for Matlab and Octave:

```
2*(-exp(1i*(sqrt(E).*delta d + Phi)) + exp(1i*(sqrt(E).*delta d + 2*sqrt(E).*d_{} + Phi)) + exp
    (2*1i*sqrt(E).*(delta d + d_{})) - 1).*exp(1i*Phi)./(-4*exp(1i*Phi) + exp(1i*(2*sqrt(E).*
    d_{} + Phi)) + exp(1i*(sqrt(E).*delta d + 2*sqrt(E).*d_{} + 2*Phi)) + exp(1i*(2*sqrt(E).*
    delta d + 2*sqrt(E).*d_{} + Phi)) + exp(1i*sqrt(E).*(delta d + 2*d_{})))
```

Expression for Mathematica:

```
2*(-Exp[I*(E^(1/2)*delta d + Phi)] + Exp[I*(E^(1/2)*delta d + 2*E^(1/2)*d_{} + Phi)] + Exp[2*I*
    E^(1/2)*(delta d + d_{})] - 1)*Exp[I*Phi]/(-4*Exp[I*Phi] + Exp[I*(2*E^(1/2)*d_{} + Phi)] +
     Exp[I*(E^(1/2)*delta d + 2*E^(1/2)*d_{} + 2*Phi)] + Exp[I*(2*E^(1/2)*delta d + 2*E^(1/2)*
    d_{} + Phi)] + Exp[I*E^(1/2)*(delta d + 2*d_{})])
```

Expression for Maple:

```
2*(-exp(I*(sqrt(E)*delta d + Phi)) + exp(I*(sqrt(E)*delta d + 2*sqrt(E)*d_{} + Phi)) + exp(2*I*
    sqrt(E)*(delta d + d_{})) - 1)*exp(I*Phi)/(-4*exp(I*Phi) + exp(I*(2*sqrt(E)*d_{} + Phi)) +
     exp(I*(sqrt(E)*delta d + 2*sqrt(E)*d_{} + 2*Phi)) + exp(I*(2*sqrt(E)*delta d + 2*sqrt(E)*
    d_{} + Phi)) + exp(I*sqrt(E)*(delta d + 2*d_{})))
```

A.3.3 Right to Left Transmission Coefficient s_{12}

Expression for Python's SymPy package:

```
2*(-exp(I*Phi) + exp(I*(2*sqrt(E)*delta d + 2*sqrt(E)*d_{} + Phi)) - exp(I*sqrt(E)*delta d) +
    exp(I*sqrt(E)*(delta d + 2*d_{})))/(-4*exp(I*Phi) + exp(I*(2*sqrt(E)*d_{} + Phi)) + exp(I
    *(sqrt(E)*delta d + 2*sqrt(E)*d_{} + 2*Phi)) + exp(I*(2*sqrt(E)*delta d + 2*sqrt(E)*d_{} +
     Phi)) + exp(I*sqrt(E)*(delta d + 2*d_{})))
```

Expression for Matlab and Octave:

```
2*(-exp(1i*Phi) + exp(1i*(2*sqrt(E).*delta d + 2*sqrt(E).*d_{} + Phi)) - exp(1i*sqrt(E).*delta
    d) + exp(1i*sqrt(E).*(delta d + 2*d_{}))./(-4*exp(1i*Phi) + exp(1i*(2*sqrt(E).*d_{} + Phi
    )) + exp(1i*(sqrt(E).*delta d + 2*sqrt(E).*d_{} + 2*Phi)) + exp(1i*(2*sqrt(E).*delta d +
    2*sqrt(E).*d_{} + Phi)) + exp(1i*sqrt(E).*(delta d + 2*d_{})))
```

Expression for Mathematica:

```
2*(-Exp[I*Phi] + Exp[I*(2*E^(1/2)*delta d + 2*E^(1/2)*d_{} + Phi)] - Exp[I*E^(1/2)*delta d] +
    Exp[I*E^(1/2)*(delta d + 2*d_{})])/(-4*Exp[I*Phi] + Exp[I*(2*E^(1/2)*d_{} + Phi)] + Exp[I
    *(E^(1/2)*delta d + 2*E^(1/2)*d_{} + 2*Phi)] + Exp[I*(2*E^(1/2)*delta d + 2*E^(1/2)*d_{} +
     Phi)] + Exp[I*E^(1/2)*(delta d + 2*d_{})])
```

Expression for Maple:

```
2*(-exp(I*Phi) + exp(I*(2*sqrt(E)*delta d + 2*sqrt(E)*d_{} + Phi)) - exp(I*sqrt(E)*delta d) +
    exp(I*sqrt(E)*(delta d + 2*d_{})))/(-4*exp(I*Phi) + exp(I*(2*sqrt(E)*d_{} + Phi)) + exp(I
    *(sqrt(E)*delta d + 2*sqrt(E)*d_{} + 2*Phi)) + exp(I*(2*sqrt(E)*delta d + 2*sqrt(E)*d_{} +
     Phi)) + exp(I*sqrt(E)*(delta d + 2*d_{})))
```

Numerical Examples of Quantum Trajectories and Current Integrals

B

Chapter 5 describes the implementation of a solver for specific stochastic Schrödinger equations that is designed to treat wave packet time evolutions of scattering problems. In Section 5.2, the probability current method is presented, which is the key to the linearly scaling algorithm. In Section 5.3, the integration of stochastically occurring quantum measurements with this algrithm is presented.

This Appendix discusses numerical examples to clarify the formulas given in the main text. The example system chosen here consists of an approximately circular dot with two leads attached (Fig. B.1). The leads continue infinitely in positive and negative x direction. The probability current $\mathcal{I}$ that flows into each of the leads is calculated at the two sites $(-25, 0)$ and $(25, 0)$. The observable used to model decoherence measures whether the particle is located in the green, orange, blue or red region (Fig. B.1) or in the leads. The four projectors $\hat{\boldsymbol{P}}_1$, $\hat{\boldsymbol{P}}_2$, $\hat{\boldsymbol{P}}_3$, $\hat{\boldsymbol{P}}_4$ project onto the respective colored region, the projector $\hat{\boldsymbol{P}}_0$ projects onto the leads.

The unitary time evolution of the wave function using the reduced site basis representation is shown in Fig. B.2. In this figure, time passes from top to bottom. The plots in the middle column show snapshots of the probability density distribution within the region of interest. The left and right columns show the integrated probability current $\mathcal{Q}_\mathrm{L}$ for the left lead and $\mathcal{Q}_\mathrm{R}$ for the right lead according to Eq. 5.11. At $t = 0$, in the top of the figure, a Gaussian wave packet is prepared in the left lead. Both probability current integrals start with a value of zero, because the entire probability density is located within the region of interest. During the time evolution the wave packet travels to the dot in the center ($t \approx 5$), moves through it ($t \approx 10$) and is then transmitted mostly transmitted ($t \approx 15$). The transmitted wave packet moves though the right lead and

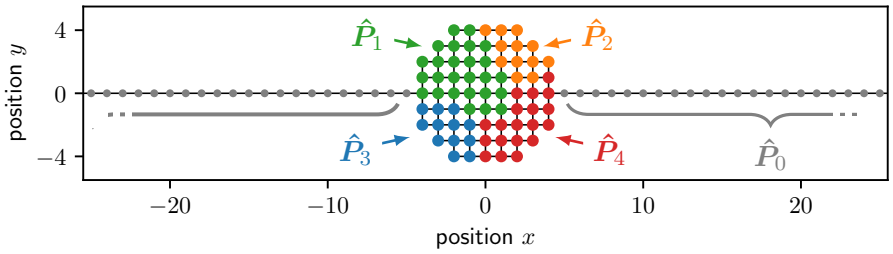


Figure B.1: Sketch of the tight-binding system used throughout this Appendix. The system is identical to the one presented in Fig. 5.5. The leads continue infinitely to the left and right, the lattice sites onto which individual projectors project, are visualized by the site colors.

finally leaves the region of interest ($t \approx 20 \ldots 25$). After it left the region of interest, the detailed probability density is not anymore accessible numerically. Only its total probability is known, which is captured by the respective probability current integral, $\mathcal{Q}_\mathrm{R} \approx 0.6$ in this case. Looking closely, one can see that a small fraction of $\approx 10\,\%$ of the wave packet was reflected during $t \approx 15 \ldots 20$. The rest of the wave packet is still moving within the dot.

To obtain the total transmission and reflection probabilities for the wave packet under consideration, the time evolution has to be calculated until the total probability within the region of interest has dropped below an acceptable error margin, e.g. $1\,\%$, $0.1\,\%$ or even $0.01\,\%$. The lower this threshold, the longer and therefore more calculationally expensive the time evolution becomes. After such a sufficiently long time evolution, the current integrals $\mathcal{Q}_\mathrm{L}$ and $\mathcal{Q}_\mathrm{R}$ yield the transmission and reflection probabilities of the wave packet.

To now implement the stochastic occurrence of quantum measurements into these time evolutions, it is required to apply site basis projection operators to the reduced site basis wave functions. Figure B.3 demonstrates the projectors' effect on an example wave function. The five different measurement outcomes occur with the probabilities $25\,\%$ for $\hat{\boldsymbol{P}}_0$, $10\,\%$ for $\hat{\boldsymbol{P}}_1$, $28\,\%$ for $\hat{\boldsymbol{P}}_2$, for $25\,\%$ for $\hat{\boldsymbol{P}}_3$ and $11\,\%$ for $\hat{\boldsymbol{P}}4$. The projected wave function is localized to the respective region. Applying the projectors $\hat{\boldsymbol{P}}_{1\ldots4}$ is as straightforward as performing a matrix multiplication according to Eq. 5.24. Applying $\hat{\boldsymbol{P}}_0$ is a special case, which requires more than a simple matrix multiplication, because the wave function outside the region of interest has to be maintained after the projection. The formula to obtain the correct eigenbasis representation is given by Eq. 5.25.

Bringing together the time evolution in the reduced site basis representation and the projection operators permits to calculate quantum trajectories that correspond to a Lindblad master equation. In the following two selected examples of such quantum trajectories are shown that demonstrate the effect of projection and renormalization on the wave functions and the current integrals.

Figure B.4 shows a quantum trajectory in analogy to Fig. B.2. The time evolution is indeed identical to the one shown in Fig. B.2 until $t \approx 28$. At this time, the wave packet has already partially left into the right leads, as indicated by the finite values of the current integrals. Then a quantum measurement occurs and one of the five projectors is randomly chosen according to the Born rule. Here, the very unlikely case of $\hat{\boldsymbol{P}}_3$ being chosen is shown, because it demonstrates particularly well how the post-measurement renormalization works. This event only occurs with a probability of $0.2\,\%$, but of course it is still relevant for the total transmission probability.

As seen in Fig. B.4b at $t \approx 28$, the post-measurement wave function is completely localized in the lower left corner of the dot now. After obtaining the measurement result we know that the particle is located within this region. The probability density in this region has therefore dramatically increased as compared to before the measurement. The probability current integrals, however, do not capture this event by themselves. If the values before the measurement event were left unchanged, the total probability given by the sum of $\mathcal{Q}_\mathrm{L}$, $\mathcal{Q}_\mathrm{R}$ and the total probability in the region of interest, would

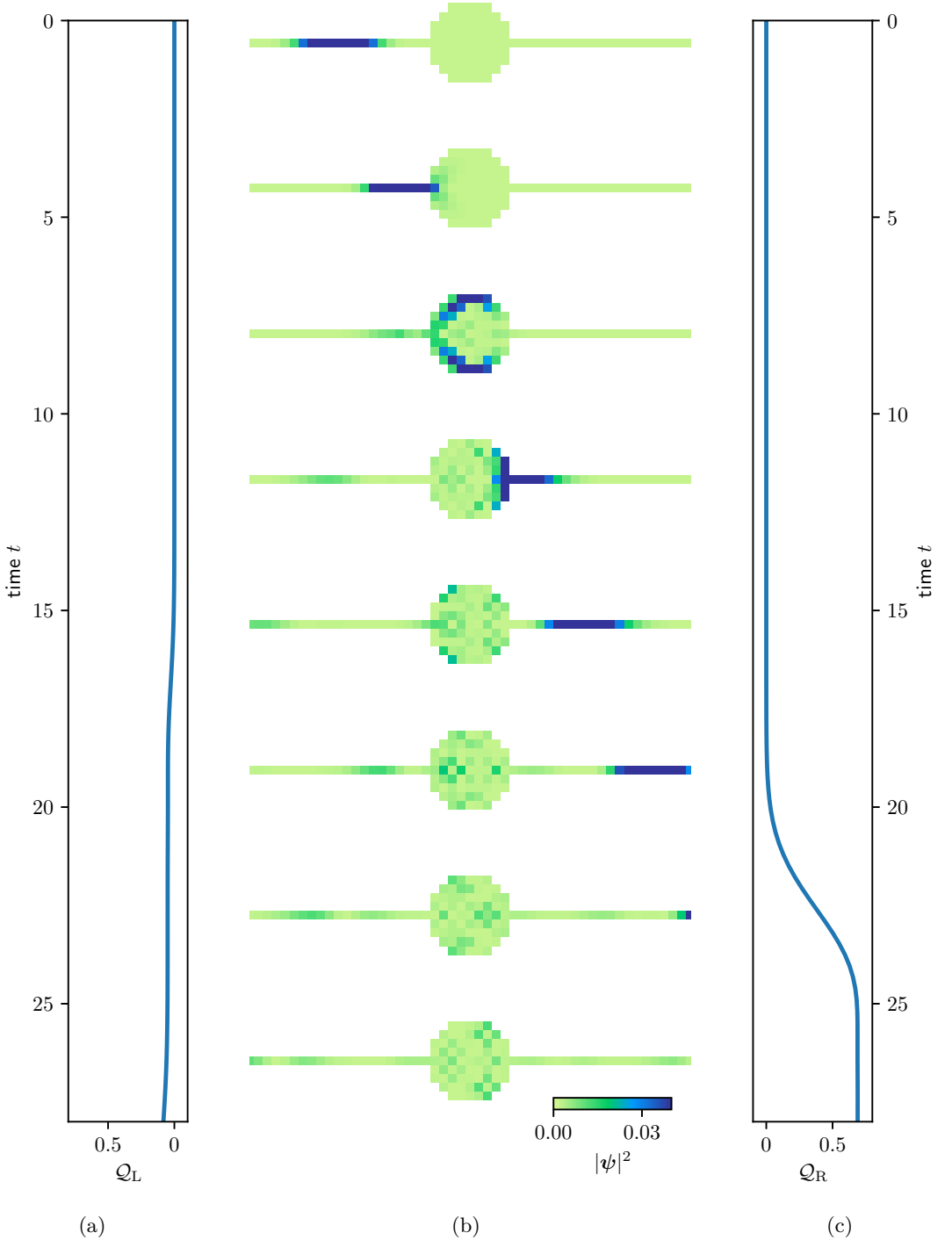


Figure B.2: Plot of the unitary time evolution of a wave packet passing from left to right through an approximately circular dot, plotted in the reduced site basis representation. (b) The site basis representation of the wave function is known at the shown sites only. (a,c) For the other sites, only the total probability is known from the integrated probability currents $\mathcal{Q}_\mathrm{L}$ and $\mathcal{Q}_\mathrm{R}$.

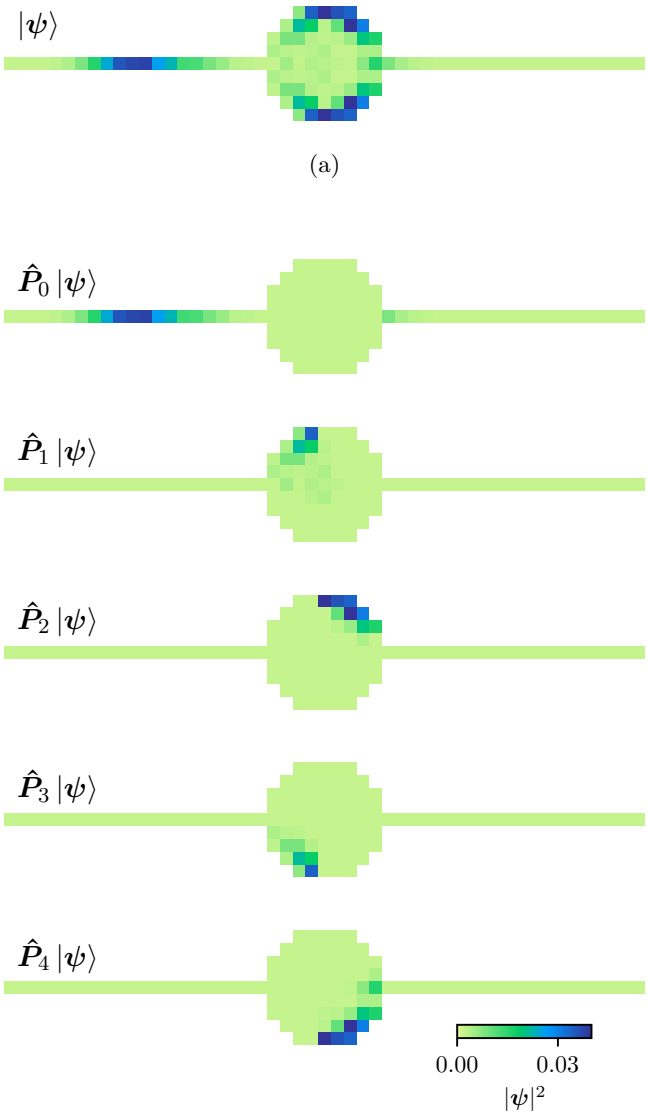


Figure B.3: Plots of the probability density distribution for an exemplary initial wave function ψ and possible outcomes of a quantum measurement. (a) Initially, the probability density is spread across the dot and the leads. (b) A quantum measurement of the observable shown in Fig. B.1 has five possible outcomes corresponding to the five projection operators. The probability of each outcome is given by the squared norm of the projected wave function $|\hat{P}_m |\psi\rangle|^2$. To obtain a physically sensible wave function, renormalization is required after the projection.

be greater than 1. Because the total probability of the wave function within the region of interest is 1 now, we have to reset the current integral values to zero in this case, as seen in Figs. B.4a and B.4c at $t \approx 28$. After this, the usual unitary time evolution and the smooth current integrals proceed to describe the evolution of $\boldsymbol{\psi}$, $\mathcal{Q}_{\mathrm{L}}$ and $\mathcal{Q}_{\mathrm{R}}$.

Again, the case of $\hat{\boldsymbol{P}}_0$ represents a special case for the renormalization procedure, because the post-measurement wave function partially resides within the region of interest, partially within the leads. The pre-measurement values of the current integrals therefore must not be discarded and set to zero. Instead, the renormalization factor has to be calculated according to Eq. 5.27 or Eq. 5.28. This factor is then applied to the previous values of the current integrals, as well as to the wave function in the region of interest, as given by Eq. 5.26. In Fig. B.5, this can be observed at $t \approx 24$. Until this time the evolution matches the unitary evolution shown in Fig. B.2. At $t \approx 24$, the wave packet partially left the region of interest through the right lead and partially remained in the dot. Then, a quantum measurement occurred resulting in the eigenvalue corresponding to the projector $\hat{\boldsymbol{P}}_0$. The wave function is set to zero inside the dot according to this projection, as shown in the latest wave function plot in Fig. B.5b. Again, leaving the current integrals $\mathcal{Q}_{\mathrm{L}}$ and $\mathcal{Q}_{\mathrm{R}}$ unchanged would lead to a deviation of the sum of all probabilities from 1. The renormalization redistributes the probability removed from the region of interest to the values of the current integrals according to the previous value of the integral. For $\mathcal{Q}_{\mathrm{R}}$ the step-like increase is therefore clearly visible, for $\mathcal{Q}_{\mathrm{L}}$ it is a bit harder to spot. But indeed, the same renormalization factor has been applied to the wave function and both current integrals.

These examples explained the use of the equations given in Sections 5.2 and 5.3 with numerical examples.

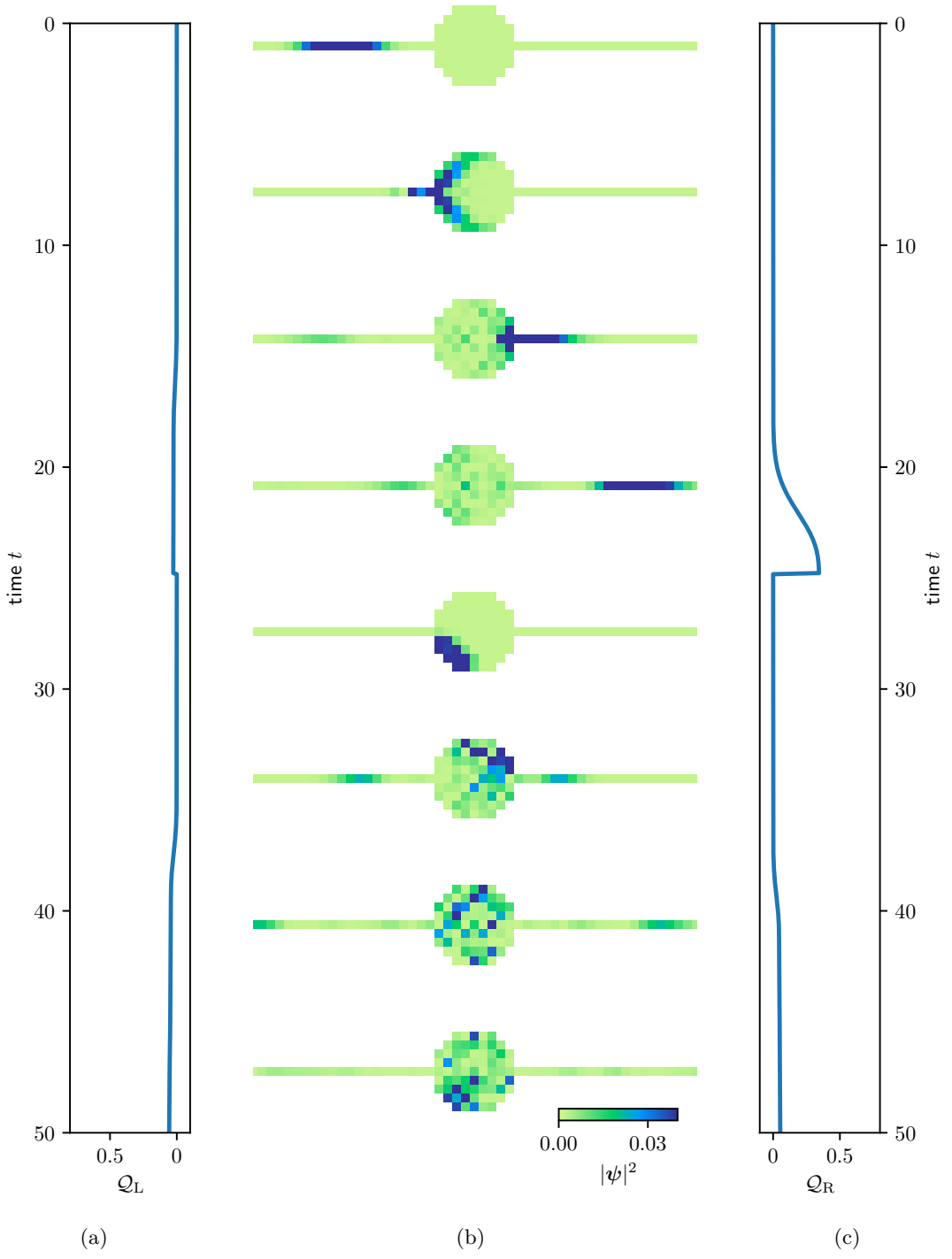


Figure B.4: Plot of the nonunitary time evolution of a wave packet in the reduced site basis representation analogous to Fig. B.2. (b) The site basis representation of the wave function is known at the shown sites only. (a,c) For the other sites, only the total probability is known from the integrated probability currents $\mathcal{Q}_\mathrm{L}$ and $\mathcal{Q}_\mathrm{R}$. At $t \approx 28$, a the occurrence of a quantum measurement discontinuously changes the wave function and current integrals.

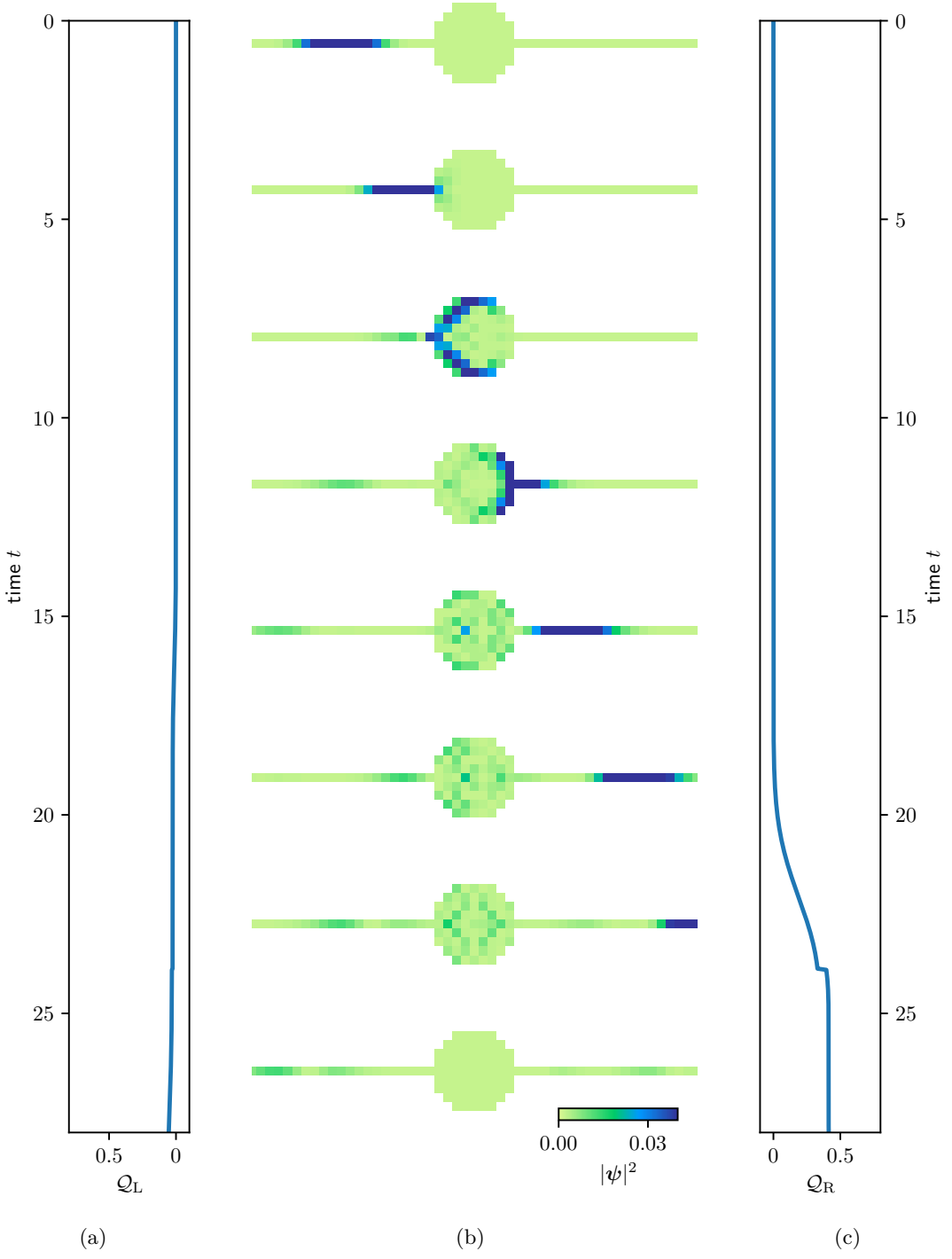


Figure B.5: Plot of the time evolution of a wave packet in the reduced site basis representation analogous to Figs. B.2 and B.4. (b) The site basis representation of the wave function is known at the shown sites only. (a,c) For the other sites, only the total probability is known from the integrated probability currents $\mathcal{Q}_\mathrm{L}$ and $\mathcal{Q}_\mathrm{R}$. At $t \approx 24$, the occurrence of a quantum measurement discontinuously changes the wave function and current integrals.

Fabrication Recipes

C

The sample boxes, labbooks etc. use the naming scheme `PBRxyz` for samples, where `xyz` is a three digit number. The correspondence to the naming scheme in this thesis is:

- sample $\mathbb{A}$ is `PBR067`
- sample $\mathbb{B}$ is `PBR064`
- sample $\mathbb{C}$ is `PBR068`
- sample $\mathbb{D}$ is `PBR061`

The fabrication recipes for samples $\mathbb{A}$, $\mathbb{B}$, $\mathbb{C}$ and $\mathbb{D}$ are mostly identical, therefore they are reported here as one single recipe. The steps in which parameters, chemicals or materials differed between the samples are indicated. If not denoted otherwise, each step in the recipe was applied to all 4 samples in the same fashion.

1. **Substrates:** undoped silicon $\langle 1\,0\,0 \rangle$ substrates measuring $5\,\text{mm} \times 5\,\text{mm} \times 0.525\,\text{mm}$ were picked from the stock
2. **SiO_2 sputtering (only sample $\mathbb{B}$ and $\mathbb{D}$):**
   - The samples were cleaned by rinsing with acetone, rinsing with isopropanol and N_2 blow drying
   - The samples were glued to a silicon wafer with AZ 1512 HS photoresist, baked at $150\,^\circ\text{C}$ for 60 min and mounted in the sputtering chamber
   - SiO_2 sputtering at 200 W RF power for 10 min, resulting in $\approx 100\,\text{nm}$ SiO_2
   - The wafer with the glued sample(s) was soaked in acetone, until the samples could be removed
   - The samples were cleaned by rinsing with acetone, rinsing with isopropanol and N_2 blow drying
3. **Spin coating:**
   - The samples were cleaned by ultrasonic cleaning in acetone, rinsing with acetone, ultrasonic cleaning in isopropanol, rinsing with isopropanol and N_2 blow drying
   - Spincoating of Allresist AR-p 6200.09 at $4000\,\text{min}^{-1}$
   - Softbake on hotplate at $150\,^\circ\text{C}$ for 1 min

4. **EBL exposure:**
   - Layout layer: "contact", layout file sample 𝔸 and ℂ: `PBRL014`, sample 𝔹: `PBRL013`, sample 𝔻: `PBRL011`,
   - Point spread function file used for proximity effect correction: `Si-320nmZEP-100kv176nm.xrz`
   - Machine: JEOL JBX-6300FS, 100 kV accelerating voltage, 2 nA beam current, 500 µm write field size, 70 µC cm^{-2} area dose, shot pitch 20 nm
5. **Development:**
   - Prepare four beakers: 1×AR 600-548, 3×AR 600-60
   - 1 min dip in AR 600-548, ≈ 10 s dip in each AR 600-60 beaker, rinsing with isopropanol and N_2 blow drying (The four beakers were reused for up to 4 samples of one batch)
6. **Thermal evaporation** in Oerlikon Leybold Univex 350:
   - Sample 𝔸 and ℂ: 5 nm Cr, then 100 nm AuPd 60/40 alloy
   - Sample 𝔹: 5 nm Ti, then 100 nm AuPd 60/40 alloy
   - Sample 𝔻: 5 nm Cr, then 50 nm AuPd 60/40 alloy
7. **Lift-off:**
   - Generally: never take the sample out of the liquid before the entire surface looks clean!
   - Sample 𝔸 and ℂ: ultrasonic bath at lowest available power at room temperature in AR 600-71 for 20 s
   - Sample 𝔹: ultrasonic bath at lowest available power in AR 600-71 at 45 °C for 10 min
   - Sample 𝔻: ultrasonic bath at lowest available power in AR 300-70 at 65 °C for 30 min
   - All samples: cleaning by rinsing with acetone, acetone dip (≈ 10 s) switched to clean tweezers, rinsing with acetone, isopropanol dip (≈ 10 s), rinsing with isopropanol, N_2 blow drying and O_2 cleaning plasma for 60 s
8. **Spin coating:**
   - Spincoating of Allresist AR-p 6200.09 at 4000 min^{-1}
   - Softbake on hotplate at 150 °C for 1 min

9. **EBL exposure:**
   - Layout layer: "structure", layout file sample 𝔸 and ℂ: `PBRL014`, sample 𝔹: `PBRL013`, sample 𝔻: `PBRL011`,
   - Point spread function file used for proximity effect correction: `Si-320nmZEP-100kv176nm.xrz`
   - Machine: JEOL JBX-6300FS, 100 kV accelerating voltage, 300 pA beam current, 500 µm write field size, 350 $\mu C\,cm^{-2}$ area dose, shot pitch 4 nm
10. **Development:**
    - Prepare four beakers: 1×AR 600-546, 3×AR 600-60
    - 1 min dip in AR 600-548, ≈ 10 s dip in each AR 600-60 beaker, rinsing with isopropanol and N_2 blow drying (The four beakers were reused for up to 4 samples of one batch)
11. **Thermal evaporation (sample 𝔸 only)** in Oerlikon Leybold Univex 350:
    - Deposited 20 nm of Au, pressure during deposition was 1×10^{-5} mbar
12. **Electron beam evaporation (sample 𝔹, ℂ and 𝔻 only):**
    - Loading sample into in 4C11, the vacuum cluster run by the group
    - Ar ion milling at 500 V accelerating voltage and 10 mA emission current for 6×10 s, with 20 s cooling breaks between iterations
    - Transferred sample to gate of electron beam evaporation chamber, ramped up Au crucible to $\approx 0.1\,nm\,s^{-1}$ deposition rate, adjusted l-N_2 flow rate through crypanels (if used), waited for 3 min, then transferred sample into the chamber and deposited 20 nm of Au
    - Pressure during deposition onto sample 𝔹 and ℂ was 1×10^{-8} mbar (with l-N_2 cooling), pressure during deposition onto sample 𝔻 was 8×10^{-8} mbar (without l-N2 cooling)

13. **Lift-off:**
    - Everything at room temperature, never take the sample out of the liquid before the entire surface looks clean!
    - Sample 𝔸: soaking in AR 600-71 for 5 min, repeatedly flushing with syringe (sample stays in liquid at all times) until sample looks clean
    - Sample 𝔹: soaking in AR 600-71 for 15 min, ultrasonic in same beaker for 1 min
    - Sample ℂ: soaking in AR 600-71 for 2 h, repeatedly flushing with syringe (sample stays in liquid at all times) until sample looks clean
    - Sample 𝔻: ultrasonic in AR 600-71 at lowest power for 10 s, soaking in same beaker for 2 h, ultrasonic in same beaker for 5 min
    - All samples: cleaning by rinsing with acetone, acetone dip ($\approx$ 10 s), switched to clean tweezers, rinsing with acetone, isopropanol dip ($\approx$ 10 s), rinsing with isopropanol and N_2 blow drying
14. **Electron microscopy:** taking pictures of all fabricated devices with Zeiss Merlin scanning electron microscope
15. **Wire bonding:** gluing sample to chip carrier, wire bonding with Al wire, stored samples in antistatic box after wire bonding
16. **Magnetotransport measurements:** in Quantum Design PPMS cryostat for RRR measurements and in Oxford Instruments Kelvinox AST Minisorb dilution refrigerator for quantum transport measurements